Development of Fluorescence-Enabled Electrochemical Microscopy for Electrochemical Imaging and Detection

Stephen Matthew Oja

A dissertation

submitted in partial fulfillment of the

requirements for the degree of

Doctor of Philosophy

University of Washington

2016

Reading Committee:

Bo Zhang, Chair

Joshua Vaughan

A.J. Boydston

Program Authorized to Offer Degree:

Chemistry

University of Washington

Abstract

Development of Fluorescence-Enabled Electrochemical Microscopy for Electrochemical Imaging and Detection

Stephen Matthew Oja

Chair of the Supervisory Committee:
Associate Professor Bo Zhang
Chemistry

This dissertation discusses various aspects of the fundamental development of fluorescence-enabled electrochemical microscopy (FEEM) into a useful analytical tool for electrochemical imaging and detection. Chapter 1 briefly introduces the technique of FEEM and discusses how it can be used to overcome current challenges in electrochemical imaging and low-level electrochemical sensing. Chapter 2 discusses the development of a new fluorogenic indicator reaction that makes possible the detection of electrochemical reduction reactions. This chapter also introduces a new fluorophore quenching scheme used to improve the spatial and temporal resolution of FEEM imaging. FEEM imaging is further developed in Chapter 3, which demonstrates the use of a bipolar electrode array to image dynamic concentration gradients in 2- and 3-dimensions. Chapter 4 moves on to a discussion of the use of electrogenerated chemiluminescence (ECL) as an optical reporter on closed bipolar electrodes as an alternative to

fluorescence. This chapter highlights the importance of carefully selecting the size-geometry of the bipolar electrode system when using an optical readout. Lastly, Chapters 5 and 6 introduce a redox particle detection scheme for use in quantifying the detection limit of FEEM. Chapter 5 focuses on the interesting coupled electrochemical and fluorescence properties of methylene blue-modified polystyrene microspheres. Chapter 6 discusses using single Ag nanoparticles for detection limit quantification and early attempts and problems in doing so. The chapter then closes with a discussion of the interesting dynamic behavior observed during the oxidation of single Ag nanoparticles.

TABLE OF CONTENTS

ACKNOWLEDGEMENTS

I first thank my research advisor, Dr. Bo Zhang, for his support and mentorship over the past several years. It has been a great learning experience working in his lab, from the first time I set foot in the lab as a summer undergraduate student until now. His excitement over new projects and encouragement to try out new things have motivated me to keep pushing to learn and strive for the next step. I'm grateful for the freedom I was given in lab and the mentorship I received that enabled me to grow as a scientist.

I also thank the members of the Zhang lab, past and present, for their support at various times. In particular, I thank Dr. Josh Guerrette for his mentorship and guidance and for teaching me the basics of electrochemistry and FEEM. I also thank Dr. Stephen Percival for his mentorship and teaching presence in the lab, Dr. Jin Lu for his helpful advice about microscopes and imaging, and Matthew Bates and Michelle David for their summer work on different aspects of the FEEM project.

I'm grateful for the support, advice, and guidance that my Ph.D. committee members, Dr. Joshua Vaughan, Dr. A.J. Boydston, and Dr. Lih Lin, have given me at various points throughout my studies. I also owe my appreciation to my undergraduate research advisor, Dr. Frank Keutsch, for the opportunity to get started in academic research and for his enthusiastic support. Going way back, I also must thank Mrs. Barb Makovec, the first chemistry teacher I ever had, for getting the ball rolling and encouraging me to follow this path.

There are various fellowships that I was lucky enough to receive during my studies that I owe my gratitude to. First is the Amgen Scholar Program, which enabled me to work for a summer as an undergraduate in an academic research lab. This lab turned out to be the Zhang

lab, so I really thank the Amgen Foundation for their support. I thank the donors who made the various fellowships from the UW chemistry department I received available, including the A. Bruce Montgomery Fellowship, the Tomas Hirschfeld Endowed Fellowship, the Dorothy Shimasaki Gilmer Endowed Fellowship, and the Alma Mater Travel Award. I also thank the Society for Electroanalytical Chemistry for their travel grant, the American Chemical Society Division of Analytical Chemistry and Eastman Chemical for their fellowship support, and the National Science Foundation for their support for the Lindau Nobel Laureate Meeting.

The last folks I thank are my family: My parents, Bob and Linda, for the upbringing they gave me and the confidence they instilled in me to pursue my goals; my siblings, Mike, Andy, and Katie for always supporting me and making life interesting; my grandparents, for their numerous life lessons and words of wisdom on enjoying life; my parents-in-law, Jim and Jenny, for the extra motivation to not let them down; and most importantly my wife, Jess, for continual support, motivation, sacrifice, advice, and everything else during the ups and downs of life.

LIST OF FIGURES

CHAPTER 1

Introduction*

1.1 Electrochemical Imaging

Imaging electrochemical processes with high spatial and temporal resolution is an important topic for a wide variety of chemical and biological applications, such as catalysis, transport, and neurochemistry. Most electrochemical imaging methods developed to date have been scanning probe techniques, such as scanning electrochemical microscopy (SECM).[1] SECM utilizes a micro- or nanoelectrode probe placed in close proximity to an interface of interest. This probe is then scanned over the interface to collect spatially resolved electrochemical information pertaining to it. Other similar scanning electrochemical probe techniques, such as scanning ion conductance microscopy (SICM),[2] scanning electrochemical cell microscopy (SECCM),[3] SECM-atomic force microscopy,[4] and SECM-SICM,[5,6] have been developed and used for a variety of imaging studies. Together, these scanning electrochemical probe techniques make a very useful suite of electrochemical imaging methods that have been applied to imaging a range of subjects, including biological cells,[7] electrocatalyst arrays,[8] surface corrosion,[9] nanopore transport,[10] and single nanoparticles.[11]

* Portions of this chapter are adapted with permission from:
Guerrette, J.P.; Oja, S.M.; Zhang, B. "Coupled electrochemical reactions at bipolar microelectrodes and nanoelectrodes." *Anal. Chem.* **2012**, *84*, 1609-1616. Copyright (2012) American Chemical Society.
Oja, S.M.; Wood, M.; Zhang, B. "Nanoscale electrochemistry." *Anal. Chem.* **2013**, *85*, 473-486. Copyright (2013) American Chemical Society.
Oja, S.M.; Fan, Y.; Armstrong, C.A.; Defnet, P.; Zhang, B. "Nanoscale electrochemistry revisited." *Anal. Chem.* **2016**, *88*, 414-430. Copyright (2016) American Chemical Society.

Despite their success in a wide array of studies, these scanning electrochemical probe techniques fall short of an ideal electrochemical imaging platform due to the necessity of scanning the probe over the sample to create an image. This scanning requirement creates a situation in which a compromise must be made between scan time, spatial resolution, and image area. An ideal platform would be capable of continuously imaging a large working area with high spatial resolution. One way of achieving this ideal platform would be using a large-area, high-density array of many individually and simultaneously addressable microelectrodes, where the current passing through each electrode could be independently monitored at the same time. Studies by various groups, particularly the Ewing group, have done this by fabricating arrays of microelectrodes and directly connecting each electrode to a separate data channel.[12,13,14] One of the better working devices published thus far consisted of 36 electrodes in a 30 μm x 30 μm array,[15] which was used to monitor the exocytosis of redox-active molecules from model neuronal cells grown on top of the array. However, increasing the number of electrodes in the array, which is desirable to increase the spatial resolution and/or size of the image, is limited by both fabrication challenges and the electronics and data acquisition required to simultaneously monitor a growing number of data channels. To significantly increase the number of addressable electrodes in an array, an alternative method of monitoring the current of each electrode is needed.

1.2 Single-Molecule Electrochemistry

Detection and analysis of single molecules represent the ultimate sensitivity in analytical chemistry. Single-molecule type experiments have several distinct advantages compared to bulk measurements, including the ability to observe true and detailed reaction mechanisms and the

ability to better understand molecular heterogeneity. Additionally, it can also be a gateway to new techniques, as demonstrated with single molecule detection via fluorescence being developed into super-resolution localization microscopy.[16] While single molecule detection has become routine in other analytical techniques, electrochemical detection of single molecules has proven to be more difficult. This is due to the difficulty of measuring the extremely small faradaic charge passed by a single electroactive molecule.

Two main methods of signal transduction have been used to study single redox molecules: direct electrical detection and optical detection. In order for direct electrical detection to work, some method of signal amplification is needed in which the number of electrons passed per unit time is significantly increased. A small handful of studies have successfully detected faradaic reactions of single redox molecules by using a thin-layer-cell geometry to achieve sufficient signal amplification via redox cycling. In this approach, two parallel electrodes are brought near each other (within 10-100 nm) and biased so that the analyte molecule is alternately reduced and oxidized. The small gap between the two electrodes enables the analyte molecule to undergo diffusion between the electrodes thousands to millions of times per second, resulting in significant charge amplification. This strategy was first employed by Fan and Bard,[17,18,19] later repeated by Sun and Mirkin,[20] and more recently taken up by the Lemay group.[21,22] While electrical detection enables a direct signal transduction pathway, it is not capable of detecting single faradaic reactions and therefore requires averaging over many redox events to produce a detectable signal.

Optical detection, on the other hand, is capable of detecting single faradaic reactions and can provide spatially resolved images of the location of those events. Fluorescence microscopy and surfaced-enhanced Raman scattering (SERS), both well-developed single-molecule

techniques, have been applied to electrochemistry by studying molecules that undergo a characteristic change in an optical property upon redox reaction, thus enabling the optical readout of electrochemical processes on a single-molecule level. In the most common scheme, a redox molecule will change fluorescence state (off to on or vice versa) upon electron transfer, thereby transferring the faradaic signal to the optical domain. Under appropriate conditions, this can be observed at the single-molecule level using standard fluorescence microscopy methods. The coupling of fluorescence state (on or off) to redox state (oxidized or reduced) was first utilized to study single-molecule electrochemistry by the groups of Bard and Barbara.[23,24] While these studies looked at the coupled electrochemical and fluorescence behavior of a conjugated polymer, the technique was soon demonstrated on small molecules by Ackerman and co-workers.[25,26] In an elegant display of how optical detection can give valuable spatial information, the Chen group used super-resolution microscopy to image the electrocatalytic reaction of single fluorogenic redox molecules on single-walled carbon nanotubes to reveal a heterogeneity in reactive sites along a single nanotube.[27] Other groups have since used similar fluorescence schemes to monitor single molecules undergoing single faradaic electron transfer events.[28,29,30] An analogous scheme has been applied to SERS imaging, whereby redox molecules that undergo a measurable change in their Raman spectrum upon faradaic reaction can be measured at the single-molecule level.[31,32]

A key difference between optical detection of single redox molecules and electrical detection via redox cycling is that the electrical signal from redox cycling is necessarily the average of many electron transfers ($>10^4$). Optical detection, on the other hand, enables the detection of single electron transfer events. However, only certain redox molecules have the requisite optical properties for detection, limiting these optical detection methods to only a

handful of redox molecules thus far. Therefore, a method capable of detecting single electron transfer events of any redox molecule is highly desirable.

1.3 Fluorescence-Enabled Electrochemical Microscopy

Recently, our group introduced[33] a technique termed fluorescence-enabled electrochemical microscopy (FEEM) that we believe is capable of overcoming the two challenges discussed in this introduction: First, using large arrays of individually addressable microelectrodes for electrochemical imaging, and second, detecting single electron transfer events of any redox molecule. Rather than directly monitoring the electrochemical current, FEEM uses a fluorogenic redox reaction to report the progress of a conventional, nonfluorogenic redox reaction of interest. The key concept of FEEM is the use of a closed bipolar electrode (BPE)[34,35,36] to electrically couple two separate redox reactions, one of which is fluorogenic, enabling the use of fluorescence microscopy to simultaneously visualize electrochemical signals on parallel electrodes. Bipolar electrodes have been of increasing interest to electroanalytical chemists over the past decade or so due to their unique properties.[37,38,39] One key property of bipolar electrodes is that no direct electrical connection is needed to drive the coupled reactions on the electrode. This wireless capability makes using large-scale arrays of bipolar electrodes technically simple.

Figure 1.1 shows the basic design of a closed BPE and closed BPE array. Two poles of a conductor are separated by an insulating membrane to form the BPE. A potential can be applied across two driving electrodes to drive coupled faradaic reactions at each pole of the BPE. We have shown that since the entire electrical current must pass through the electrode, it can be used to report the rates of faradaic processes occurring at the poles of the BPE.[40] Since

electroneutrality must be maintained, the rate of reaction at the two poles will be equivalent. Therefore, as shown in the initial report on FEEM,[33] the progress of a conventional redox reaction at one pole of a BPE can be reported by optically monitoring a fluorogenic redox reaction at the other pole. A unique feature of FEEM as compared to techniques used in other fluorescent voltammetry studies such as those mentioned in Section 1.2 is the use of fluorescence to optically monitor *non*fluorogenic redox reactions. Figure 1.2 illustrates the basic scheme used for the detection of a redox species using FEEM with a single bipolar electrode and a bipolar electrode array. Importantly, FEEM has enabled us to simultaneously monitor electrochemical reactions on large arrays containing *thousands* or more bipolar ultramicroelectrodes,[33] thus overcoming the challenge of simultaneously measuring the electrochemical signal on many parallel electrodes. Additionally, because FEEM relies on the readout of a fluorescence indicator molecule that can be detected at the single-molecule level by fluorescence microscopy, we believe that FEEM can be used to measure single electron transfer events of any redox molecule.

1.4 Overview of Chapters

This dissertation discusses both the development of FEEM for electrochemical imaging and the development of FEEM for low-level electrochemical sensing. Chapter 2 focuses on the development and implementation of a new fluorogenic indicator reaction for use in FEEM imaging. This new reaction enables the FEEM detection of reduction reactions, which was previously impossible due to the lack of a fluorogenic oxidation reaction. This new fluorogenic reaction scheme also introduces a novel fluorophore quenching method that improves the spatial and temporal resolution of the technique.

Chapter 3 focuses on using FEEM with an array of thousands of bipolar electrodes to image, in two and three dimensions, concentration gradients created on ultramicroelectrodes during dynamic electrochemistry experiments. This is the first technique shown capable of doing such imaging. This study also lays important groundwork for future FEEM imaging of concentration gradients relevant to areas outside of electrochemistry, such as the synaptic transmission of electroactive neurotransmitters from neuronal cells.

Chapter 4 focuses on the fundamentals of using electrogenerated chemiluminescence (ECL) as an optical indicator reaction in place of a fluorogenic reaction. In particular, we focus on how the size-geometry of a closed bipolar electrode can dramatically affect the optical signal despite having no effect on the electrochemical signal. This was a previously undiscussed phenomenon and is important for future sensing and imaging applications using bipolar electrodes with an ECL-based readout. Additionally, this study lays the groundwork for using ECL in an array-based imaging scheme analogous to that of Chapter 3.

Chapters 5 and 6 focus on novel methods to quantify the detection limit of FEEM. These represent early efforts to systematically study the detection limit of FEEM in order to begin lowering it to the single-molecule level. Both chapters focus on using the stochastic collision of large, redox-active nanoparticles with a detection electrode as a method to deliver a quantifiable number of electrons to the bipolar electrode in a discrete event. Chapter 5 discusses the preparation of methylene blue-modified polystyrene microspheres and the interesting coupled electrochemical and fluorescent properties that these modified microspheres possess. Chapter 6 discusses the use of Ag nanoparticles to quantify the FEEM detection limit and early attempts to do so. This chapter also discusses the interesting behavior of Ag nanoparticle electro-oxidation, which is observed on a single nanoparticle level to occur in a series of several small, discrete

steps rather than one large event. This behavior, though not yet fully understood, has been previously unobserved.

1.5 Figures

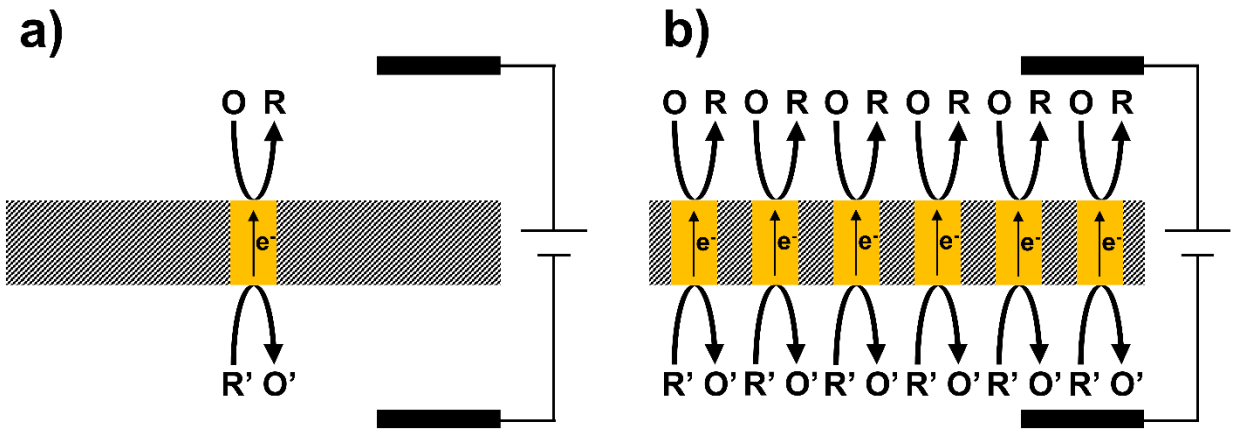

Figure 1.1. Scheme of a closed bipolar electrode and closed bipolar electrode array. Scheme of a single closed bipolar electrode (a) and an array of many closed bipolar electrodes (b). A potential applied across a bipolar electrode can drive coupled electrochemical reactions at each pole of the electrode. These reactions must occur at equivalent rates to ensure electroneutrality. Due to the wireless nature of bipolar electrodes, an array of these electrodes can be controlled in the same manner as a single electrode, with only a single simple voltage source needed.

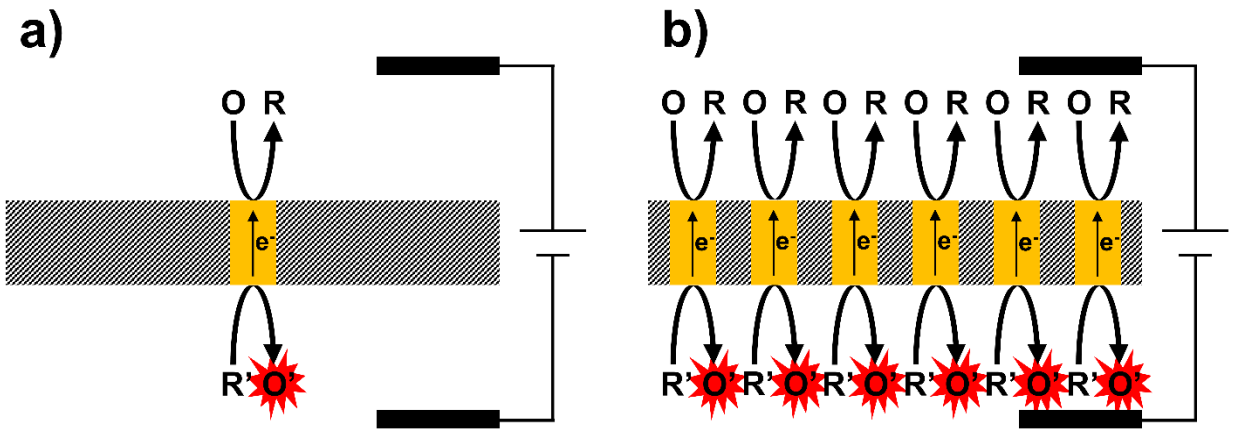

Figure 1.2. Scheme of FEEM at a single electrode and electrode array.
Scheme of FEEM using a single closed bipolar electrode (a) and an array of many closed bipolar electrodes (b). FEEM uses a fluorogenic redox reaction to report the current through a bipolar electrode. Since the coupled reactions occur at the same rate, the change in the fluorescence signal at an electrode is proportional to the current through the electrode. The progress of this fluorogenic redox reaction can be easily monitored using fluorescence microscopy. This enables one to simultaneously measure the electrochemical signal from many electrodes, enabling the use of large-scale electrode arrays for electrochemical imaging.

1.6 References

(1) Amemiya, S.; Bard, A.J.; Fan, F.-R.F.; Mirkin, M.V.; Unwin, P.R. *Annu. Rev. Anal. Chem.* **2008**, *1*, 95-131.

(2) Chen, C.-C.; Zhou, Y.; Baker, L. A. *Annu. Rev. Anal. Chem.* **2012**, *5*, 207−228.

(3) Ebejer, N.; Güell, A. G.; Lai, S. C. S.; McKelvey, K.; Snowden, M. E.; Unwin, P. R. *Annu. Rev. Anal. Chem.* **2013**, *6*, 329−351.

(4) Macpherson, J. V.; Unwin, P. R. *Anal. Chem.* **2000**, *72*, 276− 285.

(5) Takahashi, Y.; Shevchuk, A. I.; Novak, P.; Murakami, Y.; Shiku, H.; Korchev, Y. E.; Matsue, T. *J. Am. Chem. Soc.* **2010**, *132*, 10118− 10126.

(6) Comstock, D. J.; Elam, J. W.; Pellin, M. J.; Hersam, M. C. *Anal. Chem.* **2010**, *82*, 1270−1276.

(7) Schulte, A.; Nebel, M.; Schuhmann, W. *Annu. Rev. Anal. Chem.* **2010**, *3*, 299-318.

(8) Fernández, J.L.; Walsh, D.A.; Bard, A.J. *J. Am. Chem. Soc.* **2005**, *127*, 357-365.

(9) Serebrennikova, I.; Lee, S.; White, H.S. *Faraday Discuss.* **2002**, *121*, 199-210.

(10) Chen, C.-C.; Derylo, M.A.; Baker, L.A. *Anal. Chem.* **2009**, *81*, 4742-4751.

(11) O'Connell, M. A.; Wain, A. J. *Anal. Chem.* **2014**, *86*, 12100−12107.

(12) Zhang, B.; Adams, K.L.; Luber, S.J.; Eves, S.J.; Heien, M.L.; Ewing, A.G. *Anal. Chem.* **2008**, *80*, 1394-1400.

(13) Zhang, B.; Heien, M.L.A.V.; Santillo, M.F.; Mellander, L.; Ewing, A.G. *Anal. Chem.* **2011**, *83*, 571-577.

(14) Lin, Y.; Trouillon, R.; Svensson, M.I.; Keighron, J.D.; Cans, A.-S.; Ewing, A.G. *Anal. Chem.* **2012**, *84*, 2949-2954.

(15) Wang, J.; Trouillon, R.; Lin, Y.; Svensson, M.; Ewing, A.G. *Anal. Chem.* **2013**, *85*, 5600-5608.

(16) Moerner, W. E. *Angew. Chem., Int. Ed.* **2015**, *54*, 8067−8093

(17) Fan, F.R.F.; Bard, A.J. *Science* **1995**, *267*, 871-874.

(18) Bard, A.J.; Fan, F.R.F. *Acc. Chem. Res.* **1996**, *29*, 572-578.

(19) Fan, F.R.F.; Kwak, J.; Bard, A.J. *J. Am. Chem. Soc.* **1996**, *118*, 9669-9675.

(20) Sun, P.; Mirkin, M.V. *J. Am. Chem. Soc.* **2008**, *130*, 8241-8250.

(21) Zevenbergen, M.A.G.; Singh, P.S.; Goluch, E.D.; Wolfrum, B.L.; Lemay, S.G. *Nano Lett.* **2011**, *11*, 2881-2886.

(22) Lemay, S.G.; Kang, S.; Mathwig, K.; Singh, P.S. *Acc. Chem. Res.* **2013**, *46*, 369-377.

(23) Palacios, R. E.; Fan, F. -R. F.; Bard, A. J.; Barbara, P. F. *J. Am. Chem. Soc*. **2006**, 128, 9028−9029.

(24) Palacios, R. E.; Fan, F. -R. F.; Grey, J. K.; Suk, J.; Bard, A. J.; Barbara, P. F. *Nat. Mater.* **2007**, *6*, 680−685.

(25) Lei, C.; Hu, D.; Ackerman, E. J. *Chem. Commun.* **2008**, 5490− 5492.

(26) Lei, C.; Hu, D.; Ackerman, E. J. *Nano Lett.* **2009**, *9*, 655−658.

(27) Xu, W.; Shen, H.; Kim, Y. J.; Zhou, X.; Liu, G.; Park, J.; Chen, P. *Nano Lett.* **2009**, *9*, 3968−3973.

(28) Zhao, J.; Zaino, L. P., III; Bohn, P. W. *Faraday Discuss.* **2013**, *164*, 57−69.

(29) Zaino, L. P.; Grismer, D. A.; Han, D.; Crouch, G. M.; Bohn, P. W. *Faraday Discuss.* **2015**, *184*, 101-115.

(30) Akkilic, N.; Kamran, M.; Stan, R.; Sanghamitra, N. J. M. *Biosens. Bioelectron.* **2015**, *67*, 747−751.

(31) Cortes, E.; Etchegoin, P. G.; Le Ru, E. C.; Fainstein, A.; Vela,́ M. E.; Salvarezza, R. C. *J. Am. Chem. Soc*. **2010**, *132*, 18034−18037.

(32) Wilson, A. J.; Willets, K. A. *Nano Lett.* **2014**, *14*, 939−945.

(33) Guerrette, J.P.; Percival, S.J.; Zhang, B. *J. Am. Chem. Soc.* **2013**, *135*, 855-861.

(34) Ndungu, P. G. Ph.D. Thesis, Drexel University, Philadelphia, PA, 2004.

(35) Plana, D.; Shul, G.; Stephenson, M.J.; Dryfe, R.A.W. *Electrochem. Commun.* **2009**, *11*, 61-64.

(36) Plana, D.; Jones, F.G.E.; Dryfe, R.A.W. *J. Electroanal. Chem.* **2010**, *646*, 107-113.

(37) Kuhn, A.; Crooks, R.M.; Inagi, S. *ChemElectroChem* **2016**, *3*, 351-352.

(38) Crooks, R.M. *ChemElectroChem* **2016**, *3*, 357-359.

(39) Fosdick, S.E.; Knust, K.N.; Scida, K.; Crooks, R.M. *Angew. Chem. Int. Ed.* **2013**, *52*, 10438-10456.

(40) Guerrette, J.P.; Oja, S.M.; Zhang, B. *Anal. Chem.* **2012**, *84*, 1609-1616.

CHAPTER 2

Dihydroresorufin as a Fluorogenic Indicator for Fluorescence-Enabled Electrochemical Microscopy*

2.1 Introduction

Electrochemical fluorogenic and fluoroquenching reactions have been of great interest for several applications. Fluorescent-voltammetry single-molecule spectroscopy (F-V/SMS) and later single-molecule spectroelectrochemistry (SMS-EC) were developed by Bard, Barbara and coworkers. These techniques were used to monitor single, reversible electron-transfer events within nanoparticles of organic polymer dyes.[1,2,3] Chen and coworkers also demonstrated the use of fluorogenic redox reactions to study site-specific electrocatalytic activity of single-walled carbon nanotubes.[4] A key in achieving single-molecule level sensitivity in these experiments is the use of fluorescence to significantly amplify the electrochemical signal.

Recently we introduced the technique of fluorescence-enabled electrochemical microscopy (FEEM), which involves the use of a fluorogenic redox reaction to report the progress of a conventional, nonfluorogenic redox reaction of interest.[5] The key concept of FEEM includes the use of a closed bipolar electrode (BPE) to electrically couple two separate redox reactions and the use of fluorescence microscopy to simultaneously visualize electrochemical signals on parallel electrodes. A closed BPE consists of a conductor embedded in an insulative

* This chapter is adapted with permission from Oja, S.M.; Guerrette, J.P.; David, M.R.; Zhang, B. "Fluorescence-enabled electrochemical microscopy with dihydroresorufin as a fluorogenic indicator." *Anal. Chem.* **2014**, *86*, 6040-6048. Copyright (2014) American Chemical Society. This is an unofficial adaptation of an article that appeared in an ACS publication. ACS has not endorsed the content of this adaptation or the context of its use.

substrate that completely separates two solution compartments (Figure 2.1). A potential can be applied across two driving electrodes to couple faradaic reactions at each pole of the BPE, enabling control of the system without any direct electrical connection to the BPE. Bipolar electrodes, especially those found in an open microfluidic platform, have been extensively studied by Crooks[6,7,8] and others[9,10,11,12] in the last two decades due to their increasing importance in analytical chemistry.

A key fluorogenic reaction used in FEEM is the reduction of resazurin (**S**), which generates a highly fluorescent product, resorufin (**P**). As a cathodic indicator process, this reaction can be used to study electrochemical oxidation processes of various analytes (**R**) through a closed BPE or its array. This same reaction has been the core of numerous studies by the Chen group to investigate (electro)catalytic activity at single nanoparticles.[4,13,14,15,16] A unique feature of FEEM is the use of highly sensitive fluorescence microscopy to optically monitor nonfluorogenic redox reactions of interest. Importantly, FEEM has enabled us to simultaneously monitor electrochemical kinetics on large arrays containing thousands or more ultramicroelectrodes.

Figure 2.2a shows the two-electron, two-proton reduction of resazurin to form the highly fluorescent product resorufin.[17] In our previous work, we limited our discussion to the study of analyte oxidation reactions (R → O) coupled to this fluorogenic reduction process as shown in Figure 2.2b. Since the development of FEEM we have been interested in finding a suitable fluorogenic oxidation reaction to compliment the reduction of resazurin previously used with the technique. We sought a fluorophore with high extinction coefficient and quantum yield similar to resorufin in order to achieve sufficient signal amplification. Resorufin has an extinction coefficient, ε (570 nm), of approximately 57000 M^{-1} cm^{-1} and a quantum efficiency, φ, of

~0.97,[13] making it an ideal fluorophore for FEEM. Fortuitously, resorufin can also be generated from the reversible electrochemical oxidation of the non-fluorescent dihydroresorufin (**PH_2**). By starting with a solution of dihydroresorufin instead we can extend the use of FEEM to the electrochemical detection and study of analyte reduction reactions (O → R**)** (Figure 2.2c).

Dihydroresorufin can be obtained from the chemical reduction of resorufin in a basic solution containing glucose as shown in Figure 2.3. This solution is often used in a chemistry classroom demonstration[18] commonly known as the "*Vanishing Valentine Experiment*" and is similar in concept to the more popular "*Blue Bottle Experiment*",[19,20] which uses methylene blue in place of resorufin. In the classroom demonstration a pink solution of resorufin reacts with a deprotonated glucose molecule (Glu^-) to become the colorless dihydroresorufin over time. Oxygen enters the solution upon shaking, oxidizing dihydroresorufin and restoring the pink color and fluorescent properties. Alternatively, the chemically reduced species dihydroresorufin can undergo a heterogeneous electrochemical oxidation localized at the electrode surface.

Here, we demonstrate the use of dihydroresorufin for the FEEM-based detection of reducible redox species such as ferricyanide and ruthenium(III) hexamine. Our results have shown three distinct advantages of using dihydroresorufin as an indicator molecule for FEEM as compared to our previous scheme. First, the presence of a strong reducing environment shifts the chemical equilibrium to dihydroresorufin, leading to a greatly suppressed fluorescence background. Second, the fluorescent product, once generated on the electrode surface, is quickly reduced back to the non-fluorescent substrate molecule, dihydroresorufin, significantly lowering the accumulation of fluorescent species around the electrode. Therefore, diffusion becomes less significant in our current work compared to our previous study. Third, unlike resazurin reduction, the fluorescent signal detected at any given time represents the rate at which

dihydroresorufin is oxidized at the electrode. As such, one can monitor electrochemical signal by directly monitoring the total fluorescence. Together these two fluorogenic pathways shown in Figure 2.2a provide a more complete fluorescent voltammetry tool kit with the ability to optically monitor the progress of any electrochemical reaction.

2.2 Experimental Section

2.2.1 Reagents, Chemicals, and Dihydroresorufin Solution Preparation

Resazurin sodium salt (Aldrich, dye content ~75%), sodium hydroxide (J.T. Baker, 98.5%), glucose (Sigma, 99.5%), potassium ferricyanide ($K_3Fe(CN)_6$, Sigma-Aldrich, 99%), potassium chloride (J.T. Baker, 99.8%), ascorbic acid (Sigma, 98%), and hexaammineruthenium(III) chloride ($Ru(NH_3)_6Cl_3$, Aldrich, 98%) were all used without further purification. Deionized water (>18 MΩ·cm) was obtained through a Barnstead Nanopure water purification system and used for all aqueous solutions. A dihydroresorufin solution containing glucose and 0.5 M NaOH was prepared fresh daily. The dihydroresorufin concentration was 100 μM and glucose concentration was 67 mM except where noted. Ascorbic acid solutions were prepared analogously, substituting ascorbic acid for glucose and 0.5 M KCl for NaOH.

2.2.2 Fluorescence Microscopy

All fluorescence microscopy experiments were conducted on an Olympus IX70 inverted microscope equipped with an IX-FLA inverted reflected light fluorescence observation attachment. The excitation source consisted of a Thorlabs M530L2 Collimated LED powered by a DC2100 LED Driver and filtered using a cube with a HQ535/50 excitation filter, a Q565lp dichroic mirror and a HQ610/75 emission filter. The excitation and emission wavelengths were chosen based off of a fluorescence spectrum of resorufin reported by the Chen group.[13] An

Andor iXon+ EMCCD camera cooled to -80 °C and Andor SOLIS software was used to record and process all videos and images. Video was recorded at a frame rate of 33.887 Hz for all experiments using a pre-amplifier gain setting of 5.1.

2.2.3 Cyclic and Linear Sweep Voltammetry

A Chem-Clamp voltmeter/amperometer (Dagan) interfaced to a Dell computer through a PCI-6251 data acquisition board (National Instruments) via a BNC-2090 analog breakout box (National Instruments) was used for all experiments. LabView 8.5 (National Instruments) was used for voltage function generation as well as acquisition of the current-voltage data. A scan rate of 200 mV/s was used for all potential sweep experiments unless noted otherwise. All reported potentials are referenced to Ag/AgCl.

2.3 Results and Discussion

2.3.1 Fluorogenic, Reversible Oxidation of Dihydroresorufin

In order to better utilize dihydroresorufin in FEEM experiments, an understanding of its basic electrochemical behavior was needed. We used a conventional two-electrode (non-bipolar) cell to study the fluorogenic oxidation of dihydroresorufin. It was found that the chemically reduced dihydroresorufin solution provides a unique advantage over the resazurin solution previously used in FEEM experiments. Previously, we[5] and others[1,21] have demonstrated the proportionality between the time derivative of the fluorescence intensity and the electrochemical current for fluorogenic and fluoroquenching electrochemical reactions. In the resazurin/phosphate buffer solution, electrogenerated resorufin remains in solution and continues to fluoresce throughout the experiment. However, in the dihydroresorufin solution used here, the presence of glucose at a sufficiently high concentration (i.e. 67 mM, or 670 times greater than

that of the dihydroresorufin) in a basic media assures that resorufin, when generated at the anodic pole, can be rapidly consumed from the solution, restoring dihydroresorufin and effectively eliminating fluorescence accumulation. It is therefore the fluorescence intensity itself and not the time derivative that is proportional to the electrochemical current.

Figure 2.4 shows the cyclic voltammograms (CVs) of a 25 μm diameter Au electrode in a conventional two-electrode setup along with the corresponding fluorescence cyclic voltammograms (F-CVs) for potential sweep experiments of various concentrations of dihydroresorufin in 67 mM glucose and 0.5 M NaOH. As can be seen in the CVs (Figure 2.4a,b), an oxidation wave with an onset potential of -520 mV is present, which corresponds to the oxidation of glucose.[22] As expected, there is no fluorescence signal when no dihydroresorufin is present (Figure 2.4c, black trace). When dihydroresorufin is added to solution, the electrochemical and fluorescence signals become coupled in an interesting manner. Predictably, increasing the concentration of dihydroresorufin increases the overall fluorescence signal, as more of the fluorogenic redox species is present in solution and available for fluorogenic oxidation. However, somewhat surprisingly this results in a significantly diminished electrochemical current signal. As the first step of glucose oxidation involves its adsorption onto the electrode,[23,24] this pattern indicates that dihydroresorufin blocks this oxidation step, resulting in a decreased electrochemical signal as the dihydroresorufin concentration increases. It is also known that the second wave of glucose oxidation produces more weakly adsorbed products.[23,24] This results in a less-blocked surface, which we believe is the cause of the second wave of fluorescence intensity at -100 mV for dihydroresorufin concentrations from 10-200 μM. As seen in the CV for 1000 μM dihydroresorufin (Figure 2.4a,b, orange trace), a new oxidation wave arises with an onset of -600 mV. This coincides nearly exactly with the onset of the fluorescence

signal (-580 mV), indicating that this wave is from the electrochemical oxidation of dihydroresorufin. This can be seen more clearly in Figure 2.4d, which shows the simultaneously recorded CV and F-CV obtained for a solution of 1000 μM dihydroresorufin overlaid. The fluorescence signal directly correlates to the electrochemical current signal, indicating that this reaction can be used as a fluorogenic indicator for FEEM. The CV gives a steady-state current of approximately 3.8 nA. The theoretical steady-state current, i_{ss}, can be calculated from the equation:[25]

$$i_{ss} = 4nFC^{*}Dr \quad (1)$$

where n is the number of electrons transferred per molecule, F is Faraday's constant (96,485 C/mol), D is the diffusion coefficient, C^{*} is the bulk concentration of redox species, and r is the electrode radius. Using a diffusion coefficient of 4.8×10^{-6} cm^2/s,[26] the expected steady-state current for 1000 μM dihydroresorufin at a 25 μm diameter microelectrode is 4.6 nA. The experimental value corresponds nicely to this theoretical value when considering that glucose is also adsorbed onto the electrode surface and thus blocking some of the electroactive area from dihydroresorufin oxidation.

Studying variations in the oxidation of dihydroresorufin on a Au electrode as compared to a carbon fiber electrode (CFE) also provides insight into the coupled electrochemical and fluorescent properties of this system. Figure 2.5a shows the overlaid CV and F-CV for a solution of 100 μM dihydroresorufin, 67 mM glucose and 0.5 M NaOH obtained with a 25 μm diameter Au working electrode for a potential sweep from -1 to +0.3 V. During the forward scan the fluorescence onset potential is at -540 mV and a second higher intensity wave appears at approximately -100 mV. In addition to the potential-dependent blocking effect of adsorbed glucose and its oxidation products, we believe there is at least one other factor leading to the

general shape of this curve. At electrode potentials between -540 and -100 mV the fluorescence intensity is limited somewhat by the relatively high concentration of glucose in solution adjacent to the electrode. At potentials above -100 mV, glucose is electrochemically oxidized to a greater degree, as can be seen in the CV in Figure 2.5a, depleting the concentration of this species in the vicinity of the electrode surface. This process, in addition to the ongoing oxidation of dihydroresorufin, results in a second, higher intensity fluorescence wave. It is believed that both of these factors contribute to some degree to the presence of two distinct waves as well as the slightly higher fluorescence signal on the return scan. The three still-images presented in Figure 2.5b were taken from a video recorded during the F-CV experiment and show the burst of fluorescence at the 25 μm Au electrode as the potential is swept to oxidize dihydroresorufin. At +200 mV the electrode spot size is noticeably larger as well due to the depletion of glucose and therefore slower chemical reduction process.

Figure 2.5c shows the results of an experiment similar to that in Figure 2.5a except the working electrode was replaced with a 10 μm diameter carbon fiber electrode (CFE). The intensity of both the electrochemical CV and the F-CV were significantly lower than that of the Au electrode likely due to relatively lower electrocatalytic activity of carbon, but the initial fluorescence onset potential was still at approximately -540 mV. Glucose oxidation occurs at a much lower rate at carbon as compared to Au,[27] therefore leaving the concentration of glucose relatively unperturbed prior to the chemical reaction with resorufin. We believe this is why only one wave is observed in the CFE F-CV, indicating that the extent of the glucose side reactions (i.e. adsorption and electrochemical oxidation) on a CFE is much smaller as compared to on a Au electrode.

In order to more completely understand the dynamics of the fluorogenic electrochemical oxidation of dihydroresorufin and subsequent chemical reduction of the product resorufin by glucose, the effect of altering the glucose concentration was studied. Figure 2.6 presents F-CVs from potential sweep experiments conducted using a conventional two-electrode setup in which the concentration of glucose was varied from 1 to 1000 mM. A 25 μm Au working electrode was used, and the total concentration of resazurin/resorufin/dihydroresorufin was 100 μM for all solutions. The fluorescence intensity was found to increase as the glucose concentration in solution was increased from 1 to 10 mM. This can be explained by the increasing concentration of dihydroresorufin in solution. Altering the concentration of glucose will affect the equilibrium between these three species, with higher concentrations of glucose favoring the fully reduced species, dihydroresorufin. This can be observed visually (Figure 2.7), as the solution color changes from blue (resazurin) to pink (resorufin) to clear (dihydroresorufin) as the glucose concentration is increased. A higher concentration of dihydroresorufin enables the fluorogenic oxidation to proceed at a higher rate, resulting in an increased fluorescence signal.

Interestingly, further increasing the glucose concentration to 67 mM and beyond results in a clear decrease in both the recorded fluorescence intensity and the hysteresis of the F-CV. We believe two factors contribute to this decrease in intensity. First, the amount of surface-adsorbed glucose on the electrode likely increases with solution concentration. The adsorbed glucose physically blocks dihydroresorufin oxidation, resulting in a lower rate of reaction and hence a lower fluorescence intensity. Second, at higher solution concentrations more glucose will be present in solution adjacent to the electrode surface. This glucose can quench fluorescence by chemically reducing resorufin back to the non-fluorescent dihydroresorufin. This quenching effect becomes greater as the glucose concentration increases, thus decreasing overall

fluorescence intensity. The quenching effect also explains the change in hysteresis of the fluorescence voltammograms. At low concentrations of glucose (i.e. 1-10 mM), resorufin produced at the electrode via dihydroresorufin oxidation has a much longer lifetime in solution than at higher glucose concentrations, as each resorufin molecule is less likely to encounter glucose and undergo reduction back to dihydroresorufin. This time delay between resorufin production via dihydroresorufin oxidation at the electrode and resorufin consumption via reduction by glucose becomes less as the glucose concentration increases, thereby decreasing the hysteresis in the F-CV. The use of ascorbic acid as an alternative reducing agent was also briefly investigated, with the results presented in Figure 2.8. The same overall trends were observed, but the fluorescence signal was more than two orders of magnitude lower with ascorbic acid. We believe this is due to solution instability, as a precipitate began forming shortly after preparing the solutions.

2.3.2 Use of Dihydroresorufin in FEEM to Study Analyte Reduction

With an understanding of the electrochemical and fluorescence properties of the dihydroresorufin oxidation reaction, we could then use it in a bipolar FEEM setup to study analyte reduction reactions. We used a simple bipolar setup (diagram shown in Figure 2.9) to demonstrate the electrochemical coupling of the fluorogenic oxidation of dihydroresorufin to the reduction of ferricyanide ($Fe(CN)_6^{3-}$). Two 25 μm diameter Au disk electrodes were connected in series to form a closed BPE as described previously.[28,29] The cathodic pole was placed in 250 μM ferricyanide with 1 M KCl supporting electrolyte and the anodic pole was placed in a solution of 100 μM dihydroresorufin with 67 mM glucose and 0.5 M NaOH and positioned on a microscope for observation. The dihydroresorufin solution was illuminated to excite resorufin fluorescence, and a triangular waveform from +1.2 to +0.2 V was applied to two Ag/AgCl driving electrodes

to reduce ferricyanide at the cathodic pole. This reduction is coupled to the oxidation of dihydroresorufin at the anodic pole, resulting in the production of the fluorescent product, resorufin.

Figure 2.10 shows five background-corrected still-images of the anodic pole taken from a video recorded over the potential sweep experiment. The last panel of the figure displays the voltage-dependent total fluorescence intensity recorded at the anodic pole. As can be seen, the onset of the fluorescent burst occurs at approximately 830 mV. This onset potential can be understood from an analysis of the onset potentials for the reduction of ferricyanide (310 mV vs. Ag/AgCl in a two-electrode cell) and that for the oxidation of dihydroresorufin (-540 mV vs. Ag/AgCl in a two-electrode cell, Figure 2.5a). The onset potential of the coupled ferricyanide reduction/dihydroresorufin oxidation here corresponds roughly to the difference in the two onset potentials,[30] agreeing within 20 mV. As the potential is swept in the negative direction, ferricyanide is reduced at an increasing rate at the cathodic pole, resulting in an increasing rate of dihydroresorufin oxidation at the anodic pole and thus greater fluorescence intensity. As the potential is swept back in the positive direction, ferricyanide reduction slows down, resulting in a decrease in fluorescence intensity until fluorescence is no longer observed. The fluorescence intensity is also slightly higher on the return scan. This can be visualized by comparing panels 3 (+0.6 V forward scan) and 5 (+0.6 V return scan) of Figure 2.10. We believe this is due to the depletion of glucose in solution adjacent to the electrode surface on the forward scan, which lessens the quenching effect and results in a slightly higher fluorescent signal on the return scan.

We also used dihydroresorufin as an indicator molecule to report the reduction of $Ru(NH_3)_6^{3+}$. Figure 2.11 shows a series of fluorescence images recorded during the electrochemical reduction of 250 μM $Ru(NH_3)_6^{3+}$ in a separate FEEM experiment. Importantly,

the onset potential of the coupled reaction as determined by the fluorescent signal agreed to within 10 mV of the predicted onset potential. These results demonstrate that dihydroresorufin can be used in FEEM for the study of reducible redox species.

We then investigated the use of dihydroresorufin for the quantitative detection of a reducible analyte using FEEM. Again, two 25 μm Au electrodes were connected in series to produce a single BPE. The anodic pole was placed in a solution of 100 μM dihydroresorufin, 67 mM glucose, and 0.5 M NaOH and positioned on a microscope for observation, and the cathodic pole was placed in a solution containing ferricyanide with 1 M KCl supporting electrolyte. The potential was swept from +1.2 to +0.2 V at 200 mV/s. Presented in Figure 2.12a are a series of fluorescence intensity signals recorded over the course of the voltage scans with analyte concentrations from 25-750 μM. The concentration dependence of the fluorescence intensity at the switching potential is shown in Figure 2.12b. The concentration range over which the data is linear is from 50 to 400 μM ferricyanide. Above 400 μM ferricyanide the curve begins to plateau as the oxidation of dihydroresorufin at the anodic pole of the BPE becomes limiting. At ferricyanide concentrations of 50 μM and below, the fluorescence response becomes insensitive to the concentration of ferricyanide and is approximately constant, as oxygen reduction, rather than ferricyanide reduction, is now primarily coupled to the oxidation of dihydroresorufin.

Deoxygenating these low concentration solutions results in no observable fluorescence signal, however, indicating that the current from ferricyanide reduction in these solutions is below the threshold current necessary for fluorescence generation (Figure 2.13). This can be understood by considering the electrochemical and chemical processes in the dihydroresorufin solution. There are three competing processes at the anodic pole: the electrochemical oxidation of dihydroresorufin to generate resorufin, the electrochemical oxidation of glucose, and the

chemical reduction of resorufin back to dihydroresorufin. When the concentration of ferricyanide is below 50 μM, the electrochemical oxidations of dihydroresorufin and glucose are both relatively slow, resulting in a very small rate of resorufin generation. As such, in the presence of a large concentration of glucose, resorufin is quickly reduced back to dihydroresorufin. Admittedly, the range over which a linear concentration response is observed is very narrow and the lower limit of detection leaves much to be desired, limiting the use of this system as a quantitative technique to readout analyte concentrations. However, it is anticipated that modifying the electrode to selectively oxidize dihydroresorufin or using a non-fouling reducing agent that is electrochemically inactive in the desired potential range will lower the limit of detection.

2.3.3 Improved Spatial and Temporal Resolution of FEEM Using Dihydroresorufin

In spite of the relatively high limit of detection of FEEM using dihydroresorufin, we found that this system gives rise to several significant benefits. As already demonstrated, the electrochemical current signal can be reported by directly monitoring the total fluorescence signal rather than the time derivative of this signal as with our previous report. More importantly, FEEM using dihydroresorufin as the fluorogenic reporter appears to give enhanced spatial and temporal resolution over FEEM using resazurin as the reporter. A simple potential step experiment, shown in Figure 2.14, demonstrates this point. In this experiment, two 25 μm diameter Au electrodes were connected to form a closed BPE. One pole was placed in a solution that was 250 μM in both ferricyanide and ferrocyanide with 1 M KCl as supporting electrolyte. The opposite pole was placed in either 100 μM dihydroresorufin, 67 mM glucose, and 0.5 M NaOH or 100 μM resazurin in 50 mM phosphate buffer. An 8 s pulse at a potential sufficient to drive the coupled redox reactions was applied (“on” state), followed by an 8 s period at which

the potential was adjusted below the onset potential ("off" state). For the coupled dihydroresorufin oxidation/ferricyanide reduction, the "on" state was +0.3 V and the "off" state was +1.2 V. For the coupled resazurin reduction/ferrocyanide oxidation, the "on" state was +1.2 V and the "off" state was +0.3 V.

Figure 2.14a shows the normalized fluorescence intensity recorded over the length of the pulse cycle for both coupled reactions. As seen, the fluorescence response of the two fluorogenic indicators is markedly different. The dihydroresorufin system reaches a steady-state fluorescence intensity within 2 s of the start of the "on" pulse, while the fluorescence intensity of the resazurin system increases throughout the "on" pulse, failing to reach a steady-state in 8 s. When the potential is switched to the "off" state, the fluorescence intensity of the dihydroresorufin system decays to its initial intensity within 1 s, while the intensity of the resazurin system shows an immediate spike, followed by a slow decay, failing to return to its initial intensity within 8 s.

The difference in the temporal response of the two systems can be explained by considering the differing mechanisms through which the electrogenerated fluorescence decays. In the dihydroresorufin system, electrogenerated resorufin is chemically reduced back to non-fluorescent dihydroresorufin. In the resazurin system, electrogenerated resorufin is only "consumed" by photobleaching or diffusion out of the field of view. The photobleaching and diffusion processes are much slower than the chemical reduction process, which accounts for a more sluggish fluorescence response from the resazurin system. We believe the large spike in fluorescence intensity observed in the resazurin system when the potential is switched to the "off" state is due to resazurin adsorbed onto the electrode surface. In the "on" state these surface-bound molecules are fully reduced to dihydroresorufin, and upon switching the potential to the "off" state they are immediately oxidized back to resorufin, resulting in the observed spike.

The effect of fluorophore diffusion can be readily seen in Figure 2.14b, which presents a series of line scans across the electrodes over the course of the voltage pulse. The fluorescent signal from the resazurin system broadens significantly over the course of the experiment due to diffusion of electrogenerated resorufin. By comparison, the signal from the dihydroresorufin system shows minimal broadening, as the electrogenerated resorufin is chemically reduced back to dihydroresorufin before it has time to diffuse a significant distance from the electrode surface. Figure 2.14c presents background corrected images of the electrodes over the course of the voltage pulse. The different temporal response and the effect of fluorophore diffusion can be easily observed in these images. At 0.18 s into the "on" state, a strong signal is observed in the dihydroresorufin system whereas the resazurin signal is weak. At 8 s, however, both systems show strong signals, but the signal from the resazurin system has significantly broadened due to diffusion. At 8.05 s (0.05 s into the "off" state), the resazurin system shows a large spike in intensity, while the signal from the dihydroresorufin system has decayed to about half its steady-state intensity. At 10 s, no signal is observed from the dihydroresorufin, while a strong, diffusion-broadened signal is still observed from the resazurin system. As can be seen, using dihydroresorufin as a fluorogenic indicator in FEEM gives an improved temporal response and lower diffusional signal broadening than resazurin. We expect these properties of improved spatial and temporal resolution in FEEM to be especially important in FEEM imaging applications where high-density arrays of thousands or more ultramicroelectrodes would be used to image dynamic electrochemical processes. These applications include screening of new electrocatalysts and imaging transient biological processes such as neuronal exocytosis. Work is currently underway to image dynamic diffusion layers of ultramicroelectrodes, which we expect to report on in due course.

2.4 Conclusion

In summary, we have demonstrated the ability to use fluorescence-enabled electrochemical microscopy for the analytical detection of reducible species using a solution containing dihydroresorufin that undergoes a fluorogenic electrochemical oxidation to form resorufin. This process, together with the previously described fluorogenic reduction of resazurin, provides for a more complete electrochemical fluorogenic toolkit and greatly increases the applicability of FEEM. The fluorescence intensity measured from the system described here was found to be directly proportional to the electrochemical current. The signal from this system is therefore easier to interpret than the signal from the fluorogenic reduction of resazurin where we previously showed the correlation of the time derivative of fluorescence intensity and the electrochemical current. Due to the presence of a chemical reducing agent that quickly consumes the electrogenerated fluorophore, this system was found to have an improved temporal response as well as lower signal broadening from diffusion than the resazurin system.

2.5 Figures

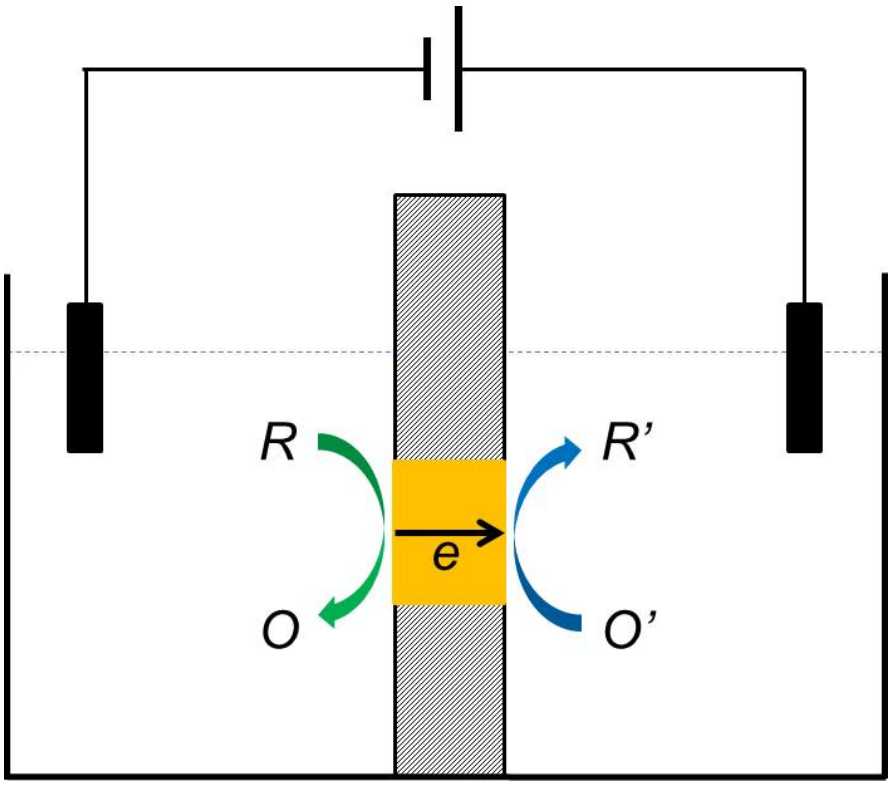

Figure 2.1. Schematic of a closed bipolar electrode.
A conductor is embedded in an insulative substrate that completely separates two solution compartments. A small voltage bias can be applied with two driving electrodes to couple faradaic reactions at the poles of the bipolar electrode, enabling control of the system without direct electrical connection to the bipolar electrode. A bipolar electrode array can be formed with several parallel electrodes in the insulating membrane. Replacing a conventional redox reaction at one of the poles of the bipolar electrode with a fluorogenic redox reaction is the central idea of FEEM. Since the rate of reaction at the two poles will be equal, the progress of a conventional redox reaction at one pole of a bipolar electrode can be reported by optically monitoring a fluorogenic redox reaction at the other pole of the bipolar electrode.

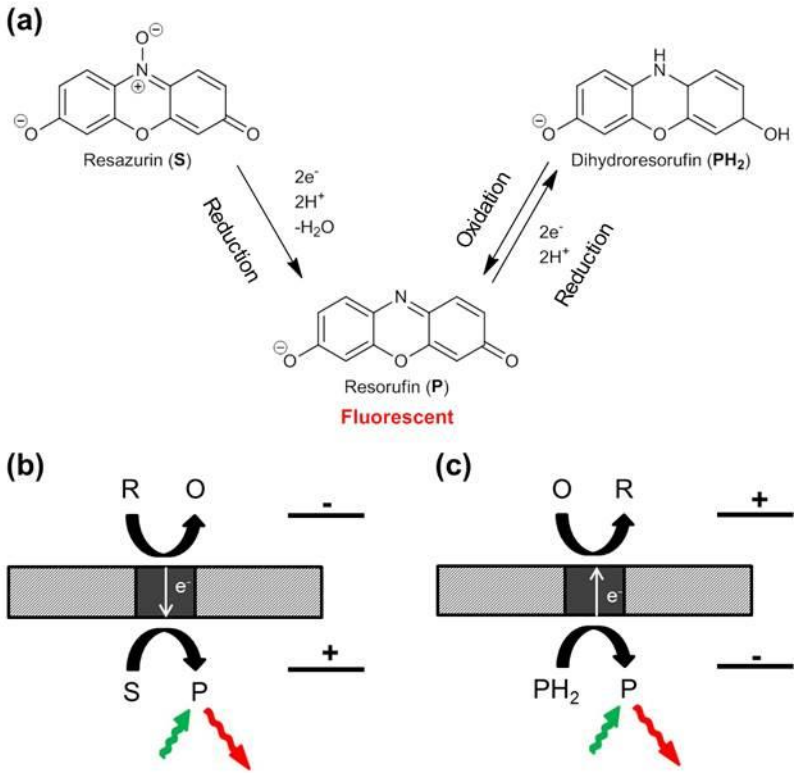

Figure 2.2. Fluorogenic reaction scheme of resorufin and its use in FEEM.
(a) Reaction scheme for the fluorogenic production of resorufin from either resazurin by reduction or from dihydroresorufin by oxidation. **(b)** and **(c)** Illustrations of FEEM for the detection of an oxidizable and a reducible species, respectively. In (b), the oxidation of an analyte (R) at the anodic pole of a BPE is coupled to the fluorogenic reduction of resazurin (S) at the cathodic pole. In (c), the reduction of an analyte (O) at the cathodic pole of a BPE is coupled to the fluorogenic oxidation of dihydroresorufin (PH_2) at the anodic pole.

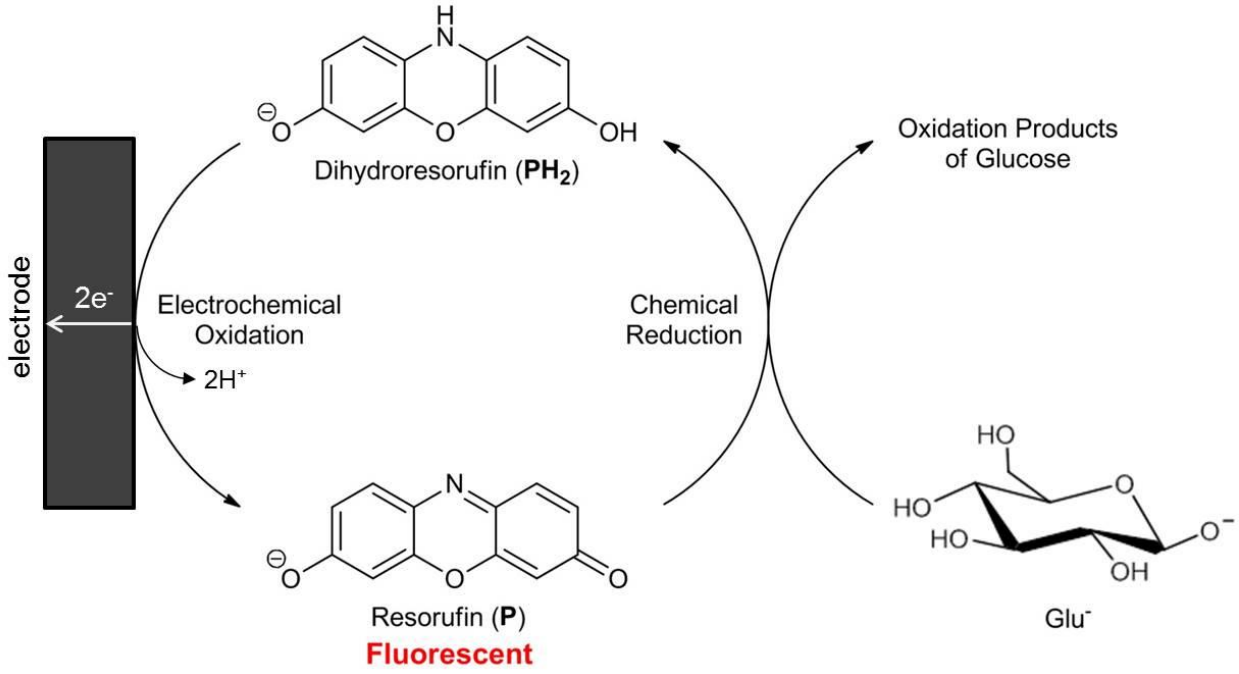

Figure 2.3. Reaction scheme of the dihydroresorufin-resorufin system.
Reaction scheme showing the fluorophore-consuming chemical reduction of resorufin and the fluorogenic production of resorufin through electrochemical oxidation. For further details regarding the deprotonation and subsequent chemical oxidation of glucose, readers are referred to reference 20.

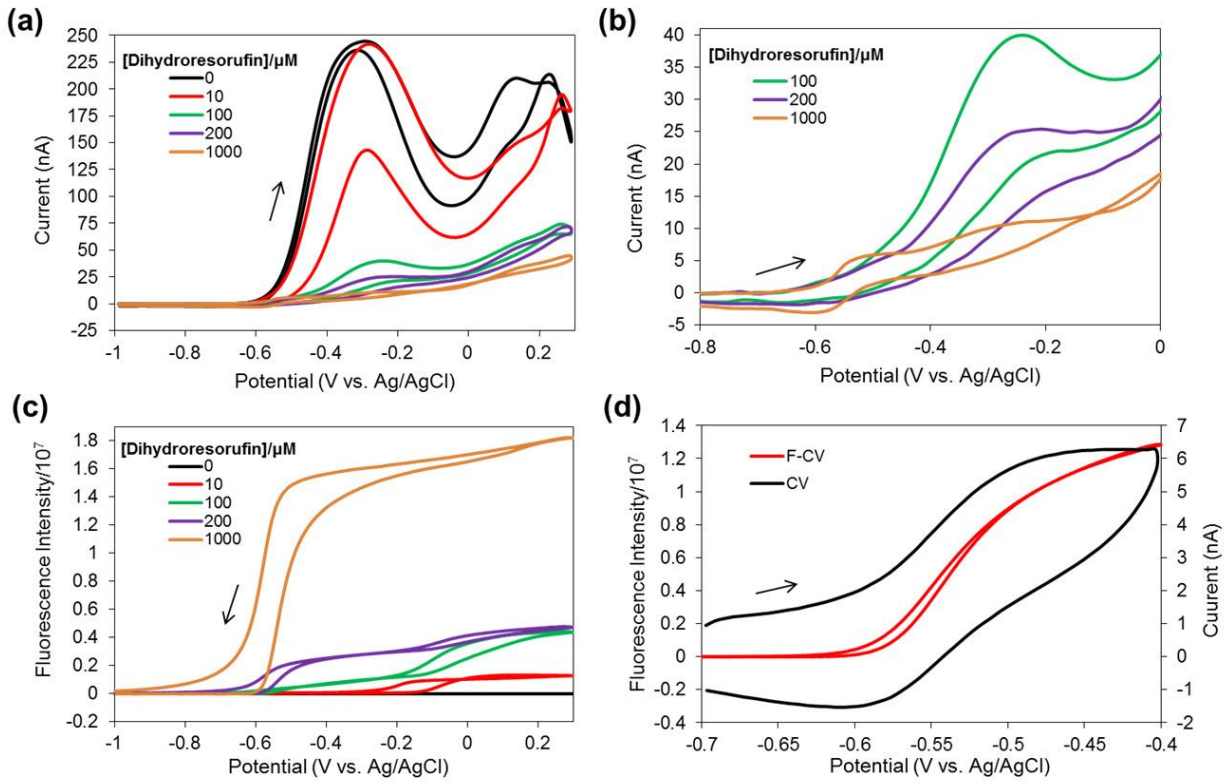

Figure 2.4. Electrochemical and fluorescence CVs of dihydroresorufin solution.
Electrochemical and fluorescence CVs obtained using a 25 µm Au electrode at various concentrations of dihydroresorufin in 67 mM glucose and 0.5 M NaOH. **(a)** Electrochemical CVs for a scan from -1 to +0.3 V. **(b)** Zoom-in of (a) for dihydroresorufin concentrations of 100, 200, and 1000 µM. Only the potential range from -0.8 to 0 V is shown. **(c)** Fluorescence CVs corresponding to the electrochemical CVs shown in (a). **(d)** Overlaid plot of the simultaneously recorded fluorescence (red trace) and electrochemical (black trace) CVs of 1000 µM dihydroresorufin for a scan from -0.7 to -0.4 V at 10 mV/s.

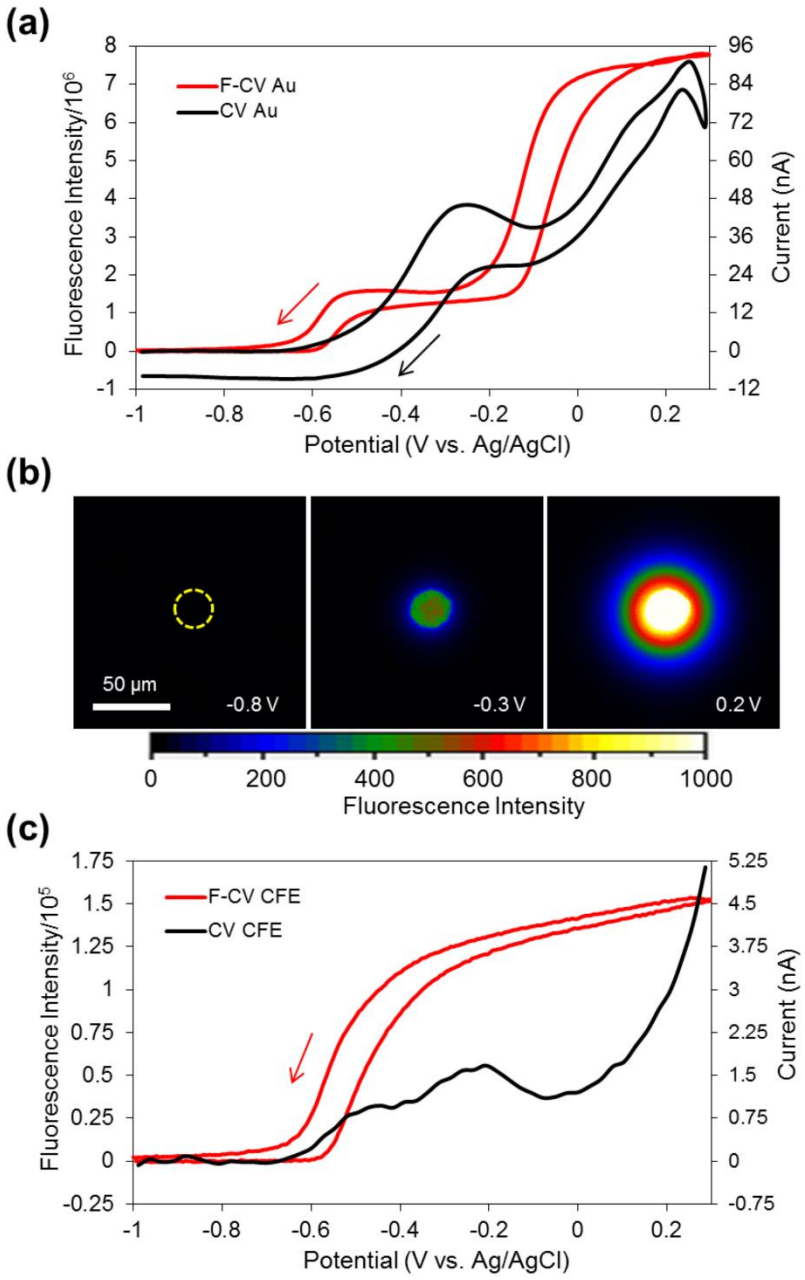

Figure 2.5. Electrochemical and fluorescence CVs of dihydroresorufin on Au and CF.
(a) and **(c)** Comparison of a conventional cyclic voltammogram (CV) with a corresponding, simultaneously recorded fluorescence cyclic voltammogram (F-CV) for (a) a 25 µm diameter Au disk electrode and (c) a 10 µm diameter CFE, direct connect (not BPE) in a solution containing 100 µM dihydroresorufin, 67 mM glucose and 0.5 M NaOH. **(b)** Fluorescence still images captured from a video recorded during the potential sweep experiment shown in (a) at select potentials. The dashed yellow ring in panel one of (b) indicates the actual size and position of the electrode. Note the different fluorescence intensity and current scales in (a) and (c). Only the forward scan of the CV is shown in (c).

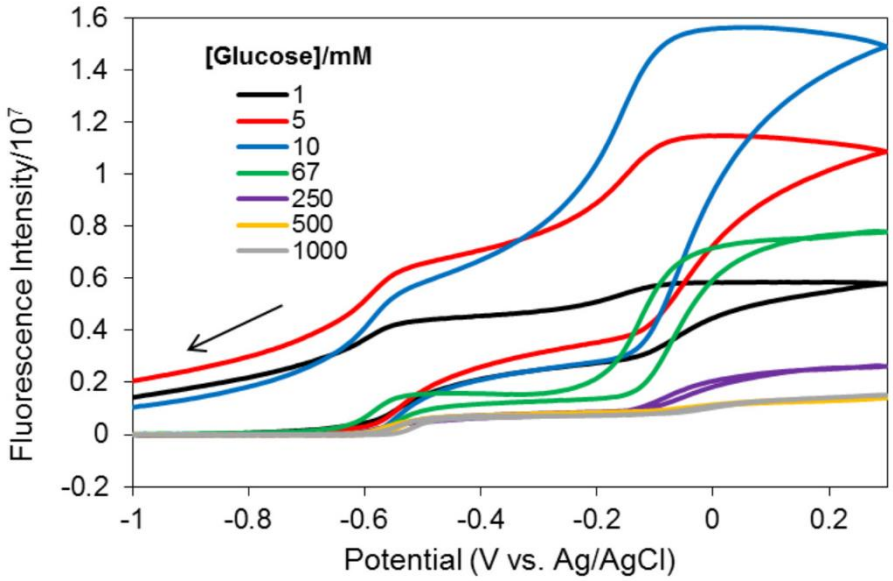

Figure 2.6. Fluorescence CVs with varying concentrations of glucose.
F-CVs obtained with a 25 µm diameter Au disk electrode in solutions with a total resazurin/resorufin/dihydroresorufin concentration of 100 µM and varying concentrations of glucose in 0.5 M NaOH. The potential was swept from -1 to +0.3 V at 200 mV/s.

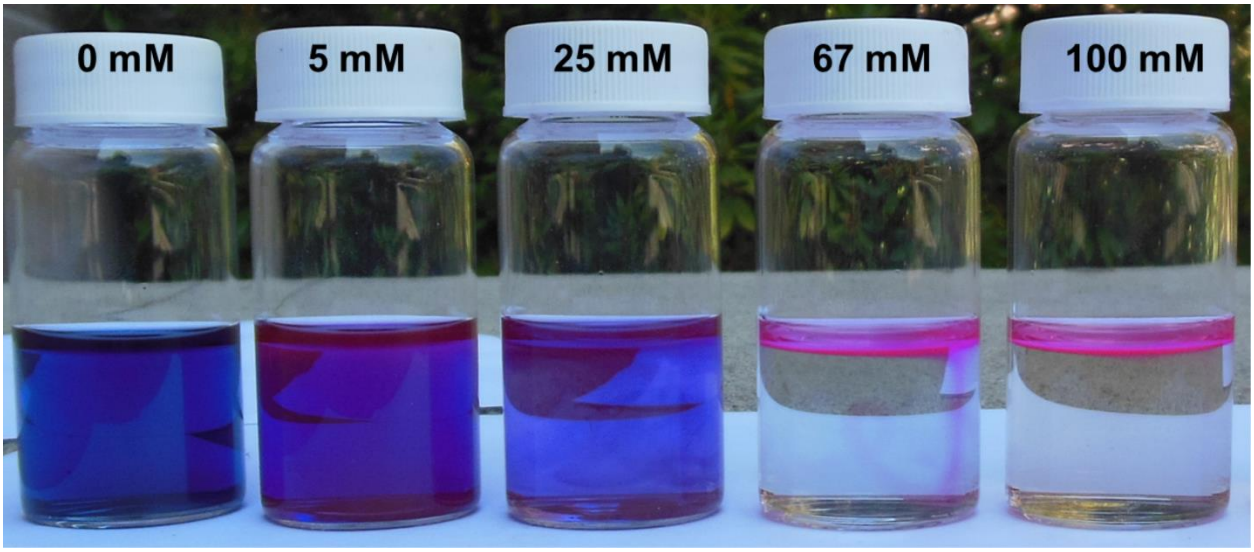

Figure 2.7. Photo of dihydroresorufin solutions with varying concentrations of glucose. Photograph of 100 µM resazurin/resorufin/dihydroresorufin solutions in 0.5 M NaOH with varying concentrations of glucose taken 10 min after adding the glucose. The leftmost solution remains as resazurin (blue) as no glucose is available to reduce it. As the glucose concentration increases, the resazurin is reduced first to resorufin (pink), and then dihydroresorufin (clear) to a greater extent. The portion of the 67 and 100 mM glucose solutions in contact with air remains pink because the oxygen present in air is enough to oxidize dihydroresorufin back to resorufin.

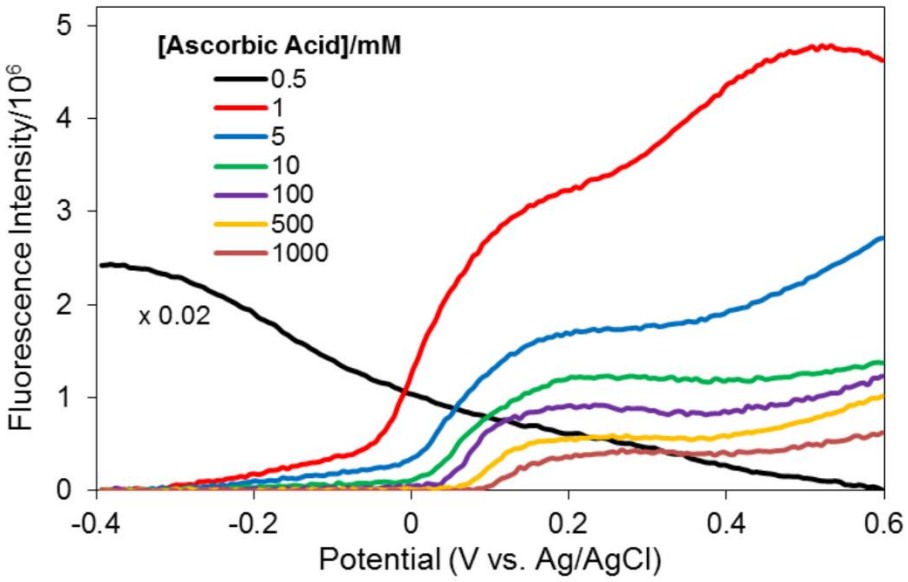

Figure 2.8. Fluorescence CVs using ascorbic acid as a reducing agent.
Forward scan of F-CVs obtained with a 25 μm diameter Au disk electrode in solutions with a total resazurin/resorufin/dihydroresorufin concentration of 100 μM and varying concentrations of ascorbic acid in 0.5 M KCl. The potential was swept from -0.4 to 0.6 V at 200 mV/s. Note that an electron multiplier gain of 300 was used (as compared to a gain of 0 for the varying glucose concentration data in Figure 2.6) to amplify the fluorescence signal.

Figure 2.8 Discussion.
At an ascorbic acid concentration of 0.5 mM, the fluorescence signal decreases as the potential is swept in the positive direction. This indicates that the solution is primarily resazurin, with the reduction of resazurin to resorufin at potentials negative of approximately -150 mV responsible for the strong fluorescence signal. At potentials positive of about -150 mV, this reaction no longer occurs to a significant extent and the fluorescence signal decays as resorufin gets reduced by ascorbic acid to the non-fluorescent dihydroresorufin. At an ascorbic acid concentration of 1 mM, the solution is primarily dihydroresorufin, and the onset of the fluorescence wave at -50 mV indicates the onset of dihydroresorufin oxidation. As the ascorbic acid concentration is increased to 5 mM and above, the fluorescence signal decreases due to the quenching effect of ascorbic acid, which chemically reduces any resorufin produced at the electrode back to the non-fluorescent dihydroresorufin. The positive potential shift in the onset of dihydroresorufin oxidation as the ascorbic acid concentration is increased is due to the decrease in solution pH. As dihydroresorufin oxidation involves the loss of two protons, decreasing the pH makes the oxidation reaction thermodynamically less favorable, thus increasing the onset potential. This also explains the difference in the onset potential of dihydroresorufin oxidation in glucose (-550 mV for 10 mM glucose) and ascorbic acid (+10 mV for 10 mM ascorbic acid).

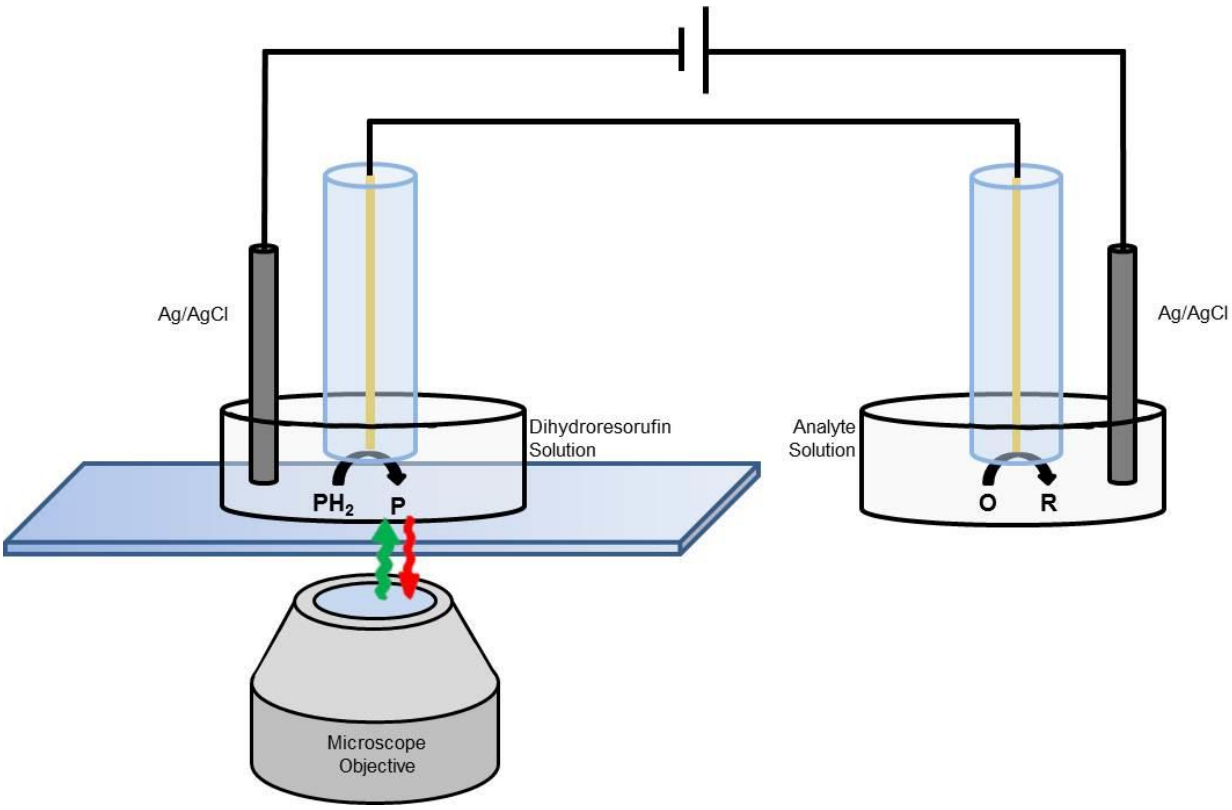

Figure 2.9. Diagram of a basic FEEM experimental setup.
A bipolar electrode is formed by electrically connecting two microelectrodes in series. The cathodic pole of the bipolar electrode is placed in the analyte solution. The anodic pole of the bipolar electrode is placed in a solution of dihydroresorufin, which is positioned on top of an inverted microscope for observation.

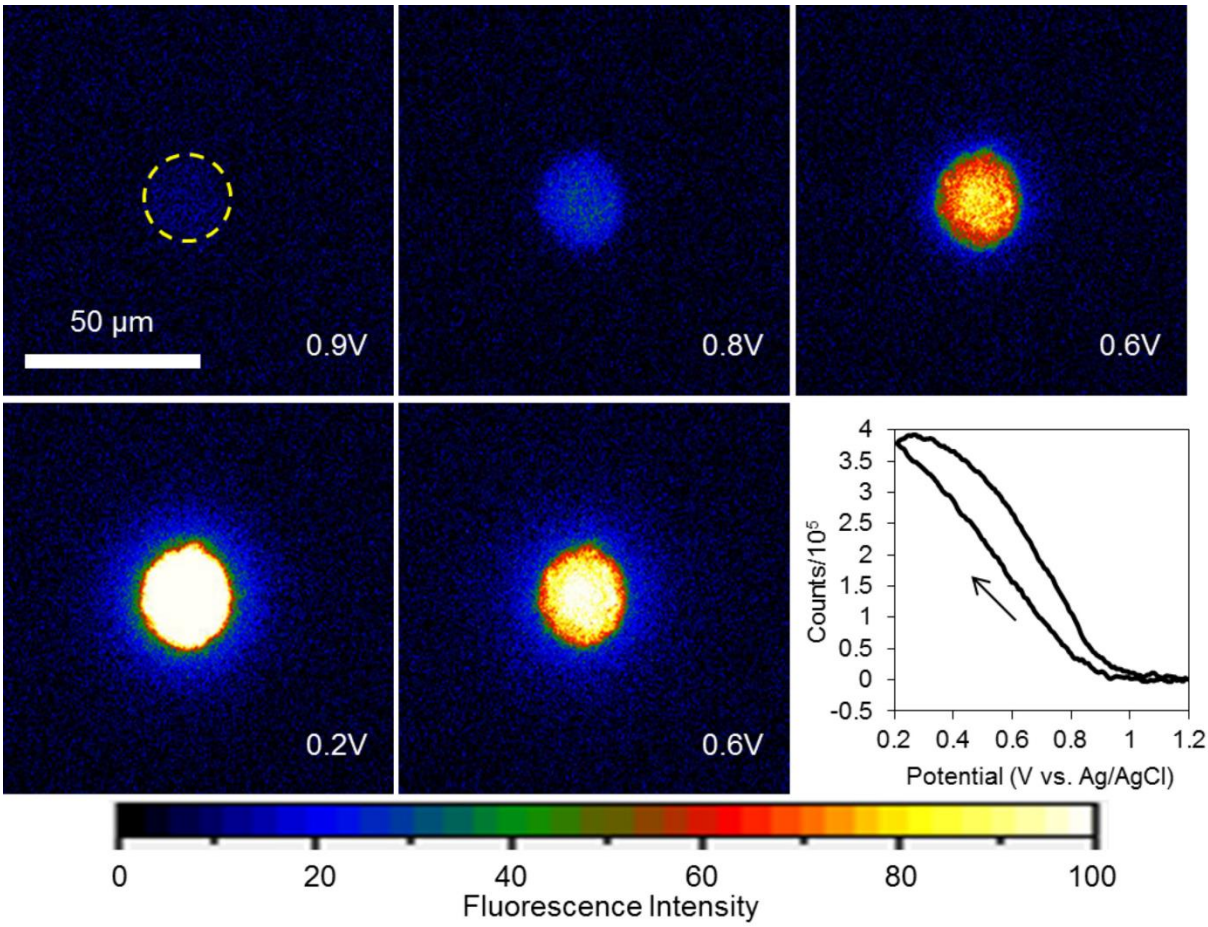

Figure 2.10. Fluorescence images of FEEM detection of ferricyanide.
Series of fluorescence still-images captured from a video of the FEEM detection of 250 µM ferricyanide at a 25 µm diameter Au disk electrode using a solution of 100 µM dihydroresorufin, 67 mM glucose, and 0.5 M NaOH. Potential was cycled from +1.2 to +0.2 V at a scan rate of 200 mV/s as applied to two Ag/AgCl driving electrodes. The last panel shows fluorescence intensity at the electrode as a function of electrode potential. The dashed yellow ring in panel one indicates the actual position and size of the electrode.

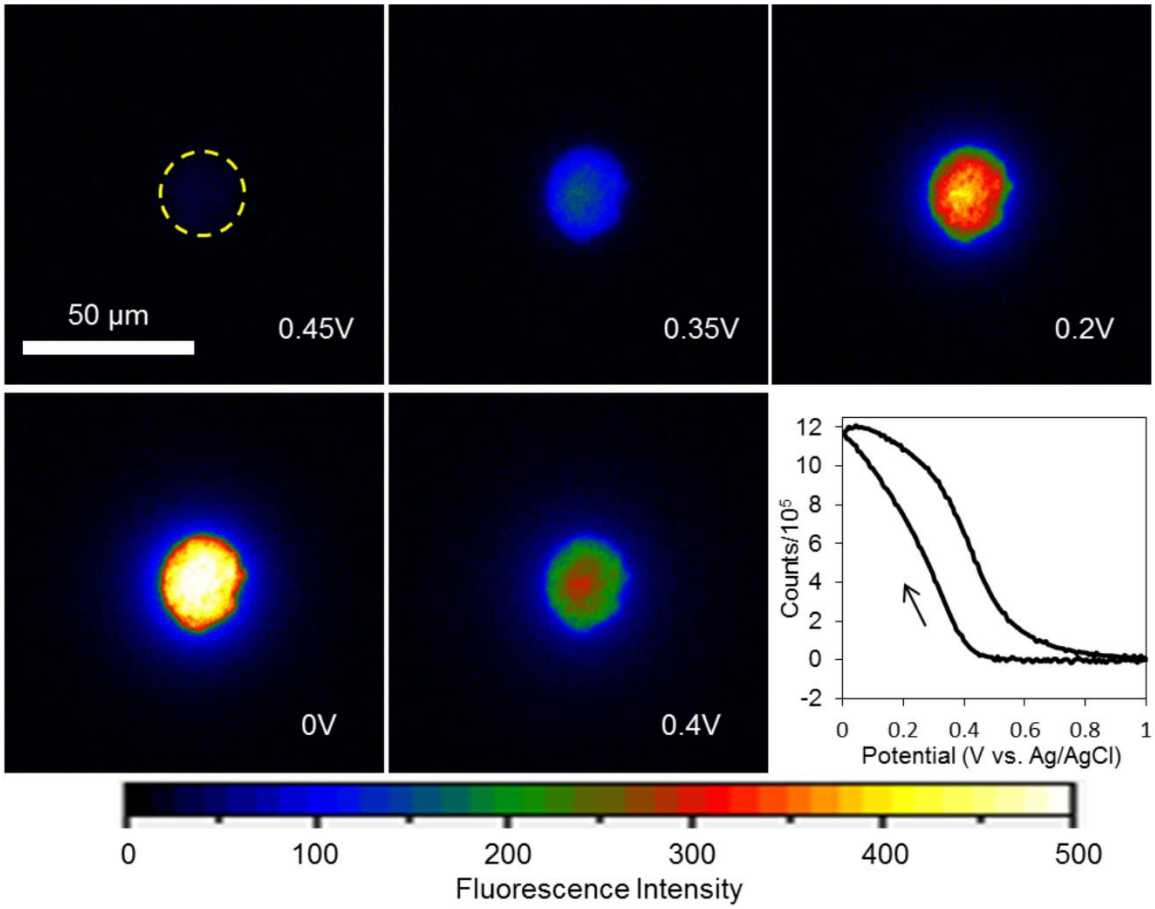

Figure 2.11. Fluorescence images of FEEM detection of hexamine ruthenium(III).
Series of fluorescence still-images taken from a video of the FEEM detection of 250 µM hexamine ruthenium(III) at a 25 µm diameter Au disk electrode using a solution of 100 µM dihydroresorufin, 67 mM glucose, and 0.5 M NaOH. Potential was cycled from +1 to 0 V at 200 mV/s as applied to two Ag/AgCl driving electrodes. The last panel shows fluorescence intensity at the electrode over the duration of the scan.

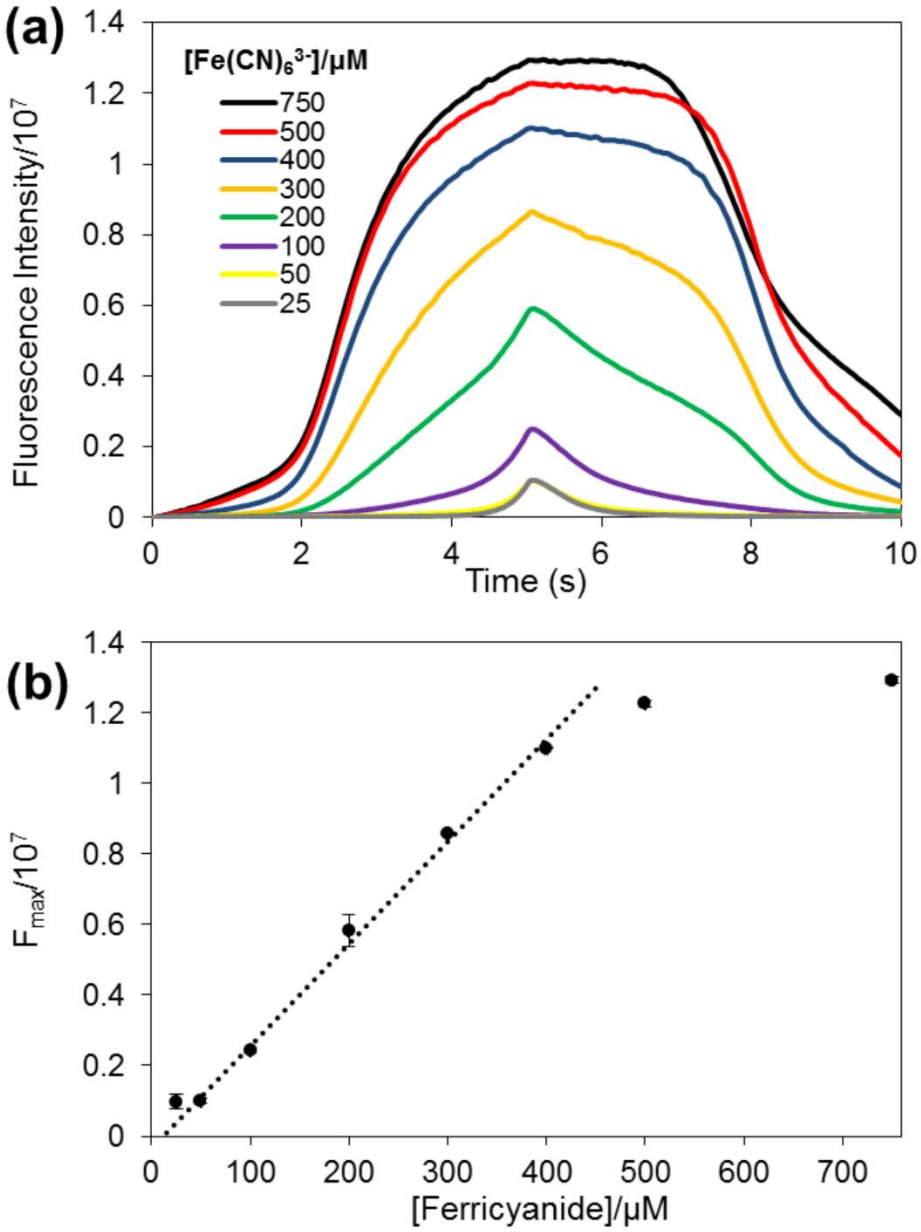

Figure 2.12. FEEM detection of various concentrations of ferricyanide.
FEEM-based detection of various concentrations of ferricyanide at a 25 µm diameter Au disk BPE using a solution containing 100 µM dihydroresorufin, 67 mM glucose and 0.5 M NaOH. Potential was cycled from +1.2 to +0.2 V at a scan-rate of 200 mV/s as applied to two Ag/AgCl driving electrodes.

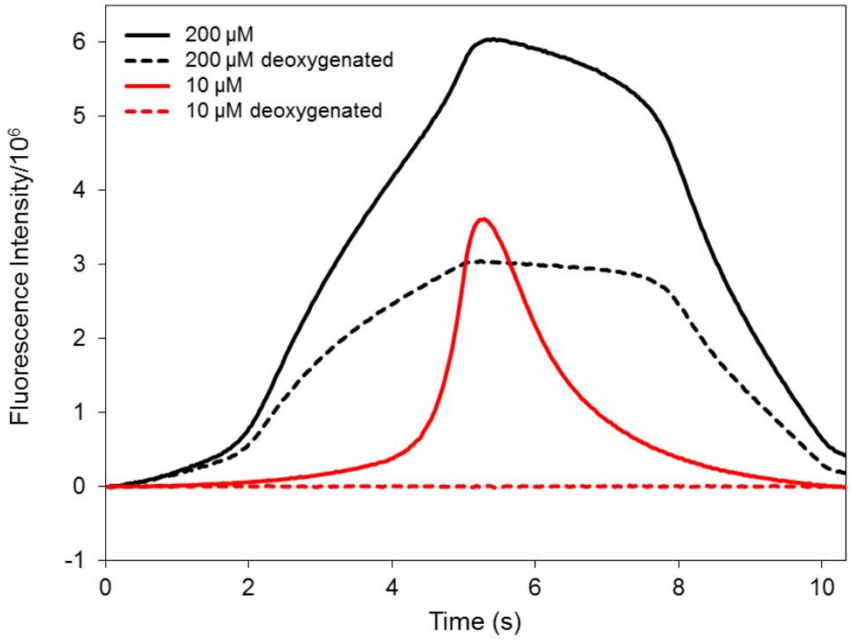

Figure 2.13. Effect of oxygen on FEEM detection of ferricyanide.
FEEM-based detection of ferricyanide in ambient and deoxygenated solutions at a 25 µm diameter Au disk electrode using a solution of 100 µM dihydroresorufin, 67 mM glucose, and 0.5 M NaOH. The potential was cycled from +1.2 V to +0.2 V at 200 mV/s as applied to two Ag/AgCl driving electrodes.

Figure 2.13 Discussion.
The solid red trace shows the signal obtained with a 10 µM ferricyanide solution. A strong fluorescence signal is observed, however upon deoxygenating the solution (dashed red trace), no signal is observed. This shows that the coupling of oxygen reduction, rather than ferricyanide reduction, to dihydroresorufin/glucose oxidation is responsible for the fluorescent signal observed. It also shows that a ferricyanide concentration of 10 µM is too low to yield enough current for fluorescence generation, indicating that the ferricyanide reduction is coupling primarily to glucose oxidation. At a higher ferricyanide concentration, such as 200 µM, it is clear that oxygen reduction contributes significantly to the fluorescence signal by comparing the ambient trace (solid black) to the deoxygenated trace (dashed black). However, the deoxygenated solution still gives a strong fluorescence signal, indicating that at a concentration of 200 µM ferricyanide reduction occurs at a rate sufficient enough to couple to both glucose and dihydroresorufin oxidation.

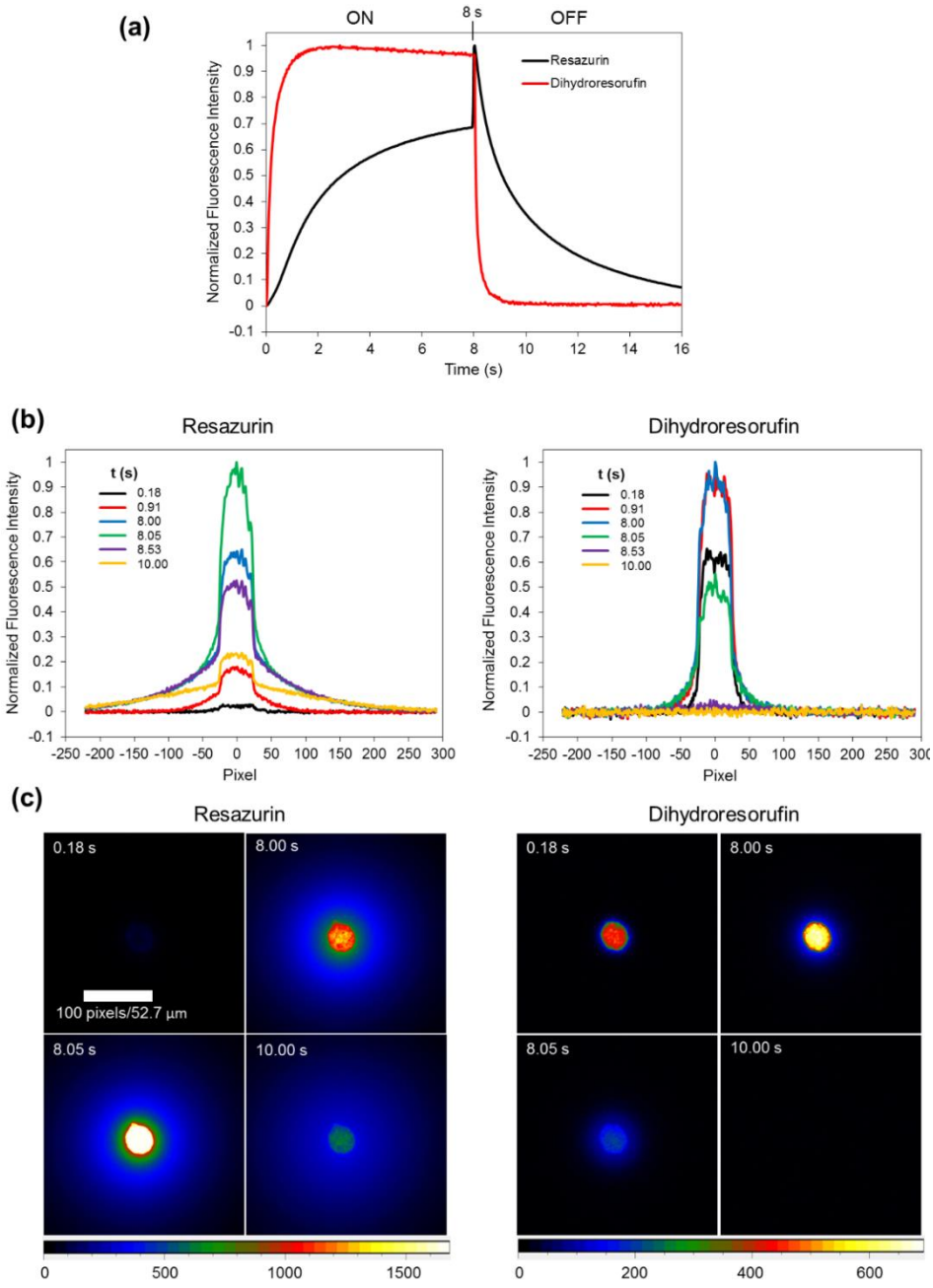

Figure 2.14. Resolution of resazurin and dihydroresorufin systems in FEEM.
Voltage pulsing experiment comparing the FEEM detection of ferricyanide using dihydroresorufin to the detection of ferrocyanide using resazurin at a 25 µm Au electrode. **(a)** Comparison of the normalized fluorescence intensity over time of the resazurin system and dihydroresorufin system. The voltage pulse was in the "on" state (a potential sufficient to drive the coupled reactions of interest) for 8 s and then switched to the "off" state for 8 s. **(b)** Linescans across the electrode over the course of the voltage pulse. **(c)** Fluorescence images of the electrode over the course of the voltage pulse. The maximum intensity on the color scale was set to the maximum pixel intensity recorded at the electrode at 8 s.

2.6 References

(1) Gesquiere, A. J.; Park, S. J.; Barbara, P. F. *J. Phys. Chem. B* **2004,** *108*, 10301–10308.

(2) Palacios, R. E.; Fan, F. R. F.; Bard, A. J.; Barbara, P. F. *J. Am. Chem. Soc.* **2006,** *128*, 9028–9029.

(3) Palacios, R. E.; Fan, F. R. F.; Grey, J. K.; Suk, J.; Bard, A. J.; Barbara, P. F. *Nat. Mater.* **2007,** *6*, 680–685.

(4) Xu, W.; Shen, H.; Kim, Y. J.; Zhou, X. C.; Liu, G. K.; Park, J.; Chen, P. *Nano Lett.* **2009,** *9*, 3968–3973.

(5) Guerrette, J. P.; Percival, S. P.; Zhang, B. *J. Am. Chem. Soc.* **2013**, *135*, 855–861.

(6) Mavre, F.; Anand, R. K.; Laws, D. R.; Chow, K. F.; Chang, B. Y.; Crooks, J. A.; Crooks, R. M. *Anal. Chem.* **2010**, *82*, 8766–8774.

(7) Fosdick, S. E.; Crooks, R. M. *J. Am. Chem. Soc.* **2012**, *134*, 863–866.

(8) Fosdick, S. E.; Knust, K. N.; Scida, K.; Crooks, R. M. *Angew. Chem. Int. Ed.* **2013**, *52*, 10438–10456.

(9) Duval, J. F. L.; Minor, M.; Cecilia, J.; van Leeuwen, H. P. *J. Phys. Chem. B.* **2003**, *107*, 4143–4155.

(10) Ulrich, C.; Andersson, O.; Nyholm, L.; Bjorefors, F. *Angew. Chem. Int. Ed.* **2008**, *47*, 3034–3036.

(11) Arora, A; Eijkel, J. C. T.; Morf, W. E.; Manz, A. *Anal. Chem.* **2001**, *73*, 3282–3288.

(12) Zhang, X.; Chen, C.; Li, J.; Zhang, L.; Wang, E. K. *Anal. Chem.* **2013**, *85*, 5335–5339.

(13) Xu, W.; Kong, J. S.; Yeh, Y. T. E.; Chen, P. *Nat. Mater.* **2008**, *7*, 992–996.

(14) Han, K. S.; Liu, G. K.; Zhou, X. C.; Medina, R. E.; Chen, P. *Nano Lett.* **2012**, *12*, 1253–1259.

(15) Zhou, X.; Andoy, N. M.; Liu, G.; Choudhary, E.; Han, K. S.; Shen, H.; Chen, P. *Nat. Nanotechnol.* **2012**, *7*, 237–241.

(16) Zhou, X.; Choudhary, E.; Andoy, N. M.; Zou, N.; Chen, P. *ACS Catal.* **2013**, *3*, 1448–1453.

(17) Twigg, R. S. *Nature* **1945**, *155*, 401–402.

(18) Shakashiri, B. Z. *Chemical Demonstrations: A Handbook for Teachers in Chemistry*, Vol. 2; University of Wisconsin Press: Madison, WI; **1989**.

(19) Campbell, J. A. *J. Chem. Ed.* **1963**, *40*, 578–583.

(20) Anderson, L.; Wittkopp, S.M.; Painter, C.J.; Liegel, J.J.; Schreiner, R.; Bell, J.A.; Shakhashiri, B.Z. *J. Chem. Ed.* **2012**, *89*, 1425-1431. Note: Although this work details the deprotonation and chemical oxidation products of glucose for the reduction of methylene blue, we believe it is highly likely that the same process is followed for the reduction of resorufin.

(21) Lei, C.; Hu, D.; Ackerman, E. J. *Chem. Commun.* **2008**, 5490–5492.

(22) Matsumoto, F.; Harada, M.; Koura, N.; Uesugi, S. *Electrochem. Commun.* **2003**, *5*, 42–46.

(23) Beden, B.; Largeaud, F.; Kokoh, K. B.; Lamy, C. *Electrochimica Acta* **1996**, *41*, 701–709.

(24) Park, S.; Boo, H.; Chung, T. D. *Anal. Chim. Acta* **2006**, *556*, 46–57.

(25) Saito, Y. *Rev. Polarogr*. **1968**, *15*, 177-182.

(26) Schilling, E.A.; Kamholz, A.E.; Yager, P. *Anal. Chem.* 2002, 74, 1798-1804.

(27) Vassilyev, Y. B.; Khazova, O. A.; Nikolaeva, N. N. *J. Electroanal. Chem.* **1985**, *196*, 127–144.

(28) Plana, D.; Jones, F. G. E.; Dryfe, R. A. W. *J. Electroanal. Chem.* **2010**, *646*, 107–113.

(29) Guerrette, J. P.; Oja, S. M.; Zhang, B. *Anal. Chem.* **2012**, *84*, 1609–1616.

(30) Cox, J. T.; Guerrette, J. P.; Zhang, B. *Anal. Chem.* **2012**, *84*, 8797–8804.

CHAPTER 3

Imaging the Transient Formation of Diffusion Layers with Fluorescence-Enabled Electrochemical Microscopy*

3.1 Introduction

Concentration gradients influence and control many different chemical and biological processes. Examples include the synaptic transmission of neurotransmitters,[1] diffusional transport of drugs across cell membranes,[2] and phase-transfer reactions.[3] In electrochemistry, concentration gradients are of the utmost importance, as they control the diffusive flux of redox species to an electrode surface.[4] In turn, this flux is what determines the electrochemical current measured at the electrode. Additionally, the concentration profile of redox species at distances away from the electrode surface may provide insight into reaction mechanisms and reactivity that would be difficult to obtain from purely voltammetric methods. Due to this importance, much effort has gone into imaging and understanding these concentration gradients.

Existing methods for electrochemical concentration profile mapping are divided between scanning techniques and those that image the entire profile in one experiment. Typically, those that image the entire profile are based on optical techniques. McCreery and coworkers developed an absorption spectroscopy-based technique, in which a collimated laser beam is passed parallel to an electrode surface and imaged on a photodiode array detector, giving concentration profiles

* This chapter is adapted with permission from Oja, S.M.; Zhang, B. "Imaging transient formation of diffusion layers with fluorescence-enabled electrochemical microscopy." *Anal. Chem.* **2014**, *86*, 12299-12307. Copyright (2014) American Chemical Society.

of planar diffusion,[5,6,7,8] and with special treatment, cylindrical and spherical diffusion.[9,10] Techniques that measure the refractive index gradient, which is affected by the concentration gradient, have also been developed, although these have a lower selectivity and sensitivity.[11,12,13]

Sojic and coworkers developed a novel technique in which an optical fiber bundle was used to image the concentration profile caused by the consumption of a fluorescent redox species at an electrode.[14] The fiber bundle was placed perpendicularly to the electrode surface and used to image the fluorescence signal, which was directly related to the concentration of the fluorescent redox species. This enabled imaging of the entire planar diffusion layer at a given time with micrometer spatial resolution and millisecond temporal resolution. While certainly useful, this technique was only demonstrated for planar diffusion and can only monitor species which change fluorescent state upon oxidation or reduction. Other studies have used fluorescence[15] or electrogenerated chemiluminescence (ECL)[16,17] to image electrochemical reactions at electrodes, but these only provide information about the electrode surface, not the entire diffusion layer. Recently, Bouffier and coworkers reported[18] qualitatively imaging a pH gradient on an open bipolar electrode[19] by using the pH-sensitive dye fluorescein.

Scanning techniques have been the more popular imaging method over the past two decades. The techniques developed thus far rely on scanning either optical or electrochemical probes throughout the diffusion layer to build an image. Fluorescence confocal laser scanning microscopy[20,21,22] and confocal resonance Raman spectroscopy[23,24] have been used to image concentration profiles from microelectrodes. Methods using electrochemical probes have received much attention and involve sampling the diffusion layer with a microelectrode.[25,26] Especially popular is scanning electrochemical microscopy (SECM),[27] which has been used to monitor concentration profiles near electrode surfaces.[28,29,30] Scanning ion conductance

microscopy (SICM)[31] has also been used to monitor ionic species.[32] Recently, two separate studies have used SECM with different positional feedback methods to generate three-dimensional (3-D) maps of diffusion layers from microelectrodes.[33,34] While these provide quantitative measurements with excellent spatial resolution, their scanning nature doesn't make them well-suited for mapping diffusion layers during common dynamic electrochemistry experiments such as cyclic voltammetry (CV).

We wish to show here that concentration profiles from ultramicroelectrodes (UMEs) can be dynamically imaged in two and three dimensions using fluorescence-enabled electrochemical microscopy (FEEM), a new electrochemical imaging tool under development in our lab. FEEM uses a closed bipolar electrode[35,36,37,38,39] to electrically couple a conventional redox reaction of interest on one pole of the electrode to a fluorogenic reporter reaction on the opposite pole.[40,41] Under conditions where the reporter pole is not limiting, the rate of the conventional redox reaction can be monitored by optically monitoring the rate of the reporter reaction via fluorescence microscopy. Thus, FEEM converts an electrical signal into an optical signal. One of the powerful aspects of FEEM is that an array of thousands or more parallel bipolar electrodes can be driven by a simple voltage source using two driving electrodes, and reaction rates can be monitored at each individual electrode in the array simultaneously provided that each electrode has an optically resolvable fluorescence signal.

We use FEEM in a setup as shown in Figure 3.1a to image the concentration profile of redox species formed by diffusion on a UME. The imaged electrode, or generator UME, is placed in a solution of a reduced species (R, i.e. ferrocyanide) and positioned orthogonally to a bipolar electrode array. A solution of dihydroresorufin (PH_2), a redox molecule that turns highly fluorescent upon oxidation (Figure 3.1b), is placed on the reporter side of the bipolar array and

positioned on a microscope for fluorescent imaging. When the potential of the generator electrode is adjusted to oxidize the reduced species (i.e. generate ferricyanide, O), the species generated at the UME will then diffuse away from the electrode surface. If the bipolar array is held at a potential appropriate to couple the reduction of the generated species to the oxidation of dihydroresorufin, molecules of the generated species that diffuse to the array will be reduced and a fluorescence signal will appear on the reporter end of the array. Because the fluorescence signal is sensitive to analyte concentration, this will result in a two-dimensional (2-D) image of a lateral cross section of the diffusion layer.

Changing the axial distance between the generator electrode and the array enables lateral cross sections of the entire diffusion layer to be imaged, and a compilation of these cross sections yields a three-dimensional (3-D) map of the diffusion layer. Importantly, the reporter reaction used is reversible so that upon electrochemical oxidation to the fluorescent form it is chemically reduced back to the non-fluorescent form.[42] This ensures that fluorophores don't significantly accumulate and diffuse on the reporter side of the array, preserving spatial and temporal resolution.[41] We note that the use of a bipolar electrode to optically record a CV experiment is not itself a new concept, as Crooks and coworkers presented a technique termed snapshot voltammetry that uses an open bipolar electrode to optically measure a voltammogram of an ECL reaction in one micrograph.[43] The focus of our work, however, is the imaging of dynamic diffusion layers in 2- and 3-dimensions, not necessarily the accurate optical recording of a voltammogram.

In this chaper, we first demonstrate the relationship between the electrochemical signal of the generator electrode and the fluorescence signal at the array as a function of electrode-array distance for CV experiments. We then present 2- and 3-D images of the diffusion layer of a 10

μm diameter carbon fiber (CF) UME over the course of a CV experiment as imaged by FEEM and provide a comparison of the FEEM images to numerically simulated concentration profiles. This comparison demonstrates that FEEM can be used to provide accurate images of the diffusion layer beyond a distance equal to ~2 times the electrode diameter for this particular electrode geometry. Lastly, to highlight the versatility of this technique, we image the diffusion layer of a two electrode array consisting of two 10 μm CFs spaced 150 μm apart during a potential step experiment.

3.2 Experimental Section

3.2.1 Reagents, Chemicals and Dihydroresorufin Solution Preparation.

Potassium ferrocyanide ($K_4Fe(CN)_6^{4-}$, Fluka, > 99.5 %), potassium chloride (J.T. Baker, 99.8%), resazurin sodium salt (Aldrich, dye content ~75%), sodium hydroxide (J.T. Baker, 98.5%), glucose (Sigma, 99.5%), 2-allylphenol (Aldrich, 98%), methanol (Fisher Scientific, 99.9%), and ammonium hydroxide (Fisher Scientific, 29.6% in H_2O) were all used without further purification. Deionized water (>18 MΩ·cm) was obtained through a Barnstead Nanopure water purification system and used for all aqueous solutions. A 100 μM dihydroresorufin solution containing 67 mM glucose and 0.5 M NaOH was prepared fresh daily as previously described.[41]

3.2.2 FEEM Setup.

Fluorescence imaging was done on an Olympus IX70 inverted microscope equipped with an IX-FLA inverted reflected light fluorescence observation attachment. The excitation source consisted of a Thorlabs M530L2 Collimated LED powered by a DC2100 LED Driver and filtered using a cube with a HQ535/50 excitation filter, a Q565lp dichroic mirror and a

HQ610/75 emission filter. A 20X 0.40NA objective (Olympus LCPlanFl 20X/0.40 Ph1) was used, with an additional 1.5X magnification on the microscope used for the single CF UME experiments. An Andor iXon+ EMCCD camera cooled to -80 °C and Andor SOLIS software was used to record and process all videos and images. All 3-D images and videos were compiled using the 3-D viewer plugin of Fiji (Fiji Is Just ImageJ).[44,45] Video was recorded at a frame rate of 10 Hz for all experiments using a pre-amplifier gain setting of 5.1 unless otherwise noted. An electron multiplier gain of 25 was used for the double barrel CFE experiment.

The potential across the bipolar electrode array was applied with two Ag/AgCl reference electrodes controlled by a Chem-Clamp potentiostat (Dagan). A separate Chem-Clamp potentiostat interfaced to a Dell computer through a PCI-6251 data acquisition board (National Instruments) via a BNC-2090 analog breakout box (National Instruments) was used to control the potential of the generator UME, which shared a common Ag/AgCl reference with the bipolar array. The position of the carbon fiber UME was controlled with a Sutter MP-285 motorized micromanipulator (Sutter Instrument Co.). For potential sweep experiments, LabView 8.5 (National Instruments) was used for voltage function generation and acquisition of the current-voltage data. A 10 mV/s scan rate was used for all potential sweep experiments. For potential step experiments, an Agilent 33220A waveform generator (Agilent Technologies) was interfaced to the potentiostat. All reported potentials are referenced vs. Ag/AgCl (3 M KCl).

3.2.3 Electrode and Electrode Array Fabrication.

Single CF UMEs were fabricated following the method published by Strein and Ewing.[46] A 10 μm diameter CF was aspirated into a 1.2 mm OD/0.69 mm ID borosilicate capillary (Sutter Instrument Co.) and pulled using a P-97 micropipette puller (Sutter Instrument Co.). A tungsten wire with Ag paint (Dupont) was used to make contact to the back end of the fiber. Epoxy (0151

Hysol, Loctite) was used to seal the gap between the protruding fiber and the capillary tip, and the protruding fiber was insulated via electropolymerization of 2-allylphenol. This was accomplished by immersing the fiber in a solution of 90 mM 2-allylphenol in 1:1 H_2O:MeOH adjusted to pH ~9 by ammonium hydroxide and applying 4 V vs. a Pt counter electrode for 10 min, followed by curing for 1 h at 150 °C. A glass knife was used to cut the insulated fiber and expose a fresh surface before each experiment.

Double-barrel carbon fiber electrodes (CFEs) were fabricated following the method published by Zhang et al.[47] A 10 μm CF was aspirated into each barrel of a double barrel borosilicate capillary (1.0 mm OD/0.50 mm ID, Sutter Instrument Co.) and pulled using a P-97 micropipette puller. The electrode was then dipped in low-viscosity epoxy (Epofix, Electron Microscopy Sciences) for 5 min to seal the gap between the fiber and the capillary tip. Electrical contact was made by inserting a tungsten wire with Ag paint into the back end of each barrel. The capillary was polished with a homemade polisher made from a computer hard drive to expose the carbon fibers. The bipolar electrode arrays were prepared as previously described.[40] Briefly, CF pultrusion rods consisting of thousands of insulated individual 6-μm diameter CFs were purchased from DPP Pultrusion through the distributor A2Z Corp. Rod sections were further sealed in Epo-Tek 301 epoxy (Epoxy Technologies, Inc.), and cross sections were then cut and polished to a thickness of ~0.5 mm.

3.2.4 Simulations.

Simulation of ferrocyanide oxidation on the CF UME was done using COMSOL Multiphysics (version 4.3a) finite element simulation software run on a 12 core PC workstation. Details of the simulation, including geometry and parameters, can be found in Appendix 1 (Figure 3.A1.1, 3.A1.2, Table 3.A1.1).

3.3 Results and Discussion

3.3.1 Imaging a Single Carbon Fiber Ultramicroelectrode During a Potential Sweep

A single 10 μm diameter CF UME was used as the generator electrode to demonstrate the principle of diffusion layer imaging with FEEM. Importantly, the insulating sheath on the CF UME is thin (on the order of 200 nm)[46] by comparison to the CF size, enabling close approach of the electrode to the bipolar electrode array and minimizing redox cycling between the electrode and the array. Figure 3.2 presents electrochemical and fluorescence data for imaging the CF UME in 5.7 mM ferrocyanide with 1 M KCl as supporting electrolyte. The potential of the CF UME is swept from 0 to 0.8 V at 10 mV/s, oxidizing ferrocyanide to ferricyanide, while the potential across the array is kept constant at 0 V, a potential sufficient to drive ferricyanide reduction coupled to dihydroresorufin oxidation on a closed bipolar electrode. The potential necessary to drive coupled reactions on a closed bipolar electrode is roughly the difference between the potentials needed to drive each reaction in a normal two or three electrode cell. As we demonstrated in our previous paper, the onset potential of the coupled ferricyanide reduction/dihydroresorufin oxidation reaction on a closed bipolar electrode is about 830 mV, roughly the difference between the onset potentials for the reduction of ferricyanide (310 mV) and the oxidation of dihydroresorufin (-540 mV).[41] We chose to apply 0 V across the array to ensure that the reactions would be driven at a mass-transfer limited rate. The axial distance between the CF UME and the array was controlled and changed from 1 to 160 μm in order to image the entire diffusion layer. The CF UME steady-state current can be plotted as a function of axial position (Figure 3.3, 3.4) to get an SECM-like approach curve. Once the electrode is determined to be within 1 μm of the array surface, this position is used as the "0 μm" electrode-

array distance. As can be seen in the electrochemical signal (Figure 3.2a), the steady-state current increases as the electrode-array distance increases, reaching over 90% of its maximum value at an electrode-array distance of 20 µm. This increase is due to reduced blockage of diffusion from the bulk solution to the CF UME as it is moved further away from the comparatively infinite surface of the bipolar array. We believe that the decrease in steady-state current in going from an electrode-array distance of 1 µm to 2 µm is due to the smaller distance resulting in an increased amount of redox cycling. Further discussion of the effect of redox cycling on the signal can be found in Appendix 2 (Figure 3.A2.1). Up to an electrode-array distance of 20 µm, the fluorescence signal recorded at the array (Figure 3.2b) mirrors the changes in the electrochemical signal. As expected, an increased rate of ferricyanide generation (as indicated by steady-state current) results in an increased fluorescence signal, as more ferricyanide diffuses the short distance between the CF UME and the array and couples to dihydroresorufin oxidation. At electrode-array distances greater than 20 µm, two distinct changes in the signal occur: the fluorescence onset is delayed, and the overall fluorescence intensity decreases. Both of these changes can be attributed to the array sampling a cross-section of the diffusion layer that is increasingly further from the CF UME. The more distal the cross-section, the lower the concentration of generated ferricyanide. We have previously shown FEEM to be sensitive to changes in analyte concentration, which explains the decrease in fluorescence signal with increasing electrode-array distance. The delay in the onset of fluorescence signal is also attributable to sampling more distal cross-sections, as it takes longer for the generated ferricyanide molecules to diffuse the gap between the CF UME and the bipolar array.

The diffusion layer is easily visualized with the fluorescence images generated on the bipolar array. Figure 3.5a presents the fluorescence images acquired during the experiment

described in Figure 3.2. Each row of images shows the fluorescence at the array over the course of the CF UME potential sweep for a fixed electrode-array distance. The four rows in Figure 3.5a therefore represent cross-sections of the diffusion layer at four different electrode-array distances: 0 μm, 25 μm, 50 μm, and 100 μm. As the CF UME potential is swept to 0.8 V, ferricyanide is being generated at an increasing rate and the diffusion layer expands. This can be clearly seen in the fluorescence images. Both the increasing delay in fluorescence onset and the decrease in fluorescence signal as the electrode-array gap increases can be clearly seen in these images as well. As the CF UME potential is swept back to 0 V, ferricyanide generation decreases and the diffusion layer contracts, which again is clearly shown in the fluorescence images. It is worthwhile to note the critical importance of the reversibility of the fluorogenic reporter reaction. Dihydroresorufin is in a reducing environment (basic glucose) to ensure that upon electrochemical oxidation to the fluorescent resorufin at the array, it is chemically reduced back to dihydroresorufin, thus quenching fluorescence before significant accumulation of the fluorophore can occur. Without this quenching effect, resorufin would accumulate, making dynamic diffusion layer imaging nonviable without some other means of consuming the generated fluorophore. The quenching of the electrogenerated fluorophore can be easily visualized in an experiment in which the generator electrode is held at a fixed potential to generate molecules while being moved laterally around the array. Without fluorophore quenching, the fluorescence signal would accumulate and quickly obscure the position of the generator electrode. However, the electrogenerated fluorophores are quickly reduced back to their non-fluorescent form, and the position of the generator electrode can be easily tracked.

2-D images, such as those in Figure 3.5a, can be compiled to form 3-D images of the generator electrode diffusion layer over the course of the potential sweep (Figure 3.5b). Note that

the images are displayed on a tilted axis for better visualization of the diffusion layer. As can be seen in the 3-D images, the diffusion layer expands in both the lateral and axial directions as the CF UME potential is swept to 0.8 V, followed by contraction of the diffusion layer as the potential is swept back to 0 V. Each 3-D image consists of a *z*-stack of all 2-D images for each electrode-array distance measured at a potential of interest. Therefore, the spatial resolution of a 3-D image in the axial direction will be determined by the increment in which the electrode-array distance was changed. For this experiment, the electrode was moved in the following increments: 5 μm from 0-50 μm, 10 μm from 50-100 μm, and 20 μm from 100-140μm. These differing levels of axial resolution are clearly demonstrated in the cross-sections shown in Figure 3.6a. Axial resolution of 280 nm should be possible with the setup used here (limited by the step-size of the micromanipulator), but imaging the entire diffusion layer was our focus and thus such a small step-size would have been prohibitively time consuming.

Clearly, simulated diffusion layers are needed to validate our technique and ensure that it is producing accurate images. Especially important is determining how significant an effect the bipolar array has on distorting the diffusion layer. Since the array is an infinite surface in comparison to the size of the CF UME, placing it near the UME will undoubtedly lead to distortions of the diffusion layer. Unfortunately, there is no way around this distortion, as the array must be within the diffusion layer to image it. However, as indicated in the electrochemical CVs presented in Figure 3.2a, this distortion is likely only a problem at smaller electrode-array distances. As noted earlier, the steady-state current of the 10 μm CF UME reached over 90% of its original value at an electrode-array distance of 20 μm, indicating that the array shouldn't significantly distort the diffusion layer at distances greater than this. Indeed, this is what a comparison between our experimental images and simulated images confirms. Presented in

Figure 3.6a are cross sections of the 3-D fluorescence images shown in Figure 3.5b, which can be compared to our simulated results (Figure 3.6b). We simulated a potential sweep experiment with conditions matching those of the FEEM experiment (i.e. ferrocyanide oxidation on a 10 μm diameter disk electrode) except that there were no surfaces near the electrode to distort the diffusion layer. Details of the simulation, including simulation parameters and geometry, can be found in Appendix 1 (Figure 3.A1.1, 3.A1.2). The black concentration contour line shown in the simulated figures represents a ferricyanide concentration of 50 μM. As can be seen, this corresponds roughly to the boundary of the FEEM-imaged diffusion layer. This concentration detection limit matches well with our previous findings, although our previous study used Au electrodes.[41] However this work seems to indicate similar detection performance between Au and CF, although more work is needed to confirm this. As predicted, there is a deviation between the FEEM-imaged diffusion layer and the simulated diffusion layer within an electrode-array distance of ~20 μm. Especially apparent in the images at 600 mV, 800 mV, and 400 mV (return scan), the FEEM-imaged diffusion layer shrinks in lateral size as the electrode-array distance decreases from 20 μm. It is important to realize that this must be an artifact caused by the experimental method, namely the array blocking diffusion to the generator electrode at small electrode-array distances, rather than the actual, unobstructed diffusion layer. Thus, at small electrode-array distances (< 2 times the electrode diameter in this case), the FEEM image is not representative of the diffusion layer of an unobstructed electrode. However, in terms of imaging the entire diffusion layer, the FEEM results agree very well with simulations and seem to provide a qualitatively accurate image.

3.3.2 Imaging a Double-Barrel Carbon Fiber Ultramicroelectrode During a Potential Step

In order to demonstrate the versatility of this imaging technique, we chose to image the diffusion layer from a more complicated electrode system (2 electrode array) under a different electrochemical experiment (potential step). A double CFE, consisting of two individually addressable 10 μm diameter CFs spaced 147 μm apart (center-to-center), was used for the 2 electrode array (Figure 3.7a). Figure 3.7b presents electrochemical CVs used to characterize the electrode. The CVs were taken in 5 mM ferrocyanide solution with 1 M KCl as supporting electrolyte at 10 mV/s with the electrode at an "infinite" distance from any surface. As can be seen, the "red lead" CF has a slower kinetic response and reaches a current level about 1 nA less than the "black lead" CF at 0.7 V. This is likely due to the red lead CF having a less pristine surface given that the CFs were exposed by mechanical polishing. Imaging of the diffusion layer was done in the same manner as the single CF UME, except ferricyanide was generated with a potential step rather than a potential sweep. Once the double CFE was aligned to the array, the potential was stepped to 0.8 V to generate ferricyanide for 15 s and then stepped back down to 0 V to stop ferricyanide generation. Array fluorescence was monitored throughout the potential step. The electrode was then backed off 5 μm from the array and the potential pulse repeated. This was repeated in 5 μm increments until the electrode-array distance was 150 μm, at which point minimal fluorescence signal was observed at the array. The potential across the array was held constant at 0 V for the duration of the experiment.

Figure 3.8 presents the FEEM images of the diffusion layer acquired for the double CFE. As seen, the diffusion layer expands throughout the time period when the double CFE is generating ferricyanide, with the diffusion layers from each individual CF beginning to overlap at 5 s. When the potential is stepped back down to 0 V, ferricyanide is no longer generated and the diffusion layer contracts. The distance between the centers of the two fluorescence hotspots

was measured to be 152 µm, which corresponds nicely to the distance between the two CFs as measured by bright-field microscopy (147 µm). Again, note the lateral contraction of the imaged diffusion layers at electrode-array distances less than ~20 µm, which is a distortion due to the array blocking diffusion. From looking at the FEEM images, it is clear that the diffusion layer from the red lead CF is significantly smaller than that from the black lead CF. We believe that two factors are causing this. First, as indicated in the CVs in Figure 3.7b, the red lead CF has a more sluggish kinetic response, which would result in a diffusion layer that is smaller and expands more slowly than that for the black lead CF. Additionally, the data suggests that the double CFE was approached to the array surface at a slight angle, resulting in the red lead CF starting at a slightly larger electrode-array distance than the black lead CF. This is evident when looking at Figure 3.9, which shows the fluorescence intensities plotted over time for the two regions outlined in green in Figure 3.8a. For the red lead CF, the fluorescence is most intense at the smallest electrode-array distance, drops slightly when the electrode is backed off 10 µm, and then drops significantly as the electrode is backed off further. This is in stark contrast to the black lead CF, where the fluorescence intensity increases as the electrode-array distance is increased from 0 to 10 µm. The signal decreases when the electrode-array is increased to 25 µm, but it is still greater than at 0 µm. This is the same pattern that was observed for the single CF UME (Figure 3.2). The decreased fluorescence signal is due to the array partially blocking diffusion to the generator electrode at small electrode-array distances, resulting in a lower rate of ferricyanide generation and, subsequently, a lower fluorescence signal. Since the red lead CF signal doesn't increase as the electrode-array distance initially increases, that CF is likely initially offset some distance from the array surface. This is easily possible, as the double CFE could have approached the array at a slight angle, resulting in the two CFs having different

electrode-array distances. This demonstrates the importance of having the generator electrode and array normal to one another to avoid any distortions, especially if the generator is an array of electrodes. Using the diffusion coefficient of ferricyanide and the difference in fluorescence onset times at the various electrode-array distances, the offset distance between the black and red lead CFs can be calculated Appendix 3 (Figure 3.A3.1). This calculation gives the red lead CF as being offset ~12 μm further from the array than the black lead CF.

We also tried imaging the diffusion layer of a double CFE with two 10 μm diameter CFs spaced by only ~30 μm (center-to-center, Figure 3.10). For this experiment, the double CFE was imaged in a solution of 5 mM ferrocene in 0.1 M $TBAPF_6$, and a potential step of 0.7 V was applied for 15 s to oxidize ferrocene followed by stepping the potential back to 0.2 V to stop the oxidation. The imaging was done at a frame rate of 33.887 Hz. We were not able to resolve two distinct diffusion layers at any point during the potential pulse. This brings up a few factors regarding the spatial and temporal resolution of the technique. At a frame rate of 33.887 Hz, a molecule of ferrocene (or ferrocenium, Fc^+) will diffuse about 12 μm (assuming a diffusion coefficient of 2.47×10^{-5} cm^2/s) per frame. Therefore after one frame, the diffusion layers of the two CFs should already have some overlap, and two distinct diffusion layers will not be resolvable. Therefore, the inability to resolve two distinct diffusion layers from UMEs spaced so closely is a challenge of temporal resolution as limited by the frame rate of the camera. The temporal resolution is also tied to the rate at which the fluorophore is turned on and off. Work is currently underway to further understand and quantify this aspect.

The spatial resolution of the technique can be broken into axial and lateral components. As mentioned previously, the step size in which the electrode-array distance is changed determines the axial resolution. The lateral resolution depends in large part upon the bipolar

array. Each electrode in the bipolar array is analogous to a pixel in the resulting FEEM image. Therefore, the lateral resolution is determined by the number of independent electrodes resolvable by fluorescence microscopy in a unit area of the array. In this work, each electrode in the array had a diameter of 6 μm, the electrode spacing was heterogeneous, and not all electrodes were independent from one another. This can be clearly seen in the FEEM images in Figure 3.10, in which the area of the array showing fluorescence is somewhat irregular. This is caused by groups of electrodes in the array being short-circuited to one another, resulting in an image unrepresentative of the diffusion layer. At small electrode spacing in the array, resolving the fluorescence signal of individual electrodes from adjacent electrodes will become crucial to achieving the highest lateral spatial resolution. A key part of this step is minimizing fluorophore diffusion, which is accomplished in this study by chemically reducing the electrogenerated fluorophore back to its non-fluorescent form. Clearly, the kinetics of this fluorophore quenching reaction influence the quality of the FEEM image obtained. Qualitatively, the slower the kinetics of the reaction, the more distorted the resulting FEEM image will be. While we presented some brief results in a previous paper,[41] the kinetics of this reaction system have not been quantitatively studied. We note that a quantitative study has been performed on a chemically analogous system using methylene blue instead of resorufin,[48] however an electrode was not used to manipulate the reaction and thus the results may not be applicable to our scheme. We reserve the quantitative kinetic study of the quenching reaction and its influence on the resulting FEEM images for future work. Other methods to limit fluorophore diffusion include increasing solution viscosity and immobilizing the fluorophore on the array surface. We have also experimented with the use of ECL as a reporting mechanism and believe that it may have an advantage in spatial resolution due to the light-generating reaction occurring very near to

electrode surfaces but may have a disadvantage in detection sensitivity compared to fluorescence. We hope to report a comparison of fluorescence and ECL reporting mechanisms in the future. Incorporating these methods into FEEM, characterizing fluorophore diffusion and lifetime, and fabricating dense, uniform bipolar arrays are part of our ongoing efforts to better understand and improve the spatial and temporal resolution of FEEM.

3.4 Conclusion

FEEM has been demonstrated as a new technique to image dynamic concentration profiles from UMEs in two and three dimensions. The technique generates a 2-D image of a lateral cross section of the diffusion layer at each time point. By altering the distance between the generator electrode and the bipolar array, different cross sections of the diffusion layer can be imaged, and a 3-D image can be constructed. Because an entire 2-D cross section is imaged at a time, these 3-D images can be constructed relatively quickly. Importantly, this enables diffusion layers to be imaged throughout the course of dynamic electrochemistry experiments, such as potential steps and cyclic voltammetry.

An attractive aspect of FEEM diffusion layer imaging over previous optical methods using fluorescence or ECL is that it should be able to image any electroactive species. Practically, we can currently only image reduced species, as we have yet to incorporate an appropriate reversible fluorogenic reduction reaction into FEEM. We expect that we can do some diffusion layer imaging by using the non-reversible, fluorogenic reduction of resazurin as the reporter, but significant temporal and spatial resolution will be sacrificed. We believe this report lays out some of the important ground work for imaging with FEEM, and we expect this

technique and variations of it to be valuable in imaging concentration gradients and diffusional flux in other systems, not just purely electrochemical ones.

3.5 Figures

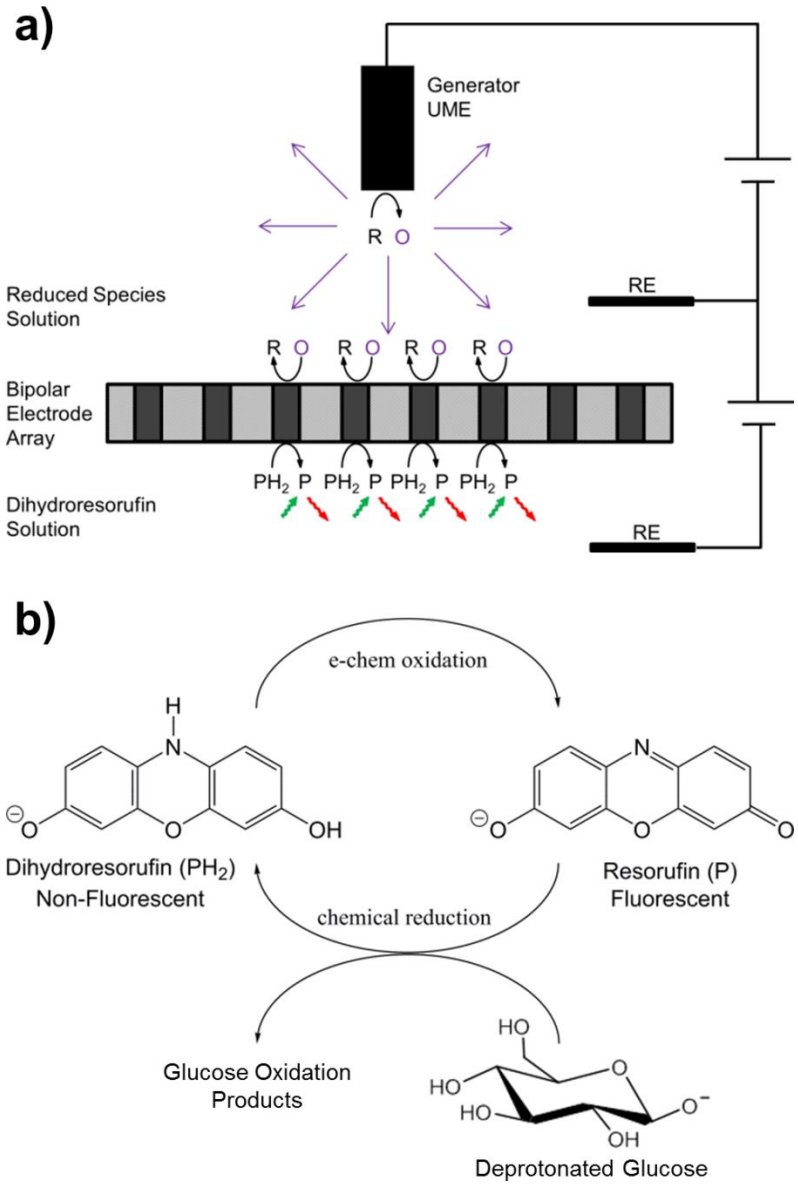

Figure 3.1. Scheme of imaging setup and dihydroresorufin system.
(a) Schematic of imaging a species (O) generated from a UME using FEEM. An array of parallel closed bipolar electrodes separates a solution of a redox species in reduced form (R) and a solution of dihydroresorufin (PH_2). Molecules generated at the UME diffuse to the array, where they are reduced. This reduction is coupled through the bipolar array to the fluorogenic oxidation of PH_2, which is monitored via fluorescence microscopy. Controlling the distance between the UME and bipolar array enables imaging different cross sections of the UME diffusion layer. **(b)** Reaction scheme showing the fluorogenic oxidation of PH_2 to resorufin (P) at an electrode and the subsequent chemical reduction of P back to PH_2 by a mild reducing agent such as deprotonated glucose.

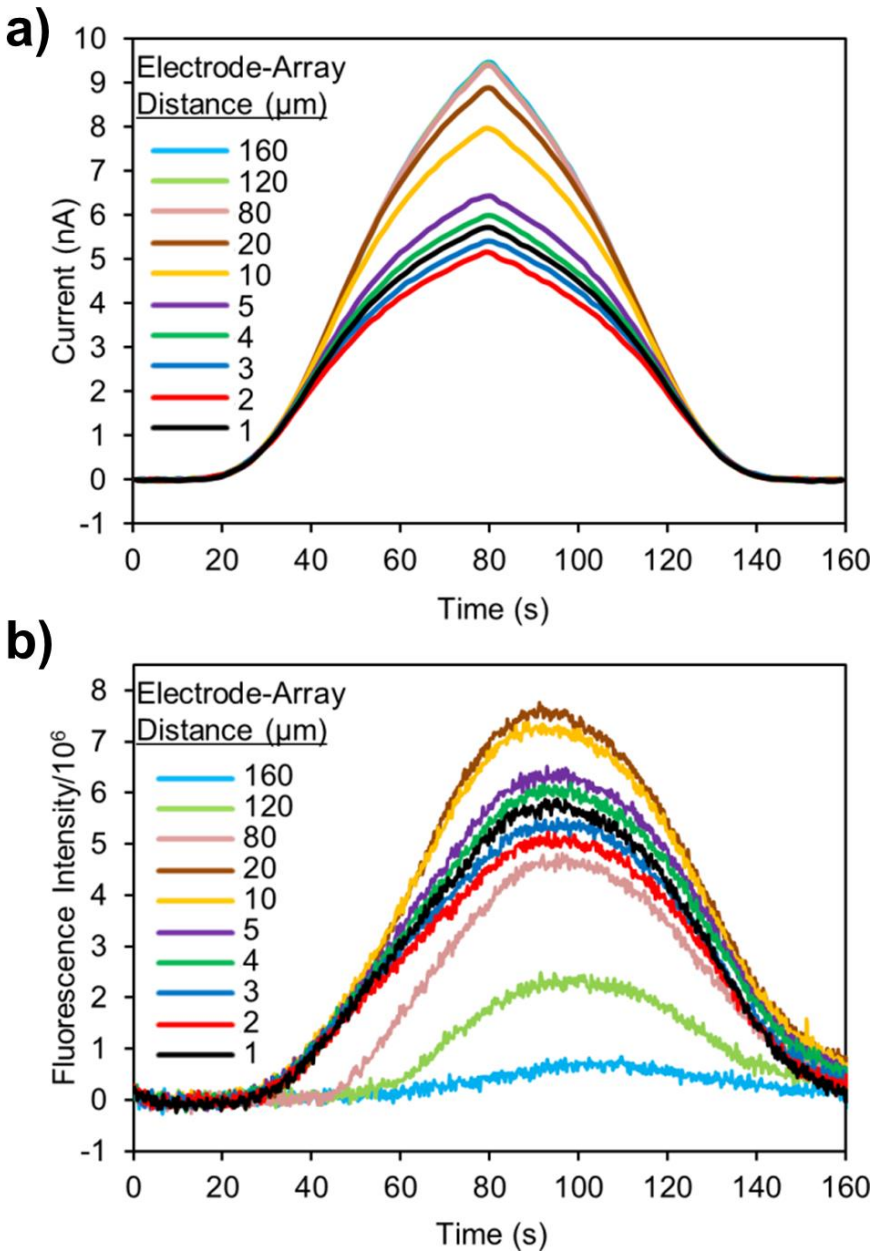

Figure 3.2. Correlated signal of generator electrode and bipolar array.
Correlation of electrochemical signal at the generator electrode and fluorescence signal at the bipolar array. **(a)** Electrochemical signal of the CF generator UME for potential sweeps from 0 to 0.8 V (scan rate = 10 mV/s) in 5.7 mM ferrocyanide at various distances from the bipolar electrode array. **(b)** Fluorescence signal recorded at the bipolar array during the potential sweep experiments in (a).

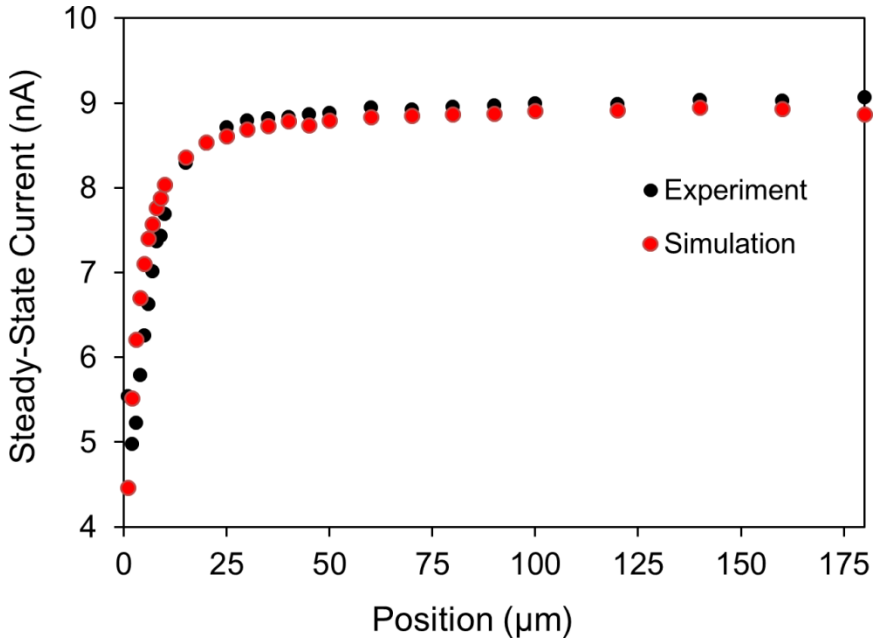

Figure 3.3. Experimental and simulated approach curves.
The steady-state current of a 10 μm diameter CF UME as a function of electrode-array distance. The black data points represent experimental values, while the red data points represent simulated values. The experimental steady-state values are given as the current recorded at the switching potential for the CVs shown in Figure 3.2. The simulated steady-state values are given as the current recorded at the switching potential for CVs simulated as laid out in Appendix 1. The electrode-array distance was altered by changing the distance *X*, which represents the electrode-array distance.

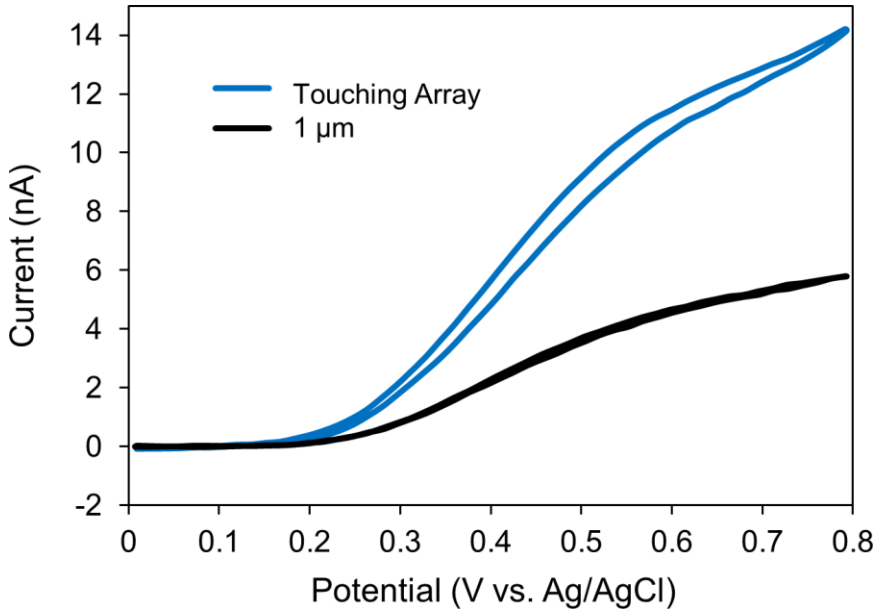

Figure 3.4. CVs to determine zero point for electrode-array distance.
CVs of a 10 µm CF UME taken in 5.7 mM ferrocyanide with 1 M KCl as supporting electrolyte at an electrode-array distance of approximately 1 µm (black trace) and a position 1 µm closer to the array (blue trace), at which point the CF UME is likely in electrical contact with the array. This results in a large increase in current due to the electrode size effectively increasing, as well as the possibility of the electrode directly controlling the electrochemical reduction of dihydroresorufin and glucose on the reporter side of the array. This signal is useful for defining a zero point for the electrode-array distance.

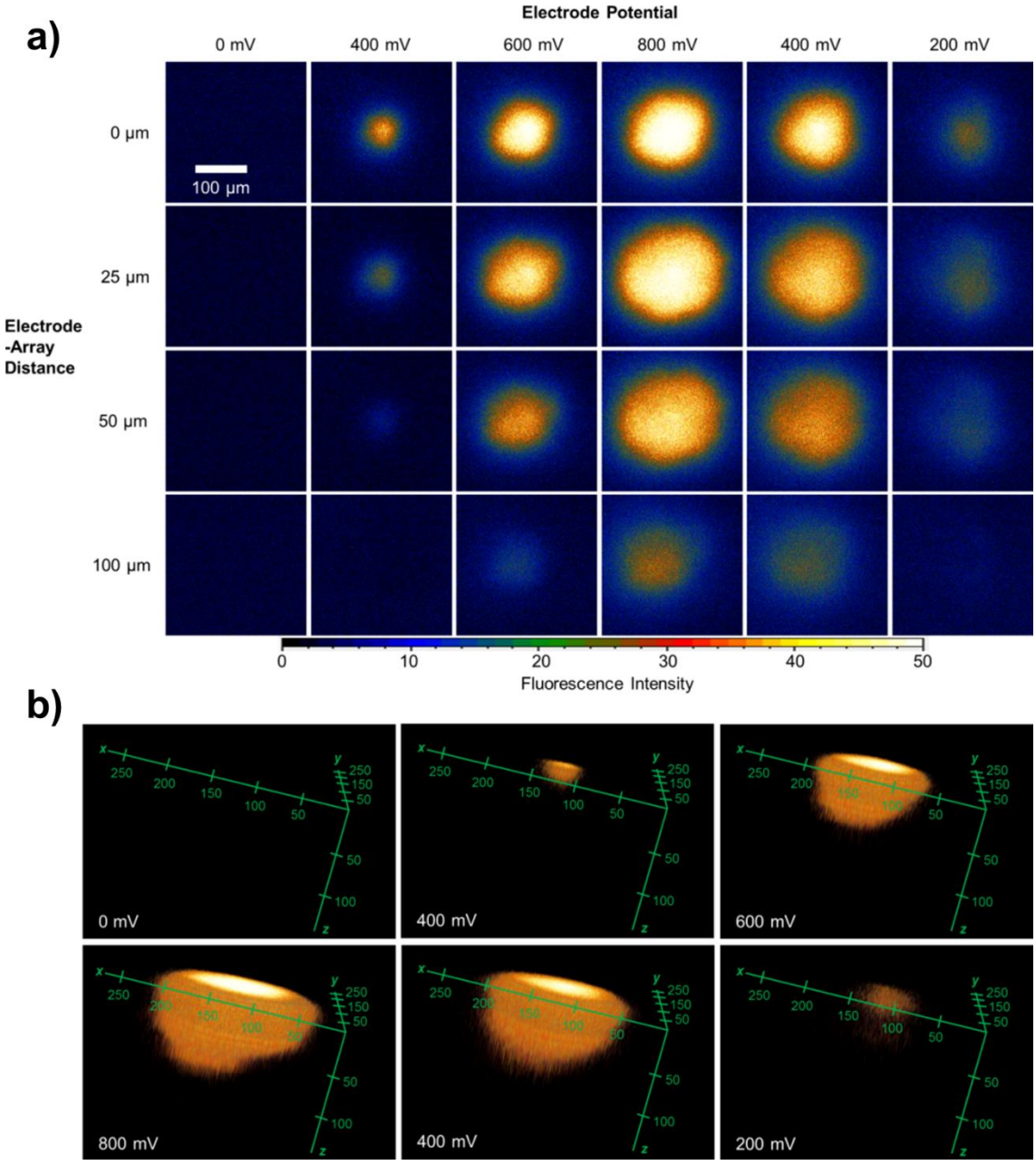

Figure 3.5. 2-D and 3-D FEEM images of a diffusion layer during a CV.
FEEM imaging of the diffusion layer from a 10 µm diameter CF UME during the course of a potential sweep in 5.7 mM ferrocyanide. **(a)** Fluorescence images of the bipolar array at various generator electrode potentials and electrode-array distances. Each row consists of images taken during a single potential sweep of the generator electrode (0 to 0.8 V at 10 mV/s) at a fixed distance from the bipolar array. **(b)** *z*-stacking of fluorescence images to recreate 3-D images of the generator electrode diffusion layer during a potential sweep. Each 3-D image consists of stacking the 2-D images acquired at a given potential for all electrode-array distances measured (i.e. stacking a column of images in (a)). Each 3-D image here consists of 18 2-D images.

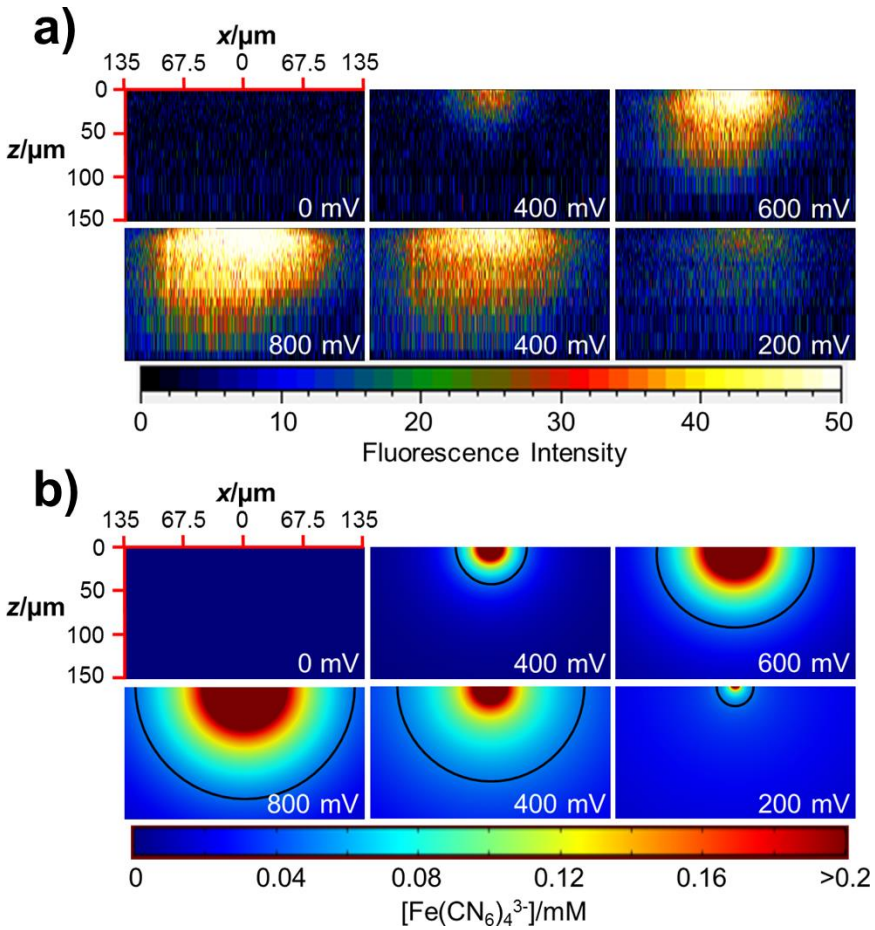

Figure 3.6. Comparison of experimental and simulated diffusion layer.
Comparison of a FEEM-imaged diffusion layer with a simulated diffusion layer. **(a)** Cross sections of the *z*-stacked 3-D fluorescence images in Figure 3.5 over the course of the potential sweep. **(b)** Simulated concentration profile of ferricyanide being generated via ferrocyanide oxidation at a 10 µm diameter UME for a potential scan from 0 to 0.8 V at 10 mV/s. The black contour line represents a ferricyanide concentration of 50 µM.

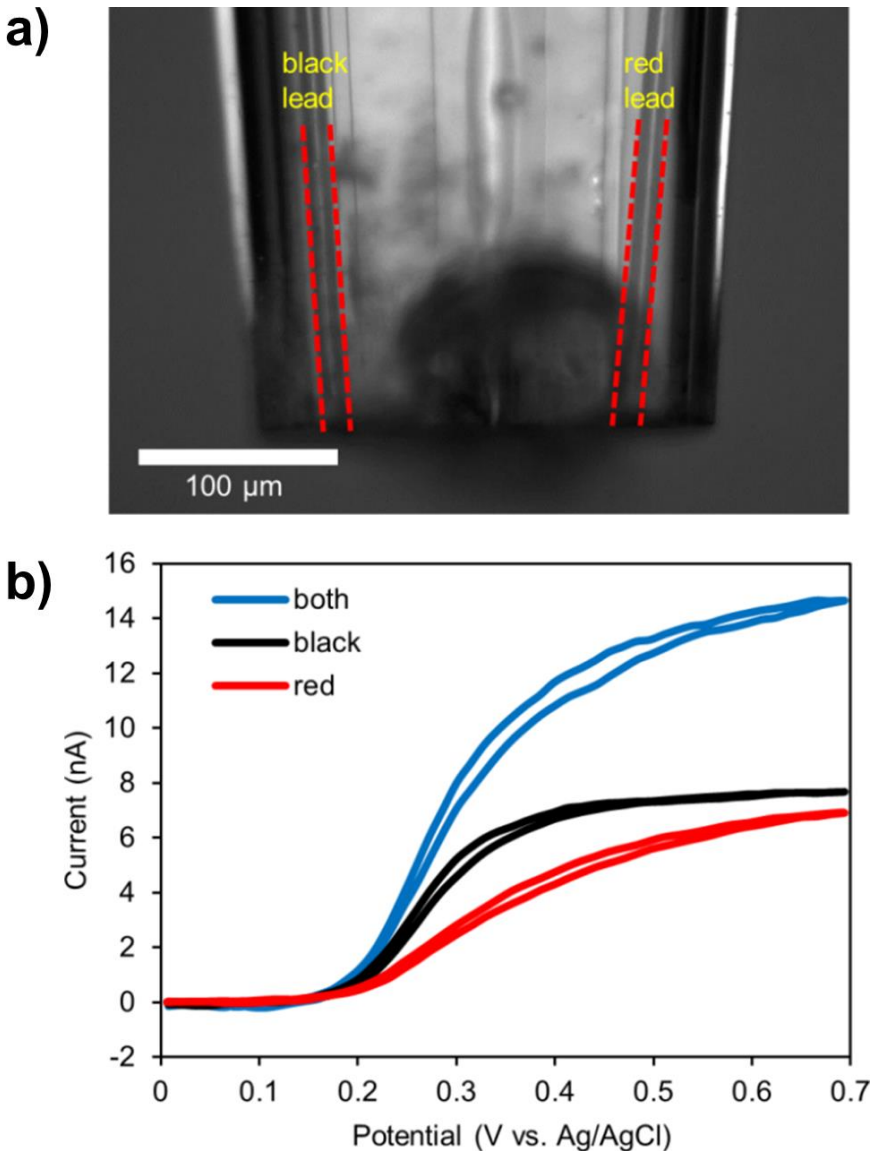

Figure 3.7. Double-barrel carbon fiber electrode.
(a) Optical micrograph of the double-barrel CFE used to acquire the data in Figure 3.8. Each fiber has a diameter of 10 µm. The center-to-center electrode spacing was measured to be 147 µm. **(b)** CVs of the double-barrel CFE in 5 mM ferrocyanide. The potential was swept from 0 to 0.7 V at 10 mV/s. CVs were taken of each fiber individually (black and red trace) and both fibers together (blue trace).

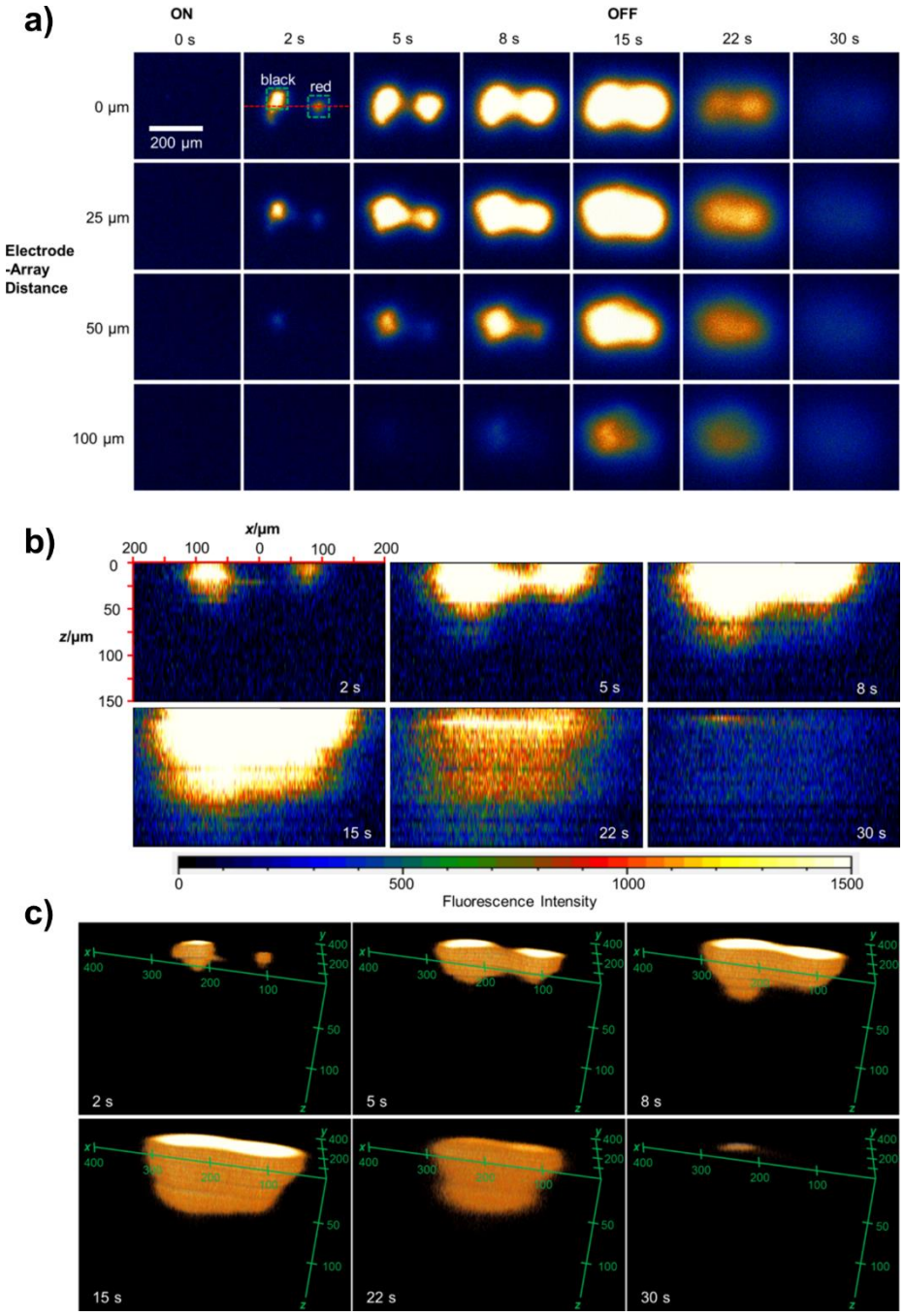

Figure 3.8. 2-D and 3-D FEEM images of a double-barrel CFE diffusion layer.
FEEM imaging of the diffusion layer of the double-barrel CFE shown in Figure 3.7 during a potential step experiment. The potential was held at 0.8 V in 5 mM ferrocyanide for 15 s and then switched to 0 V for 15 s. **(a)** Fluorescence images of the bipolar array at various times during the potential step and at various electrode-array distances. **(b)** Cross-sections of the FEEM-imaged diffusion layer at a position marked by the dashed red line in (a) at various times during the potential step. **(c)** 3-D FEEM images representing the diffusion layer over the course of the potential step.

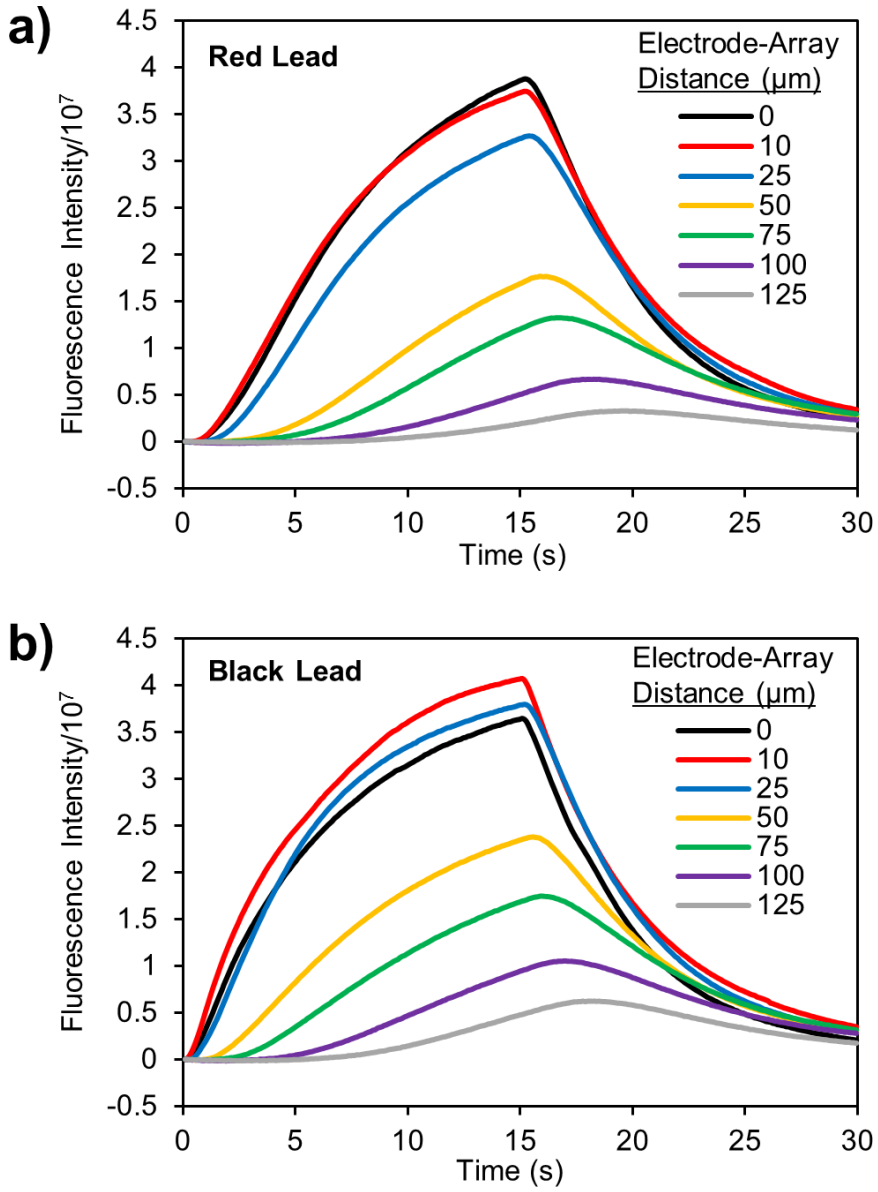

Figure 3.9. Fluorescence signal for each lead of the double-barrel CFE.
Fluorescence intensities over time for the red CF lead **(a)** and black CF lead **(b)** as a function of electrode-array distance. The signal is plotted for the green areas outlined in Figure 3.8a.

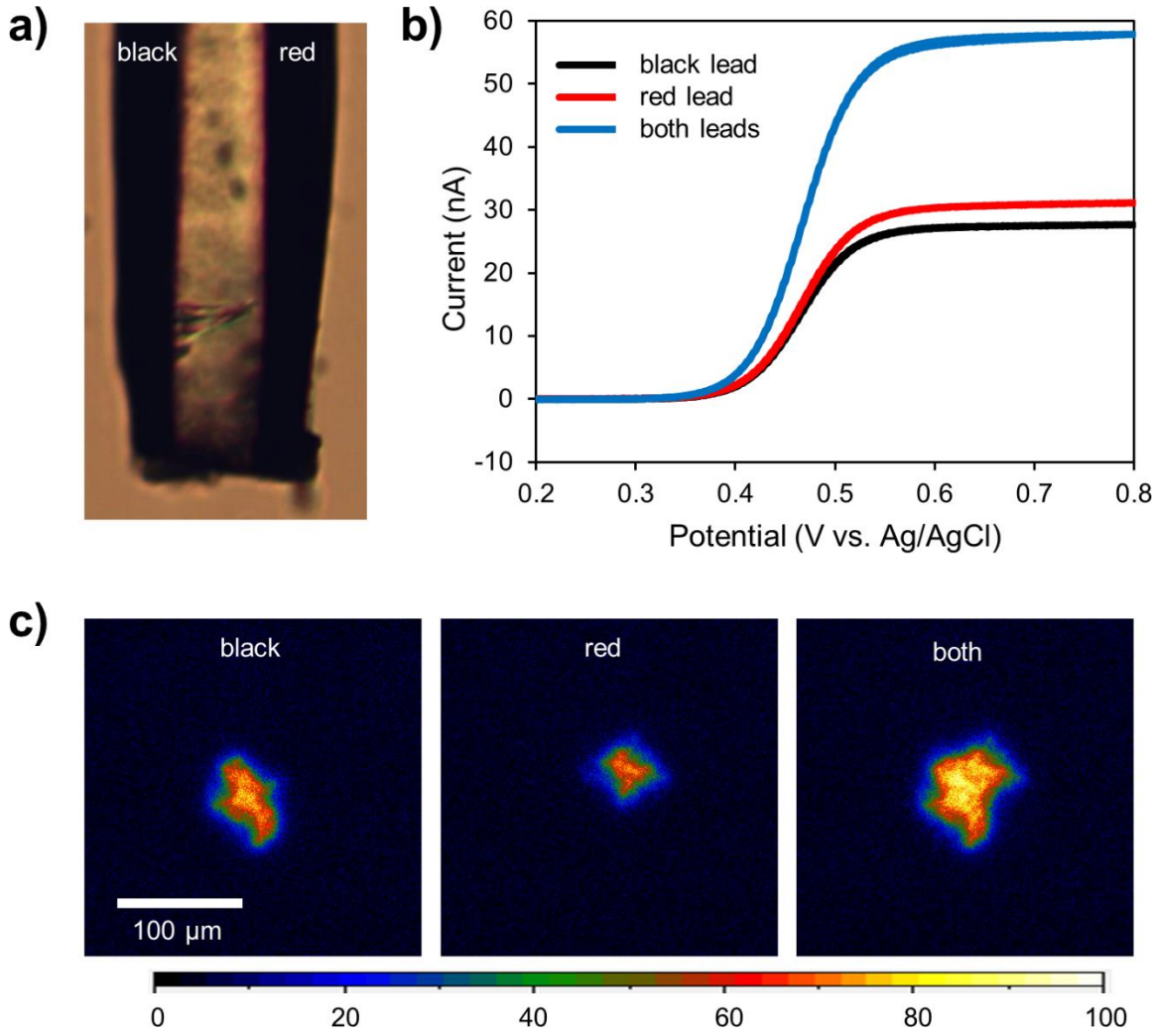

Figure 3.10. Double-barrel CFE with center-to-center distance of 30 µm.
(a) Optical micrograph of the double-barrel CFE with two 10 µm diameter CFs spaced by a center-to-center distance of 30 µm. **(b)** CV characterization of the double-barrel CFE in 5 mM ferrocene. The potential was swept from 0.2 to 0.8 V at 10 mV/s. CVs were taken of each fiber individually (black and red trace) and both fibers together (blue trace). **(c)** FEEM images of the double-barrel CFE taken 0.148 s into a potential pulse at an electrode-array distance < 1 µm. The experiment was done for each fiber individually (left and center panel) and for both fibers together (right panel).

Figure 3.10 Discussion.
Figure 3.10 shows the results of an attempt to image the diffusion layer of a double-barrel CFE with a center-to-center spacing between two 10 µm diameter CFs of 30 µm. The electrode was characterized optically (Figure 3.10a) and electrochemically (Figure 3.10b). Electrochemical characterization and the FEEM imaging experiment were carried out in a solution of 5 mM ferrocene with 0.1 M $TBAPF_6$ as supporting electrolyte. The FEEM imaging experiment was a

potential step as described in the main article. Figure 3.10c shows the FEEM images obtained 0.148 s into the potential pulse at an electrode array distance < 1 μm. Both the black lead and the red lead give a clear signal when pulsed individually (left and center panel), but when both leads are pulsed together (right panel), two separate diffusion layers are not distinguishable. At no point during the potential pulse were the two diffusion layers distinguishable, showing the limit of the camera frame rate on the temporal resolution of the technique. Also of note is the irregular shape of the diffusion layers. This is due to electrodes in the bipolar array showing cross-talk from being electrically connected, resulting in groups of connected electrodes giving signal rather than individual electrodes. This highlights the importance of having a quality bipolar array for accurate FEEM imaging.

3.6 APPENDIX 1

COMSOL Simulation

Numerical simulations were carried out using COMSOL Multiphysics finite element analysis software (version 4.3a) run on a 12 core PC workstation. The simulations, which solved Fick's second law, were run using a 2-D axisymmetric model with a geometry shown in Figure 3.A1.1. The boundary conditions for the simulation were as follows: no flux at the electrode insulator, surface 6, and the electrode array, surface 3; bulk concentration (C^*) at surfaces 1 and 2; and flux at the electrode, surface 5. This flux, J, was determined using a form of the Butler-Volmer equation:

$$J = \frac{i}{nFA} = k^0 \left[C_O(0,t) \exp\left(-\alpha F \frac{E - E^0}{RT} \right) - C_R(0,t) \exp\left((1-\alpha) F \frac{E - E^0}{RT} \right) \right] \qquad (1)$$

for a given time during a potential sweep. The terms of equation 1 are defined in table S-1. The flux at surface 5 was set to equation 1. This calculation ignores any mass transfer contributions from migration (a high concentration of supporting electrolyte was used) and convection. The electrode-array distance, X, was adjusted to match experimental conditions.

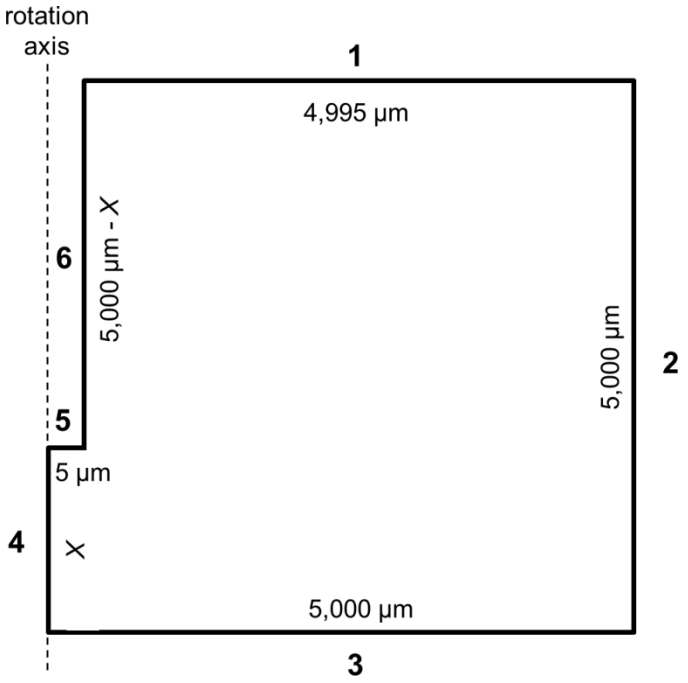

Figure 3.A1.1. COMSOL simulation geometry.
Electrode geometry used for numerical simulation with COMSOL. Surfaces 1 and 2 were set to bulk concentration, surfaces 3 and 6 were set to zero flux, and surface 5 was set to equation S1. The distance *X* (surface 4) represents the electrode-array distance and was chosen to match experimental conditions.

Term	Definition	Value
k^0	standard rate constant	5×10^{-6} m·s^{-1}
α	transfer coefficient	0.7
F	Faraday constant	96485 C·mol^{-1}
E^0	standard electrode potential	0.164 V
R	gas constant	8.314 J·mol^{-1}·K^{-1}
T	temperature	298 K
$C_O(0,t)$	concentration of O at electrode surface at time t	
$C_R(0,t)$	concentration of R at electrode surface at time t	
E	electrode potential	

Table 3.A1.1.
Definitions and values for the terms in equation 1.

The voltammetric response of a one-step, one-electron oxidation reaction, $R \rightarrow O + e$, was simulated. A diffusion coefficient of 0.63 x 10^{-5} $cm^2 \cdot s^{-1}$ was used for both species. A triangular potential waveform was simulated using a linear interpolation function defined by three time points: t = 0 s was set to E_i, the initial potential; $t = E_r/\nu$, where E_r is the potential range and ν is the scan rate, was set to E_s, the switching potential; and $t = 2E_r/\nu$ was set to E_i.

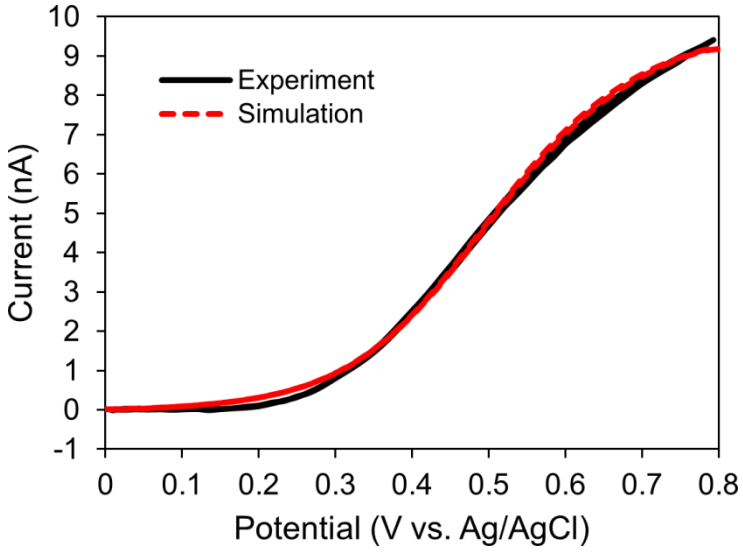

Figure 3.A1.2. Comparison of experimental and simulated CV.
Experimental and simulated CV response of a 10 μm diameter CF UME in 5.7 mM ferrocyanide with 1 M KCl positioned at an electrode-array distance of 1000 μm. The potential was swept from 0 to 0.8 V at 10 mV/s.

Figure 3.A1.2 shows the simulated and experimental CV recorded for a potential sweep experiment in which the 10 μm diameter CF UME was positioned 1000 μm from the array surface in a solution of 5.7 mM ferrocyanide in 1 M KCl. The potential was swept from 0 to 0.8 V at 10 mV/s. At this electrode-array distance, the array will not impede diffusion to the electrode surface. Therefore, these CVs represent the response of an unobstructed electrode. The kinetic parameters used to obtain the simulated CV, k^0 and α, were chosen to give the simulated

CV the best fit to the experimental CV. The concentration profiles of generated ferricyanide shown in Figure 3.6b of the main text are from this simulated CV.

3.7 APPENDIX 2

Qualitative Discussion of Redox Cycling Effects

In a solution of reduced species, R, when the generator electrode approaches a conductive substrate, the electrogenerated species, O, gets reduced at the substrate back to its original form, R. To ensure electroneutrality, this reduction must be accompanied by an oxidation reaction (R → O) elsewhere on the conductive substrate. The large area where this oxidation reaction can occur ensures that the redox cycling will not be limited by this reaction. This is a different situation than the one in this work, where the generator electrode is approaching a closed bipolar electrode array. In the bipolar array situation, each electrode is electrically insulated from one another. Therefore, the electroneutrality-ensuring oxidation reaction can only take place on the opposite pole of each electrode. The small area where this oxidation reaction can occur, coupled with the low concentration of reduced species (50 μM dihydroresorufin) and poor reaction kinetics for glucose oxidation, mean that this oxidation reaction will significantly limit the extent to which redox cycling can occur. We believe this minimization of redox cycling is why the steady-state current of the generator electrode and the resulting fluorescence signal at the bipolar array decrease as the generator electrode approaches the array, qualitatively mimicking the behavior of a generator electrode approaching an insulating substrate. This is also why we chose to treat the bipolar array surface as a no-flux boundary, rather than treating it as a continuous electrode surface, in the approach simulation shown in Figure 3.3.

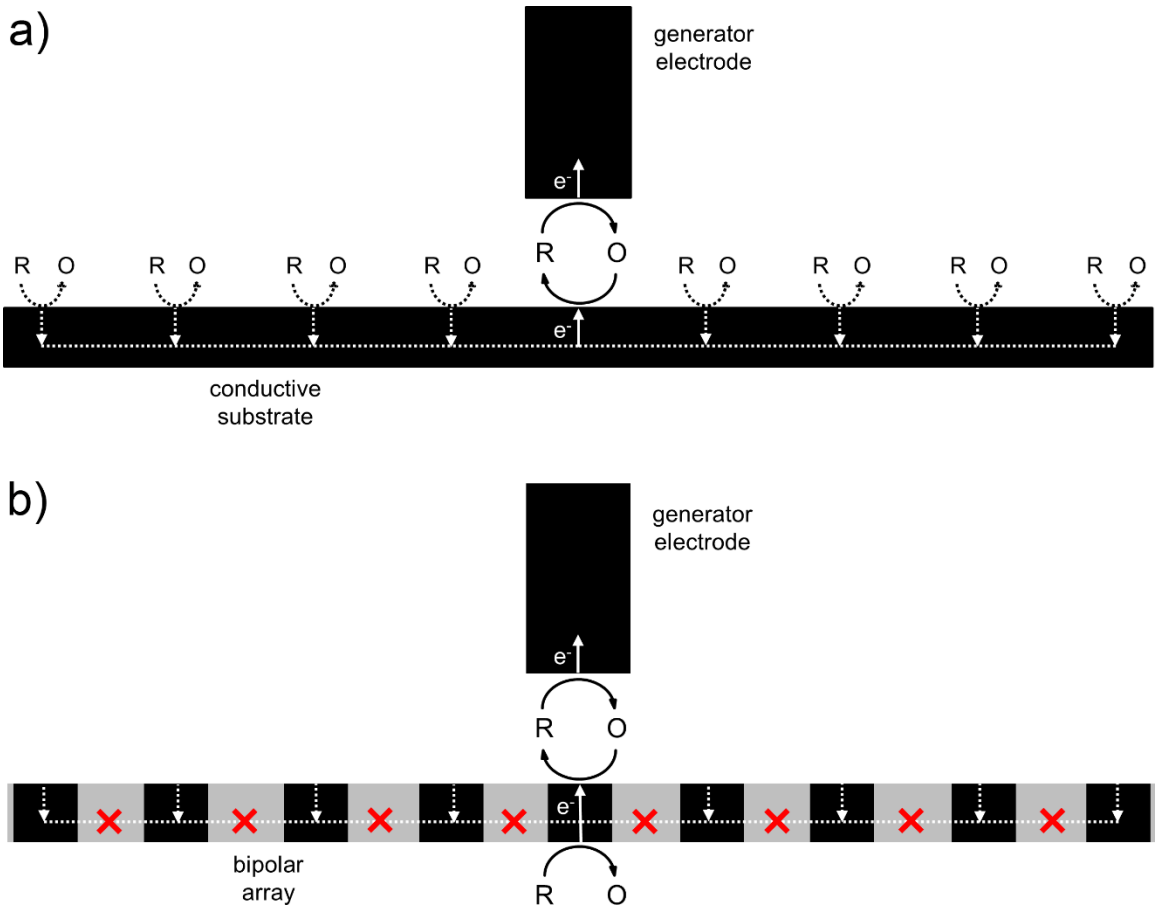

Figure 3.A2.1. Scheme of redox cycling mechanisms.
Scheme showing redox cycling mechanisms for the generator electrode approaching a conductive substrate **(a)** and a closed bipolar electrode array **(b)**.

3.8 APPENDIX 3

Determining Offset Distance Between Electrodes on a Double-Barrel CFE

The fluorescence onset times (Figure 3.A3.1a) were determined for the black lead and red lead as the time at which the fluorescence signal over the lead (ROI for each lead defined by dashed green boxes in Figure 3.8 of the main article) reached 1% above its initial value. The theoretical onset time was determined by plotting the time it would take for a molecule of ferricyanide to diffuse a distance equal to the electrode-array distance. This was calculated using the equation:

$$t = \frac{x^2}{2D} \tag{1}$$

where t is the diffusion time, x is the electrode-array distance, and D is the diffusion coefficient of ferricyanide (0.76×10^{-5} cm^2/s). The shifted red lead data is the fluorescence onset time for the red lead after applying a shift in its electrode-array distance as calculated below.

The difference in fluorescence onset time between the black and red leads can be used to determine the difference in their axial position. Plotted in Figure 3.A3.1b is the difference in fluorescence onset time as a function of the position of the distance between the black lead and the electrode array. This assumes that the black lead position is the true electrode position. The difference between the onset times can be calculated as:

$$\Delta t_{\,fluorescence\,onset} = \frac{x_{red}^2 - x_{black}^2}{2D} \tag{2}$$

where x_{red} and x_{black} are the positions of the red and black lead, respectively. By substituting in the expression:

$$\Delta x = x_{red} - x_{black} \tag{3}$$

one arrives at the following linear equation:

$$\Delta t_{fluorescence\,onset} = \frac{\Delta x}{D} \cdot x_{black} + \frac{(\Delta x)^2}{2D} \tag{4}$$

which gives the difference in fluorescence onset times as a function of the position of the black lead. This equation indicates that a plot of the difference in fluorescence onset times vs. black lead position should be a linear line with a slope equal to $\Delta x/D$. Using the slope from the fit line of the experimental data (Figure 3.A3.1b) and a diffusion coefficient of 0.76 x 10^{-5} cm^2/s, the difference in axial position between the red and black leads, Δx, is 12.4 μm. This means that the red lead is located 12.4 μm further from the array than the black lead at all electrode-array distances. The shifted red lead onset times, which were adjusted by adding 12.4 μm to the electrode-array distance for all data points, are plotted in Figure 3.A3.1a. As can be seen, these shifted values have a better agreement with the theoretical values.

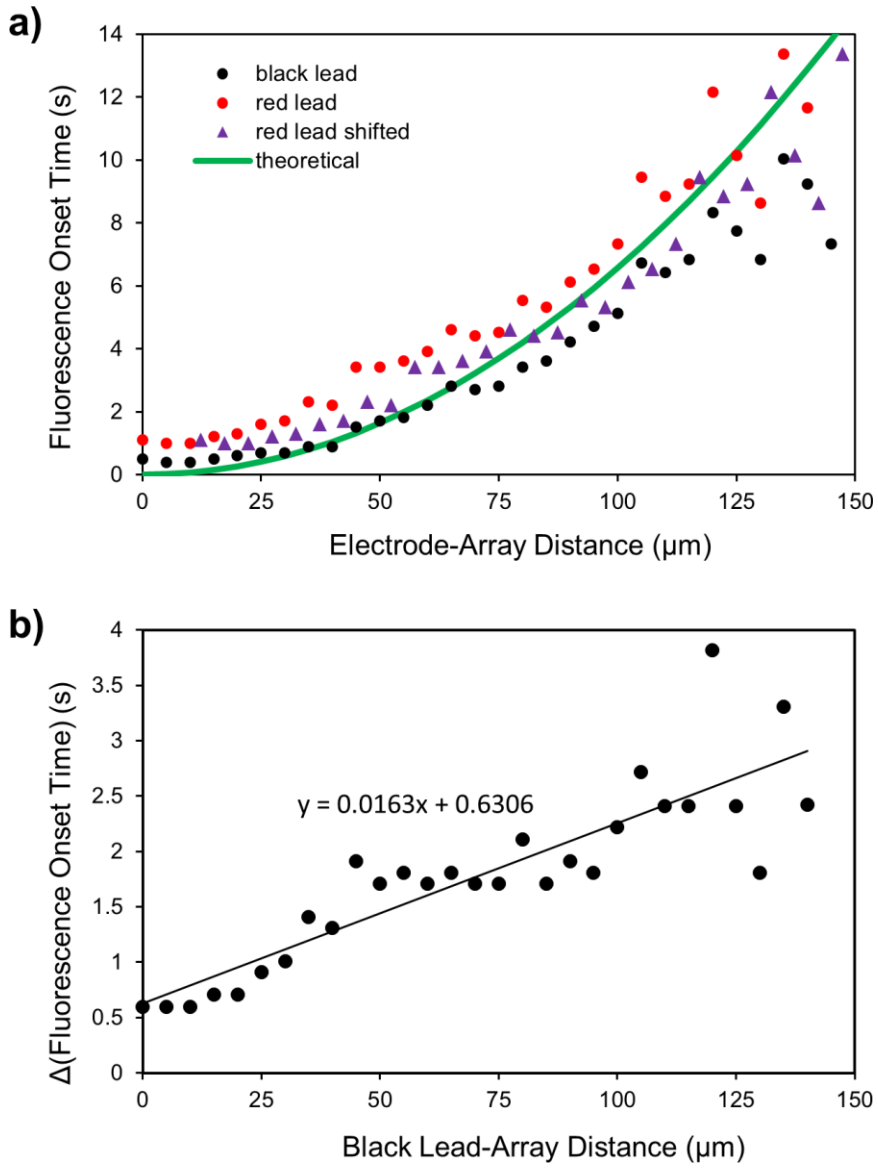

Figure 3.A3.1. Determining offset distance of two leads in a double-barrel CFE.
(a) Plot of the fluorescence onset time as a function of electrode-array distance for the black lead CF, red lead CF, and red lead CF after applying offset correction, and the theoretical diffusion time. **(b)** Plot of the difference in fluorescence onset time between the black lead and red lead as a function of the distance between the black lead and the bipolar array, and the result of a linear best fit line. The data for both plots was taken from the experiment shown in Figures 3.8 and 3.9 of the main article.

3.9 References

(1) Kandel, E.R.; Schwartz, J.H.; Jessell, T.M.; Siegelbaum, S.A.; Hudspeth, A.J. *Principles of Neural Science*, 5th ed.; McGraw-Hill: New York, **2012**.

(2) Sugano, K. Kansy, M.; Artursson, P.; Avdeef, A.; Bendels, S.; Di, L.; Ecker, G.F.; Faller, B.; Fischer, H.; Gerebtzoff, G.; Lennernaes, H.; Senner, F. *Nat. Rev. Drug Discovery* **2010**, *9*, 597-614.

(3) Zhang, J.; Slevin, C.J.; Unwin, P.R. *Chem. Commun.* **1999**, 1501-1502.

(4) Bard, A.J.; Faulkner, L.R. *Electrochemical Methods*, 2nd ed.; John Wiley & Sons: New York, **2001**.

(5) Pruiksma, R.; McCreery, R.L. *Anal. Chem.* **1979**, *51*, 2253-2257.

(6) Pruiksma, R.; McCreery, R.L. *Anal. Chem.* **1981**, *53*, 202-206.

(7) Jan, C.-C.; McCreery, R.L.; Gamble, F.T. *Anal. Chem.* **1985**, *57*, 1763-1765.

(8) Jan, C.-C.; McCreery, R.L.; Gamble, F.T. *Anal. Chem.* **1985**, *57*, 1763-1765.

(9) Wu, H.P.; McCreery, R.L. *Anal. Chem.* **1989**, *61*, 2347-2352.

(10) Posdorfer, J.; Olbrich-Stock, M.; Schindler, R.N. *Electrochim. Acta*, **1994**, *39*, 2005-2013.

(11) Muller, R.H. *Adv. Electroch. El. Eng.***1973**, *9*, 281.

(12) Pawliszyn, J.; Weber, M.F.; Dignam, M.J.; Mandelis, A.; Venter, R.D.; Park, S.-M. *Anal. Chem.* **1986**, *58*, 236-239.

(13) Pawliszyn, J.; Weber, M.F.; Dignam, M.J.; Venter, R.D.; Park, S.-M. *Anal. Chem.* **1986**, *58*, 239-242.

(14) Amatore, C.; Chovin, A.; Garrigue, P.; Servant, L.; Sojic, N.; Szunerits, S.; Thouin, L. *Anal. Chem.* **2004**, *76*, 7202-7210.

(15) Vitt, J.E.; Engstrom, R.C. *Anal. Chem.* **1997**, *69*, 1070-1076.

(16) Engstrom, R.C.; Pharr, C.M.; Koppang, M.D. *J. Electroanal. Chem.* **1987**, *221*, 251-255.

(17) Maus, R.G.; McDonald, E.M.; Wightman, R.M. *Anal. Chem.* **1999**, *71*, 4944-4950.

(18) Bouffier, L.; Doneux, T.; Bertrand, G.; Kuhn, A. *Anal. Chem.* **2014**, *86*, 3708-3711.

(19) Fosdick, S.E.; Knust, K.N.; Scida, K.; Crooks, R.M. *Angew. Chem., Int. Ed.* **2013**, *52*, 10438-10456.

(20) Cannan, S.; Macklam, I.D.; Unwin, P.R. *Electrochem. Commun.* **2002**, *4*, 886-892.

(21) Rudd, N.C.; Cannan, S.; Bitziou, E.; Ciani, I.; Whitworth, A.L.; Unwin, P.R. *Anal. Chem.* **2005**, *77*, 6205-6217.

(22) Grime, J.M.A.; Edwards, M.A.; Rudd, N.C.; Unwin, P.R. *Proc. Natl. Acad. Sci. USA*, **2008**, *105*, 14277-14282.

(23) Amatore, C.; Bonhomme, F.; Bruneel, J.-L.; Servant, L.; Thouin, L. *J. Electroanal. Chem.* **2000**, *484*, 1-17.

(24) Szunerits, S.; Garrigue, P.; Bruneel, J.-L.; Servant, L.; Sojic, N. *Electroanal.* **2003**, *15*, 548-555.

(25) Engstrom, R.C.; Weber, M.; Wunder, D.J.; Burgess, R.; Winquist, S. *Anal. Chem.* **1986**, *58*, 844-848.

(26) Engstrom, R.C.; Meaney, T.; Tople, R.; Wightman, R.M. *Anal. Chem.* **1987**, *59*, 2005-2010.

(27) Amemiya, S.; Bard, A.J.; Fan, F.-R.F.; Mirkin, M.V.; Unwin, P.R. *Annu. Rev. Anal. Chem.* **2008**, *1*, 95-131.

(28) Scott, E.R.; White, H.S.; Phipps, J.B. *Anal. Chem.* **1993**, *65*, 1537-1545.

(29) Baltes, N.; Thouin, L.; Amatore, C.; Heinze, J. *Angew. Chem., Int. Ed.* **2004**, *43*, 1431-1435.

(30) Pebay, C.; Sella, C.; Thouin, L.; Amatore, C. *Anal. Chem.* **2013**, *85*, 12062-12069.

(31) Chen, C.-C.; Zhou, Y.; Baker, L.A. *Annu. Rev. Anal. Chem.* **2012**, *5*, 207-228

(32) Zhou, L.; Zhou, Y.; Baker, L.A. *ECS Interface* **2014**, *23*, 47-52.

(33) Nebel, M.; Eckhard, K.; Erichsen, T.; Schulte, A.; Schuhmann, W. *Anal. Chem.* **2010**, *82*, 7842-7848.

(34) Lazenby, R.A.; McKelvey, K.; Unwin, P.R. *Anal. Chem.* **2013**, *85*, 2937-2943.

(35) Ndungu, P. G. Ph.D. Thesis, Drexel University, Philadelphia, PA, 2004.

(36) Plana, D.; Shul, G.; Stephenson, M.J.; Dryfe, R.A.W. *Electrochem. Commun.* **2009**, *11*, 61-64.

(37) Plana, D.; Jones, F.G.E.; Dryfe, R.A.W. *J. Electroanal. Chem.* **2010**, *646*, 107-113.

(38) Guerrette, J.P.; Oja, S.M.; Zhang, B. *Anal. Chem.* **2012**, *84*, 1609-1616.

(39) Cox, J.T.; Guerrette, J.P.; Zhang, B. *Anal. Chem.* **2012**, *84*, 8797-8804.

(40) Guerrette, J.P.; Percival, S.J.; Zhang, B. *J. Am. Chem. Soc.* **2013**, *135*, 855-861

(41) Oja, S.M.; Guerrette, J.P.; David, M.R.; Zhang, B. *Anal. Chem.* **2014**, *86*, 6040-6048.

(42) Shakashiri, B. Z. *Chemical Demonstrations: A Handbook for Teachers in Chemistry*, Vol. 2; University of Wisconsin Press: Madison,WI, 1989.

(43) Chang, B.-Y.; Mavré, F.; Chow, K.-F.; Crooks, J.A.; Crooks, R.M. *Anal. Chem.* **2010**, *82*, 5317-5322.

(44) Schindelin, I.A.-C.; Frise, E.; Kaynig, V.; Longair, M.; Pietzsch, T.; Preibisch, S.; Rueden, C.; Saalfeld, S.; Schmid, B.; Tinevez, J.-Y.; White, D.J.; Hartenstein, V.; Eliceiri, K.; Tomancak, P.; Cardona, A. *Nature Methods* **2012**, *9*, 676-682.

(45) Schmid, B.; Schindelin, J.; Cardona, A.; Longair, M.; Heisenberg, M. *BMC Bioinformatics* **2010**, *11*, 274.

(46) Strein, T.G.; Ewing, A.G. *Anal. Chem.* **1992**, *64*, 1368-1373.

(47) Zhang, B.; Adams, K.L.; Luber, S.J.; Eves, S.J.; Heien, M.L.; Ewing, A.G. *Anal. Chem.* **2008**, *80*, 1394-1400.

(48) Anderson, L.; Wittkopp, S.M.; Painter, C.J.; Liegel, J.J.; Schreiner, R.; Bell, J.A.; Shakhashiri, B.Z. *J. Chem . Ed.* **2012**, *89*, 1425-1431.

CHAPTER 4

Influence of Electrode Size on Electrogenerated Chemiluminescence Reporting at Closed Bipolar Microelectrodes*

4.1 Introduction

The use of electrogenerated chemiluminescence (ECL) as a readout mechanism of the faradaic current through a bipolar electrode (BPE) has been widely utilized in recent years.[1-19] Originally adopted for open BPEs,[1-10] it has now been used in both split-channel BPEs (and variations thereof)[11-13] and closed BPEs.[14-19] Using ECL as a reporting mechanism is advantageous, as it enables one to remotely and simultaneously monitor individual electrodes in arrays containing very large numbers of BPEs.[4] While the use of ECL as a readout mechanism in open BPEs has been well-developed, its use in closed BPEs remains less explored.[20] Although several recent reports have described using ECL reporting on closed BPEs for the quantitative detection of analytes, including hydrogen peroxide,[15-17] glucose,[15,19] various cancer biomarkers,[18] and other analytes,[15,16] or for use as an electrocatalyst screening platform,[14] there have been no studies on the fundamental behavior of ECL coupling on closed BPEs.

Similar to our previous studies,[21,22] we sought to provide a fundamental understanding of the electrochemical behavior of closed BPEs, this time focusing on ECL coupling to an analyte redox process. As the ECL readout mechanism is based on the light emission from the ECL

* This chapter is adapted with permission from Oja, S.M.; Zhang, B. "Electrogenerated chemiluminescence reporting on closed bipolar microelectrodes and the influence of electrode size." *ChemElectroChem* **2016**, *3*, 457-464. Copyright (2016) John Wiley and Sons.

process being an accurate reporter of current through the BPE, especially important is an understanding of the correlation between ECL emission intensity and electrochemical current. Based on reports from the Crooks group regarding ECL reporting in open BPEs,[2,5] we suspected electrode size-geometry would have a large effect on the optical signal and also sought to understand the nature of any size-geometry-related effects in closed BPEs.

We chose to use the oxidative tris(2,2'-bipyridine)ruthenium (II)/tri-*n*-propylamine ($Ru(bpy)_3^{2+}$/TPrA) ECL system as our ECL reporter,[23,24] as it has been widely used in BPE studies. We also chose to focus our studies on bipolar microelectrodes (loosely defined here as having a critical dimension of less than ~ 100 μm), as we believe that one of the more promising uses of closed BPEs is their microelectrode array-based use in electrochemical imaging. Our group recently demonstrated this in a method we call fluorescence-enabled electrochemical microscopy (FEEM), which uses a fluorogenic redox reaction to report faradaic current through closed BPEs and large-scale arrays thereof.[25-27] It is easy to imagine an analogous method in which ECL is used as the optical reporter in place of a fluorogenic reaction.

Figure 4.1 outlines our basic experimental setup. We form a closed BPE by electrically connecting two Pt disk microelectrodes as has been previously reported.[21,28,29] One pole of the BPE is placed in an analyte solution, and the other pole is placed in the optical reporter solution. In this study, the optical reporter is the $Ru(bpy)_3^{2+}$/TPrA ECL system. As this ECL process entails oxidation reactions, reduction must occur at the analyte pole. To maintain electroneutrality in the BPE, the rate of oxidation on the reporting pole must be the same as the rate of reduction on the analyte pole. This is the basis behind using ECL as a reporter of the faradaic current through the BPE, assuming the ECL emission intensity scales with electrochemical current. To drive the coupled reactions, a potential is applied across the solutions

using two driving electrodes. As the only electrical path from the ECL solution to the analyte solution is the BPE, the current through the system is equivalent to the current through the BPE, enabling simple measurement of the BPE current. The reporting pole is positioned on an inverted microscope to enable easy monitoring of ECL emission using a photodetector. By simultaneously measuring the current through the BPE and the ECL emission from the reporting pole, one can gain a fundamental understanding of the relationship between these two signals. In order to understand the effect of electrode sizes on these signals, we use a 25, 50, or 127 μm diameter Pt disk electrode as the reporting pole and a 25 or 127 μm diameter Pt disk electrode as the analyte pole (Figure 4.1b).

In this chapter, we first demonstrate both the basic coupling behavior of ECL to the reduction of ferricyanide on a closed BPE with equivalent pole sizes and the relationship between the optical and electrical signals. We then show the quantitative detection of various concentrations of ferricyanide using a 25 μm analyte pole and show the large changes in optical signal brought about by different size reporting poles. Using a simple voltammetric study of the ECL reaction in a non-bipolar setup, we explain this size effect. Lastly, we show how one can use information gained from the non-bipolar study of the ECL reaction to predict the optical response of the BPE to various analyte concentrations. We use this knowledge to accurately predict important trends in the calibrations curves for the BPE detection of ferricyanide using a 127 μm analyte pole and different size reporting poles.

4.2 Experimental Section

4.2.1 Chemicals

Potassium ferricyanide ($K_3Fe(CN)_6$), tripropylamine (TPrA), and tris(2,2'-bipyridyl)dichlororuthenium(II) hexahydrate ($Ru(bpy)_3Cl_2 \cdot 6H_2O$) were purchased from Sigma-Aldrich (St. Louis, Missouri). Potassium chloride was purchased from Fisher Scientific (Fair Lawn, New Jersey). All chemicals were used as received. Deionized water (>18 MΩ·cm) obtained from a Barnstead Nanopure water purification system was used for all aqueous solutions. All solutions of $Fe(CN)_6^{3-}$ were prepared in 1 M KCl. The ECL solution, which consisted of 5 mM $Ru(bpy)_3^{2+}$ and 25 mM TPrA, was prepared in 0.1 M pH 7.0 phosphate buffer.

4.2.2 Electrochemical Measurements

All voltammetry experiments were carried out using a Chem-Clamp potentiostat (Dagan Corporation) interfaced to a PC through a PCI-6251 data acquisition board (National Instruments) using a BNC-2090 breakout box (National Instruments). An in-house LabView 10.0 (National Instruments) program was used for voltage function generation and acquisition of the current-voltage data. This program receives an external trigger from a camera, enabling the synchronized recording of electrochemical and optical signals. In a non-bipolar/two-electrode setup, a traditional two-electrode system was used, with the potential being applied between the working electrode and an Ag/AgCl reference electrode. In a closed bipolar setup, the potential was applied across the BPE using two Ag/AgCl reference electrodes. Closed BPEs were formed by electrically connecting two working electrodes in separate solutions. The working electrodes used were inlaid-disk Pt microelectrodes with an electroactive diameter of 25, 50, or 127 μm. These electrodes were fabricated by sealing a Pt microwire (Alfa-Aesar) in a borosilicate capillary (Sutter Instrument Co.) and making connection to the Pt with tungsten wire and Ag paint (Dupont) through the back end of the capillary.

We chose to study microelectrodes due to their applicability to electrochemical imaging and sensor parallelization in a microelectrode array-based format. Pt was chosen as an electrode material due to its widespread prevalence as an electrode material for both micro- and nanoelectrodes. The exact sizes of the electrodes chosen (i.e. 127 μm vs. 125 or 100 μm) have no special significance and were chosen solely based on readily available Pt microwire sizes. All reported potentials are vs. Ag/AgCl (3 M KCl), and all cyclic voltammetry experiments were done at a scan rate of 20 mV/s. Onset potentials are calculated as the potential at which the current reaches 10% of its steady-state value. All reported electrochemical measurements are the average of three trials.

4.2.3 Optical Measurements

An Olympus IX70 inverted microscope and an Andor iXon EMCCD camera cooled to -80 °C were used to image the ECL signal. All imaging was done through a 10X 0.30 NA objective (Olympus UPlanFl) using an additional 1.5X magnification on the microscope. Andor SOLIS software was used to record and process all images. Images were recorded using an exposure time of 0.1 s, giving a frame rate of 9.9522 Hz. A preamplifier gain of 5.1 was used. The ECL intensity was determined by integrating the counts from the area over each electrode. Reported images and intensities are background-corrected, typically using the first frame in a series as the background. For imaging, each electrode was placed 500 μm above a coverslip using a Sutter MP-285 motorized micromanipulator (Sutter Instrument Co.). Onset potentials from the optical signal are reported as the potential at which the optical signal reaches 10% of its steady-state intensity. As with the electrochemical measurements, all reported optical measurements are the average of three trials.

4.3 Results and Discussion

4.3.1 Bipolar Coupling of Electrogenerated Chemiluminescence and Analyte

We first sought to demonstrate the basic principle of bipolar coupling of ECL to an analyte on a closed BPE. As shown in previous studies using closed BPEs, the behavior of the bipolar system can be readily understood by considering each of the poles individually.[21,22] More specifically, the potential required to drive coupled reactions on a BPE is approximately the difference between the potential required to drive each of the individual reactions in a traditional two or three electrode configuration. Additionally, one of the poles will limit the total current through the BPE, and this limit can also be understood by considering each pole individually.

Figure 4.2 shows the results of an experiment in which the ECL and analyte reactions are considered both individually in traditional two-electrode (non-bipolar) setups and coupled together in a closed BPE. The solid black trace shows the cyclic voltammogram (CV) of a 25 μm Pt electrode in 5 mM $Fe(CN)_6^{3-}$ with 1 M KCl as supporting electrolyte in a two-electrode setup. The potential was swept from 0.5 to 0 V. As seen, $Fe(CN)_6^{3-}$ reduction occurs with typical steady-state behavior and an onset potential of 0.33 V. The solid green trace shows the cyclic voltammogram of a 25 μm Pt electrode in ECL solution in a two-electrode setup during a potential sweep from 0.6 to 1.2 V. Again, typical steady-state behavior, although with a higher steady-state current, is observed for the oxidation of the ECL components ($Ru(bpy)_3^{2+}$ and TPrA) with an onset potential of 0.85 V. The dashed green trace shows the simultaneously-recorded optical signal from this same electrode. As seen, the optical signal follows the electrical signal nearly exactly, exhibiting the same steady-state behavior and an onset potential of 0.87 V. The red traces show the simultaneously-recorded electrical (solid trace) and optical (dashed trace) signals for these individual reactions coupled together on a closed BPE. Both poles of the BPE were 25 μm Pt electrodes, with one (the analyte/cathodic pole) placed in 5 mM $Fe(CN)_6^{3-}$ and

the other (the reporting/anodic pole) placed in ECL solution. In this setup, the reduction of $Fe(CN)_6^{3-}$ on the cathodic pole will be coupled to the oxidation of the ECL components on the anodic pole. The potential was applied to two Ag/AgCl driving electrodes and swept from -0.1 to -1 V.

As can be seen, the electrical and optical signals follow one another very well, indicating that the ECL signal generated on the anode is a good reporter of the current through the BPE. Of note, there is a significant potential shift in the signal of the BPE as compared to the signal of the individual reactions, with the onset of the BPE electrical and optical signals at -0.50 V and -0.57 V, respectively. As previously stated, this potential shift can be predicted by taking the difference in the onset potentials of the individual reactions. The predicted onsets of the electrical signal (0.33 V – 0.85 V = -0.52 V) and optical signal (0.33 V – 0.87 V = -0.54 V) agree very well with the observed bipolar onset potentials. The onset of the optical signal is easily visualized in Figure 4.2b, which shows images of the anodic pole at three potentials during the forward sweep of the BPE. As seen, an optical signal appears between -0.5 V and -0.6 V and grows until it reaches a steady-state at -0.8 V.

Additionally, one can see that the steady-state current reached in the bipolar setup is the same as that reached in the two-electrode reduction of 5 mM $Fe(CN)_6^{3-}$, indicating that the BPE signal is limited by the cathodic pole. Further discussion of limiting poles can be found in Appendix 1 **(**Figure 4.A1.1**)**, as well as in our previous reports on closed BPE systems.[21,22] As expected, the optical signal also shows a similar decrease in magnitude from that obtained in a two-electrode setup. This is because the current through the BPE is lower due to the limitation from the cathodic pole, meaning that the rate of oxidation of the ECL components is slower and hence less light is emitted. Because ECL intensity is correlated to the reaction rate of the ECL

components, which is in turn determined by the current through the BPE, the ECL intensity should correlate to the concentration of the analyte at the cathodic pole as long as the cathodic pole is limiting. This is the basis of using ECL as a reporter in a BPE sensing experiment.

4.3.2 Quantitative Detection and Influence of Anode Size

With an understanding of how ECL oxidation couples to analyte reduction and, in particular, how information from the individual reactions can inform on the behavior of the coupled reactions, we moved on to study the quantitative detection of analyte on a BPE using ECL as a reporting mechanism. We studied both the electrical and optical response of a closed BPE to $Fe(CN)_6^{3-}$ concentrations ranging from 10 to 0.01 mM. In this experiment, a 25 μm Pt electrode was used as the cathodic pole and placed in $Fe(CN)_6^{3-}$ solution. To see what effect the size of the anode had on the signal, we used a 25, 50, or 127 μm Pt electrode as the anodic pole and placed it in ECL solution. We connected the two poles to form a closed BPE and applied a potential sweep from 0 to -1 V using two Ag/AgCl driving electrodes, during which we monitored the electrical and optical signals simultaneously. Figure 4.3a plots the steady-state current and steady-state ECL intensity (taken as the signal at -0.8 V during the forward sweep) for each anode size and $Fe(CN)_6^{3-}$concentration. Examples of the full traces of these signals can be found in Figure 4.4.

As expected, the steady-state current shows a linear dependence on $Fe(CN)_6^{3-}$ concentration that is independent of the size of the anodic pole, indicating that the cathodic pole is limiting in all cases. The ECL signal also has a linear dependence on $Fe(CN)_6^{3-}$ concentration as expected. However, quite unexpectedly, there is a striking change in the ECL intensity as the size of the anodic pole changes, with the ECL intensity significantly decreasing with increasing anode size for a given analyte concentration. Figure 4.5 contains images of the anodes at different cathodic concentrations of $Fe(CN)_6^{3-}$ for easy visualization of this phenomenon. With

the basis of using ECL as a reporting mechanism being that it is an accurate reporter of the current, this data brought up a large discrepancy: How can the magnitude of the current through the BPE be independent of anode size yet the magnitude of the ECL intensity be strongly dependent on anode size?

Figure 4.3b shows this discrepancy clearly, displaying the current and ECL traces for the three different size anodes during potential sweeps using a $Fe(CN)_6^{3-}$ concentration of 5 mM at the cathodic pole.[30] The steady-state ECL intensity decreases by more than a factor of 2 when the anode is changed from a 25 μm diameter disk to a 50 μm diameter disk. With a 127 μm diameter disk anode, there is no detectable ECL signal. These differences in intensity are very strikingly seen in the images of the anode at steady-state (Figure 4.3c). Notably, the noise in the ECL signal increases dramatically as the anode size increases. As there is no inherent background light emission in ECL, this noise is due to the camera and is the result of integrating the signal over a larger number of pixels as the anode size increases (~ 25 times more pixels for the 127 μm anode vs. the 25 μm anode). However, this increase in noise cannot be responsible for a decrease in mean signal intensity. This consideration of camera noise does bring up an important point, however. If the same ECL intensity is observed on two different sized electrodes, the signal to noise ratio will be more favorable on the smaller electrode, as the same signal will be recorded on fewer pixels of the camera, resulting in less noise.[31] Figure 4.A2.1 in Appendix 2 clearly demonstrates this point. We note that a recent paper has reported on the effects of exposure time of a CCD camera on both the ECL signal and signal to background ratio for a paper-based microfluidic open BPE.[10] These observations highlight the additional imaging-related parameters that must be taken into account when relying on an optical signal rather than a purely electrical signal.

The current traces in Figure 4.3b provide the first clue into solving our discrepancy. While the three anode sizes produce the same steady-state current, there is a marked potential shift between the different anode sizes, with the onset of current shifting from -0.50 V to -0.44 V to -0.34 V with anode sizes of 25, 50, and 127 μm, respectively. Despite this shift in the onset of current, the onset of ECL remains constant at -0.57 V for the 25 μm and 50 μm anodes. This clearly shows that as the anode size increases, an increasing fraction of the current through the BPE is resulting in no light emission. To further explore this interesting result and explain our discrepancy, we chose to carefully study the ECL reaction in a non-bipolar, two-electrode setup.

4.3.3 Predicting Bipolar Behavior and Calibration Curves

We did a simple two-electrode potential sweep experiment, using as working electrodes the same electrodes that served as anodes in our bipolar experiment (25, 50, or 127 μm diameter Pt disk microelectrodes). The potential was swept from 0.6 to 1.2 V to oxidize the ECL components while simultaneously recording the electrical and optical signals. Figure 4.6 presents the results of this experiment. As seen in Figure 4.6a, the ECL traces follow the current traces very closely. As expected, a larger electrode results in an increased current, which in turn results in a larger ECL signal due to a higher oxidation rate of the ECL components. However, notice that at the onset of the reactions, the current and ECL signal do not follow one another exactly. Figure 4.6b shows a zoom-in of the plot in 4a. The differences between the onset of current (solid lines) and the onset of ECL (dashed lines) become especially apparent here, with the difference growing as the electrode size increases.

It has been previously shown that TPrA undergoes oxidation on Pt at a potential closer to 0 V than $Ru(bpy)_3^{2+}$, explaining why there is current without ECL, as $Ru(bpy)_3^{2+}$ must be oxidized for light emission to occur.[24,32,33] Due to an increased surface area where oxidation may occur, a larger electrode enables the same TPrA oxidation current to pass at a lower potential.

This point is demonstrated in Figure 4.7 by a bipolar coupling experiment in which the analyte pole is placed in $Fe(CN)_6^{3-}$ solution and the reporting pole is placed in a solution of only TPrA in phosphate buffer (no $Ru(bpy)_3^{2+}$). Very interestingly, the Crooks group found this same phenomenon to be the cause limiting the ECL reporting signal at low faradaic currents on open BPEs[5] and showed that decreasing the anode size relative to the cathode could boost the ECL signal.[2] Our results apparently confirm this same phenomenon in closed BPEs.

We realized that this was the key to explaining the observed discrepancy between current and ECL signals in a bipolar setup. The solid black line in Figure 4.6b marks the steady-state current obtained for the bipolar detection of 5 mM $Fe(CN)_6^{3-}$ (experiment shown in Figure 4.3b). The dashed black lines mark the potential where that steady-state current is reached for each electrode in the two-electrode setup and extrapolate to the ECL curve to mark the ECL intensity achieved at that potential. This shows that a 127 μm electrode can reach the bipolar steady-state current before the onset of ECL, a 50 μm electrode reaches the steady-state current just after the onset of ECL, and a 25 μm electrode reaches the steady-state current well after the onset of ECL. One immediately notices that these ECL intensities (marked by the asterisks) match nearly exactly with the steady-state intensities observed for the bipolar detection of 5 mM $Fe(CN)_6^{3-}$ (shown in Figure 4.3b), showing how in a closed BPE the ECL intensity can be dependent on anode size while the current remains independent of anode size. As the anode size increases, the magnitude of "non-light-emitting current" also increases, resulting in less light emission.

To see if the information from a two-electrode experiment as in Figure 4.6 could accurately predict the BPE response to a range of analyte concentrations, we made calibration curves based on the data in Figure 4.6 and compared them to the curves obtained in an actual bipolar experiment as shown in Figure 4.3a. To make the predicted calibration curves, for each

electrode size we found the potential where the steady-state current for a given $Fe(CN)_6^{3-}$ concentration was reached and marked the ECL intensity at that potential. Those ECL intensities were then plotted vs. $Fe(CN)_6^{3-}$ concentration, and the results are shown in Figure 4.8. As can be seen, this predicted calibration plot follows the calibration plot obtained in an actual bipolar experiment (Figure 4.3a) remarkably well. Figure 4.9 contains a side-by-side view of the plots for easier comparison.

Importantly, note that the predicted plot is based on data from a simple non-bipolar, two-electrode setup, but can be used to accurately predict important trends seen in the actual bipolar detection data. For example, the predicted calibration plot shows the linear region for the 25 μm anode to extend from 1-10 mM, the linear region for the 50 μm electrode to extend from 2.5-10 mM, and the 127 μm anode to only show a signal at 10 mM. These same trends are seen in the experimental bipolar detection data in Figure 4.3a. Additionally, the relative intensities for the three different size anodes at a given $Fe(CN)_6^{3-}$ concentration are accurately predicted. As can be seen, the information gained from studying the ECL reaction in a two-electrode setup is not only useful in understanding the bipolar response, but can be used to accurately predict a calibration plot for detecting an analyte in a bipolar detection experiment. This is a rather interesting point, as the predicted calibration plot can be built from one simple potential sweep experiment and with the only knowledge of the analyte needed the steady-state current it will produce at a given concentration.[34] This can be visualized in another way by plotting the ECL intensity vs. the current from the two-electrode setup for each electrode size (Figure 4.10). We note that the noise level in the current and ECL curves such as shown in Figure 4.6b is a key factor in the accuracy of the predicted bipolar signal. With increasing noise in either curve, a wider range of ECL intensities must be considered.

4.3.4 Applying Predicted Calibration Curves to Bipolar Detection

It is apparent from the discussion in the previous section that in order to increase the ECL signal from a given analyte concentration, the current through the BPE should be maximized. One way of doing this is to increase the size of the analyte pole (in this case the cathodic pole) of the BPE. In fact, using the two-electrode data shown in Figure 4.6, we can predict the calibration plots for bipolar detection using a larger cathode. As an example, we made a calibration plot for $Fe(CN)_6^{3-}$ detection on a BPE with a 127 μm cathodic pole and either a 25, 50, or 127 μm anodic pole. To do this, we first measured the steady-state current for each $Fe(CN)_6^{3-}$ concentration on a 127 μm electrode using a two-electrode setup (Figure 4.11). Then, using the data shown in Figure 4.6, for each anode size we found the potential where the steady-state current of a given $Fe(CN)_6^{3-}$ concentration was reached and marked the ECL intensity at that potential. These ECL intensities were plotted vs. $Fe(CN)_6^{3-}$ concentration to complete the calibration plot. This predicted plot is shown in Figure 4.12a. An alternative way of visualizing the formation of the predicted calibration curve is presented in the Figure 4.13.

Some very interesting trends are immediately seen in this plot. First, as compared to the plot in Figure 4.8 (which is based on a 25 μm cathode), the ECL signal is roughly an order of magnitude greater. This confirms that a larger cathode, and hence a larger current through the BPE, produces a larger ECL signal. More interestingly, the relative intensities between the anode sizes show a much different trend than in Figure 4.8. A 25 μm anode only shows sensitivity to $Fe(CN)_6^{3-}$ concentrations below 1 mM, while a 50 μm anode only shows sensitivity to concentrations below 5 mM. This is because at these concentrations and above, the ECL reaction at the anodic pole has reached its mass transfer-limited maximum, meaning the current through the BPE is limited by the anodic pole. Therefore, the steady-state current through the BPE and

hence, the steady-state ECL intensity, remain constant regardless of $Fe(CN)_6^{3-}$ concentration. The 127 μm anode shows no such limitation, as the theoretical maximum steady-state current at the anode is still greater than the current demand at the cathode for these $Fe(CN)_6^{3-}$ concentrations. The third significant difference is that there is a significant shift in the linear region of the calibration curves to lower concentrations. The 127 μm anode shows a linear response from 2.5-10 mM, the 50 μm anode shows a linear response from 0.25-2.5 mM, and the 25 μm anode shows a linear response from 0.01-0.1 mM.

Overall, the plot in Figure 4.12a predicts a very marked difference between using a 127 μm cathode and a 25 μm cathode for bipolar detection. For example, when using a 127 μm cathode, a 25 μm anode should show a linear range two orders of magnitude lower in analyte concentration than if using a 25 μm cathode but should show no sensitivity to analyte concentrations over 2.5 mM. To verify that the predicted calibration plot shows the correct trends, we did the same bipolar detection experiment outlined in Figure 4.3, but used a 127 μm cathode rather than a 25 μm cathode. The results of this experiment are plotted in Figure 4.12b. As can be seen, the overall trends predicted in 6a are accurate, which is the point we wish to emphasize. The ECL signal is roughly an order of magnitude greater, the linear range of the curves shift to lower concentrations for all three anode sizes, and the 25 and 50 μm anodes show limited to no sensitivity at higher $Fe(CN)_6^{3-}$ concentrations for detection using a 127 μm cathode as compared to using a 25 μm cathode.

4.4 Conclusion

The fundamental behavior of ECL coupling to analyte redox reaction on a closed bipolar microelectrode has been described for the oxidative $Ru(bpy)_3^{2+}$/TPrA ECL system using a Pt BPE. We explicitly demonstrated the correlation between current through the BPE and ECL

intensity at the reporting pole of the BPE, showing how these two signals change with changing analyte concentrations. Importantly, we also demonstrated the effect that changing the size-geometry of the BPE poles has on the optical signal and explained the origin of this size effect. We found that changing the size-geometry of the BPE can significantly alter its sensing performance and show how one can take advantage of this to tune the BPE to different analyte concentration ranges. A smaller reporting pole relative to analyte pole showed a lower linear concentration detection range as well as better signal to noise ratio. Using data obtained from simple non-bipolar experiments, we demonstrated how calibration curves for BPE sensing experiments can be accurately predicted. We believe this report will be useful and provide valuable insight to those designing sensing systems based on ECL reporting on closed BPEs, both in a single-electrode, and more excitingly, an array-based format.

4.5 Figures

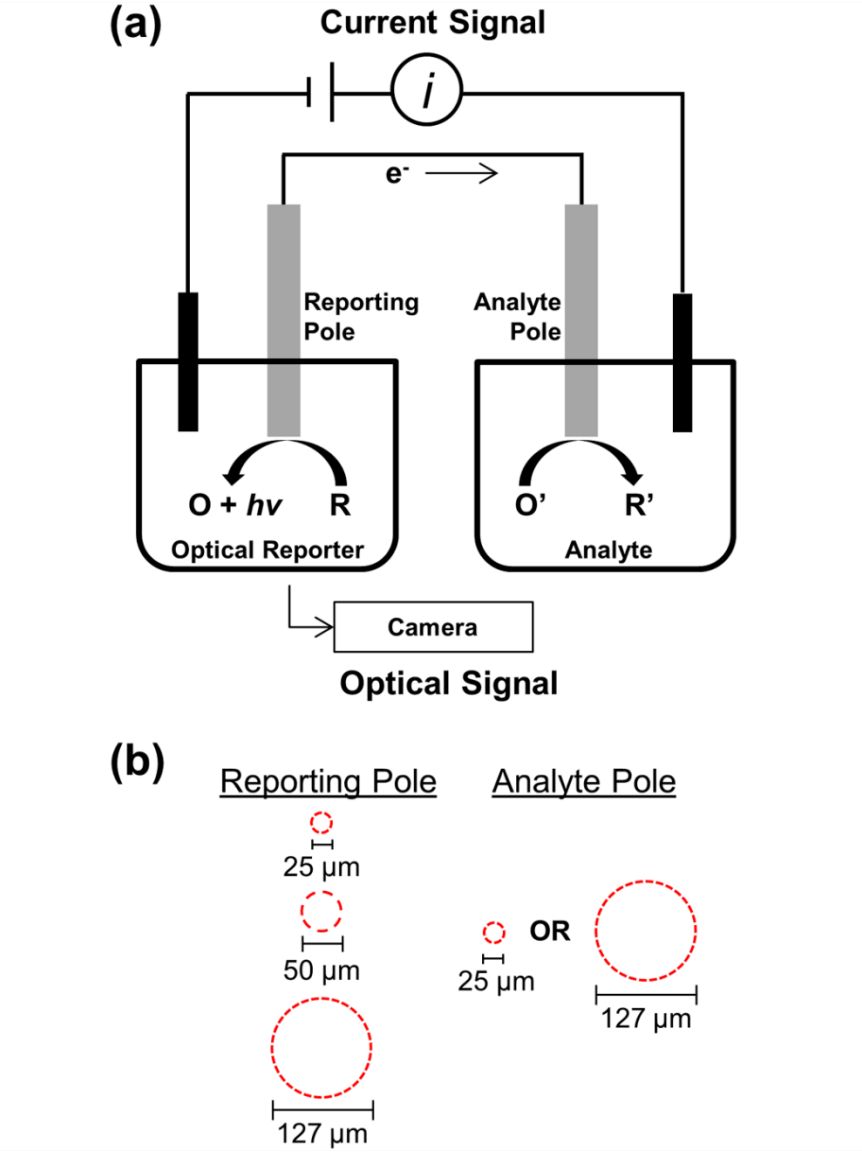

Figure 4.1. Diagram of the bipolar setup with ECL reporting.
Diagram of the experimental setup used. **(a)** Schematic of the closed BPE setup, which enables simultaneous measurement of the current through the BPE and light emission from the reporting pole. In this report, the optical reporter (R) is $Ru(bpy)_3^{2+}$ and TPrA, which are co-oxidized at the reporting pole and emit light through a complex reaction cascade. **(b)** Outlines of the electroactive areas of the different disk microelectrodes used as the two poles to make closed BPEs of different size-geometries.

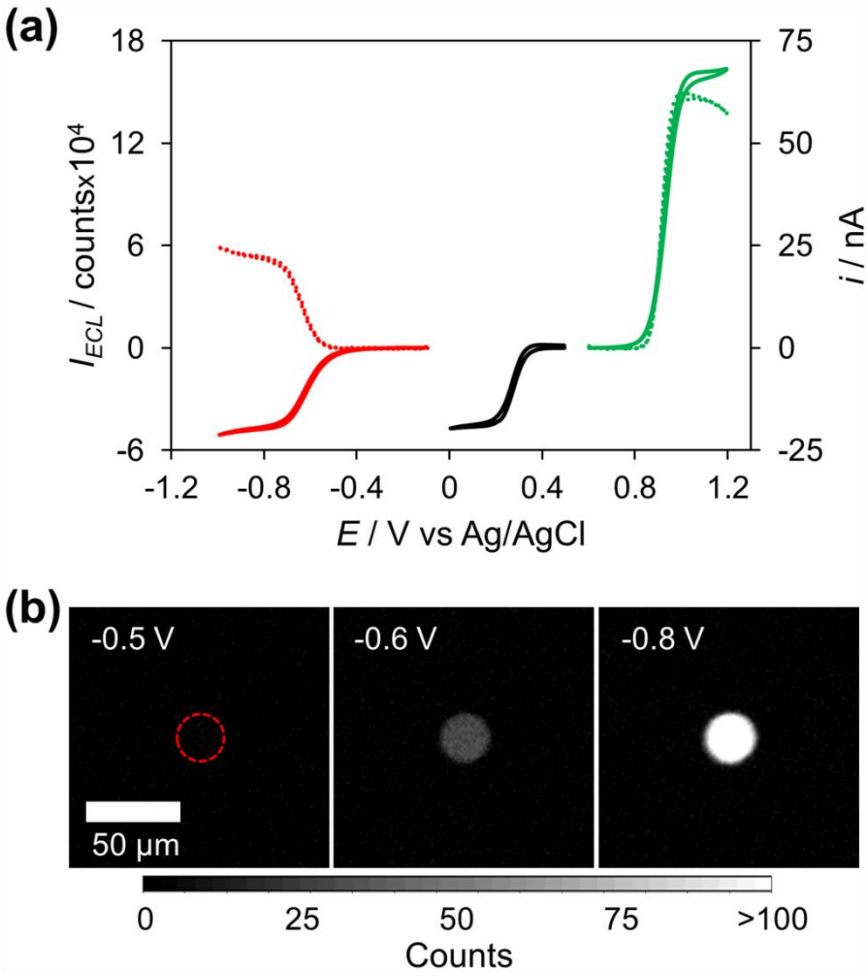

Figure 4.2. Current and ECL signals for two-electrode and bipolar setups.
Relationship between two-electrode and bipolar potentials, electrical, and optical signals. All electrodes used were 25 µm Pt. **(a)** Black line: CV for an electrode in a two-electrode setup in 5 mM $Fe(CN)_6^{3-}$. Solid green line: CV for an electrode in a two-electrode setup in ECL solution. Dashed green line: simultaneously-recorded optical signal from the same electrode during the same scan as shown with the solid green line. Red lines: simultaneously-recorded electrical (solid) and optical (dashed) signals for a bipolar setup in which the cathode was placed in 5 mM $Fe(CN)_6^{3-}$ and the anode was placed in ECL solution. **(b)** Images of the anode of the BPE at various potentials during the forward potential sweep. The actual position of the electrode is indicated by the dashed red ring.

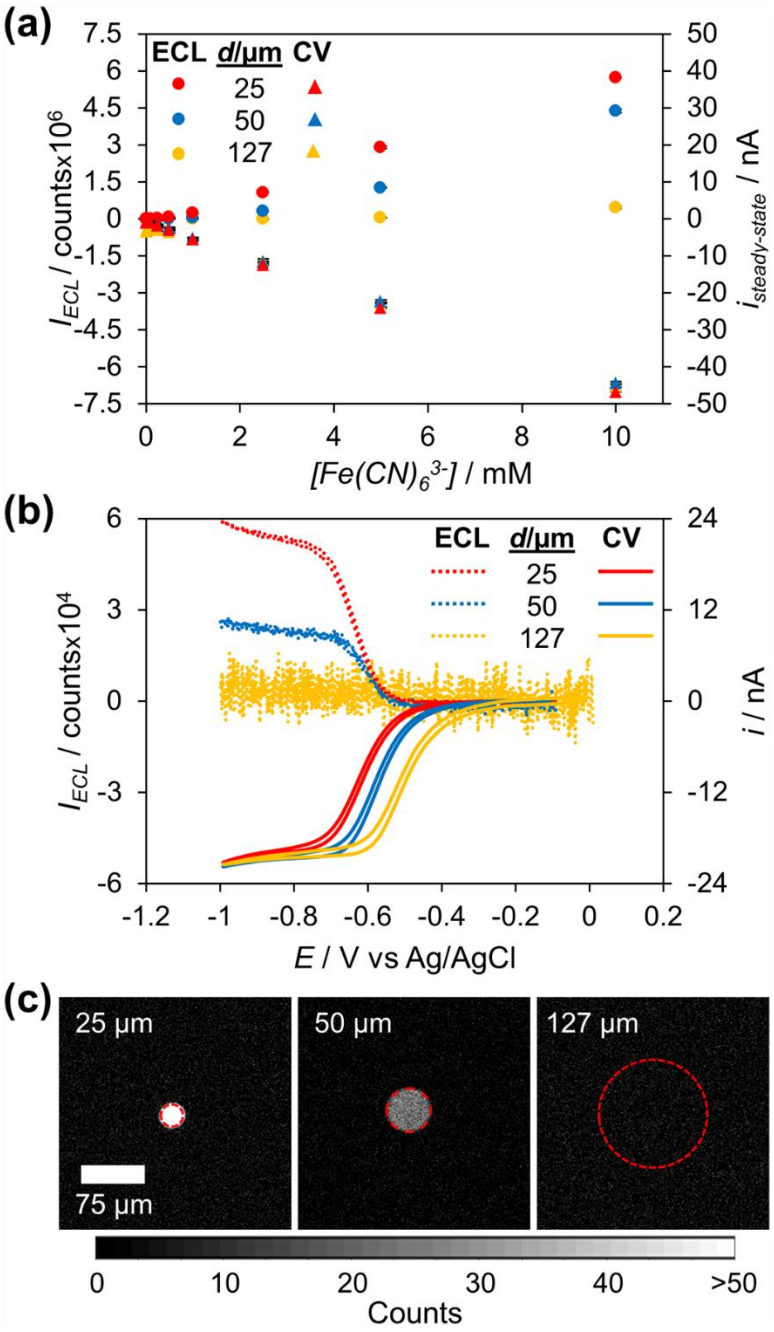

Figure 4.3. Quantitative detection of ferricyanide.

Results of a quantitative bipolar detection experiment. (a) Plot of the steady-state ECL intensity (circles) and steady-state current (triangles) for different $Fe(CN)_6^{3-}$ concentrations using three different anode sizes. An EM gain of 50 was used to collect the optical data. (b) ECL intensity (dashed lines) and current (solid lines) during potential sweeps for the detection of 5 mM $Fe(CN)_6^{3-}$. No EM gain was used to collect the optical data. (c) Images of each anode at steady-state (-0.8 V forward sweep) during the detection experiment shown in (b). The actual electrode positions are outlined in red.

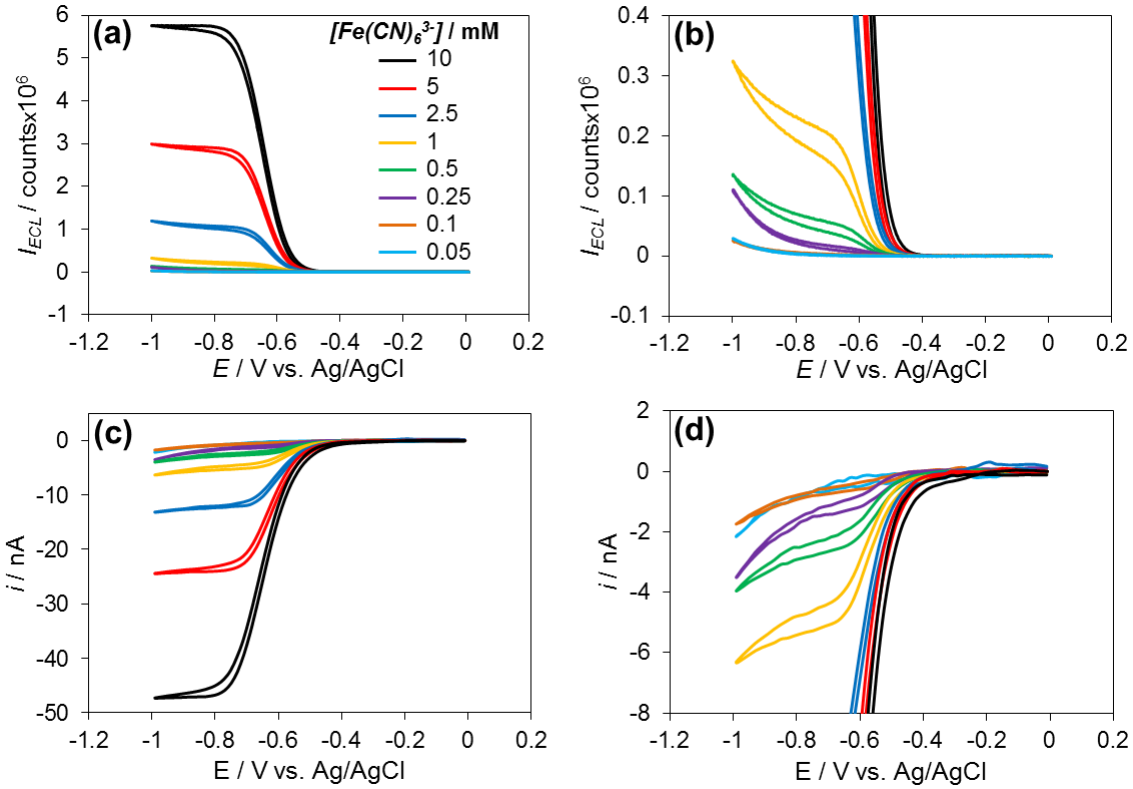

Figure 4.4. ECL and current signals for the detection of ferricyanide.
Traces of the simultaneously-recorded ECL intensity [**(a)** and **(b)**] and current [**(c)** and **(d)**] during the potential sweep BPE sensing experiment discussed in Figure 4.3. In this experiment, the cathode was 25 µm and placed in different concentrations of $Fe(CN)_6^{3-}$, and the anode was of various sizes and placed in ECL solution. The data shown in this figure is for a 25 µm anode. (b) and (d) are zoom-ins of (a) and (c), respectively. A calibration curve is formed from this data by taking the intensity of the signal (either ECL intensity or current) at -0.8 V during the forward sweep for each concentration of $Fe(CN)_6^{3-}$. This intensity is approximated as the steady-state signal intensity, which can then be plotted against $Fe(CN)_6^{3-}$ concentration. The calibration curves from the data shown here are represented by the red circles (for ECL) and red triangles (for current) in Figure 4.3a.

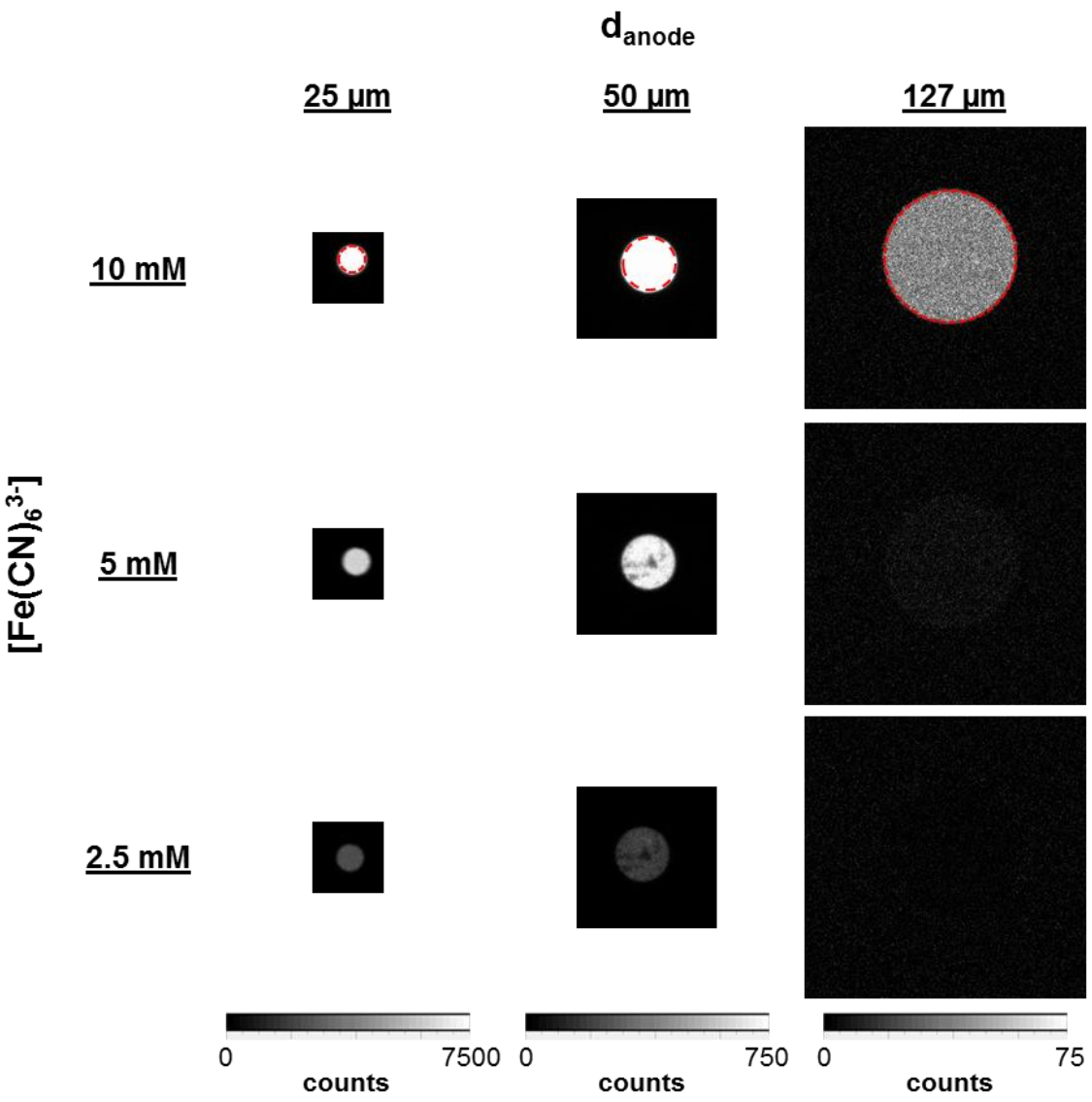

Figure 4.5. Images of different size anodic poles for the detection of ferricyanide.
Images of the anodic poles of the BPEs for different cathodic concentrations of $Fe(CN)_6^{3-}$ during the BPE sensing experiment described in Figure 4.3a. Each image was taken at -0.8 V during the forward sweep of the potential scan. The integrated counts over each anode gives the total ECL intensity, which are the steady-state ECL intensity values reported in Figure 4.3a. The cathodic pole in all cases was a 25 µm electrode. Note the different intensity scales for the images of each anode size. The actual anode positions are indicated by the dashed red rings.

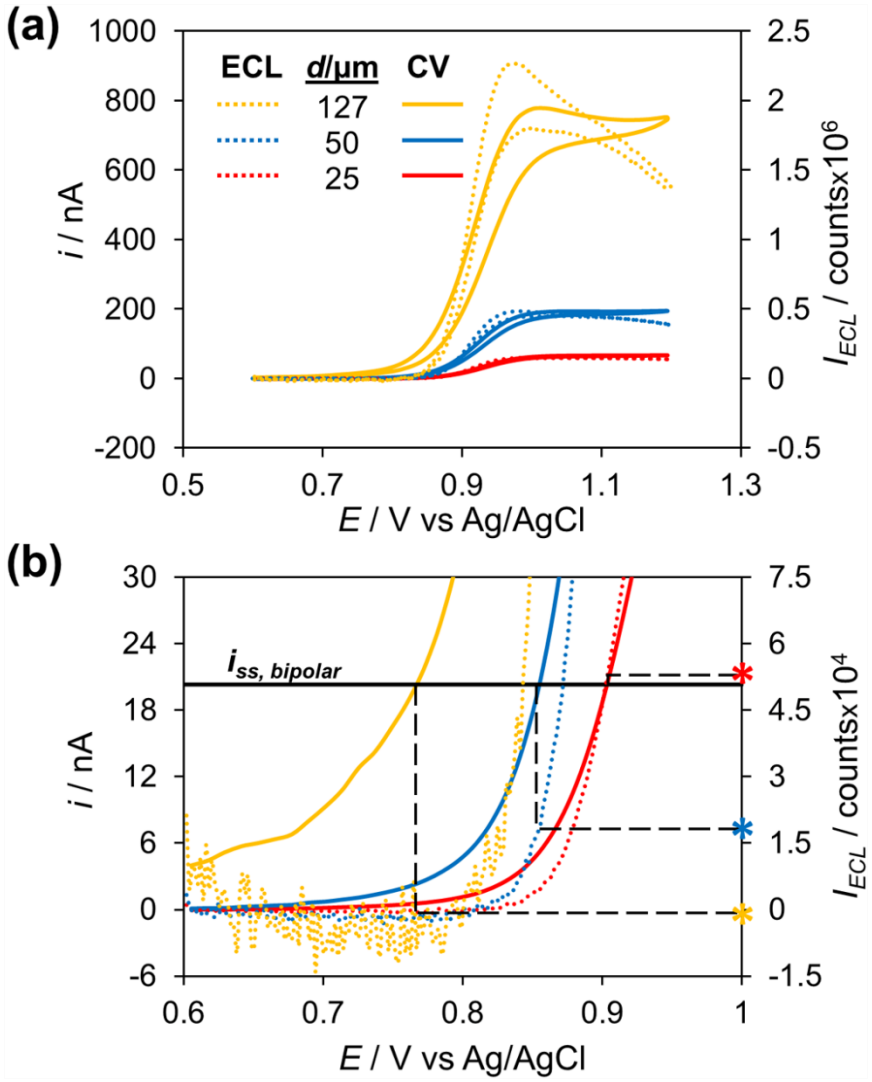

Figure 4.6. Two-electrode CVs of different size electrodes in ECL solution.
Results of a two-electrode potential sweep experiment with different size electrodes placed in ECL solution. The potential was swept from 0.6 to 1.2 V at 20 mV/s and the ECL signal (dashed lines) and current (solid lines) were simultaneously recorded. **(b)** is a zoom-in of **(a)**, with the ECL intensities at the potential at which each electrode reaches the steady-state current produced by 5 mM $Fe(CN)_6^{3-}$ in the bipolar detection experiment in Figure 4.3b marked with asterisks. No EM gain was used to collect this data.

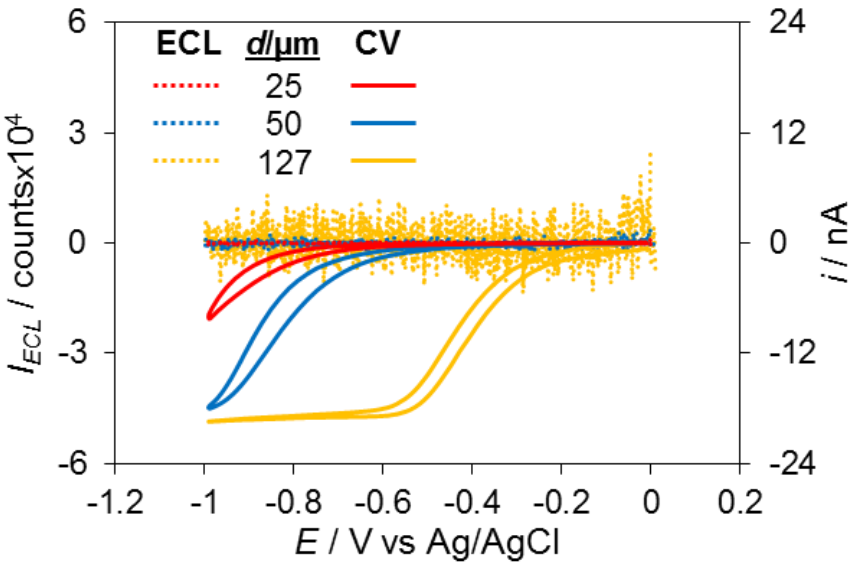

Figure 4.7. Bipolar coupling of ferricyanide to tripropylamine.
Results of a bipolar coupling experiment in which the reporting pole was immersed in a solution of 25 mM TPrA and 0.1 M pH 7.0 phosphate buffer (no $Ru(bpy)_3^{2+}$). The analyte pole was a 25 µm Pt electrode and immersed in a solution of 5 mM ferricyanide with 1 M KCl. The reporting pole was either a 25, 50, or 127 µm Pt electrode. A potential sweep from 0 to -1 V at 20 mV/s was applied to two Ag/AgCl driving electrodes and the current through the BPE and light emission from the reporting pole were simultaneously recorded. This experiment is the same as that shown in Figure 4.3b, except $Ru(bpy)_3^{2+}$ is not present in the reporting pole solution used here.

Figure 4.7 Discussion.
As can be seen, no light emission is observed from the reporting poles. This is expected as the ECL process cannot occur without $Ru(bpy)_3^{2+}$ oxidation. The CV traces clearly show that increasing the size of the reporting pole increases the amount of current that passes through the BPE at a given potential, with larger currents passing at potentials closer to 0 V as the reporting pole size increases. For the 127 µm reporting pole, the steady-state current (limited by the analyte pole) is reached before -0.6 V (the approximate onset potential of ECL emission as determined in Figure 4.3b). As no $Ru(bpy)_3^{2+}$ was used in the experiment here, this shows that the steady-state current can be reached with solely TPrA oxidation occurring on the reporting pole. This explains why no ECL emission is observed for the 127 µm electrode in Figure 4.3b. For the 50 and 25 µm reporting poles, TPrA oxidation is only able to support a fraction of the steady-state current, meaning that in a typical ECL solution (i.e. one containing $Ru(bpy)_3^{2+}$), $Ru(bpy)_3^{2+}$ oxidation will still occur and there will be ECL emission from the electrode.

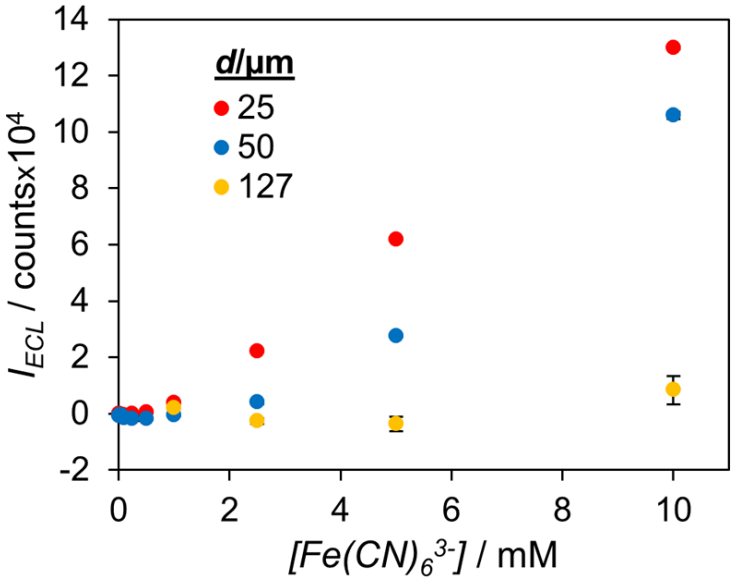

Figure 4.8. Predicted calibration plot for the detection of ferricyanide.
Predicted calibration plot for the bipolar detection of $Fe(CN)_6^{3-}$ using different sized anodes and a 25 µm cathode.

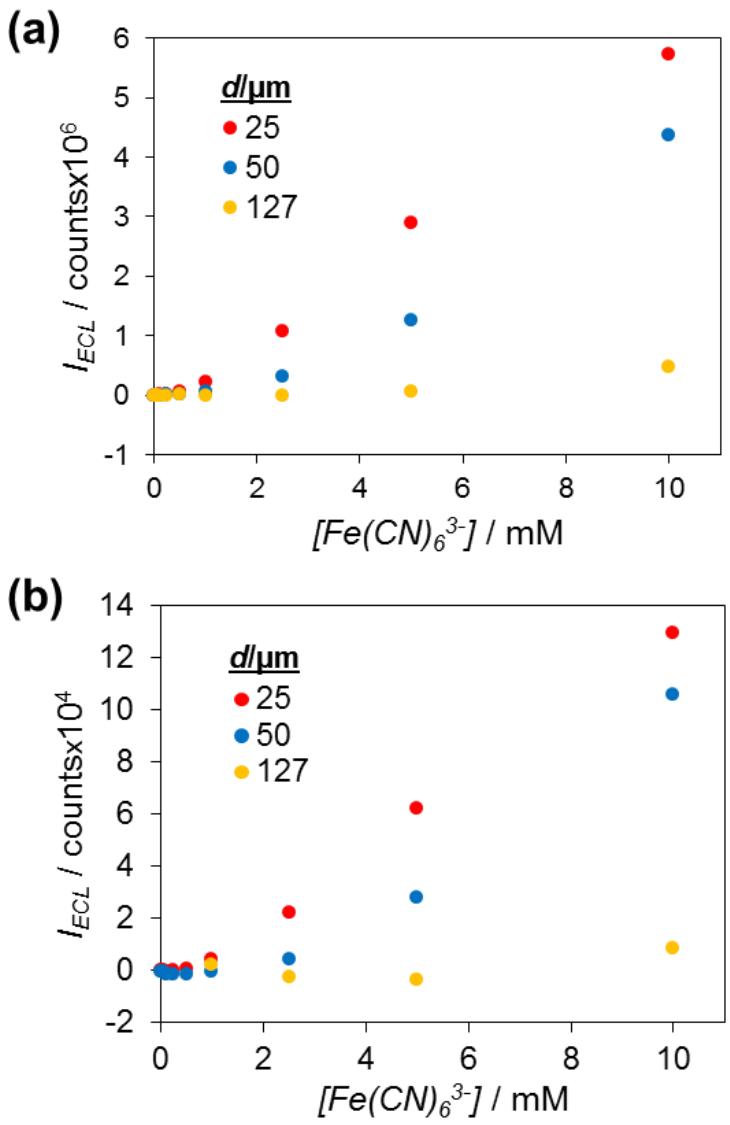

Figure 4.9. Experimental and predicted calibration plots for ferricyanide detection.
Side-by-side comparison of the experimental **(a)** and predicted **(b)** calibration plots for the BPE detection of $Fe(CN)_6^{3-}$ using a 25 µm cathode and various sized anodes. The data in (a) is shown in Figure 4.3a, and (b) is shown as Figure 4.8. The differences in ECL intensity magnitude between the plots are because an EM gain of 50 was used to acquire the data in (a), while no EM gain was used to acquire the data used to make the predicted curves shown in (b). Therefore, the intensities in (a) are ~50 times greater than the intensities in (b).

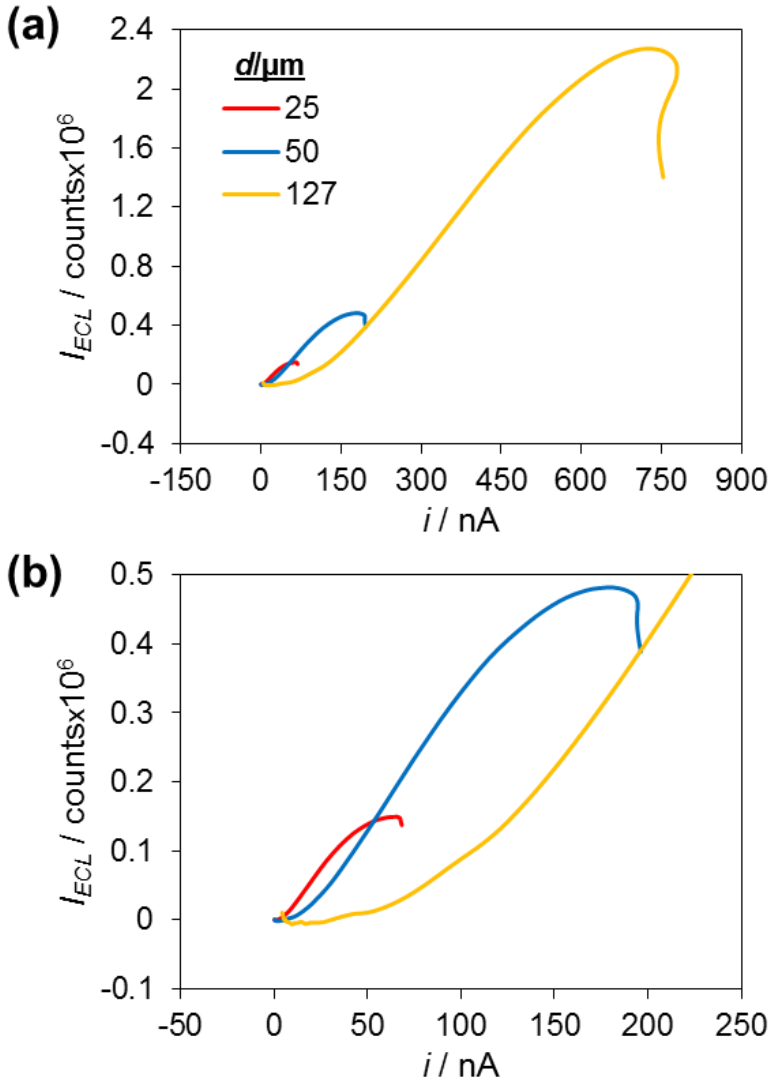

Figure 4.10. ECL intensity vs. current for different size electrodes.
Plots of ECL intensity vs. current for the three different electrode sizes in a two-electrode setup. **(b)** is a zoom-in of **(a)**. These plots are made from the same data shown in Figure 4.6. In this experiment, a Pt electrode serves as the working electrode and is placed in the ECL solution. A potential sweep from 0.6 to 1.2 V at 20 mV/s is applied while simultaneously monitoring the ECL intensity and the current. Only the forward scan is shown in these plots. These plots clearly demonstrate a couple of key points. First, the ECL intensity is higher at lower currents for smaller electrodes. Second, the ECL intensity levels off to a steady-state maximum for each electrode. As the electrode size increases, this maximum increases in magnitude and is reached at higher currents. The behavior of the ECL signal in BPE sensing experiments can be readily explained from plots like these. With knowledge of the current that an analyte will produce at the cathode, the ECL intensity from each anode can be easily predicted using this plot by taking the ECL intensity at that current for each anode.

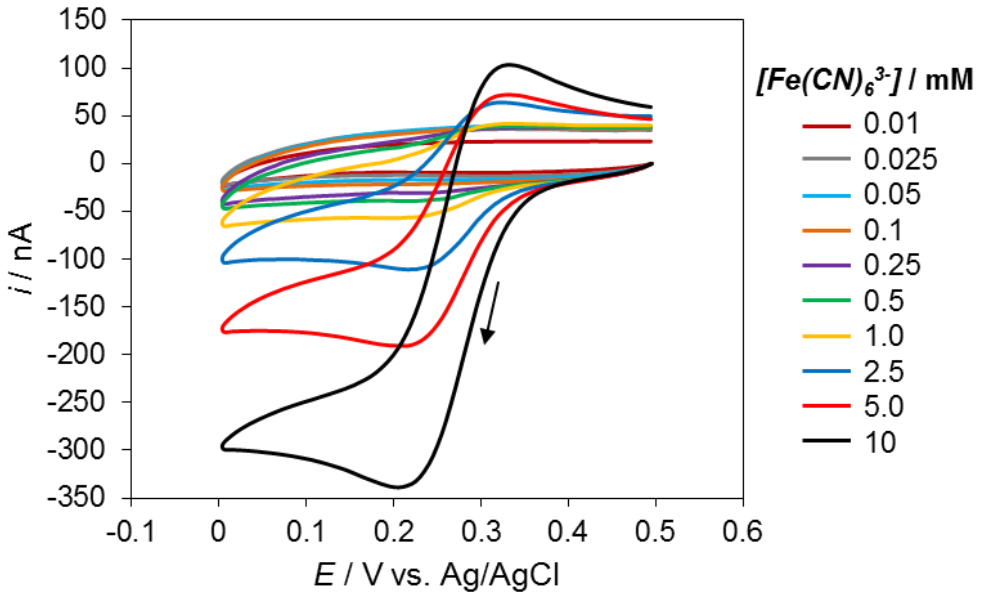

Figure 4.11. CVs of different concentrations of ferricyanide.
CVs obtained for different concentration of ferricyanide in 1 M KCl using a 127 µm Pt electrode in a two-electrode setup. The potential was swept from 0.5 to 0 V at 20 mV/s. The forward scan is indicated by the black arrow. The steady-state current for each concentration was approximated as the current at 0.1 V during the forward sweep.

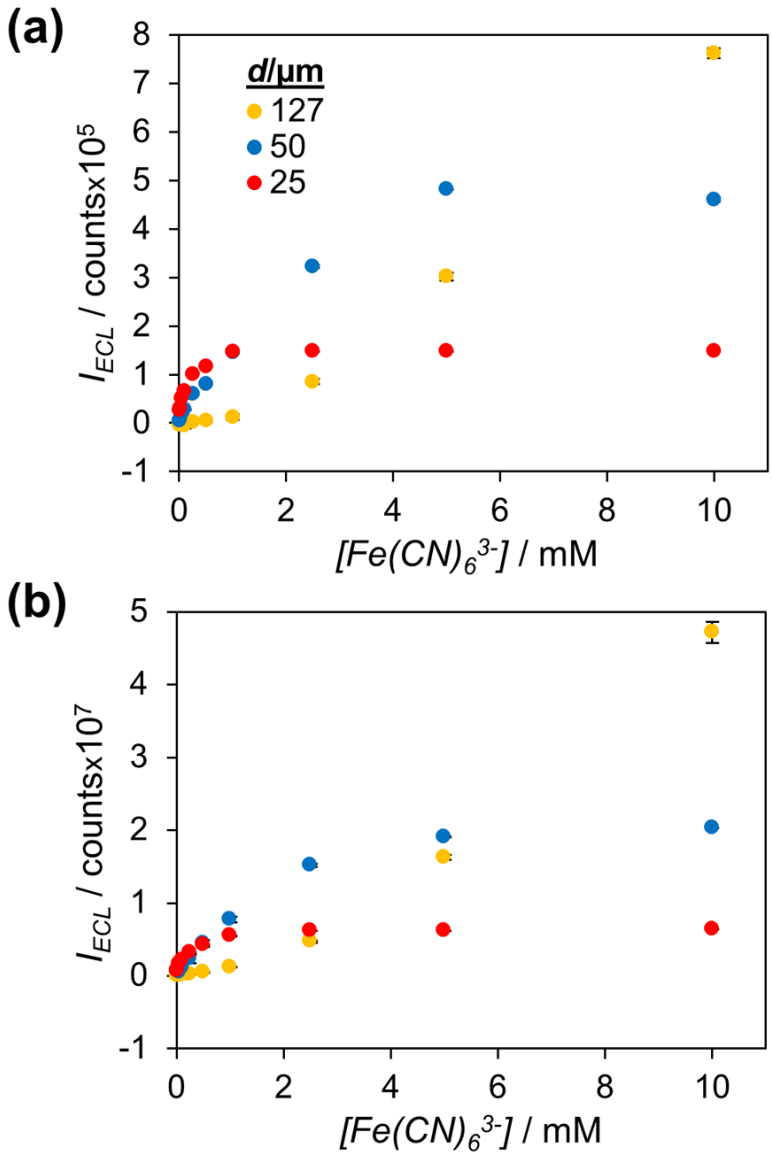

Figure 4.12. Calibration plots for ferricyanide detection using a 127 µm cathode.
Predicted **(a)** and experimental **(b)** calibration plots for the bipolar detection of $Fe(CN)_6^{3-}$ using different sized anodes and a 127 µm cathode. An EM gain of 50 was used for the experiment in (b), while (a) is predicted from data collected using no EM gain.

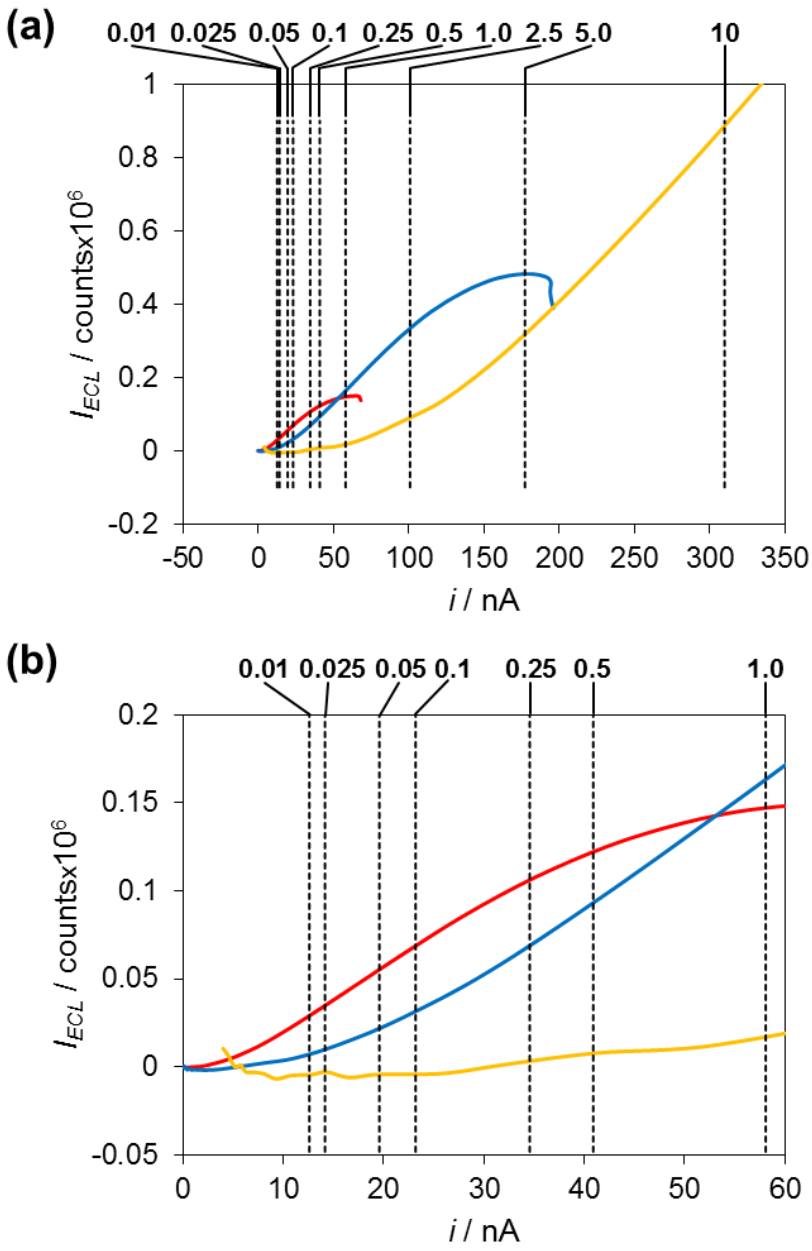

Figure 4.13. ECL intensity vs. current overlaid with steady-state currents.
Plots of two-electrode ECL intensity vs. current for each electrode size overlaid with the steady-state currents measured for each ferricyanide concentration using a 127 µm Pt electrode. The ECL intensity vs. current plots are the same as those presented in Figure 4.10. The vertical dashed black lines represent the steady-state current measured for a particular ferricyanide concentration using a 127 µm Pt electrode. The steady-state currents were taken as the current at 0.1 V in the forward sweep of the CV data presented in Figure 4.11. The numbers above the dashed black lines indicate ferricyanide concentration in mM. As in Figure 4.10 **(b)** is a zoom-in of **(a)** and the red, blue, and yellow traces are for a 25, 50, and 127 µm electrode, respectively.

Figure 4.13 Discussion.
A calibration plot for the BPE sensing of ferricyanide using a 127 µm cathode and a given size anode can be predicted from this data by taking the ECL intensity for a given electrode size at each steady-state current marked and plotting those intensities against the respective $Fe(CN)_6^{3-}$ concentration. For example, the predicted calibration curve for a 127 µm anode (shown by the yellow points in Figure 4.12a) is given by plotting the ECL intensity at each point where the ECL curve (solid yellow line) is intersected by a vertical dashed black line against the respective ferricyanide concentration represented by each steady-state current.

4.6 Appendix 1

Limiting Poles in Bipolar Electrochemistry

One of the poles will always limit the current through a closed BPE, unless both poles are equally "balanced." Considered individually, under steady-state conditions each pole will have a maximum current at a given potential. That maximum current can easily be measured by taking a CV of the individual pole in a two-electrode setup. When the two poles are connected to form a closed BPE, the current through the BPE at each potential will be limited by the individual pole with the lowest maximum current at that potential. This pole is termed the limiting pole. Figure 4.A1.1 demonstrates this concept. The CV represented by the dashed black line is the two-electrode CV for a 127 μm electrode in 5 mM $Fe(CN)_6^{3-}$. The CVs represented by the dashed red and dashed blue lines are the two-electrode CVs for either a 25 μm or 50 μm electrode, respectively, in ECL solution. As seen, all three CVs exhibit steady-state behavior, with the mass transfer-limited steady-state current representing the maximum current for each electrode under the conditions present.

The solid lines show the CVs obtained when these two poles are connected to form a closed BPE. The cathode of the BPE is a 127 μm electrode and is placed in 5 mM $Fe(CN)_6^{3-}$. The anode of the BPE is either a 25 μm (red) or 50 μm (blue) electrode and is placed in ECL solution. For the BPE with the 25 μm anode, note that the magnitude of the steady-state current is equivalent to the magnitude of the steady-state current of the 25 μm electrode in ECL solution in a two-electrode setup (dashed red trace). This is because a 25 μm electrode in ECL solution has a lower magnitude steady-state current than a 127 μm electrode in 5 mM $Fe(CN)_6^{3-}$ and

therefore limits the current through the BPE. Hence, in this setup, the anode is the limiting pole. Conversely, for the BPE with the 50 µm anode, the magnitude of the steady-state current is equivalent to the magnitude of the steady-state current of the 127 µm electrode in 5 mM $Fe(CN)_6^{3-}$ in a two-electrode setup (dashed black trace). This is because a 50 µm electrode in ECL solution has a higher magnitude steady-state current than a 127 µm electrode in 5 mM $Fe(CN)_6^{3-}$ and therefore does not limit the current through the BPE. Hence, in this setup, the cathode is the limiting pole.

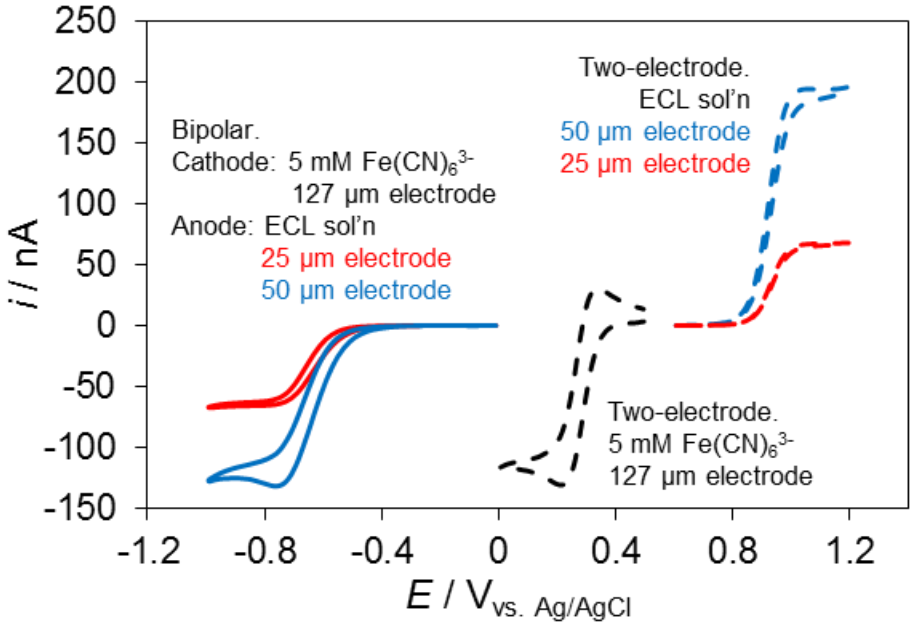

Figure 4.A1.1. Relationship between two-electrode and bipolar setup CVs.
Relationships between two-electrode and bipolar setup currents and potentials for different size anodic poles for the detection of 5 mM $Fe(CN)_6^{3-}$. The cathodic pole in the bipolar setup was 127 µm. Dashed lines show two-electrode setup CVs, while solid lines show bipolar setup CVs.

4.7 Appendix 2

Enhanced Signal to Noise Ratio on Smaller Anodes

As mentioned in the main text, if an equivalent ECL intensity is found on two electrodes of different sizes, the signal to noise ratio will be greater on the electrode of smaller size if a pixel-based detector (such as a CCD camera, which is used here) is used. While a pixel-based detector is not necessary in a one-electrode sensing experiment, it becomes necessary if one desires to do sensing/imaging on an electrode array due to the need to image several electrodes simultaneously. This signal to noise effect can be thought of in two ways. If considering the total ECL intensity (i.e. integrating the intensity over the entire electrode area), a larger electrode will give a larger noise value. This can be seen, somewhat subtly, in the ECL intensity traces displayed in Figure 4.A2.1 below, and can be very clearly seen in Figures 4.3b and 4.4b of the main text. This is because a larger electrode requires a larger area (and hence a larger number of pixels) to be integrated to get the total ECL intensity. As long as the same camera settings are used, the per pixel noise level remains constant regardless of electrode size. This means the increased noise associated with the total ECL intensity of a large electrode is due to multiplying the per pixel noise by a larger factor due to using more pixels to measure the ECL signal.

If considering the per pixel ECL intensity (i.e. an image), a larger electrode will have a smaller signal per unit area, corresponding to a smaller signal per pixel on the camera. This is because the same total ECL signal is emitted from a larger area, meaning a large electrode effectively "spreads out" the signal. This causes a lower per pixel signal to noise ratio, and can be clearly seen in the images in Figure 4.A2.1 below.

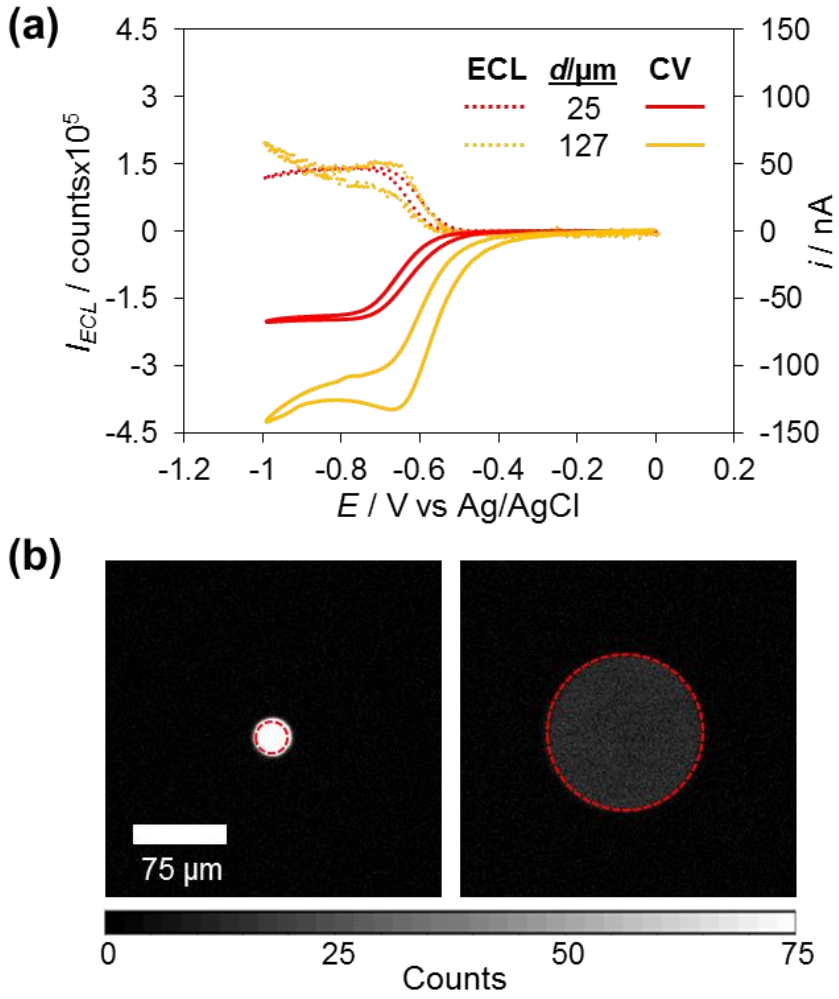

Figure 4.A2.1. Enhanced signal to noise ratio on smaller anodes.
Results of a BPE sensing experiment in which the cathode was 127 µm and placed in 5 mM $Fe(CN)_6^{3-}$. The anode was either 25 or 127 µm and placed in ECL solution. **(a)** The total ECL intensity (dashed lines) and current (solid lines) for each anode size during a potential sweep from 0 to -1 V. As seen, the steady-state ECL intensities are approximately the same for both anode sizes. Discussion of why this is (and relatedly, why the current magnitudes are different) can be found in the main text. **(b)** Images of each anode at -0.8 V during the forward sweep of the potential scan. Despite having approximately the same total ECL intensities, one can clearly see that the signal to noise ratio of the 25 µm anode is markedly better than that of the 127 µm anode. The actual anode positions are indicated by the dashed red rings.

4.8 References

(1) Arora, A; Eijkel, J. C. T.; Morf, W. E.; Manz, A. *Anal. Chem.* **2001**, *73*, 3282–3288.

(2) Zhan, W.; Alvarez, J.; Crooks, R.M. *J. Am. Chem. Soc*. **2002**, *124*, 13265-13270.

(3) Chow, K.-F.; Mavré, F.; Crooks, R.M. *J. Am. Chem. Soc.* **2008**, *130*, 7544-7545.

(4) Chow, K.F.; Mavré, F.; Crooks, J.A.; Chang, B.-Y.; Crooks, R.M. *J. Am. Chem. Soc.* **2009**, *131*, 8364-8365.

(5) Mavré, F.; Chow, K.-F.; Sheridan, E.; Chang, B.-Y.; Crooks, J.A.; Crooks, R.M. *Anal. Chem.* **2009**, *81*, 6218-6225.

(6) Fosdick, S.E.; Crooks, J.A.; Chang, B.-Y.; Crooks, R.M. *J. Am. Chem. Soc.* **2010**, *132*, 9226-9227.

(7) Chang, B.-Y.; Mavré, F.; Chow, K.-F.; Crooks, J.A.; Crooks, R.M. *Anal. Chem.* **2010**, *82*, 5317-5322.

(8) Wu, M.-S.; Xu, B.-Y.; Shi, H.-W.; Xu, J.-J.; Chen, H.-Y. *Lab Chip*, **2011**, *11*, 2720-2724.

(9) Wu, M.-S.; Qian, G.-S.; Xu, J.-J.; Chen, H.-Y. *Anal. Chem.* **2012**, *84*, 5407-5414.

(10) Lui, R.; Zhang, C.; Liu, M. *Sensor Actuat B-Chem* **2015**, *216*, 255-262.

(11) Chang, B.-Y.; Chow, K.-F.; Crooks, J.A.; Mavré, F.; Crooks, R.M. *Analyst* **2012**, *137*, 2827-2833.

(12) Wu, M.-S.; Yuan, D.-J.; Xu, J.-J.; Chen, H.-Y. *Chem. Sci.* **2013**, *4*, 1182-1188.

(13) Zhang, X.; Chen, C.; Li, J.; Zhang, L.; Wang, E. K. *Anal. Chem.* **2013**, *85*, 5335–5339.

(14) Lin, X.; Zheng, L.; Gao, G.; Chi, Y.; Chen, G. *Anal. Chem.* **2012**, *84*, 7700-7707.

(15) Zhang, X.; Li, J.; Jia, X.; Li, D.; Wang, E. *Anal. Chem.* **2014**, *86*, 5595-5599.

(16) Wu, S.; Zhou, Z.; Xu, L.; Su, B.; Fang, Q. *Biosens. Bioelectron.* **2014**, *53*, 148-153.

(17) Zhang, J.-D.; Yu, T.; Li, J.-Y.; Xu, J.-J.; Chen, H.-Y. *Electrochem. Commun.* **2014**, *49*, 75-78.

(18) Wu, M.-S.; Liu, Z.; Shi, H.-W.; Chen, H.-Y.; Xu, J.-J. *Anal. Chem.* **2015**, *87*, 530-537.

(19) Eßmann, V.; Jambrec, D.; Kuhn, A.; Schuhmann, W. *Electrochem. Commun.* **2015**, *50*, 77-80.

(20) Fosdick, S. E.; Knust, K. N.; Scida, K.; Crooks, R. M. *Angew. Chem. Int. Ed.* **2013**, *52*, 10438–10456.

(21) Guerrette, J. P.; Oja, S. M.; Zhang, B. *Anal. Chem.* **2012**, *84*, 1609–1616.

(22) Cox, J. T.; Guerrette, J. P.; Zhang, B. *Anal. Chem.* **2012**, *84*, 8797–8804.

(23) Noffsinger, J.B.; Danielson, N.D. *Anal. Chem.* **1987**, *59*, 865-868.

(24) Zu, Y.; Bard, A.J. *Anal. Chem.* **2000**, *72*, 3223-3232.

(25) Guerrette, J. P.; Percival, S. P.; Zhang, B. *J. Am. Chem. Soc.* **2013**, *135*, 855–861.

(26) Oja, S.M.; Guerrette, J.P.; David, M.R.; Zhang, B. *Anal. Chem.* **2014**, *86*, 6040-6048.

(27) Oja, S.M.; Zhang, B. *Anal. Chem.* **2014**, *86*, 12299-12307.

(28) Hotta, H.; Akagi, N.; Sugihara, T.; Ichikawa, S.; Osakai, T. *Electrochem. Commun.* **2002**, *4*, 472-477.

(29) Plana, D.; Jones, F. G. E.; Dryfe, R. A. W. *J. Electroanal. Chem.* **2010**, *646*, 107–113.

(30) The data shown in (b) is from a different trial than the data shown in (a). For the data shown in (a), an electron multiplier (EM) gain of 50 was used, while no EM gain was used for the data displayed in (b). This is why the ECL intensities are ~50 times greater in (a) than in (b).

(31) We emphasize that this only holds true for a pixel-based detector, such as a CCD camera (as opposed to a single-channel detector such as a photomultiplier tube).

(32) Kanoufi, F.; Zu, Y.; Bard, A.J. *J. Phys. Chem B.* **2001**, *105*, 210-216.

(33) Miao, W.; Choi, J.-P.; Bard, A.J. *J. Am. Chem. Soc.* **2002**, *124*, 14478-14485.

(34) The steady-state current for a given analyte concentration can be easily calculated for a known electrode geometry. See: A.J. Bard, L.R. Faulkner in Electrochemical Methods, 2nd ed, John Wiley & Sons, New York, 2001, Chapter 5. For the inlaid-disk microelectrodes used in this report, the steady-state current, i_{ss}, will be given by the equation: $i_{ss} = 4nFC^*Dr$, where n is the number of electrons transferred per analyte molecule reacted, F is the Faraday constant, C^* is the bulk concentration of the analyte, D is the diffusion coefficient of the analyte, and r is the radius of the electrode.

CHAPTER 5

Coupled Electrochemical and Fluorescence Properties of Methylene Blue-Modified Polystyrene Microspheres

5.1 Introduction

Nanoparticles functionalized with redox-active moieties have been of interest to researchers as a novel electrochemical material with the potential for high-capacity charge storage.[1,2,3,4,5] These particles are typically either polymer,[1,4] silica,[2,5] or gold[3] and have a redox-active molecule such as ferrocene covalently linked to the particle surface. Interestingly, these particles typically behave as a sort of "super" redox molecule, as each particle can contain anywhere from 10 to 10^8 active redox moieties, depending on both the particle size and functionalization method. Importantly, the electrochemical characterization of these particles relied on bulk, rather than single-particle, measurements.

Since the time these initial publications appeared, the ability to electrochemically detect single nanoparticles has been developed[6] and applied in various schemes to detect a multitude of different types of nanoparticles.[7] Collectively these methods are frequently referred to as stochastic particle collision amperometry. In these experiments, a small detection electrode is placed in a dilute solution of dispersed nanoparticles that collide with the electrode in a stochastic manner. The current through the electrode is measured over time, and each collision of a particle with the electrode produces a detectable change in the current. There are many specific schemes used to induce this current change, but typically the particle either catalyzes an

electrochemical reaction, producing a sharp increase in the current, or gets directly oxidized or reduced, again producing a sharp increase in the current.

Despite the many different types of particles studied in this manner, it is important to note that to date, no redox-functionalized nanoparticles have been studied using this technique. These particles, however, should be very readily amenable to detection via a stochastic particle collision method. If the detection electrode is poised at a potential sufficient to induce the faradaic reaction of the redox-active moieties, a spike in the current signal should be observed each time a particle collides with the electrode. The area of this spike could then be used to quantify the number of redox molecules reacted in the collision and the time scale of the event could be used to help understand whether complete reaction of the redox moieties is due to rotational diffusion of the particles or an electron hopping mechanism. [4,5]

Our interest in this type of particle initially arose from a desire to test the detection limit of our new electrochemical imaging method, fluorescence-enabled electrochemical microscopy (FEEM).[8,9,10] We would like to use FEEM for imaging the synaptic transmission of electroactive neurotransmitters such as dopamine from neuronal cells. Model neuronal cells that would be used for this type of study secrete on the order of 10^5 dopamine molecules per quantal release, meaning our technique must have the sensitivity to detect ~10^5 electrons.[11] In order to systematically study the performance of FEEM in detecting this type of event, we propose using redox-functionalized nanoparticles in a stochastic particle collision detection scheme as outlined in Figure 5.1. Each redox-modified nanoparticle acts as a "super" redox molecule, injecting a discrete number of electrons into the bipolar electrode upon collision, resulting in a fluorescence burst on the reporter side of the electrode as the fluorogenic indicator undergoes coupled faradaic reaction. By changing the number of redox molecules on each nanoparticle, we can study the

fluorescence response caused by a specific number of electrons being injected into the system. While individual collision events will be detectable by stochastic collision amperometry at higher redox molecule loadings, they will be below the detection limit at lower loading levels. In order to correlate these events with the FEEM signal, we propose modifying the nanoparticles with a fluorophore to enable collision observation via fluorescence microscopy.

In deciding on which particle substrate-redox molecule-fluorophore combination to use, we sought to take advantage of our knowledge of redox-active fluorophores by combining the redox-active and fluorescent molecule into one species. This has the significant advantage of simplifying the particle modification process and enables the observation of the particle collision event. Additionally, if the molecule has coupled redox and fluorescence states, this has the additional benefit of enabling the visual observation of the faradaic reaction of the modified particle. Two molecules that have these properties are resorufin and methylene blue, which are both fluorescent molecules that can be reversibly reduced to a non-fluorescent form.[12,13] As for the particle substrate, we decided to utilize polystyrene microspheres, as they are readily available in a wide range of monodisperse sizes, and there is an extensive existing literature on modifying these particles with redox-active, fluorescent, and other interesting moieties.[14,15,16,17] Conveniently, the cationic methylene blue has been previously shown to adsorb onto anionic polystyrene microspheres via electrostatic interaction.[17] Therefore, we chose methylene blue-modified polystyrene microspheres as a redox-active, fluorescent particle to develop for use in our FEEM detection scheme as shown in Figure 5.1.

We note some interesting similarities and differences in our idea of electrochemically and optically detecting the collision and subsequent faradaic reaction of single redox-active particles to some previous studies. The Bard group has developed a system of electrochemically detecting

the collision of polydisperse, submicron oil droplets containing hydrophobic redox molecules.[18,19,20] If the droplet contains a luminophore and coreactant, electrogenerated chemiluminescence (ECL) can occur, resulting in a concurrent optical signal.[21] This idea is similar in nature to the modified particles discussed here, however our particles contain redox molecules adsorbed to a particle surface (as opposed to freely diffusing within an oil droplet) and should have a very monodisperse size distribution. The Crooks group presented a study in which they optically monitored the collision of fluorescent polymer microspheres with a microelectrode and the subsequent blocking effect the microsphere had on an electrochemical reaction occurring on the electrode surface at a diffusion-limited rate.[22] Their study uses the idea of monitoring the collision of particles by using fluorescent polymer microspheres, but the microspheres in their case are electrochemically inert.

In this chapter, we first demonstrate the coupled electrochemical and fluorescence properties of free methylene blue in an aqueous solution as it is reversibly reduced on a microelectrode. We then discuss the modification of polystyrene microspheres with methylene blue and the resulting visual appearance and fluorescence of the modified microspheres. We show that the fluorescence of the modified microspheres can be reversibly switched between an on and off state by potential control. Lastly, we show that collision events of single modified microspheres can be observed both optically and electrochemically. This demonstrates that redox-modified particles can be detected via stochastic particle collision amperometry and that the methylene blue-modified microspheres are suitable for the FEEM detection scheme outlined in Figure 5.1.

5.2 Experimental Section

5.2.1 Chemicals

Methylene blue (MB, Aldrich Chemical) was used as received. Polystyrene (PS) microspheres (Polysciences, Inc.) were used as received for the preparation of the MB-modified PS microspheres as described in section 5.2.2. Microspheres were dispersed in 50 mM pH 7.5 phosphate buffer for all imaging and electrochemistry experiments.

5.2.2 Preparation of Modified Microspheres

We followed a very simple procedure from Galembeck and coworkers[17] that relies on adsorption to modify the PS microspheres with MB. We mixed 0.5 mL of 752 ± 21 nm diameter PS microsphere solution (1.08×10^{11} particles/mL) as received from the manufacturer with 0.5 mL of 5 mM MB in 25 mM pH 7.5 phosphate buffer. We sonicated this solution for 60 min to ensure that the PS microspheres were dispersed and then let the solution sit overnight at room temperature. This was followed by 10 wash cycles, with a cycle consisting of centrifuging the microsphere solution at 8,000 RPM for 10 min, removing the supernatant, adding 1 mL of fresh 50 mM pH 7.5 phosphate buffer to the microspheres, and sonicating the resulting solution for 2 min to redisperse the microspheres. The supernatant was a deep blue color after the first wash cycle and progressively became clearer with each subsequent wash cycle. By the tenth cycle, the supernatant had no visible color, while the PS microspheres retained a visibly blue color, indicating successful modification with MB. Following the final centrifugation, the modified MB-PS microspheres (taking up a volume ~ 0.3 mL) were dispersed with 1.5 mL of fresh 50 mM pH 7.5 phosphate buffer to a final volume of 1.8 mL. Assuming no particle loss during the wash cycles, this results in a particle concentration of 3×10^{10} particles/mL, giving an approximate maximum particle concentration. This solution was used as the stock MB-PS microsphere solution and was stored between experiments at 4 °C. PS microspheres with

diameters of 532 nm, 356 nm, and 112 nm were also successfully modified with MB using this procedure. However, only results from the 752 nm diameter microspheres are discussed here. Unmodified PS microspheres were used as a control. A stock solution of these was created by dispersing 0.5 mL PS microsphere solution as received from the manufacturer in 1.3 mL 50 mM pH 7.5 phosphate buffer.

5.2.3 Electrochemical Measurements

The voltammetry experiment in Figure 5.3 was carried out using a Chem-Clamp potentiostat (Dagan Corporation) interfaced to a PC through a PCI-6251 data acquisition board (National Instruments) using a BNC-2090 breakout box (National Instruments). An in-house LabView 10.0 (National Instruments) program was used for voltage function generation and acquisition of the current-voltage data. This program receives an external trigger from a camera, enabling the synchronized recording of electrochemical and optical signals. For the voltage pulsing experiments in Figures 5.6 and 5.7, the potential was controlled using a Chem-Clamp potentiostat. An ITO-coated glass coverslip was used as the working electrode in the experiment in Figure 5.6. Electrical connection was made to the ITO coverslip through a tungsten wire connected to the ITO surface with silver paint (Dupont). The working electrode in the experiments shown in Figures 5.3 and 5.7-5.10 was a 25 μm diameter Au electrode with an inlaid disk geometry. This electrode was fabricated by sealing a 25 μm diameter Au microwire (Alfa-Aesar) in a borosilicate capillary (Sutter Instrument Co.) and making connection to the Au with tungsten wire and Ag paint (Dupont) through the back end of the capillary. A Ag/AgCl reference electrode was used for all experiments, and all potentials are reported vs. Ag/AgCl. Onset potentials were determined by taking the potential at which 10% of the steady-state current was reached.

The single-particle amperometry experiments were carried out using an Axopatch 200B integrating patch-clamp amplifier (Molecular Devices) interfaced to a PC through a Digidata 1440A digitizer (Molecular Devices). The Axopatch was operating in V-clamp mode with whole cell $\beta = 1$ and the low-pass filter set to 10 kHz. Amperometric traces were recorded using pClamp 10.4 Axoscope software (Molecular Devices) with a 50 kHz sampling rate. Current spikes were analyzed and integrated using pClamp 10.4 Clampfit software (Molecular Devices), and histograms of the events were created using Origin software (OriginLab Corporation).

5.2.4 Optical Measurements

A Nikon Eclipse Ti inverted microscope and an Andor iXon EMCCD camera cooled to -80 °C were used for brightfield and fluorescence imaging. A mercury lamp (Nikon Intensilight C-HGFIE, ND1 filter setting) coupled to the microscope via an optical fiber was used as the excitation source. Light was passed through a filter cube containing a 625/26 excitation filter (Semrock Brightline), a 660 dichroic mirror (ChromaTechnology), and a 692/40 emission filter (Semrock Brightline). The imaging in Figure 5.3 was done through a 40X 0.6 NA objective (Nikon CFI S Plan Fluor ELWD). All other imaging was done through a 100X 1.49 NA oil immersion objective (Nikon CFI Apo TIRF) using an additional 1.5X magnification on the microscope. Nikon Type A immersion oil was used. All fluorescence imaging was done in epifluorescence mode. Andor SOLIS software was used to record and process all images. The exposure time and EM gain used to acquire the fluorescence images are as follows: Figure 5.3 = 0.1 s exposure, 100 EM gain; Figure 5.5 = 0.5 s exposure, 100 EM gain for (a), 300 EM gain for (b); Figure 5.6 = 0.1 s exposure, 300 EM gain; Figure 5.7 = 0.5 s exposure, 300 EM gain. A preamplifier gain of 5.1 was used. For the experiments in Figure 5.3 and Figure 5.7, the electrode

was positioned 300 μm or 50 μm, respectively, above a glass coverslip using a motorized micromanipulator (Sutter Instruments MP-285).

5.3 Results and Discussion

5.3.1 Coupled Electrochemical and Fluorescence Properties of Free Methylene Blue

We first sought to demonstrate the coupled behavior of the fluorescence state and redox state of solution phase methylene blue (MB). MB is a redox-active molecule that can undergo a reversible two-electron reduction reaction to leucomethylene blue (LMB) (Figure 5.2). MB has an absorbance maximum at 665 nm, which explains its characteristic deep blue color.[13] It has a corresponding fluorescence maximum at 682 nm, although MB is a weak fluorophore with a quantum yield < 0.05. LMB only absorbs in the UV range, which explains its colorless appearance, and although it has a quantum yield similar to that of MB, the fluorescence maximum is shifted to 452 nm. This difference in optical properties between MB and LMB enables one to optically monitor the redox state of the molecules. The popular "Blue Bottle Experiment" classroom demonstration utilizes this change in optical properties, as glucose chemically reduces a solution of MB to LMB, turning the solution from blue to colorless.[23,24]

We utilize the change in fluorescence state to optically monitor the redox state of MB. In its oxidized form, MB will fluoresce around 680 nm, while the reduced form, LMB, will show no fluorescence in that wavelength region. To demonstrate this property, we performed an experiment in which the current and fluorescence from a 25 μm diameter Au microelectrode were simultaneously monitored during a potential sweep in MB solution. The electrode was placed in an argon-bubbled solution of 100 μM MB in 50 mM pH 7.5 phosphate buffer and positioned on an inverted microscope for fluorescence imaging. The potential of the electrode

was swept between 0 and -0.8 V vs. a Ag/AgCl reference electrode at 20 mV/s. The current and fluorescence intensity at the electrode were simultaneously monitored during the potential sweep and the averaged results of three scans are plotted in Figure 5.3a (dashed black trace = current, red trace = fluorescence). As can be seen, the current follows the expected sigmoidal-shaped curve with an onset potential of -0.34 V, indicating the onset of reduction of MB to LMB. The current then decreases until it reaches a steady-state current of -0.40 nA. Using a diffusion coefficient of 8.3×10^{-10} m^2/s for MB, this current matches the theoretical steady-state current.[25,26] On the return scan, the current increases as the potential is scanned back to 0 V and a small oxidation peak is present at -0.35 V. This behavior is likely due to the reoxidation of the reduction product, LMB, which can be adsorbed onto the electrode surface.[27]

The fluorescence signal follows the current nearly exactly. The fluorescence intensity starts off at a maximum, as the solution around the electrode contains only MB. The intensity begins to decrease as the current decreases, signifying the reduction of the fluorescent MB to the non-fluorescent LMB. This decreases the local concentration of MB near the electrode, thus decreasing the fluorescence intensity at the electrode. As the potential decreases to -0.8 V, the fluorescence intensity reaches a steady-state value along with the current. On the return scan, the fluorescence intensity doesn't initially follow the same increase as the current does, which may indicate that this current increase is due to a charging current. A charging current, which is a non-faradaic process, would not produce a change in the fluorescence signal. The change in fluorescence intensity at the electrode can clearly be seen in Figure 5.3b. The first image shows the electrode at a potential of -0.2 V, which is before the onset of MB reduction. The second image shows the electrode at a potential of -0.8 V, where the reduction of MB to LMB is being

driven at its diffusion-limited maximum. As can be seen, the electrode exhibits a much brighter fluorescence signal at -0.2 V.

As is clear, the electrochemical reduction of MB to LMB can be monitored by imaging the fluorescence signal at an electrode. The fluorescence intensity correlates extremely well to the current and is directly proportional to it. The fluorescence intensity (rather than the time-derivative of the fluorescence intensity) is directly proportional to the current in this system because a fluorophore is being turned off upon faradaic reaction, meaning that once the fluorophore is reduced, signal is no longer generated from it. This system is in many ways analogous to the dihydroresorufin system discussed in Chapter 2, but opposite in the regard that the dihydroresorufin system converts a fluorophore from an off to an on state via faradaic reaction, while this system with MB converts a fluorophore from an on to an off state via faradaic reaction.

5.3.2 Coupled Electrochemical and Fluorescence Properties of MB-PS Microspheres

After successfully demonstrating the ability to monitor the redox state of free MB using fluorescence microscopy, we sought to measure the electrochemical and fluorescence properties of the MB-modified PS microspheres. Successful modification of the PS microspheres is easily visible to the naked eye, as can be seen in Figure 5.4. Figure 5.4a-b shows unmodified PS microspheres (5.4a) and MB-modified PS microspheres (5.4b) after centrifuging a prepared solution of each. The precipitate from the unmodified microspheres is white, while the precipitate from the MB-modified microspheres is a distinct blue, indicating successful adsorption of MB onto the microspheres. This color change can also easily be seen in the dried form of the microspheres. Figure 5.4c-d shows a photograph of the unmodified (5.4c) and MB-modified (5.4d) PS microspheres after 150 µL of dispersed solution of each was dropped and

dried onto a glass coverslip. Once again, the unmodified microspheres are white, while the MB-modified microspheres exhibit the characteristic color of methylene blue. Previous studies indicate that the cationic methylene blue adsorbs onto the surface of the PS microspheres, which contain a net anionic charge, via electrostatic attraction.[17,28,29,30] This explanation is supported by our unsuccessful attempt to modify the microspheres with an anionic redox-active fluorophore, resorufin. We repeated the MB modification procedure, substituting resorufin for MB, and found that after washing, the microspheres remained white, indicating no adsorption of resorufin onto the PS microsphere surfaces.

We used fluorescence imaging of the microspheres to show that MB-modification imparts fluorescence to the modified PS microspheres. Figure 5.5 shows images from a simple fluorescence microscopy experiment. Figure 5.5a shows brightfield and fluorescence images of dispersed solutions of unmodified and MB-modified PS microspheres on a glass coverslip. The brightfield images clearly show single microspheres and clusters of microspheres resting on the coverslip. When switched over to fluorescence mode, the unmodified microspheres are no longer visible, indicating no fluorescence. However, the MB-modified microspheres are clearly visible, indicating that MB-modification imparts fluorescence to the microspheres. There is also a noticeable fluorescence background in the image, which is likely due to residual MB in solution that was either not successfully removed during the washing cycles or desorbed from the microsphere surfaces over time. Figure 5.5b shows brightfield and fluorescence images of dispersed solutions of unmodified and MB-modified PS microspheres dried onto a glass coverslip before imaging. Again, the brightfield images clearly show single microspheres and clusters of microspheres for both unmodified and modified PS, but only the modified microspheres are clearly visible in the fluorescence images. As opposed to the fluorescence

image of the modified microspheres in solution, single microspheres are easily discernible in the fluorescence image of the dried particles, which is likely due to the higher signal to noise ratio in the dried particle image caused by not having a background of residual MB in solution. Overall, it is clear that MB imparts fluorescence behavior to the PS microspheres.

We were then interested to see if the MB-modified microspheres displayed electrochemical activity. Specifically, we wanted to know if the fluorescence state of a microsphere could be switched via redox reaction in an analogous way to switching the fluorescence state of an individual MB molecule by reversible reduction to LMB. To test this idea, we devised a fluorescence imaging experiment similar to that in Figure 5.5, except we replaced the glass coverslip with an ITO-coated glass coverslip. The ITO-coated coverslip served as a transparent working electrode, enabling us to image the PS microspheres while applying potentials to drive faradaic reactions. Figure 5.6 shows the results of an experiment of this type. A solution of dispersed MB-modified microspheres was dropped onto an ITO-coated glass coverslip that was positioned on a microscope for fluorescence imaging. The ITO coverslip served as a working electrode, and the potential of it was switched between 0 and -1 V vs. a Ag/AgCl reference electrode. Fluorescence imaging of the ITO coverslip was carried out simultaneously with this potential switching.

Figure 5.6a is a brightfield image of the area of the ITO coverslip that was imaged in this experiment. As can be seen, there are several microspheres and clusters of microspheres on the ITO surface. Figures 5.6b-5.6e are fluorescence images of this same area at various times during the experiment as indicated by the arrows on Figure 5.6f. Figures 5.6b and 5.6d are images taken when the potential of the ITO is at -1 V, and Figure 5.6c and 5.6e are images taken when the potential of the ITO is at 0 V. It is clear that at 0 V, there is a fluorescence signal and

individual/clusters of microspheres can be easily seen, while at -1 V, the fluorescence signal significantly diminishes and the microspheres can no longer be seen. This behavior matches the expected behavior for MB, which should remain in its oxidized, fluorescent form at 0 V and be reduced to the non-fluorescent LMB at -1 V. This behavior indicates that the MB molecules adsorbed onto the PS surface retain their electrochemical activity and can be reversibly switched on and off through the reversible electrochemical reduction of MB to LMB. This is a very interesting behavior, as the modification in a sense turns the PS microsphere into a large MB "molecule." That is, it appears that the modified PS microspheres retain the same coupled and reversible electrochemical and fluorescence behavior that is expected for individual MB molecules.

Figure 5.6f is a plot of the background-corrected fluorescence intensity-time traces over the duration of the experiment for the four individual/clusters of microspheres indicated in Figures 5.6a-5.6e. 1 and 4 are larger clusters of microspheres, while 2 is an individual microsphere and 3 is a cluster of two microspheres. One can see that the signal for all four areas is highly reversible, which can be explained by the reversibility of the MB reduction reaction. One can also see that the fluorescence intensity of areas 1 and 4 is much greater, owing to those areas being large clusters of modified microspheres. Additionally, the intensity of area 3 is roughly twice that of area 2, which is expected as area 3 is a cluster of two microspheres while area 2 is a single microsphere. Of interest is the observation that at -1 V, the fluorescence intensity drops to about 20% or less of the intensity at 0 V for all four areas. For area 2, the single microsphere, the intensity drops to less than 5%. This suggests that the majority of the MB molecules adsorbed onto the PS microspheres are available for electrochemical reduction. As the microsphere diameter is much greater than the distance a MB molecule needs to be from the

electrode to undergo electron transfer (~1 nm), this suggests a self-exchange type mechanism may be responsible for the reduction of adsorbed MB molecules held away from the ITO surface. The dynamics of the on-off fluorescence behavior of the microspheres and the relationship of that behavior to individual microsphere size and microsphere cluster size, as well as electrode potential, should be the subject of further study. Nevertheless, this experiment makes it clear that the MB-modified PS microspheres exhibit reversible, potential-controlled, on-off fluorescence behavior.

5.3.3 Optical and Electrochemical Detection of Single MB-PS Microsphere Collisions

We decided to use a single-particle collision type experiment to further study the MB-modified microspheres. These experiments have recently garnered much interest in the field of electrochemistry, being used to electrochemically detect single nanoparticles in solution and elucidate various properties of the particles. Of particular interest to us was the use of this method to quantify the number of electrochemically-active MB molecules on a PS microsphere. In our experiment, a 25 μm diameter Au microelectrode was placed in a diluted solution of dispersed MB-modified PS microspheres. The microspheres will randomly diffuse in the solution and occasionally collide with the Au electrode surface. If the electrode is poised at a potential sufficient to reduce MB, any electrochemically-active MB molecules adsorbed onto the PS microsphere surface will be reduced to LMB, resulting in a current spike. By Faraday's Law, the charge passed during this current spike can be converted to the number of methylene blue molecules reacted, giving us a quantitation of the number of electrochemically-active MB molecules on the microsphere. Additionally, due to the fluorescence properties of MB and LMB, the microsphere should switch from an on fluorescence state to an off fluorescence state. A small electrode must be used in order to reduce the noise associated with current monitoring, as

collision experiments of this type typically give currents on the order of 10 or 100 pA. This precludes the use of the ITO-coated coverslip electrode used in the experiment shown in Figure 5.6 unless fabrication methods are used to significantly reduce the electrode surface area.

Figure 5.7 shows the results of a collision experiment in which the electrode surface was monitored via fluorescence microscopy. A 25 μm diameter Au working electrode was placed in a dilute solution of dispersed MB-modified PS microspheres that was dropped onto a glass coverslip. This electrode and coverslip were set up on a microscope to enable fluorescence imaging. The potential of the Au electrode was switched between 0 and -1 V to control the redox state of the MB-modified microspheres. Figures 5.7a-5.7f are fluorescence images at various points during the experiment as noted in Figure 5.7g. As can be seen in Figure 5.7a several spots of high fluorescence intensity are visible on the electrode, which indicates that individual/clusters of microspheres already collided and attached to the electrode while the electrode was being aligned for imaging. Figures 5.7b-5.7d show a small cluster of microspheres diffusing near the electrode surface and then colliding and sticking to it. After this collision, the potential of the electrode is switched to -1 V to reduce MB to LMB. As can be seen in Figure 5.7e, this causes the fluorescence intensity to significantly diminish, indicating successful reduction of MB. The potential is then switched back to 0 V to oxidize LMB back to MB. This restores the fluorescence signal, as can be seen in Figure 5.7f.

Figure 5.7g shows the background-corrected fluorescence intensity-time trace over the duration of the experiment for the 20x20 pixel area outlined by the green box in Figure 5.7a. This is the area of the electrode onto which the microsphere cluster collides and sticks. As can be seen, the intensity sharply increases when the fluorescent microsphere cluster collides with the electrode and then is reversibly switched between an on and off state by switching the electrode

potential between 0 and -1 V, respectively. Again, this shows that the MB-modified microspheres exhibit potential-controlled, on-off fluorescence behavior. As in the experiment in Figure 5.6, the dynamics of this switching should be the subject of future investigation. A negative aspect of this type of observation is that it is doesn't allow for brightfield imaging of the particles on the electrode due to the geometry of the experimental setup. This makes it difficult to discern whether colliding microspheres are individual microspheres or clusters, and if clusters, how many microspheres are in a cluster. In future experiments, a transparent working electrode, such as the one used in the experiment shown in Figure 5.6, fabricated to have a small surface area would be ideal for imaging microsphere collisions.

Figure 5.8 shows the results of a collision experiment where the current of the Au working electrode was monitored over time. In this experiment, the electrode was placed in either a dilute solution of dispersed, unmodified PS microspheres (Figure 5.8a) or a dilute solution of dispersed, MB-modified PS microspheres (Figure 5.8b). The potential of the electrode was initially held at -0.6 V (a potential sufficient to reduce MB) for 1200 s, then switched and held at 0 V (a potential insufficient to reduce MB) for about 1000 s, then finally switched back to -0.6 V for the remainder of the experiment. As seen in Figure 5.8a, the unmodified PS microspheres show no currents above the baseline for the duration of the experiment. For the MB-modified PS microspheres (Figure 5.8b), however, reductive spikes in the current with typical amplitudes on the order of 10 pA can be observed when the electrode potential is held at -0.6 V. When the potential is held at 0 V, no current spikes are observed. We believe this spike behavior is likely due to the electrochemical reduction of surface-adsorbed MB when the microspheres collide with the electrode, with each current spike representing one microsphere or cluster of microspheres colliding with the electrode and being reduced. This idea

is further supported by the experiment shown in Figure 5.9, which shows current-time traces for an electrode in a dilute solution of dispersed MB-modified PS microspheres held at different potentials. There are no reductive spikes in current at -0.1 V and only a small number of low-amplitude spikes at -0.2 V. However, when the electrode reaches -0.3 V, the frequency and amplitude of the spikes increases dramatically. This potential matches very well with the onset potential for MB reduction we measured in the experiment in Figure 5.3, indicating that the spikes in current are indeed due to the reduction of MB adsorbed on the modified particles.

Assuming this is true, one can use Faraday's Law, $Q = nFN$, to calculate the number of MB molecules reduced in each collision event. Q is the total charge, n is the number of electrons transferred per reaction, F is the Faraday constant, and N is the moles of reactant consumed. This is done by integrating the area under each spike in the current-time trace, which gives the total charge passed in the event, Q. Using $n = 2$ (the reduction of MB is a two-electron process) one can then calculate the number of MB molecules needed to pass Q charge. We did this for a collision detection experiment of MB-modified PS microspheres where the Au working electrode was held at -0.4 V for the duration of the detection. We integrated the area under each reductive spike in the current-time trace and converted each area to a number of MB molecules using Faraday's Law. This resulted in a distribution of MB molecules detected per event, which is plotted as a histogram in Figure 5.10. A Gaussian fit to this histogram gives an average number of MB molecules detected per event of 6.4×10^5. If our assumption that the reductive spikes in current are solely due to the reduction of MB adsorbed onto the modified microsphere surface is true, this value is the average number of electrochemically-active MB molecules per microsphere. Future experiments should combine simultaneous fluorescence and electrochemical detection of single modified microsphere collisions. This would show very strong evidence that

the reductive spikes in the current-time traces are indeed due to the reduction of the surface-adsorbed MB molecules, as the fluorescence signal could be directly correlated to the current signal.

5.4 Conclusion

This study demonstrated and examined the interesting coupled behavior between the electrochemical and fluorescence properties of methylene blue-modified polystyrene microspheres. We first demonstrated fluorescence monitoring of the electrochemical reduction of free methylene blue in solution, which can be reduced from the fluorescent methylene blue to the non-fluorescent leucomethylene blue. Following other studies, we made the modified microspheres through a very simple procedure in which methylene blue, a cationic dye, adsorbs to the surface of slightly anionic polystyrene microspheres via electrostatic attraction. The resulting microspheres exhibit the characteristic blue color of methylene blue and are fluorescent. These particles appear to follow the same electrochemical and fluorescence behavior as methylene blue, indicating that the adsorbed methylene blue molecules remain electrochemically active. This results in the particles possessing a very interesting, potential-controlled on-off fluorescence behavior. We were able to optically monitor single microsphere collisions using fluorescence microscopy and have experimental results indicating the successful electrochemical detection of single microsphere collisions, which can be used as a way to quantify the number of electrochemically-active methylene blue molecules per microsphere.

5.5 Figures

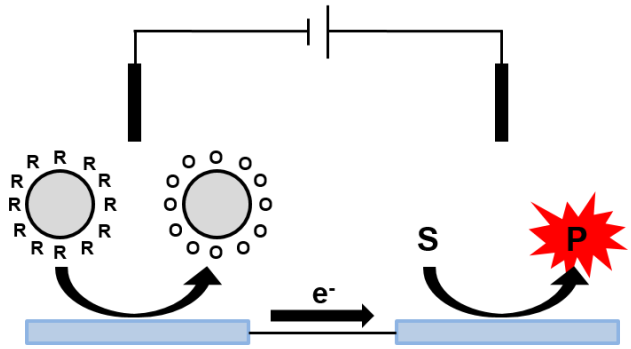

Figure 5.1. Proposed scheme for quantitatively studying the detection limit of FEEM. In this scheme, two electrodes are connected to form a bipolar electrode. One electrode is placed in a solution of redox-modified particles, while the other is placed in a solution of fluorogenic indicator (in this example, resazurin (**S**)). A potential is applied across the two solutions so that when a particle stochastically collides with the electrode, the redox moieties undergo faradaic reaction, injecting (or withdrawing) a discrete number of electrons. These electrons are coupled to the faradaic reaction of the fluorogenic indicator at the other pole of the electrode, resulting in a burst of fluorescence (in this example, creation of resorufin (**P**)). Systematically changing the redox loading of the particles will change the number of electrons passing through the electrode, thus giving a quantitative method to study how the fluorescence signal changes with the number of electrons. Additionally, the redox-modified particles could be labeled with a fluorophore, enabling the observation of particle collision events.

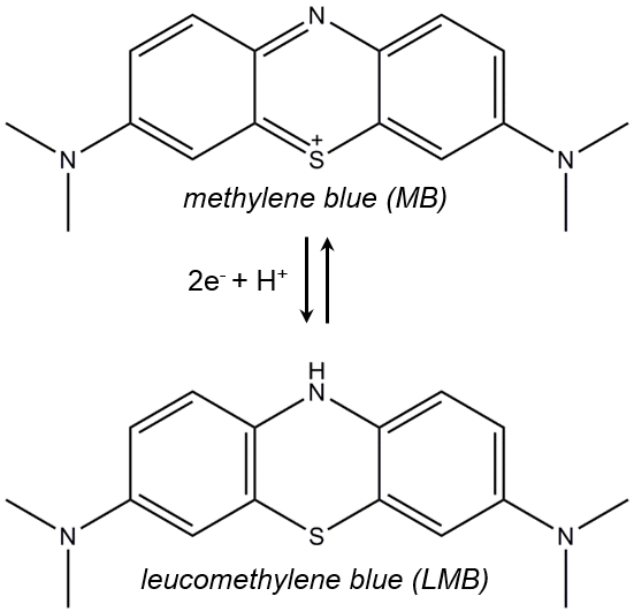

Figure 5.2. Reaction scheme of the reversible reduction of methylene blue.
The reversible, two-electron electrochemical reduction of methylene blue (MB) to leucomethylene blue (LMB).

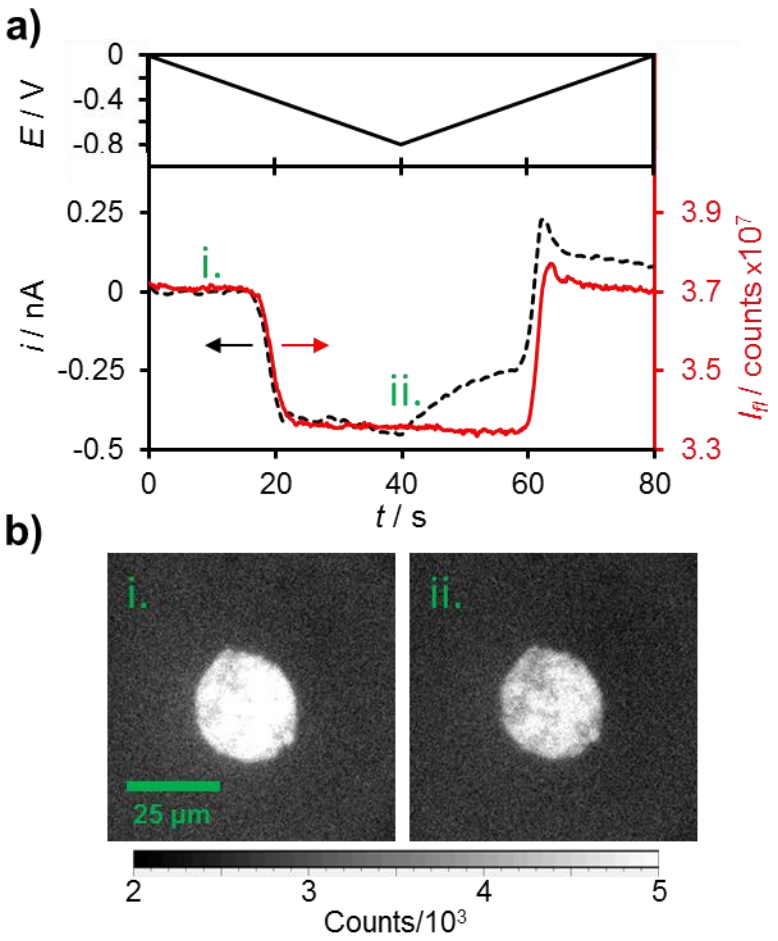

Figure 5.3. Current and fluorescence signal of methylene blue during a CV experiment. Results of a potential sweep experiment in which a 25 µm diameter Au electrode was placed in 100 µM MB solution and the potential swept from 0 to -0.8 V at 20 mV/s. **(a)** The potential waveform and the simultaneously-measured current (dashed black trace) and fluorescence intensity (solid red trace). The traces are the average of 3 trials. **(b)** Fluorescence images of the electrode at -0.2 V during the forward scan and at -0.8 V.

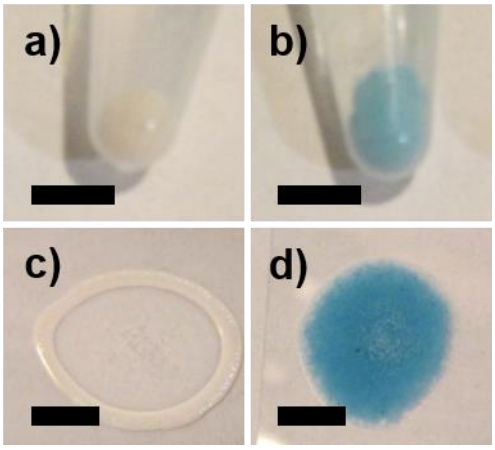

Figure 5.4. Photos of unmodified and methylene blue-modified polystyrene microspheres. Photos of unmodified **(a)** and **(c)** and methylene blue-modified **(b)** and **(d)** polystyrene microspheres. (a) and (b) are photos of the precipitate in a microcentrifuge tube following centrifugation of a dispersed solution of each type of particle. (c) and (d) are photos of a dispersed solution of each type of particle dropped onto a glass slide and dried. The scale bar in each photo is 5 mm.

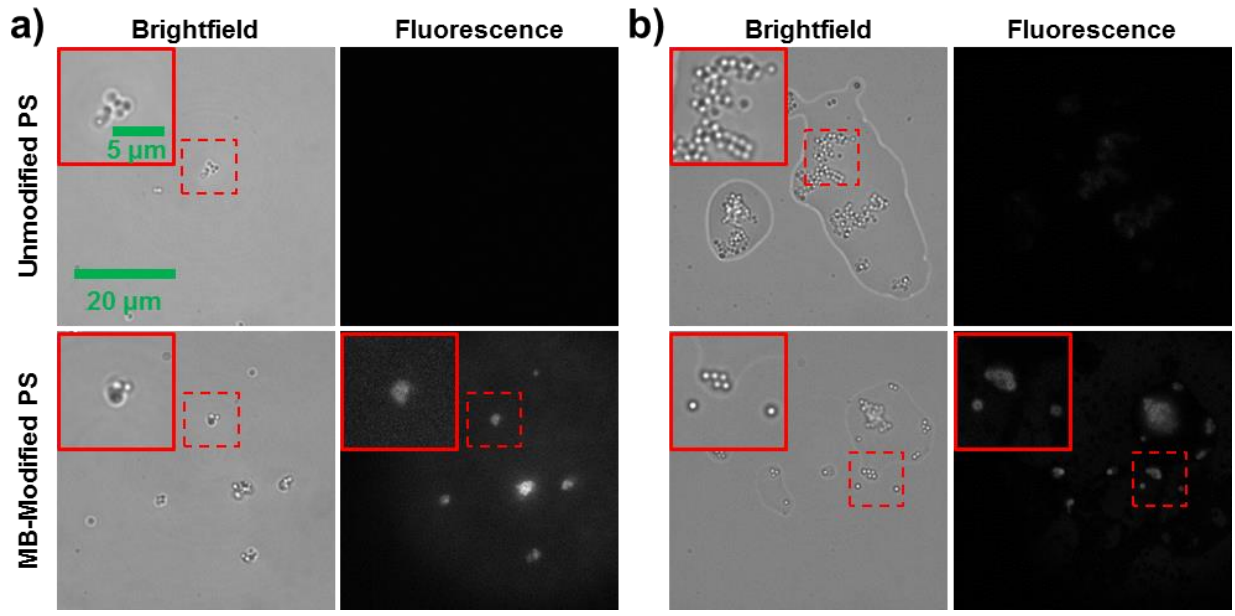

Figure 5.5. Micrographs of unmodified and MB-modified PS microspheres.
Brightfield and fluorescence images of unmodified and MB-modified PS microspheres. The fluorescence images are of the same area as the corresponding brightfield images. The insets outlined in the solid red lines are zoom-in views of the 100x100 pixel areas indicated by the dashed red lines. In **(a)** solutions of dispersed microspheres were dropped onto glass coverslips and imaged, whereas in **(b)** solutions of dispersed microspheres were dropped onto glass coverslips and dried before imaging. The scale for the fluorescence images in (a) is 0-5000 counts, while the scale for the fluorescence images in (b) is 0-9000 counts.

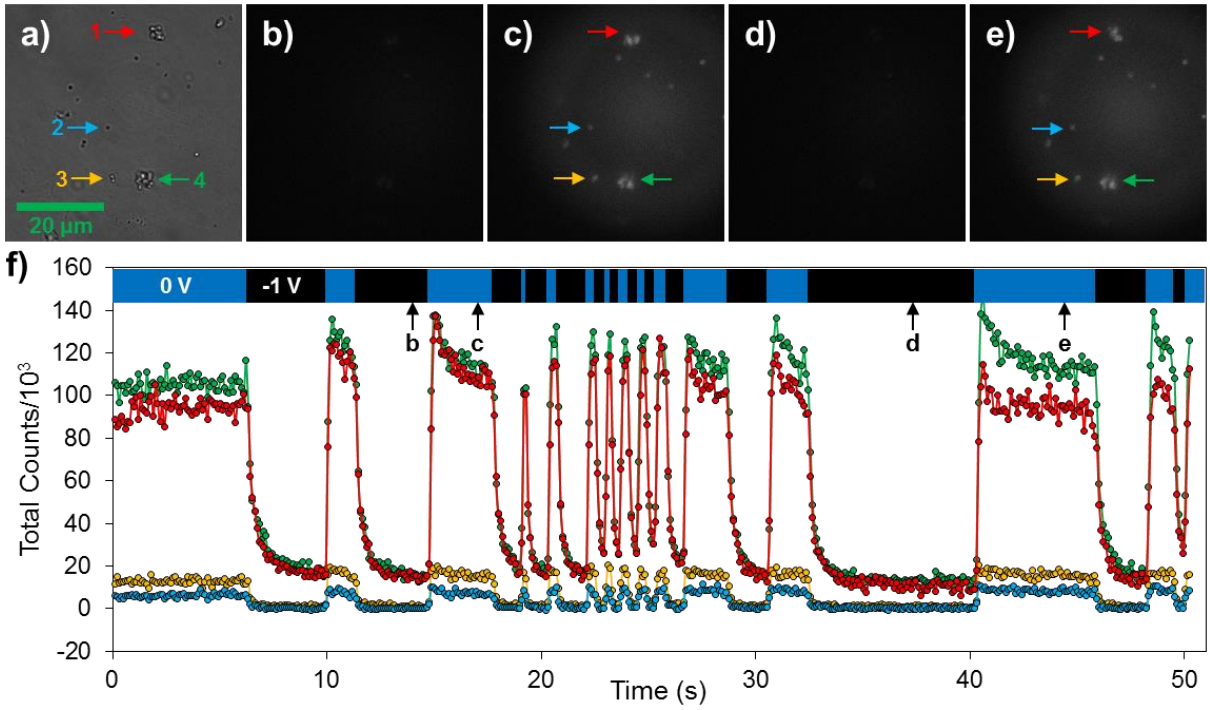

Figure 5.6. Fluorescence of MB-modified PS microspheres during potential switching. Imaging results from a potential switching experiment in which a solution of dispersed MB-modified PS microspheres was dropped onto an ITO-coated coverslip, which served as a transparent working electrode. The potential of the electrode was pulsed between 0 and -1 V with simultaneous fluorescence imaging. **(a)** Brightfield image of the area of the ITO coverslip under observation. **(b)-(e)** Fluorescence images of the ITO coverslip at various points (indicated in (f)) during the experiment. **(f)** Background-corrected fluorescence intensity-time traces over the duration of the experiment for the individual or clusters of microspheres indicated in (a)-(e).

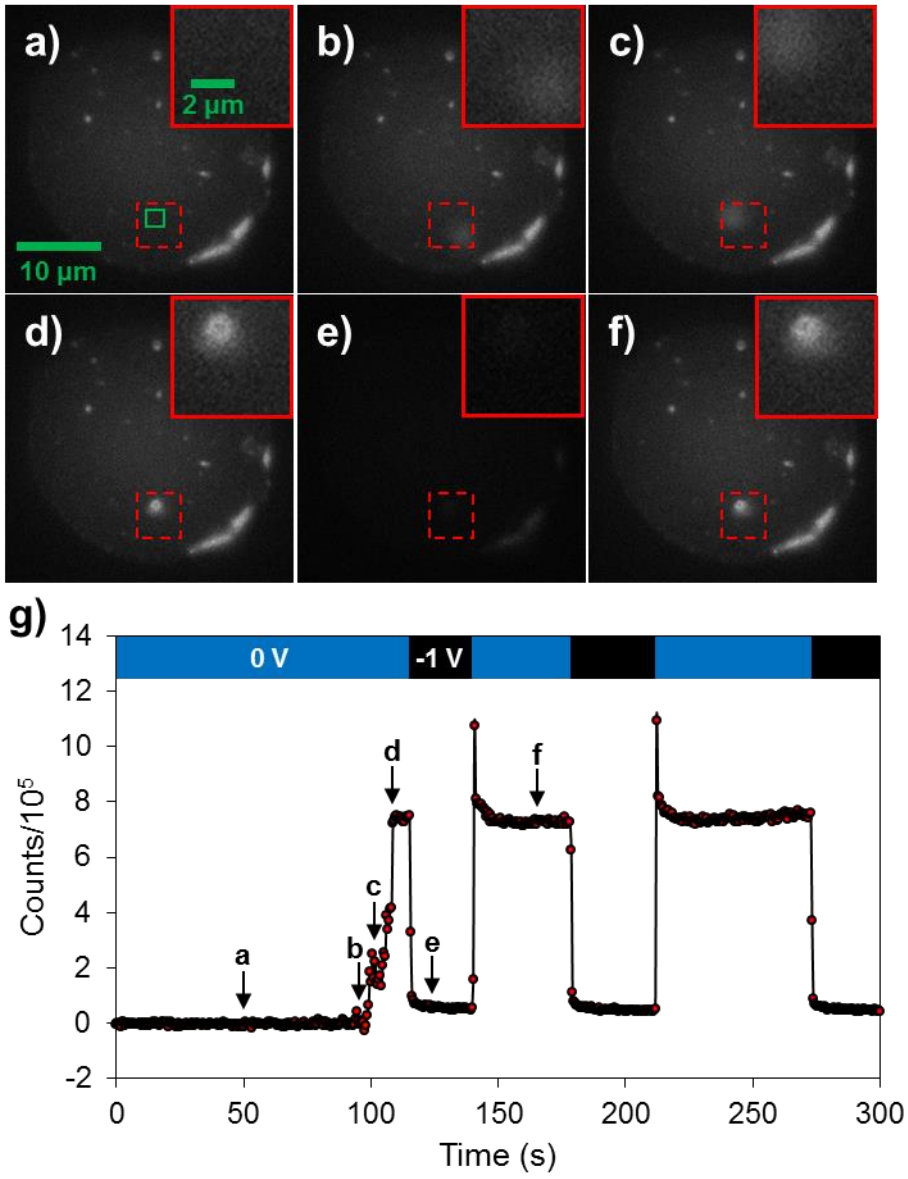

Figure 5.7. Imaging single microsphere collision and subsequent potential switching. Fluorescence imaging of a MB-modified microsphere cluster collision and subsequent potential-controlled on-off fluorescence switching of the cluster. **(a)-(f)** Fluorescence images of the 25 µm diameter electrode surface at various points during the experiment as indicated in (g). The electrode was held at a distance of 50 µm from the glass coverslip. The insets outlined in solid red lines are zoom-in views of the 48x48 pixel area indicated by the dashed red lines. **(g)** Background-corrected fluorescence intensity-time trace for the 20x20 pixel area of the electrode onto which the microsphere cluster collides and sticks. This area is indicated by the solid green box in (a).

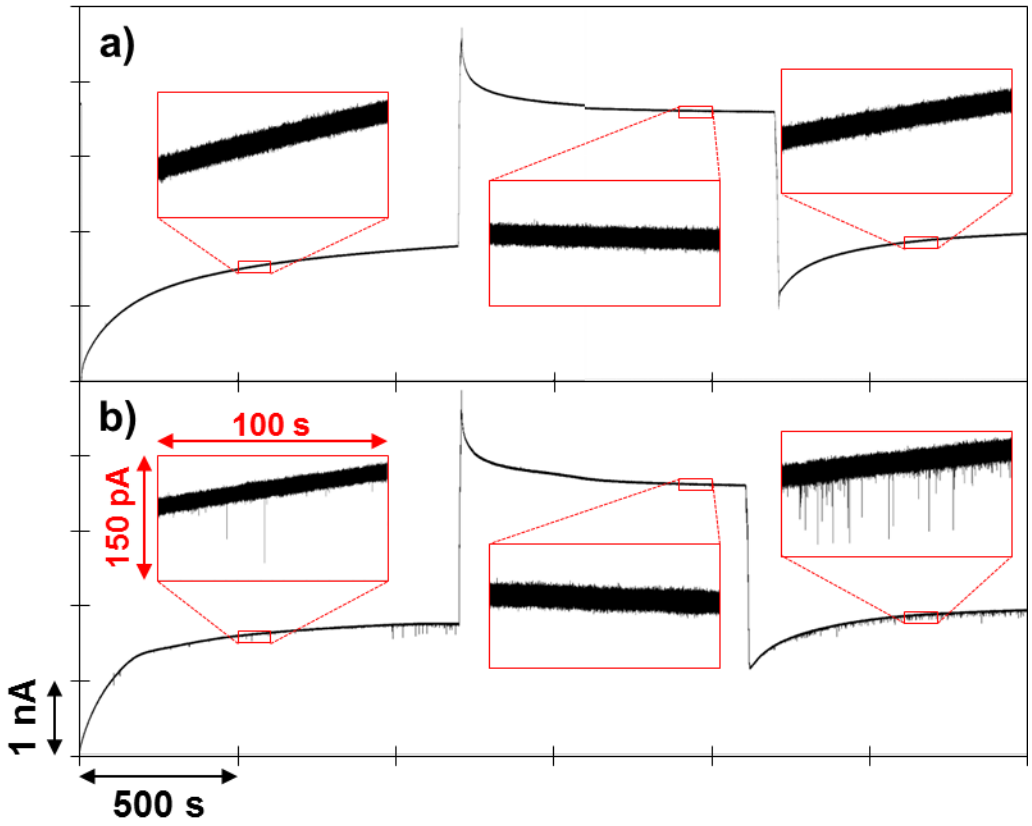

Figure 5.8. Current-time traces for unmodified and MB-modified microsphere collisions. Current-time traces for a collision experiment where a 25 µm diameter Au working electrode was placed in a dilute solution of either unmodified **(a)** or MB-modified **(b)** PS microspheres. For both experiments, the electrode was held at -0.6 V for 1200 s, then switched and held at 0 V for about 1000 s, and then switched back to -0.6 V for the remainder of the experiment. The traces outlined in red show zoom-ins of selected portions of the current-time signal. The scales of the axes of these zoom-in traces are all the same, as are the scales of the axes in (a) and (b).

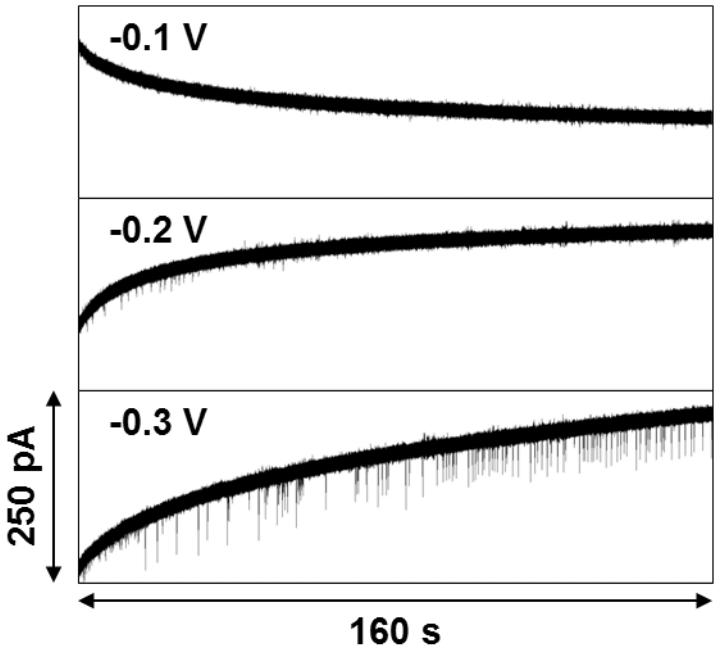

Figure 5.9. MB-modified microsphere collision detection at different potentials.
Current-time traces for a collision experiment where a 25 μm diameter Au working electrode was placed in a dilute solution of MB-modified PS microspheres. The potential of the electrode was changed between -0.1, -0.2, and -0.3 V.

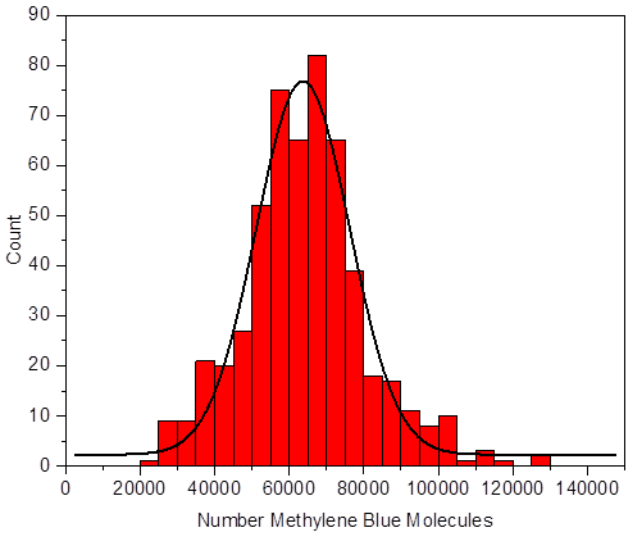

Figure 5.10. Calculated number of MB molecules detected per collision event.
Histogram of detection events for a collision experiment where a 25 µm Au working electrode was placed in a dilute solution of MB-modified PS microspheres and held at -0.4 V. The area under each spike in the current-time trace was integrated and this value was converted to the number of methylene blue molecules using Faraday's Law. The black line is a Gaussian fit to the histogram.

5.6 References

(1) Han, L.; Chen, J.; Ikeda, I. *Chem. Lett.* **2005**, *34*, 1512-1513.

(2) Budny, A.; Novak, F.; Plumeré, N.; Schetter, B.; Speiser, B.; Straub, D.; Mayer, H.A.; Reginek, M. *Langmuir* **2006**, *22*, 10605-10611.

(3) Wolfe, R.L.; Balasubramanian, R.; Tracy, J.B.; Murray, R.W. *Langmuir* **2007**, *23*, 2247-2254.

(4) Han, L.; Chen, J.; Aoki, K. *J. Electroanal. Chem.* **2007**, *602*, 123-130.

(5) Beasley, C.A.; Murray, R.W. *Langmuir* **2009**, *25*, 10370-10375.

(6) Xiao, X.; Bard, A.J. *J. Am. Chem. Soc.* **2007**, *129*, 9610-9612.

(7) Cheng, W.; Compton, R.G. *TRAC-Trend. Anal. Chem.* **2014**, *58*, 79-89.

(8) Guerrette, J. P.; Percival, S. P.; Zhang, B. *J. Am. Chem. Soc.* **2013**, *135*, 855–861.

(9) Oja, S.M.; Guerrette, J.P.; David, M.R.; Zhang, B. *Anal. Chem.* **2014**, *86*, 6040-6048.

(10) Oja, S.M.; Zhang, B. *Anal. Chem.* **2014**, *86*, 12299-12307.

(11) Wang, J.; Trouillon, R.; Lin, Y.; Svensson, M.; Ewing, A.G. *Anal. Chem.* **2013**, *85*, 5600-5608.

(12) Twigg, R.S. *Nature* **1945**, *155*, 401-402.

(13) Lee, S.-K.; Mills, A. *J. Fluoresc.* **2003**, *13*, 375-377.

(14) Caruso, F. *Adv. Mater.* **2001**, *13*, 11-22.

(15) *Working with Microspheres*, Tech Note 201; Bangs Laboratories, Inc.: Fisher, IN; **2002**.

(16) Miao, W.; Bard, A.J. *Anal. Chem.* **2004**, *76*, 5379-5386.

(17) Braga, M.; Leite, C.A.P.; Galembeck, F. *Langmuir* **2003**, *19*, 7580-7586.

(18) Kim, B.-K.; Boika, A.; Kim, J.; Dick, J.E.; Bard, A.J. *J. Am. Chem. Soc.* **2014**, *136*, 4849-4852.

(19) Kim, B.-K.; Kim, J.; Bard, A.J. *J. Am. Chem. Soc.* **2015**, *137*, 2343-2349.

(20) Li, Y.; Deng, H.; Dick, J.E.; Bard, A.J. *Anal. Chem.* **2015**, *87*, 11013-11021.

(21) Dick, J.E.; Renault, C.; Kim, B.-K.; Bard, A.J. *Angew. Chem., Int. Ed.* **2014**, *53*, 11859-11862.

(22) Fosdick, S.E.; Anderson, M.J.; Nettleton, E.G.; Crooks, R.M. *J. Am. Chem. Soc.* **2013**, *135*, 5994-5997.

(23) Campbell, J. A. *J. Chem. Ed.* **1963**, *40*, 578–583.

(24) Anderson, L.; Wittkopp, S.M.; Painter, C.J.; Liegel, J.J.; Schreiner, R.; Bell, J.A.; Shakhashiri, B.Z. *J. Chem. Ed.* **2012**, *89*, 1425-1431.

(25) Leaist, D.G. *Can. J. Chem.* **1988**, *66*, 2452-2457.

(26) The steady-state current for a given analyte concentration can be easily calculated for a known electrode geometry. See: A.J. Bard, L.R. Faulkner in Electrochemical Methods, 2nd ed., John Wiley & Sons, New York, 2001, Chapter 5. For the inlaid-disk microelectrodes used in this report, the steady-state current, i_{ss}, will be given by the equation: $i_{ss} = 4nFC^*Dr$, where n is the number of electrons transferred per analyte molecule reacted, F is the Faraday constant, C^* is the bulk concentration of the analyte, D is the diffusion coefficient of the analyte, and r is the radius of the electrode.

(27) Komura, T.; Niu, G.Y.; Yamaguchi, T.; Asano, M.; Matsuda, A. *Electroanal.* **2004**, *16*, 1791-1800.

(28) Méallet-Renault, R.; Denjean, P.; Pansu, R.B. *Sensor. Actuat. B-Chem.* **1999**, *59*, 108-112.

(29) Eckenrode, H.M.; Jen, S.-H.; Han, J.; Yeh, A.-G.; Dai, H.-L. *J. Phys. Chem. B* **2005**, *109*, 4646-4653.

(30) Mubarekyan, E.; Santore, M. *Langmuir* **1998**, *14*, 1597-1603.

CHAPTER 6

Single Ag Nanoparticle Detection via Stochastic Collisions:

Use in Quantifying FEEM Detection Limit and the Observation of Multipeak Behavior

6.1 Introduction

Stochastic single-nanoparticle (NP) collision amperometry is a method used to electrochemically detect single NPs that was first introduced by the Bard group.[1] The literature published on this method has grown significantly since the initial report, as it has been applied in various schemes to detect a multitude of different types of NPs.[2,3,4] In the original scheme, an electrocatalytic amplification method is used where a particle is detected by catalyzing an electrochemical reaction of a solution-based species upon collision with a UME, resulting in a sharp change in current.[1] This has proven a useful method, enabling the measurement of important parameters such as size[5] and eletrocatalytic activity[6] on a single-NP level.

The Compton group adapted this idea to the detection of NPs via the direct faradaic reaction of the NPs themselves in a method they call anodic particle coulometry. In their initial report, the group reported the detection of single Ag NPs using a glassy carbon UME.[7] When the UME was held at oxidizing potentials, oxidative spikes in the current signal were observed that were credited to the direct electro-oxidation of colliding Ag NPs. Additionally, the charge associated with each collision event was found to be in agreement with the charge expected based on the NP size, indicating complete oxidation of the NPs. This method was extended to the detection of Au and Ni NPs as well.[8,9]

We became interesting in using single Ag NP collisions as a way to quantify the detection limit of FEEM in regard to the detection of small, discrete redox events. Detecting these types of events is of interest to us for two main reasons. First, we are interested in using FEEM to image the synaptic transmission of electroactive neurotransmitters such as dopamine from neuronal cells. The model neuronal cells that would be used for this type of study secrete ~10^5 dopamine molecules per quantal release, which can be electrochemically detected over a time period of several milliseconds.[10] This means that our system must have the capability to detect a discrete redox event that injects ~10^5 electrons into a bipolar electrode over a period of a few milliseconds. The second reason we are interested in these types of events is the exciting possibility of using FEEM for detecting single electron transfer events, which are by definition discrete. Detecting larger discrete redox events is the natural starting point for probing the possibility of single-molecule electrochemistry using FEEM.

In order to systematically study the detection performance of FEEM for these types of redox events, a method of reproducibly delivering small quantities of electrons to the bipolar electrode in discrete events is needed. This was the initial motivation behind developing the methylene blue-modified polystyrene microspheres discussed in Chapter 5. We believe that we can use Ag NPs as an even simpler method of achieving this goal. Our idea is outlined schematically in Figure 6.1. In this scheme, the anodic pole of a bipolar electrode is placed in a dilute solution of Ag NPs, and the cathodic pole is placed in a solution of the non-fluorescent resazurin, which can be reduced to the fluorescent resorufin. The cathodic pole is positioned on a microscope so it can be imaged via fluorescence microscopy. A potential is applied across the bipolar electrode that is sufficient to drive the coupled reactions of Ag oxidation at the anodic pole and resazurin reduction at the cathodic pole. Typically, there will be nothing to oxidize at

the anodic pole, so the current through the bipolar electrode and the fluorescence at the cathodic pole will remain at baseline. However, Ag NPs will randomly diffuse to the anodic pole and be oxidized. This will result in the periodic injection of electrons into the bipolar electrode, which can be observed as an oxidative spike in the current through the bipolar electrode. If these electrons couple to resazurin reduction, each Ag NP collision event will result in a burst of fluorescence at the cathodic pole. The area of each spike on the current-time trace can be integrated to yield the total number of electrons injected into the bipolar electrode. This enables a way to directly correlate the fluorescence signal with the number of electrons injected into the system. Additionally, the size of the Ag NPs can be changed to alter the number of electrons injected, giving a way to easily quantify and test detection performance. Since the delivery of Ag NPs to the anodic pole is very repeatable, this method offers an excellent way to idealize the conditions of the cathodic pole while ensuring that the anodic pole remains constant.

In this chapter, we first demonstrate the bipolar coupling of the oxidation of bulk Ag to the reduction of resazurin. We show that the current through the bipolar electrode can be correlated to the fluorescence detected at the cathodic pole and that a detection signal is only present when Ag is present at the anodic pole. We then demonstrate the successful detection of single Ag NP collisions on a bipolar electrode via current monitoring. However, we show that a fluorescence signal is not present at the cathodic pole during these collisions. We find that Ag NP detection is possible without any resazurin present at the cathodic pole, indicating that the electrons from Ag NP oxidation are instead coupled to some non-fluorogenic scavenger reaction(s) at the cathodic pole. This study highlights the utility of using this Ag NP detection method to test the detection performance of FEEM. This chapter also discusses a unique behavior observed in the current-time traces of single Ag NP oxidation events. We find that each

oxidation event occurs in a series of small, discrete events spaced apart by ~1 ms rather than one large event as previously assumed. We discuss the preliminary details of this previously unobserved "multipeak" behavior, which indicates interesting dynamic interactions occurring between these single metal NPs and an electrode surface. This highlights the type of information that can only be gained by studying NPs on a single-particle basis.

6.2 Experimental Section

6.2.1 Chemicals and Nanoparticle Detection Solution

Silver nitrate, trisodium citrate, citric acid, and potassium nitrate were all used as received. Deionized water (>18 MΩ·cm) was obtained through a Barnstead Nanopure water purification system and used for all aqueous solutions. The Ag NPs were made in house via a citrate reduction method described in the following section. The typical NP detection solution was prepared by combining the stock NP solution, 100 mM KNO_3, and 10 mM trisodium citrate in a 1:1:3 ratio by volume. This results in a solution of about 30 pM Ag NPs, 20 mM KNO_3, and 8 mM trisodium citrate. This solution has a pH of 7.7 and was found to give stable NP detection over a period of tens of minutes.

Ag NP detection at different concentrations of KNO_3 was carried out as follows. We started with a solution of 4:1 by volume 10 mM trisodium citrate:Ag NP solution. Since the Ag NP solution also contained 10 mM trisodium citrate, this gave an initial concentration of 10 mM trisodium citrate. Particle detection was carried for about 10 min at a detection potential of 0.6 V vs. Ag/AgCl using this solution. The KNO_3 concentration was then increased by adding an aliquot of solution that was 100 mM KNO_3 and 10 mM trisodium citrate, along with an appropriate aliquot of Ag NP solution to ensure that both the trisodium citrate concentration and

Ag NP concentration remained constant. Particle detection was then carried out using this new solution for about 10 min. Sequential increases in KNO_3 concentration were continued in this fashion. Ag NP detection at different concentrations of trisodium citrate was carried out in the same manner as the KNO_3 concentration experiment, adding aliquots of 100 mM trisodium citrate instead of KNO_3.

Ag NP detection at different pH values (Figure 6.12) was carried out as follows. The pH 7.7 detection solution was the normal detection solution used: a 1:1:3 by volume solution of Ag NP solution, 100 mM KNO_3, and 10 mM trisodium citrate. As opposed to the KNO_3 and trisodium citrate concentration adjustment experiments, a completely new detection solution was made for each pH value tested. To adjust the pH to 10.1, a small amount of 1 M KOH solution was added to the normal detection solution. The pH 5.5 solution was 1:1:1:2 by volume of Ag NP solution, 100 mM KNO_3, 10 mM citric acid, and 10 mM trisodium citrate. The pH 4.4 solution was 1:1:2:1 by volume of the same components. A pH 3.4 solution was also tested, which was 1:1:3 by volume of Ag NP solution, 100 mM KNO_3, and 10 mM citric acid, however no NP oxidation events were detected. For all detection solutions, the detection electrode was held at 0.6 V vs. Ag/AgCl for about 10 min.

6.2.2 Preparation of Ag Nanoparticles

Ag NPs were synthesized using citrate reduction. All glassware used in the synthesis was cleaned with Aqua Regia prior to use. 100 mL of 1 mM $AgNO_3$ was brought to a boil. While stirring, 2 mL of 1% (wt.) trisodium citrate was added. The reaction solution first turned yellow and then grey-orange after a few minutes. This solution was stirred and refluxed for 1 h, after which point it was cooled to room temperature. The solution was then centrifuged at 8,000 RPM for 20 min, and the resulting supernatant was removed. The precipitate was redispersed in 100

mL of fresh 10 mM trisodium citrate and sonicated for 5 min. This centrifugation cycle was repeated once, and the precipitate was again dispersed in 100 mL of 10 mM trisodium citrate. This solution was used as the stock NP solution for all experiments. The resulting Ag NPs were imaged and sized using TEM (Figure 6.2). For TEM imaging, the NPs were dropcast onto a carbon-coated Formvar copper TEM grid (Ted Pella) and imaged with an FEI Technai G2 F20 Supertwin TEM operating at 200 kV. NP sizes were measured using ImageJ software.[11] The histogram of the NP size distribution and corresponding Gaussian fit were created using Origin software (OriginLab Corporation). The particles were approximately spherical with an average diameter of 62 ± 13 nm. Using this average diameter and the amount of Ag ions used in the synthesis, a maximum particle concentration for the stock solution of 9.1×10^{10} particles/mL (or 150 pM) can be calculated. This concentration assumes that all Ag ions were reduced into NPs and that no NPs were lost in the centrifugation steps.

6.2.3 Electrochemical Measurements

Voltammetry experiments were carried out using a Chem-Clamp potentiostat (Dagan Corporation) interfaced to a PC through a PCI-6251 data acquisition board (National Instruments) using a BNC-2090 breakout box (National Instruments). An in-house LabView 10.0 (National Instruments) program was used for voltage function generation and acquisition of the current-voltage data. This program receives an external trigger from a camera, enabling the synchronized recording of electrochemical and optical signals.

The Ag electrodeposition experiment and potential step experiments shown in Figures 6.3 and 6.4 were carried out using a Chem-Clamp potentiostat interfaced to a PC through a Digidata 1440A digitizer (Molecular Devices). A N = 0.01 headstage and 1 kHz filter were used for the FEEM detection of electrodeposited Ag. The current-time traces for these experiments were

recorded using pClamp 10.4 Axoscope software (Molecular Devices) with a 50 kHz sampling rate. The potential steps were generated with an in-house LabView program.

The single-NP amperometry experiments were carried out using an Axopatch 200B integrating patch-clamp amplifier (Molecular Devices) interfaced to a PC through a Digidata 1440A digitizer. The Axopatch was used in V-clamp mode with whole cell $\beta = 1$ and the low-pass filter set to 1 kHz. The single-NP detection experiment with potential pulsing (Figure 6.13) was carried out using a Chem-Clamp potentiostat in place of the Axopatch 200B. A N = 0.01 headstage and 1 kHz filter were used with the potentiostat. The potential pulses were generated with an in-house LabView program. Amperometric traces were recorded using pClamp 10.4 Axoscope software with a 50 kHz sampling rate. Current spikes were analyzed and integrated using pClamp 10.4 Clampfit software (Molecular Devices), and histograms of the events with corresponding Gaussian fits were created using Origin software.

All bipolar electrode experiments were done using two 12.7 μm diameter Au electrodes electrically connected to form a bipolar electrode. These electrodes possessed an inlaid disk geometry and were fabricated by sealing a 12.7 μm diameter Au microwire (Alfa-Aesar) in a borosilicate capillary (Sutter Instrument Co.). Electrical connection was made to the Au with tungsten wire and Ag paint (Dupont) through the back end of the capillary. The Au electrodes were cleaned via mechanical polishing before each detection experiment. A potential was applied across the bipolar electrode using two Ag/AgCl wire driving electrodes. All non-bipolar electrode experiments were done using a two-electrode setup with a 12.7 μm diameter Au working electrode and an Ag/AgCl wire counter/quasi reference electrode. For all experiments, the electrodes were setup in a home built Faraday cage. All potentials are reported vs. Ag/AgCl.

6.2.4 Optical Measurements

Fluorescence imaging was done on an Olympus IX70 inverted microscope equipped with an IX-FLA inverted reflected light fluorescence observation attachment. The excitation source consisted of a Thorlabs M530L2 Collimated LED powered by a DC2100 LED Driver run at 1500 mA. For filtering, we used a HQ535/50 excitation filter, a Q565lp dichroic mirror and a HQ610/75 emission filter. A 40X 0.75NA objective (Olympus UPlanFl) with an additional 1.5X magnification on the microsope was used. An Andor iXon+ EMCCD camera cooled to -80 °C and Andor SOLIS software was used to record and process all videos and images. Video was recorded at a frame rate of 10 Hz for all experiments using a pre-amplifier gain setting of 5.1. An EM gain of 150 was used for the imaging in the experiments shown in Figures 6.3 and 6.4. An EM gain of 200 was used for the imaging in the experiment shown in Figure 6.6.

6.3 Results and Discussion

6.3.1 Detection of Bulk Ag Oxidation with FEEM

Before attempting to detect single Ag NPs with FEEM, we first wished to detect bulk Ag to demonstrate the principle of coupling Ag oxidation to resazurin reduction on a bipolar electrode. To do this, we adopted an experimental scheme as outlined in Figure 6.3a. In this setup, two 12.7 μm diameter Au electrodes are electrically connected to form a bipolar electrode. The cathodic pole of the bipolar electrode is immersed in a solution of 5 μM resazurin and 50 mM pH 7.5 phosphate buffer and placed on a microscope for fluorescence imaging. The anodic pole of the bipolar electrode contains bulk Ag electrodeposited onto the Au surface of the electrode. The Ag electrodeposition procedure is carried out by placing the Au electrode in a solution of 15 mM $AgNO_3$ containing 100 mM KNO_3 as supporting electrolyte and biasing the electrode at -0.15 V vs. Ag/AgCl. This causes Ag^+ ions to be reduced at the Au electrode

surface, resulting in the deposition of solid Ag onto the electrode. The deposition is stopped by breaking the circuit. The amount of Ag deposited onto the electrode can conveniently be adjusted by changing the deposition parameters (Ag^+ concentration and/or deposition time). Figure 6.3b shows a current-time trace for a 5 s electrodeposition. As seen, there is a sharp jump in reductive current when the potential is stepped to -0.15 V, indicating Ag^+ reduction onto the electrode. This current increases in magnitude with time due to the surface area of the electrode growing as more Ag is deposited. When the circuit is broken after 5 s, the deposition immediately stops.

The electrodeposited Ag can be easily oxidized off the Au surface. Figure 6.3c shows a two-electrode (non-bipolar) cyclic voltammetry experiment using a Au electrode modified by a 5 s Ag electrodeposition. The Ag-coated electrode is placed in a solution of 100 mM KNO_3 and the potential is swept from -0.15 V to 0.3 V at 50 mV/s for three consecutive cycles. As seen in the first cycle (black trace), a large oxidation peak appears centered at 0.2 V, with the current returning back to baseline at higher potentials. This indicates complete oxidation of the deposited Ag back to Ag^+ ions. This is confirmed by the second (red trace) and third (blue trace) cycles, which no longer show an oxidation peak.

The Ag oxidation process can also readily be observed using FEEM. Figure 6d shows the results of a FEEM experiment coupling the oxidation of deposited Ag at the anodic pole to the reduction of resazurin at the cathodic pole. In this experiment, the anodic pole was placed in a solution of 100 mM KNO_3 and was either a bare Au electrode (control, red traces) or a Ag-coated Au electrode (black traces). A bare Au electrode was used as the cathodic pole and placed in a solution of 5 µM resazurin and 50 mM pH 7.5 phosphate buffer. A potential sweep from 0 to 1 V at 50 mV/s was applied using two Ag/AgCl driving electrodes and the current through the bipolar electrode and fluorescence from the cathodic pole were simultaneously monitored. As

seen in the control experiment, no current or fluorescence signal is observed over this potential range. This is expected, as there is no oxidation reaction occurring at the anodic pole. However, when the anodic pole contains Ag, there is a coupled increase in the current and fluorescence signals at potentials above 0.6 V. This indicates that Ag oxidation at the anodic pole is coupled to resazurin reduction at the cathodic pole, leading to a coupled current and fluorescence signal. The onset potential of the coupled signal supports this, as the onset potential for coupled bipolar reactions is expected to be roughly the difference between the two individual reactions in a traditional setup (0.15 V for Ag oxidation, Figure 6.3b; -0.4 to -0.5 V for resazurin reduction[12]).

Bulk Ag oxidation can also be detected in a FEEM setup using a potential step experiment. We desired to demonstrate the FEEM detection of Ag in this manner because a potential step is more similar in nature to how single NP experiments are performed, where the potential is held constant during detection. For this experiment, we used the same experimental setup as used for the experiment in Figure 6.3d, except a potential step was applied to the bipolar electrode rather than a potential sweep. The potential applied across the bipolar electrode was initially 0 V, which is insufficient to drive the coupled Ag oxidation and resazurin reduction reactions. After about 10 s, the potential was stepped to 0.8 V, which is sufficient to drive the coupled reactions. Figure 6.4 shows typical results from this experiment. As seen in 6.4a, the current and fluorescence signals are initially at baseline. However, upon stepping the potential to 0.8 V, both the current at fluorescence signals rapidly increase, indicating successful coupling of Ag oxidation to resazurin reduction. After about 55 s, both signals begin to drop back to the baseline, indicating that all of the Ag has been oxidized off the anodic pole. As seen, the fluorescence response is much more sluggish than the current response. This is primarily due to the irreversibility of the resazurin reduction reaction, which causes a slow buildup of

fluorophores. This effect was discussed in more detail in Chapter 2. Another interesting observation is the long overall duration (~ 45 s) of the signal. For comparison, oxidation of this amount of deposited Ag in a two-electrode setup takes less than 0.1 s. This indicates that the cathodic pole is the limiting pole, meaning that Ag oxidation is occurring at a rate limited by the rate of resazurin reduction at the cathodic pole.

A final interesting observation is the occurrence of spikes in the current after the average current drops back down to baseline. This is intriguing behavior that seems to indicate discrete "bursts" of reaction after the majority of the Ag has been oxidized away. We don't yet have a good explanation for this behavior, but it was observed in nearly all of the trials we did. Figure 6.4b shows the current and fluorescence traces of another trial of this same experiment in which the current spikes are even more pronounced. As seen, the fluorescence signal seems to correlate with the current signal for some of the bigger spike events. Figure 6.4c overlays the fluorescence signal with the unaveraged current signal. This highlights the many sharp, discrete spikes in current observed. Again, it appears that the fluorescence signal correlates with the current signal for some of the bigger spikes/clusters of spikes. These current spikes are reminiscent, though much larger, than the current spikes observed in the Ag NP collision experiments discussed in the rest of this chapter. This leads to one possible explanation for the observed current spikes, which is that the oxidation of the bulk Ag leads to the formation of some Ag particles in solution that are then detected as current spikes when they diffuse into the electrode and oxidize. Whatever the case, an important takeaway is that fluorescence can successfully detect some of the larger current spikes. This is the first evidence of FEEM detecting discrete redox events of this nature. However, as can be seen by Figure 6.4, the vast majority of current spikes are not detected by fluorescence, thus leaving much desire for improvement.

6.3.2 Attempts at Detection of Single Ag Nanoparticle Oxidation with FEEM

After successfully demonstrating the FEEM detection of bulk Ag, we moved onto attempts to detect single Ag NPs. Figure 6.5 shows a current-time trace in which single Ag NPs are detected using a 12.7 μm Au electrode in a two-electrode setup. The electrode is placed in a dilute solution of dispersed Ag NPs and held at a potential of 0.6 V throughout the experiment. Each oxidative spike in current is associated with a single Ag NP diffusing to the electrode surface and undergoing oxidation. As seen, this is a great method to repeatedly deliver quantifiable amounts of electrons to an electrode in discrete events. We noticed very interesting behavior in the current-time traces of these single oxidation events, where each NP seems to be oxidized is a series of discrete steps. We elaborate on this intriguing behavior in section 6.3.3 of this chapter and reserve this section for the discussion of experiments focused on the FEEM detection of these NPs.

For the FEEM-based detection of single Ag NPs, we used a very similar setup to that outlined in Figure 6.3a, where two 12.7 μm diameter Au working electrodes are electrically connected to form a bipolar electrode. Once again, the cathodic pole is placed in a solution of 5 μM resazurin and 50 mM pH 7.5 phosphate buffer and placed on a microscope for fluorescence imaging. The difference here is that instead of using an anodic pole that is modified with deposited Ag, the anodic pole is placed in a solution of Ag NPs. In this scheme, a discrete quantity of charge is delivered to the bipolar electrode by each Ag NP. By applying a potential across the bipolar electrode, we hoped that each time a Ag NP diffused to the surface of the anodic pole, it would be oxidized and the electrons from that oxidation would be coupled to the reduction of resazurin. Therefore, each NP impact should result in a burst of fluorescence at the cathodic pole. Figure 6.6 shows the simultaneously recorded current and fluorescence signal

from such an experiment where a potential of 0.6 V was applied across the bipolar electrode. As seen in the current signal (black trace), discrete oxidative spikes in the current are observed, indicating that Ag NPs are indeed stochastically diffusing into the electrode and being oxidized. However, the fluorescence signal (red trace) shows no spikes or correlation to the current signal. This suggests that although Ag NPs are being oxidized at the anodic pole, resazurin is either not being reduced at the cathodic pole or the amount of resazurin being reduced is not detectable with our fluorescence setup. We found this behavior (spikes in current, but no spikes in fluorescence) to occur at potentials ranging from 0.3 V up to 1 V. This supports the explanation that resazurin may not be reduced at all at the cathodic pole, as 0.3 V is well below the 0.6 V needed to couple Ag oxidation to resazurin reduction (Figure 6.3d).

A control experiment provided very strong additional evidence for this explanation. Figure 6.7 shows current-time traces for Ag NP detection experiments using a bipolar setup. For both 6.7a and 6.7b, the anodic pole was placed in a solution of Ag NPs. However, in 6.7a the cathodic pole was placed in a solution containing only 50 mM pH 7.5 phosphate buffer (i.e. no added redox species), while in 6.7b the cathodic pole was placed in a solution of 50 mM pH 7.5 phosphate buffer containing 5 μM resazurin. As seen, both traces give very similar NP detection. The fact that Ag NP detection occurs when the cathodic pole is placed in a solution containing no resazurin shows that the NP oxidation occurring at the anodic pole must be coupling to a non-fluorogenic reaction at the cathodic pole. This explains the absence of any fluorescence signal in Figure 6.6, as the electrons from Ag NP oxidation are not coupling to resazurin reduction. This begs the obvious question: Where are the electrons going?

We tested multiple cathodic solutions containing no added redox species and found that NP detection occurred uninhibited in every solution tested. These solutions included solutions of

KCl ranging from 0.01 to 1 M and solutions of KNO_3. One possible explanation is that the Ag NP oxidation is coupling to the reduction of dissolved oxygen in the cathodic solution. However, purging the cathodic solution of oxygen via Ar bubbling did not affect the detection signal. This indicates that either the low concentration of oxygen left in solution after Ar bubbling is sufficient to couple to Ag NP oxidation or that oxygen is not responsible for the coupling. Another possible explanation is that the cathodic solution gets contaminated with Ag^+ ions leached from the reference electrode, which can be reduced at the cathodic pole. However, using Pt driving electrodes in place of the usual Ag/AgCl driving electrodes did not affect detection. Another possible explanation is that protons in the cathodic solution are being reduced. This idea has yet to be tested, but testing it by using an aprotic solvent (which likely will have the dual benefit of having a lower solubility for oxygen) is the logical next step.

Thus far, the FEEM detection of Ag NP oxidation has been unsuccessful. However, using this method has made a number of very important revelations. First, it shows that as is, FEEM is not capable of detecting small, discrete redox events such as the exocytosis of electroactive neurotransmitters. This is the first evidence of this limitation. Second, it has shown that this limitation is due to oxidation reactions coupling to non-fluorogenic side reactions rather than resazurin reduction. This suggests that at the very least, the resazurin solution needs to be altered. Most importantly, this study shows the utility of using this detection scheme. Ag NP collisions represent an extremely simple way to repeatedly deliver small quantities of charge to the bipolar electrode in discrete events. Monitoring the current through the bipolar system gives proof that Ag NP oxidation is occurring. Therefore, if no fluorescence burst is detected at the cathodic pole, one knows that this is the pole limiting FEEM detection. The easy repeatability of Ag NP collision experiments makes it simple to adjust parameters on the cathodic side of the bipolar

electrode (solution conditions, fluorescence microscopy setup, electrode size/material, etc.) in an attempt to get fluorescence detection while keeping the anodic side constant. Once fluorescence detection is successful, this will be a useful scheme to further idealize the cathodic pole.

6.3.3 Observation of Multipeak Behavior during Single Ag Nanoparticle Oxidation

We now move on to a discussion of the current-time traces measured for single Ag NP oxidation events for the remainder of the chapter. All of the experiments discussed here were performed in a two-electrode setup and only involve electrochemical measurements (i.e. no FEEM). As previously mentioned, we noticed interesting behavior in the detection traces for the oxidation of single Ag NPs. Figure 6.8a shows an example amperometric trace of Ag NP detection where a 12.7 μm diameter Au detection UME is held at a potential of 0.6 V. As seen, several large oxidative spikes are present on top of a stable baseline current. The frequency of these oxidative spikes is 1.3 Hz and is in fairly good agreement with the theoretical detection frequency of 3.2 Hz, which can be calculated based on the size of the NPs (see Appendix 1).[13] We noticed that upon zooming in on the time axis of a detection event each event consists of several discrete oxidative spikes in current. Figure 6.8b shows an example of this. Multipeak behavior, where an oxidation event consists of >1 "subpeak," is observed in ~90% of detection events. This interesting behavior, which indicates that the oxidation of single Ag NPs on the Au UME typically occurs in several discrete events, has not been reported in the literature.

This behavior begs the question of why a Ag NP is typically oxidized in several small, discrete events rather than a single large one. To better understand this behavior, we analyzed the subpeaks present in Ag NP oxidation events recorded at four different detection potentials. 25 random events from each detection potential were chosen for analysis. Figure 6.9 shows examples of these events with labeled subpeaks. Figure 6.10 shows the results of the analysis for

the first six subpeaks of an event. The mean area, height, and duration of each subpeak are plotted in 6.10a, 6.10b, and 6.10c, respectively, and the mean duration between subpeaks is plotted in 6.10d. In terms of the number of subpeaks present per event, both the mean and median number were 4-5 subpeaks per event at all four detection potentials.

This analysis reveals some interesting overall trends. The first subpeak typically has the largest area and height. The area progressively decreases with subsequent subpeaks and levels out after the fourth subpeak. The height sharply decreases after the first subpeak and is roughly constant for subsequent subpeaks. The height of the first subpeak shows a very clear potential dependence, with a higher detection potential yielding a greater height. This is likely due to an increasing overpotential driving the electro-oxidation at a greater rate. It is interesting to note that very high maximum current densities are observed (calculated as the peak height/NP surface area), with the first subpeak at a potential of 0.6 V yielding a density of nearly 10 A/cm^2. The typical duration of each subpeak is roughly 1 ms, as is the typical duration between each subpeak.

An additional key observation is that the total charge passed during each event indicates incomplete oxidation of the Ag NP. Figure 6.11 shows a plot of the size distribution of the NPs as determined by TEM imaging (dashed black line) and as calculated from the charge measured by single NP detection at different potentials (solid lines). The NP size was calculated as shown in previous reports (see Appendix 2).[7,14] As seen, the particle size measured by TEM (62 nm) is significantly larger than the particle size determined from electrochemical detection (~37 nm). This indicates incomplete oxidation of the Ag NPs upon collision with the electrode. The diameters reported here suggest that only about 25% of a Ag NP is oxidized. This result is different from earlier reports using this method, which found the electrochemical measurement

of Ag NPs particles to agree well with their known size.[7,14] This discrepancy may be due to our use of a Au detection electrode (as opposed to glassy carbon) or different detection solutions.

We found that both the multipeak behavior and partial oxidation behavior persisted under a variety of detection conditions. We altered the concentration of trisodium citrate in the detection solution from 10 to 26 mM. While the frequency of detection changed, all concentrations showed multipeak detection and partial NP oxidation. We also altered the concentration of KNO_3 from 0 to 25 mM (in the presence of 10 mM trisodium citrate). Again, we found that although the detection frequency changed, multipeak and partial NP oxidation behavior occurs. We also tried detection at four different pH conditions: 10.1, 7.7, 5.5, and 4.4. Figure 6.12 shows 20 ms amperometry traces of representative detection events at the four different pH values. As can be seen, multipeak behavior again occurs under all four conditions. A charge analysis of the detection events also indicated partial NP oxidation under all four pH values.

We performed a final experiment designed to help determine the product resulting from the electro-oxidation of the Ag NPs. An early hypothesis we had to explain the multipeak behavior of Ag NP oxidation involved the formation of an insulating layer of Ag oxide. Since our typical detection solution is slightly basic (pH ~8), we hypothesized that the Ag NPs may be oxidized to Ag oxide rather than Ag^+ ions. To test this, we devised an experiment in which the detection UME was rapidly pulsed between a reducing (-0.2 V) and oxidizing (0.4 V) potential while measuring the current. The goal was to see if any product created during the oxidation of a Ag NP could be collected by electrochemical reduction. Figure 6.13a shows a 1 s section of a current-time trace for a pulsing frequency of 5 Hz. As can be seen an occasional collision event is observed when the electrode is at an oxidizing potential (Figure 6.13b).

To analyze this data, we integrated the charge associated with each potential pulse and background-subtracted this value by the average charge of the ten pulses before and after it. We then plotted these values as a scatter plot (Figure 6.13c and 6.13d), with one x,y data point representing the oxidation and reduction charges associated with one potential pulse cycle. As seen in the scatter plots, the majority of the data points are clustered about the origin, indicating no above-average charge detection. However, it is clear that there are several points with above-average oxidation charges, which indicate the detection of a collision event. In Figure 6.13c, which is the result of potential pulsing at 5 Hz, these points are centered about y = 0, indicating no product collection on the subsequent reduction pulse. However, in Figure 6.13d, which is the result of potential pulsing at 50 Hz, these points are centered on a negatively-sloped line. This indicates product collection on the subsequent reduction pulses in an amount proportional to the amount oxidized. Since collection of the oxidation product only occurs at a high pulsing frequency, this suggests that the oxidation product diffuses away from the electrode upon oxidation, which we believe is consistent with the formation of Ag^+ ions as the electro-oxidation product.

Drawing on all of the results discussed, we hypothesize that the multipeak behavior of single Ag NP electro-oxidation events may be due to diffusion of the Ag NP in and out of contact with the detection UME. As faradaic oxidation of the Ag NP should only occur when the NP is within ~1 nm of the electrode surface, diffusion in and out of this distance could repeatedly turn the oxidation off and on, giving rise to multiple, closely-spaced oxidation peaks. This explanation fits with much of the observed data here. For example, the decrease in the charge passed with each subsequent subpeak could be due to the NPs decreasing size, as part of it oxidizes away each time it contacts the electrode. Additionally, the observation of multipeak

behavior in all conditions tested (different potentials, electrolyte concentrations, and pH values) is consistent with this explanation, as none of these conditions should significantly change the diffusion of the NPs. Lastly, the observation of incomplete NP oxidation is consistent with this explanation, as the NP may only be in the ~1 nm vicinity of the electrode surface for a brief period of time before permanently diffusing away from the electrode surface. Therefore, only a portion of the NP may oxidize.

6.4 Conclusion

In the first part of this chapter, we demonstrated the successful bipolar coupling of the bulk oxidation of Ag to the reduction of resazurin. We showed the correlation between the current and fluorescence signal, proving that FEEM can be used to detect Ag oxidation. We then implemented a novel detection scheme using the stochastic collision of Ag NPs to deliver a specific, quantifiable number of electrons to the bipolar electrode in order to test the detection performance of FEEM. Although we were able to successfully detect single Ag NP oxidation events at a bipolar electrode through the current signal, we were unable to detect any corresponding change in the fluorescence signal. This revealed the present limitation in the ability of FEEM to detect small, discrete redox events. It also revealed the cause of this limitation to be the coupling of electrons to non-fluorogenic side reactions, giving important guidance to future studies aimed at overcoming this limitation. Most importantly, this study shows the utility of using this detection scheme. The easy repeatability of Ag NP collision experiments makes it simple to adjust parameters on the cathodic side of the bipolar electrode in an attempt to get fluorescence detection while keeping the anodic side constant. This detection

scheme will be very useful in future FEEM studies aimed at improving the detection performance.

In the second part of this chapter, we revealed that the electro-oxidation of single Ag NPs colliding with an Au detection UME is a highly dynamic process. A typical detection event is observed as a series of discrete oxidation peaks rather than one large peak, as previously assumed. We have also revealed that the Ag NPs do not undergo complete oxidation. Both of these behaviors were shown to exist under a wide range of detection conditions. We have evidence that suggests this behavior may be due to the diffusion of Ag NPs in and out of contact with the UME surface, however further experiments and simulations are needed to support this hypothesis. This study reveals that NP interactions with an electrode surface are highly dynamic, and it should be broadly relevant to many current studies focused on the electrochemical detection and study of single NPs.

6.5 Figures

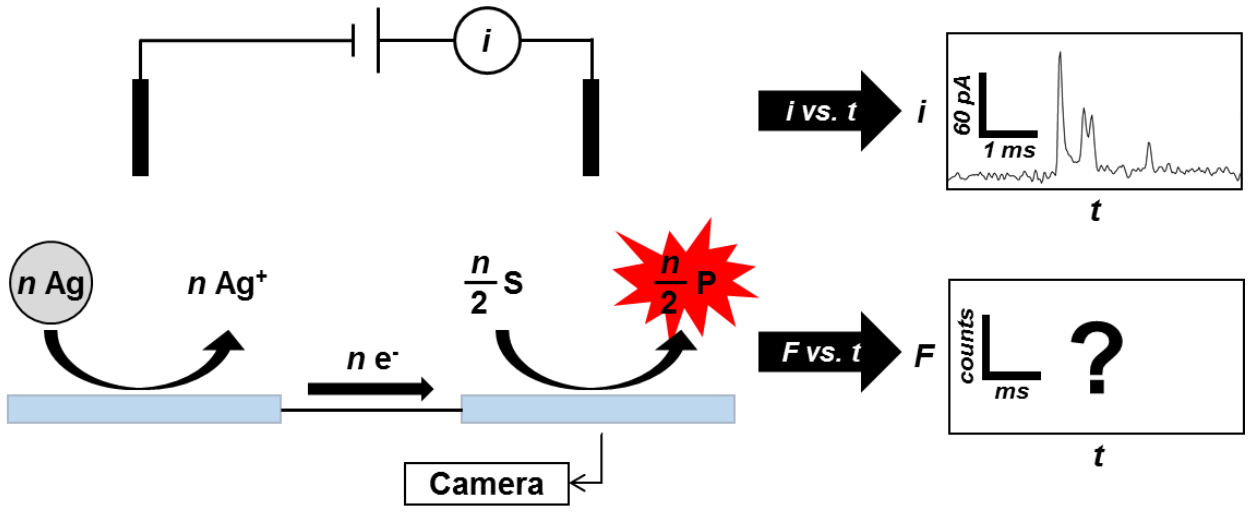

Figure 6.1. Detection scheme for FEEM detection of stochastic Ag NP collisions.
In this scheme, the anodic pole of a bipolar electrode is placed in a solution of Ag NPs, and the cathodic pole is placed in a solution of resazurin (S). Resazurin is a non-fluorescent molecule that can undergo a two-electron reduction to the fluorescent resorufin (P). The cathodic pole is placed on a microscope for observation via fluorescence microscopy. A potential sufficient to drive the coupled reaction of Ag oxidation and resazurin reduction is applied across the bipolar electrode using two driving electrodes, while the current through the bipolar electrode and the fluorescence of the cathodic pole are simultaneously monitored. Each time a Ag NP randomly diffuses to the anodic pole, it will be oxidized, injecting a number of electrons into the bipolar electrode in a discrete event. This results in an oxidative spike in the current signal. If these electrons couple to the reduction of resazurin, this will also result in a burst of fluorescence at the cathodic pole

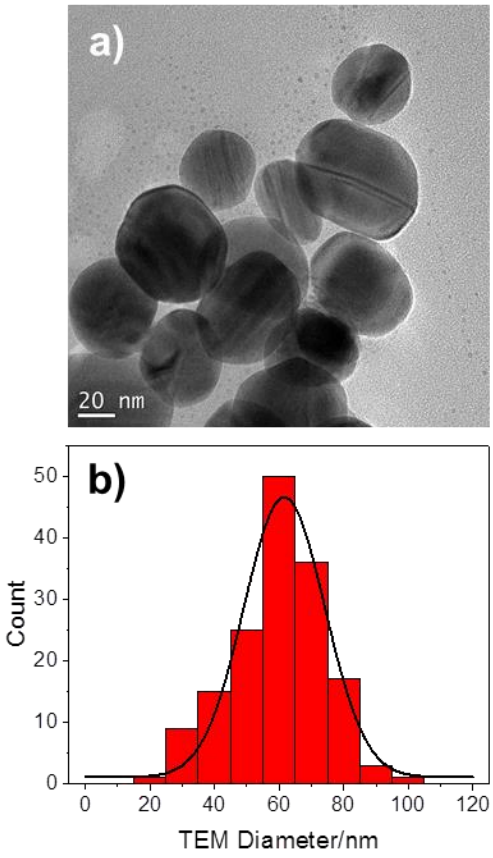

Figure 6.2. TEM image and size distribution of Ag nanoparticles.
(a) TEM image of synthesized citrate-capped Ag NPs. **(b)** Size distribution of NPs as determined from TEM imaging. The black trace represents a Gaussian fit to the histogram.

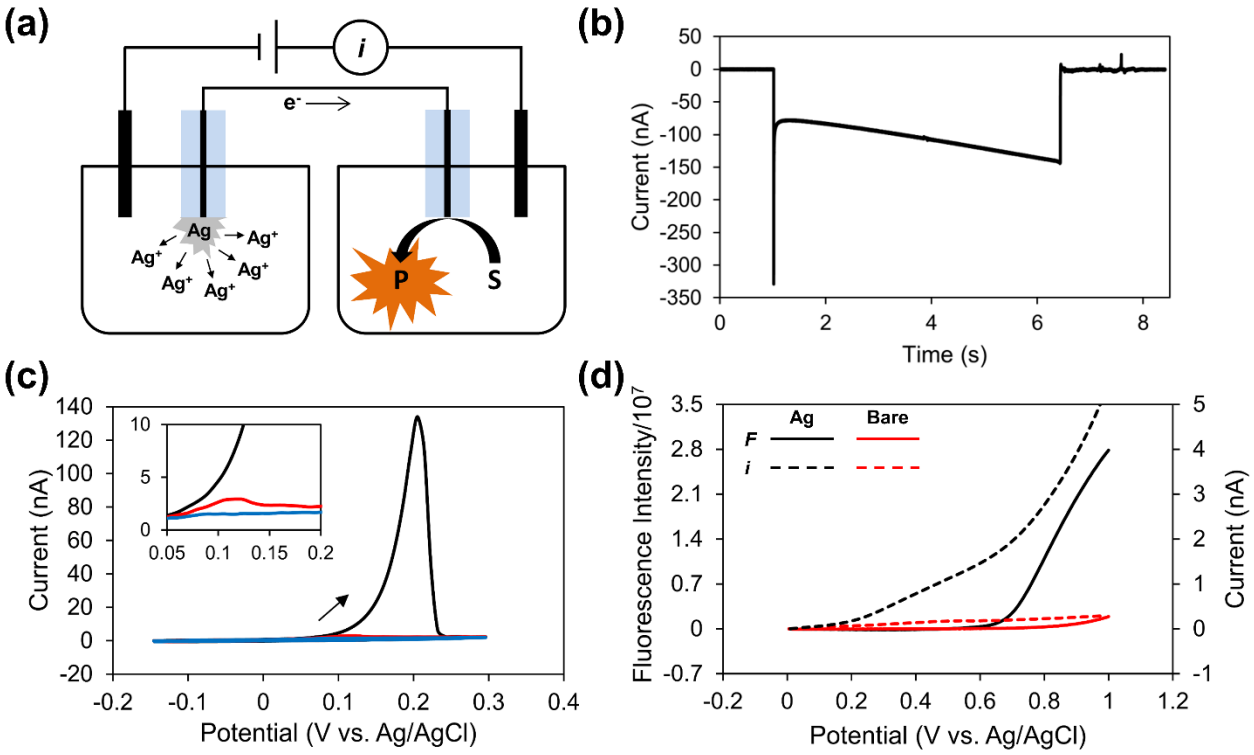

Figure 6.3. Experimental scheme and data for FEEM detection of bulk Ag.
Experimental scheme for the FEEM detection of bulk Ag electrodeposited onto the anodic pole of a bipolar electrode (a). (b) is the current-time trace recorded for a 5 s electrodeposition of Ag onto a 12.7 µm diameter Au electrode using a two-electrode setup. (c) is a series of three consecutive cyclic voltammograms taken of an Ag-coated Au electrode immersed in a solution of supporting electrolyte in a two-electrode setup. (d) shows a FEEM detection experiment as outlined in (a), where the current and fluorescence signal from a bipolar electrode are simultaneously monitored during a potential sweep from 0 to 1 V. In this experiment, the anodic pole of the bipolar electrode is either bare Au (red traces), or Au with Ag electrodeposited onto the surface (black traces).

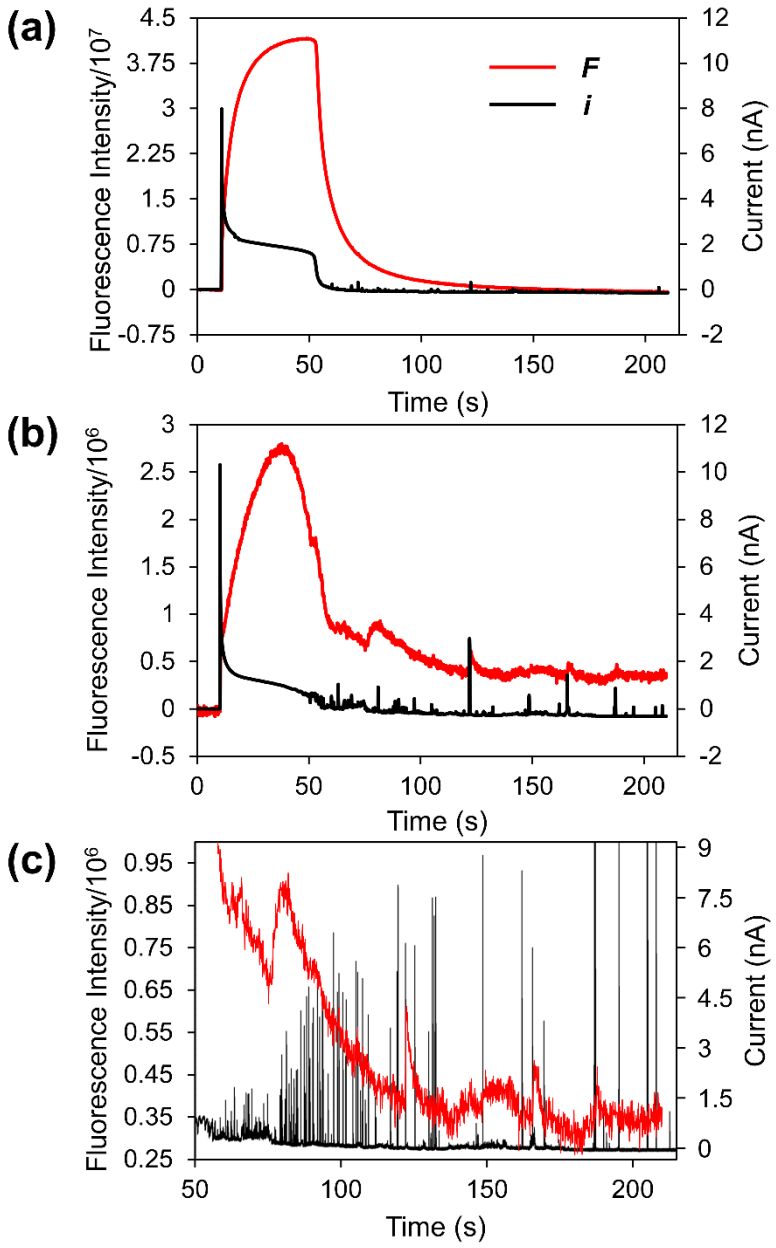

Figure 6.4. FEEM detection of bulk Ag using a potential step.
FEEM detection experiment as outlined in Figure 6.3a, where the fluorescence and current signal from a bipolar electrode are simultaneously monitored during a potential step. In (a) and (b), the anodic pole of the bipolar electrode is an Au electrode with Ag electrodeposited onto the surface, while the cathodic pole is immersed in a solution containing resazurin. The potential is initially held at 0 V for 10 s and then is stepped to 0.8 V for the remainder of the experiment. (c) is a zoom-in of the current and fluorescence signals of (b) from 50 s to the end of the experiment. The current signal in (a) and (b) is averaged to a 10 Hz sampling rate, while the current signal in (c) is left in the original form (1000 Hz sampling rate).

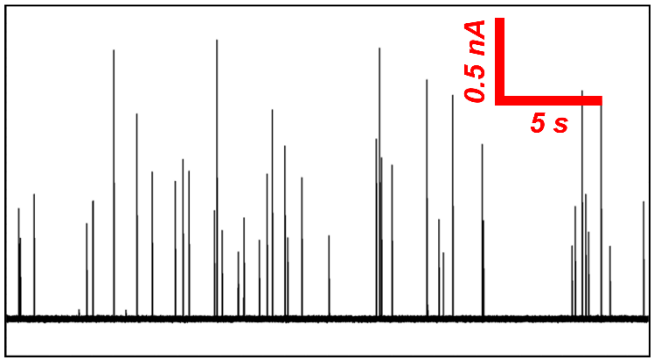

Figure 6.5. Two-electrode detection of single Ag nanoparticles.
Example current-time trace showing Ag NPs colliding with a 12.7 μm diameter Au UME poised at 0.6 V vs. Ag/AgCl. Each spike in the current corresponds to a Ag NP colliding with the UME and undergoing oxidation.

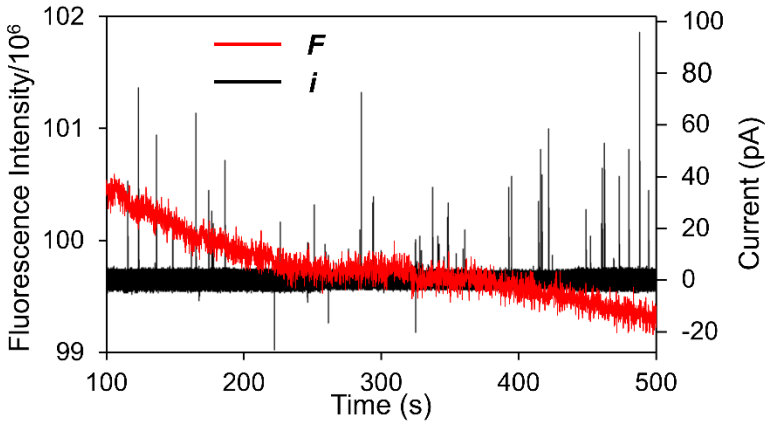

Figure 6.6. Attempt at FEEM detection of single Ag nanoparticles.
Simultaneously monitored fluorescence and current signals for the FEEM detection of single Ag NP collisions. Two Au electrodes were connected to form a bipolar electrode as shown in Figure 6.3a, with the cathodic pole immersed in a solution of resazurin and the anodic pole immersed in a dispersed solution of Ag NPs. The potential was held at 0.6 V for the duration of the experiment.

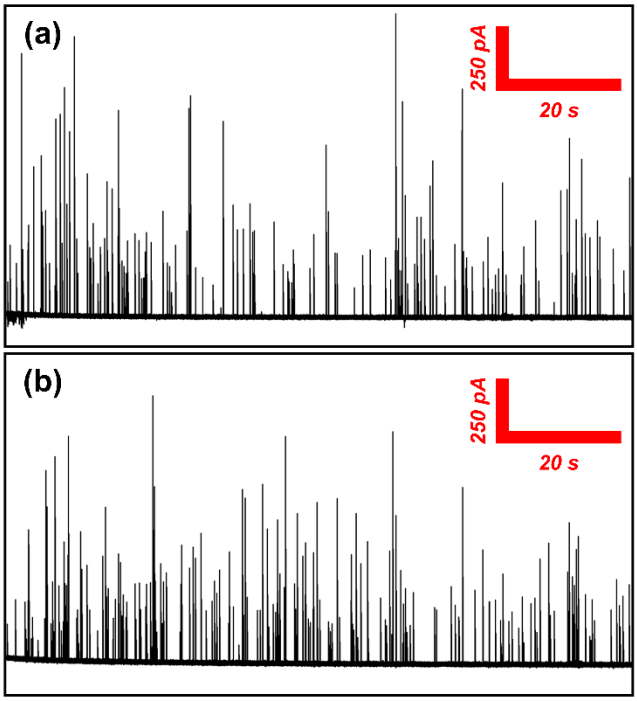

Figure 6.7. Bipolar detection of single Ag nanoparticles with and without resazurin. Current-time traces for the bipolar detection of single Ag NPs. For (a), the cathodic pole of the bipolar electrode was placed in a solution of 50 mM pH 7.5 phosphate buffer. For (b), the cathodic pole was placed in a solution of 50 mM pH 7.5 phosphate buffer containing 5 µM resazurin. For both (a) and (b), the anodic pole of the bipolar electrode was placed in a solution of dispersed Ag NPs. The potential was held at 0.6 V for the duration of both experiments.

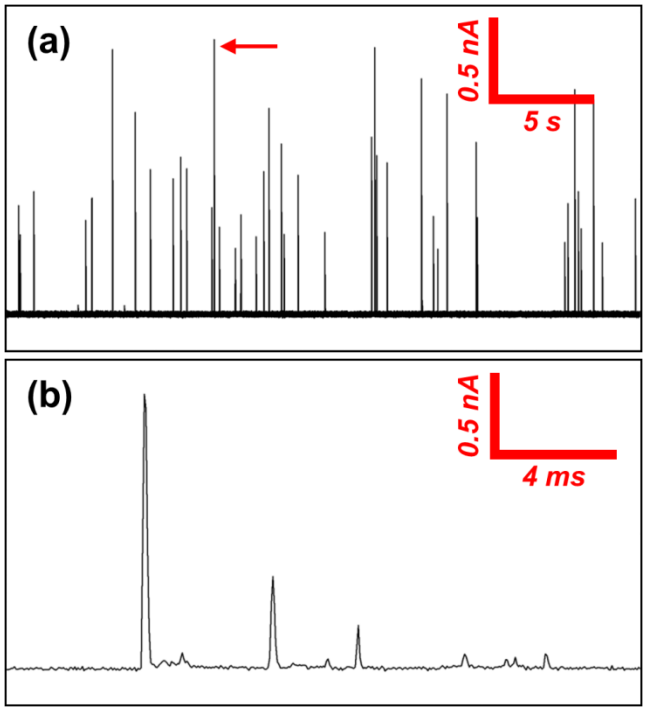

Figure 6.8. Example of the multipeak behavior observed during Ag nanoparticle oxidation. Example detection trace of Ag NPs colliding with an Au UME poised at 0.6 V vs. Ag/AgCl. (a) 30 s detection trace, with each spike corresponding to a particle colliding with the UME and undergoing oxidation. This is the same trace shown in Figure 6.5. (b) 20 ms zoom-in trace of the event in (a) indicated with the red arrow. As seen, this event is made up of several smaller, discrete spikes.

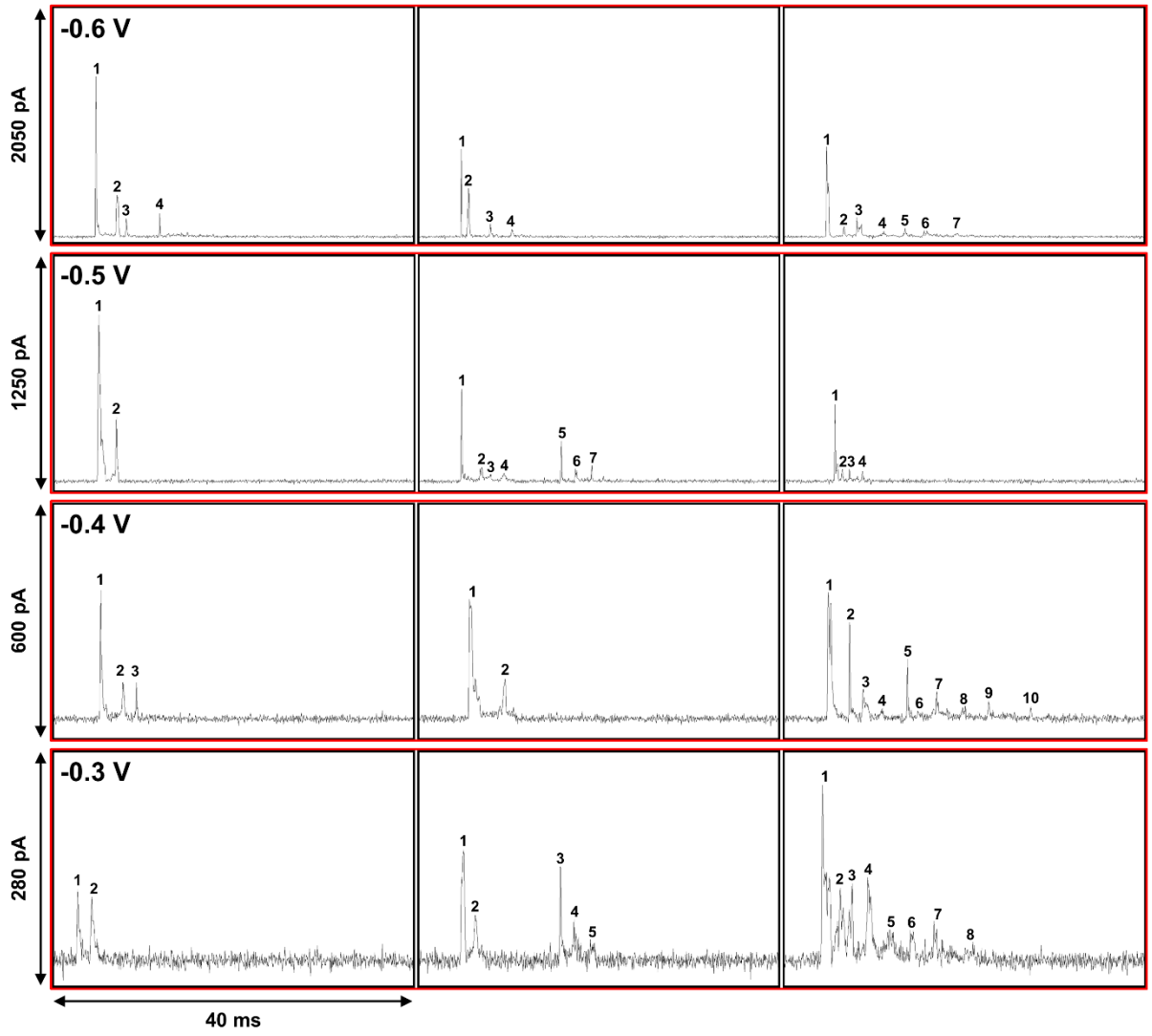

Figure 6.9. Example current-time traces of events used for subpeak analysis.
Current-time traces showing three of the oxidation events at each potential used for the subpeak analysis presented in Figure 6.10. The time scale is 40 ms for all traces. Note the different current scales for each potential.

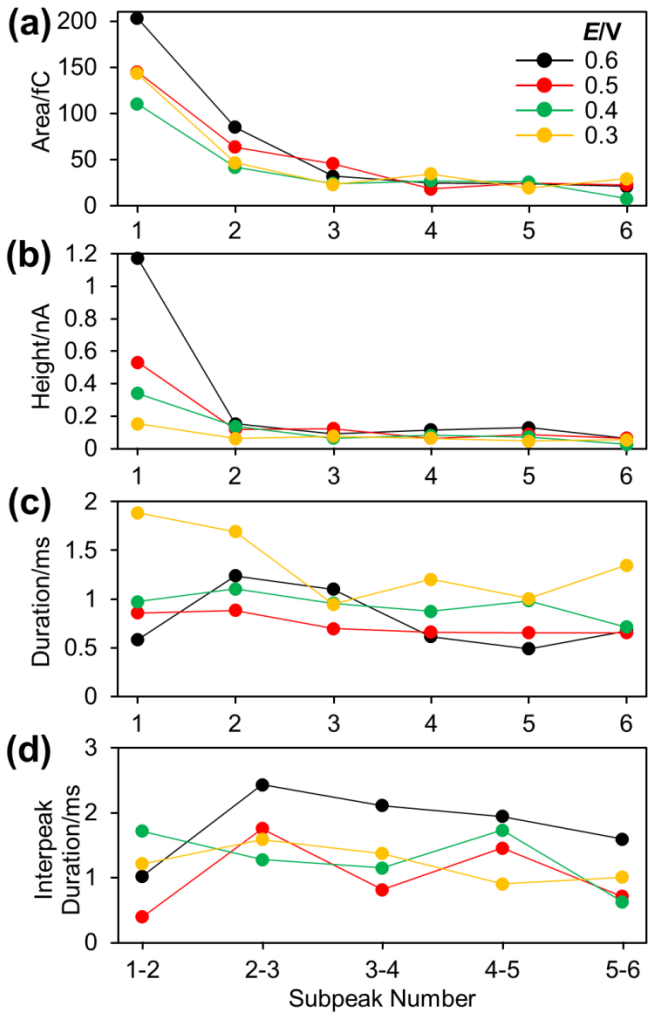

Figure 6.10. Subpeak analysis of Ag nanoparticle oxidation events.
Analysis of the first six subpeaks for 25 random oxidation events recorded at each of four different detection potentials. (a), (b), and (c) give the mean subpeak area, height, and duration, respectively. (d) gives the mean duration between subpeaks.

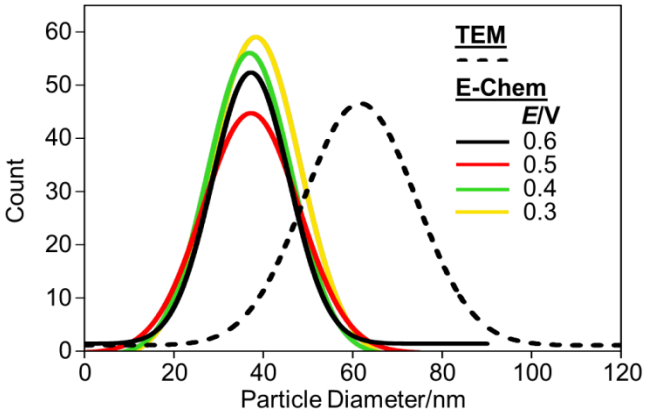

Figure 6.11. TEM and electrochemical measurement of Ag nanoparticle diameter.
Comparison of Ag NP diameters as measured by TEM imaging and single-NP electrochemical detection.

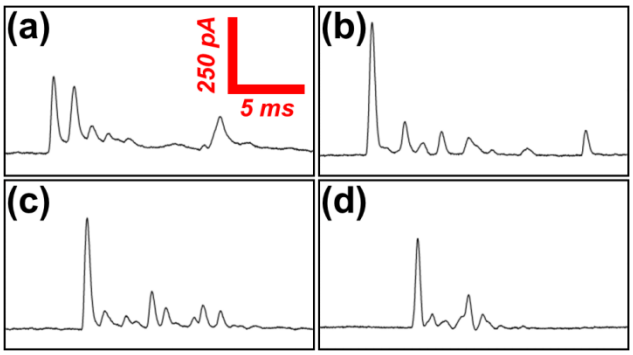

Figure 6.12. Typical Ag nanoparticle oxidation events at different pH values.
20 ms amperometric traces showing a representative detection event at each of four pH values: (a) pH 10.1 (b) pH 7.7 (c) pH 5.5 (d) pH 4.4. As seen, similar multipeak behavior is observed under all four conditions.

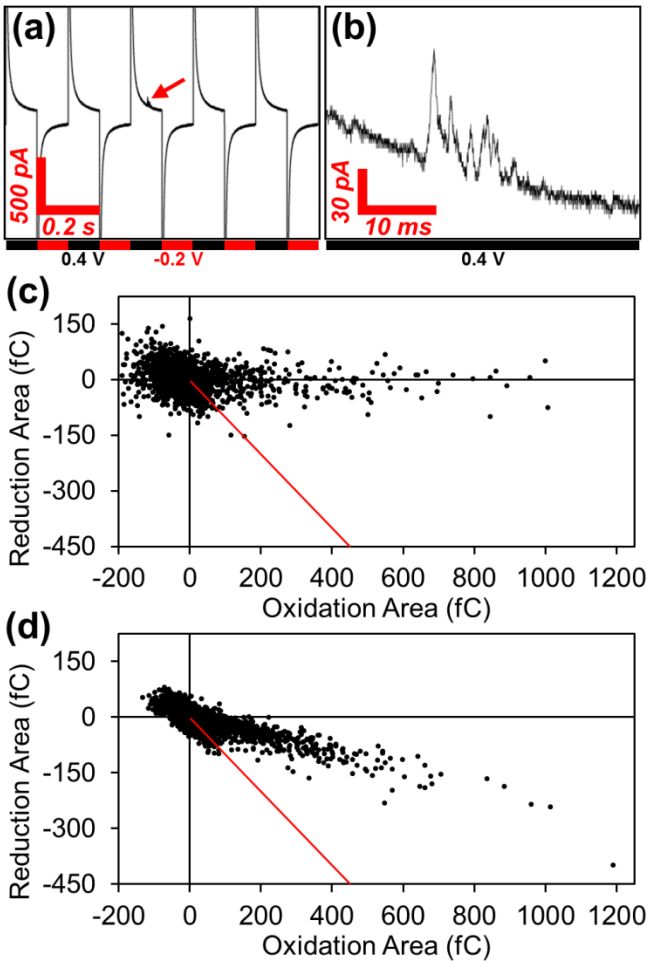

Figure 6.13. Ag nanoparticle detection with potential pulsing.
Results of an Ag NP detection experiment with potential pulsing. (a) Section of a current-time trace from a detection experiment with a pulsing frequency of 5 Hz. (b) Zoom-in of the collision event indicated in (a) with the red arrow. (c) and (d) Scatter plots of detection experiments with pulsing frequencies of 5 Hz and 50 Hz, respectively. The solid red lines in (c) and (d) are lines with a slope of -1 and intercept of 0 and indicate 100% collection efficiency (i.e. oxidation area = -reduction area).

6.6 Appendix 1

Calculation of Expected Collision Frequency

As previously reported,[13] a theoretical NP collision frequency, *f*, for detection on a disk-shaped UME can be calculated using the following equation:

$$f = 4 D_{NP} C_{NP} r_{electrode} N_A$$

where D_{NP} is the NP diffusion coefficient, C_{NP} is the molar concentration of NPs, $r_{electrode}$ is the radius of the detection electrode, and N_A is the Avogadro constant. The diffusion coefficient of the approximately spherical NPs can be calculated using the Stokes-Einstein equation:

$$D_{NP} = \frac{k_B T}{6\pi\eta r_{NP}}$$

where k_B is the Boltzmann constant, T is the solution temperature, η is the solution viscosity, and r_{NP} is the radius of the NPs. Using a temperature of 293 K, a viscosity of 1.002×10^{-3} kg/m·s, and an average NP radius of 31 nm gives a NP diffusion coefficient of 6.91×10^{-12} m^2/s. Using this value for D_{NP} with a 6.35 μm radius detection electrode and a 30 pM NP concentration gives a theoretical NP collision frequency of 3.2 collisions/s.

6.7 Appendix 2

Calculation of Nanoparticle Size from Measured Charge

As previously reported,[7] a silver NP radius, *r*, can be calculated from the charge measured during an oxidation event using the following equation:

$$r = \left(\frac{3 AM_{Ag} Q}{4\pi F \rho_{Ag}} \right)^{\frac{1}{3}}$$

where AM_{Ag} is the atomic mass of silver, Q is the charge measured from the oxidation event, F is the Faraday constant, and ρ_{Ag} is the density of silver. The equation assumes that the NP has a spherical shape. To make the Gaussian fits shown in Figure 6.11, we first integrated the charge associated with each detection event and converted this number to a NP diameter using the equation above. These diameter values were then plotted in histograms, which are shown below in Figure 6.A2.1. A Gaussian fit was performed on each of these histograms. These fits, which are overlaid on the histograms in Figure 6.A2.1, are the same as those shown in Figure 6.11. Table 6.A2.1 gives numbers associated with each histogram and respective Gaussian fit.

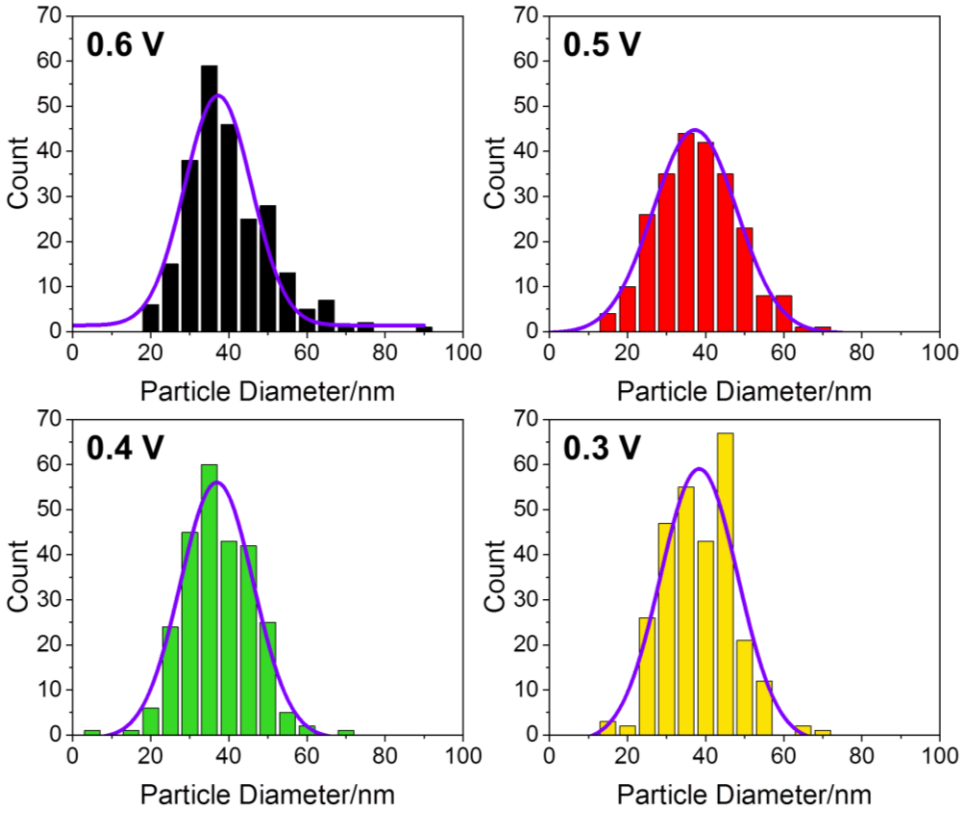

Figure 6.A2.1. Nanoparticle diameters calculated from electrochemical detection data. Histograms and corresponding Gaussian fits of calculated Ag NP diameters from electrochemical detection at different potentials.

E/V vs. Ag/AgCl	*n*	*d*/nm	*Std. Dev.*/nm
0.6	246	37.2	8.6
0.5	237	37.2	10.7
0.4	255	36.9	9.3
0.3	279	38.3	9.9

Table 6.A2.1. Histogram and Gaussian fit data for Ag NP detection at different potentials. *E* is the potential of the detection electrode, *n* is the number of NP oxidation events recorded, *d* is the estimated mean value of the calculated NP diameter as determined by the center of the Gaussian fit, and *Std. Dev.* is the standard deviation associated with *d*.

6.8 References

(1) Xiao, X.; Bard, A.J. *J. Am. Chem. Soc.* **2007**, *129*, 9610-9612.

(2) Cheng, W.; Compton, R.G. *TRAC-Trend. Anal. Chem.* **2014**, *58*, 79-89.

(3) Oja, S.M.; Wood, M.R.; Zhang, B. *Anal. Chem.* **2013**, *85*, 473-486.

(4) Oja, S.M.; Fan, Y.; Armstrong, C.; Defnet, P.; Zhang, B. *Anal. Chem.* **2016**, *88*, 414-430.

(5) Xiao, X.; Fan, F.-R.F.; Zhou, J.; Bard, A.J. *J. Am. Chem. Soc.* **2008**, *130*, 16669-16677.

(6) Guo, Z.; Percival, S.J.; Zhang, B. *J. Am. Chem. Soc.* **2014**, *136*, 8879-8882.

(7) Zhou, Y.-G.; Rees, N.V.; Compton, R.G. *Angew. Chem. Int. Ed.* **2011**, *50*, 4219-4221.

(8) Zhou, Y.-G.; Rees, N.V.; Pillay, J.; Tshikhudo, R.; Vilakazib, S.; Compton, R.G. *Chem. Commun.* **2012**, *48*, 224-226.

(9) Stuart, E.J.E.; Zhou, Y.-G.; Rees, N.V.; Compton, R.G. *RSC Advances* **2012**, *2*, 6879-6884.

(10) Wang, J.; Trouillon, R.; Lin, Y.; Svensson, M.; Ewing, A.G. *Anal. Chem.* **2013**, *85*, 5600-5608.

(11) Schneider, C.A.; Rasband, W.S.; Eliceiri, K.W. *Nat. Methods* **2012**, *9*, 671-675.

(12) Guerrette, J. P.; Percival, S. P.; Zhang, B. *J. Am. Chem. Soc.* **2013**, *135*, 855–861.

(13) Kwon, S.J.; Zhou, H.; Fan, F.-R.F.; Vorobyev, V.; Zhang, B.; Bard, A.J. *Phys. Chem. Chem. Phys.* **2011**, *13*, 5394-5402.

(14) Rees, N.V.; Zhou, Y.-G.; Compton, R.G. *ChemPhysChem* **2011**, *12*, 1645-1647.

BIBLIOGRAPHY

Akkilic, N.; Kamran, M.; Stan, R.; Sanghamitra, N. J. M. *Biosens. Bioelectron.* **2015**, *67*, 747−751.

Amatore, C.; Bonhomme, F.; Bruneel, J.-L.; Servant, L.; Thouin, L. *J. Electroanal. Chem.* **2000**, *484*, 1-17.

Amatore, C.; Chovin, A.; Garrigue, P.; Servant, L.; Sojic, N.; Szunerits, S.; Thouin, L. *Anal. Chem.* **2004**, *76*, 7202-7210.

Amemiya, S.; Bard, A.J.; Fan, F.-R.F.; Mirkin, M.V.; Unwin, P.R. *Annu. Rev. Anal. Chem.* **2008**, *1*, 95-131.

Anderson, L.; Wittkopp, S.M.; Painter, C.J.; Liegel, J.J.; Schreiner, R.; Bell, J.A.; Shakhashiri, B.Z. *J. Chem. Ed.* **2012**, *89*, 1425-1431.

Arora, A; Eijkel, J. C. T.; Morf, W. E.; Manz, A. *Anal. Chem.* **2001**, *73*, 3282–3288.

Baltes, N.; Thouin, L.; Amatore, C.; Heinze, J. *Angew. Chem., Int. Ed.* **2004**, *43*, 1431-1435.

Bard, A.J.; Fan, F.R.F. *Acc. Chem. Res.* **1996**, *29*, 572-578.

Bard, A.J.; Faulkner, L.R. *Electrochemical Methods*, 2nd ed.; John Wiley & Sons: New York, **2001**.

Beasley, C.A.; Murray, R.W. *Langmuir* **2009**, *25*, 10370-10375.

Beden, B.; Largeaud, F.; Kokoh, K. B.; Lamy, C. *Electrochimica Acta* **1996**, *41*, 701–709.

Bouffier, L.; Doneux, T.; Bertrand, G.; Kuhn, A. *Anal. Chem.* **2014**, *86*, 3708-3711.

Braga, M.; Leite, C.A.P.; Galembeck, F. *Langmuir* **2003**, *19*, 7580-7586.

Budny, A.; Novak, F.; Plumeré, N.; Schetter, B.; Speiser, B.; Straub, D.; Mayer, H.A.; Reginek, M. *Langmuir* **2006**, *22*, 10605-10611.

Campbell, J. A. *J. Chem. Ed.* **1963**, *40*, 578–583.

Cannan, S.; Macklam, I.D.; Unwin, P.R. *Electrochem. Commun.* **2002**, *4*, 886-892.

Caruso, F. *Adv. Mater.* **2001**, *13*, 11-22.

Chang, B.-Y.; Chow, K.-F.; Crooks, J.A.; Mavré, F.; Crooks, R.M. *Analyst* **2012**, *137*, 2827-2833.

Chang, B.-Y.; Mavré, F.; Chow, K.-F.; Crooks, J.A.; Crooks, R.M. *Anal. Chem.* **2010**, *82*, 5317-5322.

Chen, C.-C.; Derylo, M.A.; Baker, L.A. *Anal. Chem.* **2009**, *81*, 4742-4751.

Chen, C.-C.; Zhou, Y.; Baker, L.A. *Annu. Rev. Anal. Chem.* **2012**, *5*, 207-228.

Cheng, W.; Compton, R.G. *TRAC-Trend. Anal. Chem.* **2014**, *58*, 79-89.

Chow, K.F.; Mavré, F.; Crooks, J.A.; Chang, B.-Y.; Crooks, R.M. *J. Am. Chem. Soc.* **2009**, *131*, 8364-8365.

Chow, K.-F.; Mavré, F.; Crooks, R.M. *J. Am. Chem. Soc.* **2008**, *130*, 7544-7545.

Comstock, D. J.; Elam, J. W.; Pellin, M. J.; Hersam, M. C. *Anal. Chem.* **2010**, *82*, 1270-1276.

Cortes, E.; Etchegoin, P. G.; Le Ru, E. C.; Fainstein, A.; Vela,́ M. E.; Salvarezza, R. C. *J. Am. Chem. Soc*. **2010**, *132*, 18034−18037.

Cox, J. T.; Guerrette, J. P.; Zhang, B. *Anal. Chem.* **2012**, *84*, 8797–8804.

Crooks, R.M. *ChemElectroChem* **2016**, *3*, 357-359.

Dick, J.E.; Renault, C.; Kim, B.-K.; Bard, A.J. *Angew. Chem., Int. Ed.* **2014**, *53*, 11859-11862.

Duval, J. F. L.; Minor, M.; Cecilia, J.; van Leeuwen, H. P. *J. Phys. Chem. B.* **2003**, *107*, 4143–4155.

Ebejer, N.; Güell, A. G.; Lai, S. C. S.; McKelvey, K.; Snowden, M. E.; Unwin, P. R. *Annu. Rev. Anal. Chem.* **2013**, *6*, 329−351.

Eckenrode, H.M.; Jen, S.-H.; Han, J.; Yeh, A.-G.; Dai, H.-L. *J. Phys. Chem. B* **2005**, *109*, 4646-4653.

Engstrom, R.C.; Meaney, T.; Tople, R.; Wightman, R.M. *Anal. Chem.* **1987**, *59*, 2005-2010.

Engstrom, R.C.; Pharr, C.M.; Koppang, M.D. *J. Electroanal. Chem.* **1987**, *221*, 251-255.

Engstrom, R.C.; Weber, M.; Wunder, D.J.; Burgess, R.; Winquist, S. *Anal. Chem.* **1986**, *58*, 844-848.

Eßmann, V.; Jambrec, D.; Kuhn, A.; Schuhmann, W. *Electrochem. Commun.* **2015**, *50*, 77-80.

Fan, F.R.F.; Bard, A.J. *Science* **1995**, *267*, 871-874.

Fan, F.R.F.; Kwak, J.; Bard, A.J. *J. Am. Chem. Soc.* **1996**, *118*, 9669-9675.

Fernández, J.L.; Walsh, D.A.; Bard, A.J. *J. Am. Chem. Soc.* **2005**, *127*, 357-365.

Fosdick, S.E.; Anderson, M.J.; Nettleton, E.G.; Crooks, R.M. *J. Am. Chem. Soc.* **2013**, *135*, 5994-5997.

Fosdick, S.E.; Crooks, J.A.; Chang, B.-Y.; Crooks, R.M. *J. Am. Chem. Soc.* **2010**, *132*, 9226-9227.

Fosdick, S. E.; Crooks, R. M. *J. Am. Chem. Soc.* **2012**, *134*, 863–866.

Fosdick, S. E.; Knust, K. N.; Scida, K.; Crooks, R. M. *Angew. Chem. Int. Ed.* **2013**, *52*, 10438–10456.

Gesquiere, A. J.; Park, S. J.; Barbara, P. F. *J. Phys. Chem. B* **2004,** *108*, 10301–10308.

Grime, J.M.A.; Edwards, M.A.; Rudd, N.C.; Unwin, P.R. *Proc. Natl. Acad. Sci. USA*, **2008**, *105*, 14277-14282.

Guerrette, J. P.; Oja, S. M.; Zhang, B. *Anal. Chem.* **2012**, *84*, 1609–1616.

Guerrette, J. P.; Percival, S. P.; Zhang, B. *J. Am. Chem. Soc.* **2013**, *135*, 855–861.

Guo, Z.; Percival, S.J.; Zhang, B. *J. Am. Chem. Soc.* **2014**, *136*, 8879-8882.

Han, K. S.; Liu, G. K.; Zhou, X. C.; Medina, R. E.; Chen, P. *Nano Lett.* **2012**, *12*, 1253–1259.

Han, L.; Chen, J.; Aoki, K. *J. Electroanal. Chem.* **2007**, *602*, 123-130.

Han, L.; Chen, J.; Ikeda, I. *Chem. Lett.* **2005**, *34*, 1512-1513.

Hotta, H.; Akagi, N.; Sugihara, T.; Ichikawa, S.; Osakai, T. *Electrochem. Commun.* **2002**, *4*, 472-477.

Jan, C.-C.; McCreery, R.L.; Gamble, F.T. *Anal. Chem.* **1985**, *57*, 1763-1765.

Jan, C.-C.; McCreery, R.L.; Gamble, F.T. *Anal. Chem.* **1985**, *57*, 1763-1765.

Kandel, E.R.; Schwartz, J.H.; Jessell, T.M.; Siegelbaum, S.A.; Hudspeth, A.J. *Principles of Neural Science*, 5th ed.; McGraw-Hill: New York, **2012**.

Kanoufi, F.; Zu, Y.; Bard, A.J. *J. Phys. Chem B.* **2001**, *105*, 210-216.

Kim, B.-K.; Boika, A.; Kim, J.; Dick, J.E.; Bard, A.J. *J. Am. Chem. Soc.* **2014**, *136*, 4849-4852.

Kim, B.-K.; Kim, J.; Bard, A.J. *J. Am. Chem. Soc.* **2015**, *137*, 2343-2349.

Komura, T.; Niu, G.Y.; Yamaguchi, T.; Asano, M.; Matsuda, A. *Electroanal.* **2004**, *16*, 1791-1800.

Kuhn, A.; Crooks, R.M.; Inagi, S. *ChemElectroChem* **2016**, *3*, 351-352.

Kwon, S.J.; Zhou, H.; Fan, F.-R.F.; Vorobyev, V.; Zhang, B.; Bard, A.J. *Phys. Chem. Chem. Phys.* **2011**, *13*, 5394-5402.

Lazenby, R.A.; McKelvey, K.; Unwin, P.R. *Anal. Chem.* **2013**, *85*, 2937-2943.

Leaist, D.G. *Can. J. Chem.* **1988**, *66*, 2452-2457.

Lee, S.-K.; Mills, A. *J. Fluoresc.* **2003**, *13*, 375-377.

Lei, C.; Hu, D.; Ackerman, E. J. *Chem. Commun.* **2008**, 5490-5492.

Lei, C.; Hu, D.; Ackerman, E. J. *Nano Lett.* **2009**, *9*, 655-658.

Lemay, S.G.; Kang, S.; Mathwig, K.; Singh, P.S. *Acc. Chem. Res.* **2013**, *46*, 369-377.

Li, Y.; Deng, H.; Dick, J.E.; Bard, A.J. *Anal. Chem.* **2015**, *87*, 11013-11021.

Lin, X.; Zheng, L.; Gao, G.; Chi, Y.; Chen, G. *Anal. Chem.* **2012**, *84*, 7700-7707.

Lin, Y.; Trouillon, R.; Svensson, M.I.; Keighron, J.D.; Cans, A.-S.; Ewing, A.G. *Anal. Chem.* **2012**, *84*, 2949-2954.

Lui, R.; Zhang, C.; Liu, M. *Sensor Actuat B-Chem* **2015**, *216*, 255-262.

Macpherson, J. V.; Unwin, P. R. *Anal. Chem.* **2000**, *72*, 276-285.

Matsumoto, F.; Harada, M.; Koura, N.; Uesugi, S. *Electrochem. Commun.* **2003**, *5*, 42-46.

Maus, R.G.; McDonald, E.M.; Wightman, R.M. *Anal. Chem.* **1999**, *71*, 4944-4950.

Mavre, F.; Anand, R. K.; Laws, D. R.; Chow, K. F.; Chang, B. Y.; Crooks, J. A.; Crooks, R. M. *Anal. Chem.* **2010**, *82*, 8766–8774.

Mavré, F.; Chow, K.-F.; Sheridan, E.; Chang, B.-Y.; Crooks, J.A.; Crooks, R.M. *Anal. Chem.* **2009**, *81*, 6218-6225.

Méallet-Renault, R.; Denjean, P.; Pansu, R.B. *Sensor. Actuat. B-Chem.* **1999**, *59*, 108-112.

Miao, W.; Bard, A.J. *Anal. Chem.* **2004**, *76*, 5379-5386.

Miao, W.; Choi, J.-P.; Bard, A.J. *J. Am. Chem. Soc.* **2002**, *124*, 14478-14485.

Moerner, W. E. *Angew. Chem., Int. Ed.* **2015**, *54*, 8067−8093

Mubarekyan, E.; Santore, M. *Langmuir* **1998**, *14*, 1597-1603.

Muller, R.H. *Adv. Electroch. El. Eng.***1973**, *9*, 281.

Ndungu, P. G. Ph.D. Thesis, Drexel University, Philadelphia, PA, **2004**.

Nebel, M.; Eckhard, K.; Erichsen, T.; Schulte, A.; Schuhmann, W. *Anal. Chem.* **2010**, *82*, 7842-7848.

Noffsinger, J.B.; Danielson, N.D. *Anal. Chem.* **1987**, *59*, 865-868.

O'Connell, M. A.; Wain, A. J. *Anal. Chem.* **2014**, *86*, 12100-12107.

Oja, S.M.; Fan, Y.; Armstrong, C.; Defnet, P.; Zhang, B. *Anal. Chem.* **2016**, *88*, 414-430.

Oja, S.M.; Guerrette, J.P.; David, M.R.; Zhang, B. *Anal. Chem.* **2014**, *86*, 6040-6048.

Oja, S.M.; Wood, M.R.; Zhang, B. *Anal. Chem.* **2013**, *85*, 473-486.

Oja, S.M.; Zhang, B. *Anal. Chem.* **2014**, *86*, 12299-12307.

Oja. S.M.; Zhang, B. *ChemElectroChem* **2016**, *3*, 457-464.

Palacios, R. E.; Fan, F. R. F.; Bard, A. J.; Barbara, P. F. *J. Am. Chem. Soc.* **2006,** *128*, 9028-9029.

Palacios, R. E.; Fan, F. R. F.; Grey, J. K.; Suk, J.; Bard, A. J.; Barbara, P. F. *Nat. Mater.* **2007,** *6*, 680-685.

Park, S.; Boo, H.; Chung, T. D. *Anal. Chim. Acta* **2006**, *556*, 46-57.

Pawliszyn, J.; Weber, M.F.; Dignam, M.J.; Mandelis, A.; Venter, R.D.; Park, S.-M. *Anal. Chem.* **1986**, *58*, 236-239.

Pawliszyn, J.; Weber, M.F.; Dignam, M.J.; Venter, R.D.; Park, S.-M. *Anal. Chem.* **1986**, *58*, 239-242.

Pebay, C.; Sella, C.; Thouin, L.; Amatore, C. *Anal. Chem.* **2013**, *85*, 12062-12069.

Plana, D.; Jones, F. G. E.; Dryfe, R. A. W. *J. Electroanal. Chem.* **2010**, *646*, 107-113.

Plana, D.; Shul, G.; Stephenson, M.J.; Dryfe, R.A.W. *Electrochem. Commun.* **2009**, *11*, 61-64.

Posdorfer, J.; Olbrich-Stock, M.; Schindler, R.N. *Electrochim. Acta*, **1994**, *39*, 2005-2013.

Pruiksma, R.; McCreery, R.L. *Anal. Chem.* **1979**, *51*, 2253-2257.

Pruiksma, R.; McCreery, R.L. *Anal. Chem.* **1981**, *53*, 202-206.

Rees, N.V.; Zhou, Y.-G.; Compton, R.G. *ChemPhysChem* **2011**, *12*, 1645-1647.

Rudd, N.C.; Cannan, S.; Bitziou, E.; Ciani, I.; Whitworth, A.L.; Unwin, P.R. *Anal. Chem.* **2005**, *77*, 6205-6217.

Saito, Y. *Rev. Polarogr*. **1968**, *15*, 177-182.

Schilling, E.A.; Kamholz, A.E.; Yager, P. *Anal. Chem.* 2002, 74, 1798-1804.

Schindelin, I.A.-C.; Frise, E.; Kaynig, V.; Longair, M.; Pietzsch, T.; Preibisch, S.; Rueden, C.; Saalfeld, S.; Schmid, B.; Tinevez, J.-Y.; White, D.J.; Hartenstein, V.; Eliceiri, K.; Tomancak, P.; Cardona, A. *Nature Methods* **2012**, *9*, 676-682.

Schmid, B.; Schindelin, J.; Cardona, A.; Longair, M.; Heisenberg, M. *BMC Bioinformatics* **2010**, *11*, 274.

Schneider, C.A.; Rasband, W.S.; Eliceiri, K.W. *Nat. Methods* **2012**, *9*, 671-675.

Schulte, A.; Nebel, M.; Schuhmann, W. *Annu. Rev. Anal. Chem.* **2010**, *3*, 299-318.

Scott, E.R.; White, H.S.; Phipps, J.B. *Anal. Chem.* **1993**, *65*, 1537-1545.

Serebrennikova, I.; Lee, S.; White, H.S. *Faraday Discuss.* **2002**, *121*, 199-210.

Shakashiri, B. Z. *Chemical Demonstrations: A Handbook for Teachers in Chemistry*, Vol. 2; University of Wisconsin Press: Madison, WI; **1989**.

Strein, T.G.; Ewing, A.G. *Anal. Chem.* **1992**, *64*, 1368-1373.

Stuart, E.J.E.; Zhou, Y.-G.; Rees, N.V.; Compton, R.G. *RSC Advances* **2012**, *2*, 6879-6884.

Sugano, K. Kansy, M.; Artursson, P.; Avdeef, A.; Bendels, S.; Di, L.; Ecker, G.F.; Faller, B.; Fischer, H.; Gerebtzoff, G.; Lennernaes, H.; Senner, F. *Nat. Rev. Drug Discovery* **2010**, *9*, 597-614.

Sun, P.; Mirkin, M.V. *J. Am. Chem. Soc.* **2008**, *130*, 8241-8250.

Szunerits, S.; Garrigue, P.; Bruneel, J.-L.; Servant, L.; Sojic, N. *Electroanal.* **2003**, *15*, 548-555.

Takahashi, Y.; Shevchuk, A. I.; Novak, P.; Murakami, Y.; Shiku, H.; Korchev, Y. E.; Matsue, T. *J. Am. Chem. Soc.* **2010**, *132*, 10118-10126.

Twigg, R. S. *Nature* **1945**, *155*, 401-402.

Ulrich, C.; Andersson, O.; Nyholm, L.; Bjorefors, F. *Angew. Chem. Int. Ed.* **2008**, *47*, 3034-3036.

Vassilyev, Y. B.; Khazova, O. A.; Nikolaeva, N. N. *J. Electroanal. Chem.* **1985**, *196*, 127-144.

Vitt, J.E.; Engstrom, R.C. *Anal. Chem.* **1997**, *69*, 1070-1076.

Wang, J.; Trouillon, R.; Lin, Y.; Svensson, M.; Ewing, A.G. *Anal. Chem.* **2013**, *85*, 5600-5608.

Wilson, A. J.; Willets, K. A. *Nano Lett.* **2014**, *14*, 939-945.

Wolfe, R.L.; Balasubramanian, R.; Tracy, J.B.; Murray, R.W. *Langmuir* **2007**, *23*, 2247-2254.

Working with Microspheres, Tech Note 201; Bangs Laboratories, Inc.: Fisher, IN; **2002**.

Wu, H.P.; McCreery, R.L. *Anal. Chem.* **1989**, *61*, 2347-2352.

Wu, M.-S.; Liu, Z.; Shi, H.-W.; Chen, H.-Y.; Xu, J.-J. *Anal. Chem.* **2015**, *87*, 530-537.

Wu, M.-S.; Qian, G.-S.; Xu, J.-J.; Chen, H.-Y. *Anal. Chem.* **2012**, *84*, 5407-5414.

Wu, M.-S.; Xu, B.-Y.; Shi, H.-W.; Xu, J.-J.; Chen, H.-Y. *Lab Chip*, **2011**, *11*, 2720-2724.

Wu, M.-S.; Yuan, D.-J.; Xu, J.-J.; Chen, H.-Y. *Chem. Sci.* **2013**, *4*, 1182-1188.

Wu, S.; Zhou, Z.; Xu, L.; Su, B.; Fang, Q. *Biosens. Bioelectron.* **2014**, *53*, 148-153.

Xiao, X.; Bard, A.J. *J. Am. Chem. Soc.* **2007**, *129*, 9610-9612.

Xiao, X.; Fan, F.-R.F.; Zhou, J.; Bard, A.J. *J. Am. Chem. Soc.* **2008**, *130*, 16669-16677.

Xu, W.; Kong, J. S.; Yeh, Y. T. E.; Chen, P. *Nat. Mater.* **2008**, *7*, 992–996.

Xu, W.; Shen, H.; Kim, Y. J.; Zhou, X. C.; Liu, G. K.; Park, J.; Chen, P. *Nano Lett.* **2009,** *9*, 3968–3973.

Zaino, L. P.; Grismer, D. A.; Han, D.; Crouch, G. M.; Bohn, P. W. *Faraday Discuss.* **2015**, *184*, 101-115.

Zevenbergen, M.A.G.; Singh, P.S.; Goluch, E.D.; Wolfrum, B.L.; Lemay, S.G. *Nano Lett.* **2011**, *11*, 2881-2886.

Zhan, W.; Alvarez, J.; Crooks, R.M. *J. Am. Chem. Soc*. **2002**, *124*, 13265-13270.

Zhang, B.; Adams, K.L.; Luber, S.J.; Eves, S.J.; Heien, M.L.; Ewing, A.G. *Anal. Chem.* **2008**, *80*, 1394-1400.

Zhang, B.; Heien, M.L.A.V.; Santillo, M.F.; Mellander, L.; Ewing, A.G. *Anal. Chem.* **2011**, *83*, 571-577.

Zhang, J.; Slevin, C.J.; Unwin, P.R. *Chem. Commun.* **1999**, 1501-1502.

Zhang, J.-D.; Yu, T.; Li, J.-Y.; Xu, J.-J.; Chen, H.-Y. *Electrochem. Commun.* **2014**, *49*, 75-78.

Zhang, X.; Chen, C.; Li, J.; Zhang, L.; Wang, E. K. *Anal. Chem.* **2013**, *85*, 5335–5339.

Zhang, X.; Li, J.; Jia, X.; Li, D.; Wang, E. *Anal. Chem.* **2014**, *86*, 5595-5599.

Zhao, J.; Zaino, L. P., III; Bohn, P. W. *Faraday Discuss.* **2013**, *164*, 57−69.

Zhou, L.; Zhou, Y.; Baker, L.A. *ECS Interface* **2014**, *23*, 47-52.

Zhou, X.; Andoy, N. M.; Liu, G.; Choudhary, E.; Han, K. S.; Shen, H.; Chen, P. *Nat. Nanotechnol.* **2012**, *7*, 237–241.

Zhou, X.; Choudhary, E.; Andoy, N. M.; Zou, N.; Chen, P. *ACS Catal.* **2013**, *3*, 1448–1453.

Zhou, Y.-G.; Rees, N.V.; Compton, R.G. *Angew. Chem. Int. Ed.* **2011**, *50*, 4219-4221.

Zhou, Y.-G.; Rees, N.V.; Pillay, J.; Tshikhudo, R.; Vilakazib, S.; Compton, R.G. *Chem. Commun.* **2012**, *48*, 224-226.

Zu, Y.; Bard, A.J. *Anal. Chem.* **2000**, *72*, 3223-3232.

VITA

Stephen Matthew Oja was born and raised in Walworth, Wisconsin, a small town on the Wisconsin-Illinois border. He attended Big Foot High School, graduating in 2008. He then attended St. Norbert College in De Pere, WI for a year before transferring to the University of Wisconsin—Madison. He graduated with distinction from UW-Madison with a B.S. in chemistry in 2012. At UW-Madison, he worked as an undergraduate researcher in Dr. Frank Keutsch's lab. He also completed an internship at the Brady Corporation in Milwaukee, WI and spent a summer working in Dr. Bo Zhang's lab at the University of Washington, Seattle as part of the Amgen Scholar Program. This experience led him back to the University of Washington and Dr. Zhang's lab for graduate school, where he has worked on his Ph.D. in chemistry since 2012. During this time, he also fell in love with and married his wife, Jess.